The University Of Sheffield.

Effective Computational Coronary Haemodynamics for Clinical Application

Marco Frison

Faculty of Medicine, Dentistry and Health
Department of Infection and Immunity and Cardiovascular Disease
Mathematical Modelling and Medicine Group

Submitted for the degree of PhD

Date of submission
September 2018

Abstract

Background

Coronary artery disease (CAD) is one of the most common causes of death in the world. Diagnosis is based on imaging of the artery, either by CT or conventional angiography. Conventional angiography is an invasive technique which involves the introduction of a system of guide-wires, catheters and radiopaque contrast agent into the patient's coronary arteries. Fractional Flow Reserve (FFR) is widely considered to be the gold-standard assessment of the physiological significance of CAD. FFR is measured invasively by the passage of a pressure wire through the diseased artery.

Hypothesis and Aims

It is hypothesised that a computational model can be employed to characterise the haemodynamics of blood flow in patient-specific coronary arteries in order to compute clinical indices of interest, including FFR, in an effective and reliable way. The aims of this project are to combine a coronary artery reconstruction tool with Computational Fluid Dynamics (CFD) and Reduced Order Modelling (ROM) techniques to estimate the pressure drop and FFR in patient-specific coronary arteries in a fast and accurate way.

Methods & Results

This thesis comprises two parts, both associated with the effective computation of FFR from angiographic data:

i. The first part addresses the problem of accurate reconstruction of coronary artery anatomy from multiple, single-plane coronary angiography (MSPCA), to underpin the creation of a computational model. A segmentation tool with a user-friendly graphical user interface (GUI) was developed in MATLAB to generate the surfaces meshes required for the CFD studies and to obtain other clinically-relevant coronary parameters.

ii. The second part focuses on the effective and accurate computation of the pressure gradient and the FFR using ROMs built from CFD solutions in ANSYS-Fluent, exploiting the ANSYS ROMBuilder suite. The methods were applied to compute pressure profiles along the length of the artery, and FFR, in representations of coronary stenosis. The study includes the identification of an appropriate parameterisation of the artery shape to support the effective construction and operation of a ROM, as well as an evaluation of the sources of error and a comparison between results from Bernoulli

estimates, from 1D models, from ROM, from CFD and from clinical measurement. Sequential increases in complexity of the anatomical representation are made, from axisymmetric with idealised stenoses to realistic radius variations from a coronary artery dataset and finally to curved arteries. In all cases each arterial cross-section is assumed to be circular. The study includes analysis of the interaction between idealised serial stenoses, and of a dataset of 140 patient-specific arteries characterised by angiography

Results and Conclusions

It was demonstrated that ROM applied to idealised coronary geometries achieved accuracies comparable with CFD results, and better than other approaches, in dramatically reduced timescales (order 900 times reduction relative to CFD). Limitations and opportunities for improvement include more accurate reconstruction of the cross-sectional profiles, more comprehensive representation of 3D curvature in the ROM and improved automation of segmentation, but the ROM approach shows great promise for this application in the delivery of solutions of sufficient accuracy in timescales consistent with the clinical process.

Statement of Contribution

This thesis investigates the combination of a developed segmentation algorithm, Computational Fluid Dynamics and Reduced Order Methods to achieve a fast, reliable and objective prediction of patient-specific pressure gradient and FFR. The main contributions of this thesis are:

1) A segmentation tool able to reconstruct in 3D coronary arteries starting from 2D projection images.
2) Reduce Order Methods applied to idealised geometries for a fast computation of the pressure gradient plus fluid flow interactions between multiple lesions;
3) A shape parameterisation with an optimisation method to describe the variation of the radius along the length for patient-specific coronary arteries in 2D;
4) Creation of clinical ROMs for real-time computation of the FFR clinical index, which can support the objectivity of the definition of the FFR on which the clinical decision is made;
5) A centreline based parameterisation to describe the curvature of any coronary artery with numerical parameters and 3D ROM construction.

ACKNOWLEDGEMENTS

After four years of research and here we are…it has been an incredible adventure and experience I would suggest everyone to do.

First of all, I would like to express my sincere gratitude to my supervisors Prof. Rod Hose, Prof. Patricia Lawford and Prof. Julian Gunn for their academic and educational support during all my PhD. However, I owe a big thank you to Prof. Hose for his patience and his help in all these years and his invaluable guidance. I would also like to thank ANSYS-France for their technical and financial support together with the University of Sheffield.

A special thank you to Dr. Paul Morris for his clinical guidance; my acknowledgments are extended to the Mathematical Modelling in Medicine Group old and new staff members and students, who have been like a second family for me. To Steve for teasing me with his pineapple pizza. I would also like to thank the Rolls-Royce UTC colleagues, for their support during the last year.

I would like to thank all my friends in Italy, they have been very supportive and encouraging even if they could not understand anything about my PhD.

My special thoughts go to my family: my father, my mother, my sister for their unconditional optimism and belief; my nephews who always make me laugh when I am at home and finally to my grandmother for her invaluable cooking experience. If I have reached this important achievement in my life is thank to you.

Last, but not least, I would like to thank Martina, my partner, for her patience, support and care during the most difficult moments, for her encouragement day-by-day; you are very special to me, thank you.

CONTENTS

LIST OF TABLES

LIST OF FIGURES

LIST OF ABBREVIATIONS

3DR: Three dimensional Reconstruction;

CAD: Coronary Artery Disease;

CAD geometry: Computed Aided Design geometry;

CAU: Caudal Angulation;

CC: Cranial Caudal

CFD: Computational Fluid Dynamics;

CPU: Central Processing Unit;

CTCA: Computed Tomography Coronary Angiography;

DOE: Design Of Experiments;

DX: Diagonal Artery;

ECG: Electrocardiogram;

FFR: Fractional Flow Reserve index;

FVM: Finite Volume Methods;

FEM: Finite Element Methods;

GPU: Graphics Processing Unit;

GUI: Graphic User Interface;

HR: Heart Rate;

ICA: Invasive Coronary Angiography;

LAD: Left Descendent Artery;

LAO: Left Anterior Oblique;

LC: Left Coronary;

LCX: Left Circumflex Artery;

LHS: Latin Hypercube Samplings;

LMS: Left Main Stem Artery;

MSPCA: Multiple Single Plane Coronary Angiography;

P_a: proximal pressure;

P_d: distal pressure;

P_v: venous pressure;

POD: Proper Orthogonal Decomposition;

RAM: Random Access Memory;

RAO: Right Anterior Oblique;

RoCA: Rotational Coronary Angiography;

ROI: Region Of Interest;

ROM: Reduction Order Method;

SVD: Singular Value Decomposition;

vFFR: virtual Fractional Flow Reserve;

NOMENCLATURE

Symbol	Description	Units
r_0	Initial vessel radius	mm
r_{max}	Radius	mm
A	Area	mm^2
D	Diameter	mm
dt	Time step	s
E	Young's Modulus	kg m^{-1} s^{-2} (Pa)
g	Gravity	m s^{-2}
L	Length	mm
ΔP	Pressure Gradient	mmHg
P	Pressure	mmHg
Q	Mass flow rate	kg s^{-1} or ml s^{-1}
r	Radial distance from the centreline	mm
R	Resistance	mmHg s ml^{-1}
Re	Reynolds number	Dimensionless
t	Time	s
U	Fluid velocity vector	m s^{-1}
u	Fluid velocity in x-direction	m s^{-1}
v	Fluid velocity in y-direction	m s^{-1}
w	Fluid velocity in w-direction	m s^{-1}
x	Position in first of three orthogonal spatial dimensions	m
y	Position in second of three orthogonal spatial dimensions	m
z	Position in third of three orthogonal spatial dimensions	m
V	Volume	m^3
π	Pi	Dimensionless
ρ	Fluid density	kg m^{-3}
τ	Shear stress	Pa
μ	Fluid Viscosity	kg m^{-1} s^{-1} (Pa s)
C	Correlation matrix	
S	Matrix of snapshots	
K	Total number of snapshots	
M	Total number of modes	
$\|\cdot\|_{L^2}$	L^2 $norm$	

Chapter 1
Introduction

The goal of this thesis is to develop and to report a process for fast and effective computation of an important measure of coronary physiology, namely Fractional Flow Reserve (FFR) [1].

The underpinning methods are:

i. Reconstruction of coronary arteries in three dimensions from coronary angiography images.
ii. Computational Fluid Dynamics (CFD) analyses to compute pressure distributions in the coronary arteries.
iii. Coupling between CFD analysis and simple lumped parameter models to provide appropriate boundary conditions for the coronary analysis.
iv. Parameterisation of coronary anatomy to provide a representation to support a Reduced Order Model (ROM) protocol.
v. Development of ROM models, with the aim to support the very rapid computation of FFR in clinically-viable timescales (a few minutes).
vi. Validation of ROM against measured clinical data.

In this first chapter the context and background material is described, together with a brief overview of the technologies that are deployed in this work. The chapter commences with the motivation of the project, followed by an introduction to the relevant cardiovascular anatomy and physiology. Particular attention is given firstly to coronary circulation in order to understand the physiology and secondly to the clinical assessment and treatment of coronary artery disease, including the processes of coronary angiography and the measurement or computation of FFR.

1.1 Motivation

Modelling and simulating biological processes in a virtual environment has never been an easy task to achieve. Thanks to *in silico* medicine, clinical decision making with the usage of computer modelling simulations to describe the biomechanics interactions in our human body

have been improved [2]. Nevertheless, it remains a major challenge to achieve a fast, effective and robust patient specific simulation in time-scales that are consistent with the clinical process, which often requires close to real-time operation. Dramatic reduction in the whole process time, including both model building from medical image data and execution of simulation, could improve clinical decision-making with benefits not only for patients but also for the health service.

1.2 The cardiovascular system

The cardiovascular system is composed by three elements: the heart, the blood and the blood vessels; its main role is to allow the blood to circulate through our organs and body. The heart is the muscular pump which distributes the blood flow through the vessels [3]. The blood is the fluid which circulates through our body and organs supplying them with nutrients, such as oxygen, glucose and amino-acids, also hormones and electrolytes, whilst simultaneously removing waste, such as carbon dioxide and metabolic breakdown products. Finally, the blood vessels make up the circuit through which the blood can flow.

1.2.1 Cardiovascular and coronary anatomy

The cardiovascular system consists of a heart and a closed system of vessels containing the blood (Figure 1.1).

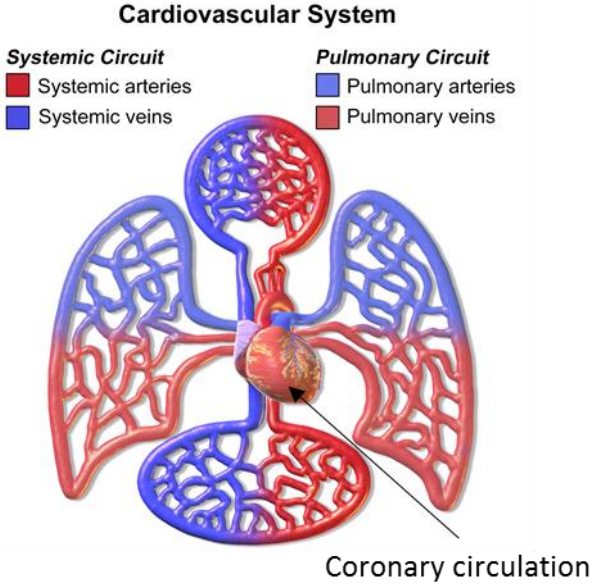

Figure 1.1: Cardiovascular system.
Figure adapted from Blausen Medical Communications, Inc. via Wikimedia Commons Attribution 3.0 Unreported (CC BY 3.0 - https://creativecommons.org/licenses/by/3.0/deed.en).

The role of the heart is to pump blood through the vessels in order to distribute it throughout all the tissues. The heart has four chambers, two atria and two ventricles (Figure 1.1). Since the heart works continuously, even in a rest state, it needs a continuous supply of oxygenated blood, delivered through the coronary arteries and coronary microvasculature to the myocardium.

Coronary arteries are small vessels (of the order of 3-4 mm in diameter) which arise at the origin of the aorta; more precisely from the coronary ostia which are located just downstream

of the aortic valve leaflets. There are two main coronary arteries in the human heart which are described in more details below; the left and the right [4] (Figure 1.2).

- Left coronary artery: the first part of the left coronary artery is called the common trunk. After the first 2-4 cm the vessel divides into two branches, these are; the circumflex and the left anterior descending branches. The left coronary artery supplies blood to the left and anterior parts of the heart.
- Right coronary artery: this supplies the right ventricle and also carries blood to the posterior aspect and the base of the left ventricle.

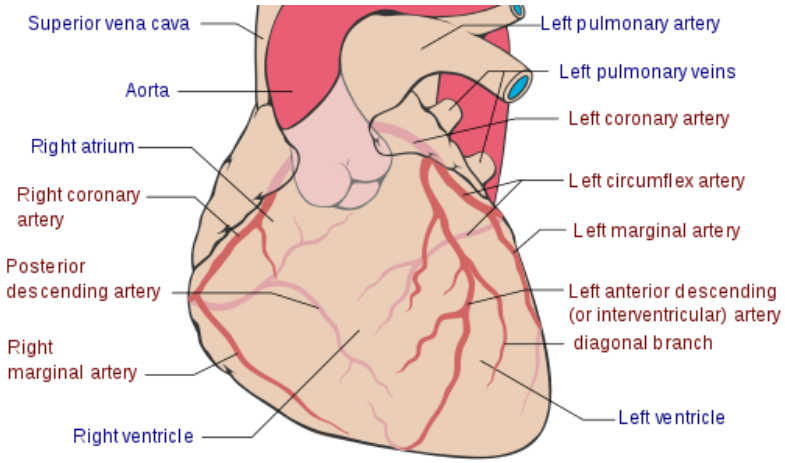

Figure 1.2: Anterior view of the heart and coronary circulation.
Figure by Coronary.pdf: Patrick J. Lynch, medical illustrator, derivative work: Fred the Oyster (talk), adaption and further labeling: Mikael Häggström - Coronary.pdf, CC BY-SA 3.0.

https://commons.wikimedia.org/w/index.php?curid=9967381

Due to pathology, coronary arteries may be unable to provide adequate blood flow to the heart. In this case the pumping action of the myocardium will be impaired and may ultimately prove fatal.

Significant changes in both the function and structure of the coronary vessels are caused by Coronary artery disease (CAD) which is a very common pathology. Plaque formation due to the abnormal deposition of lipids in the vessel wall lead to a narrowing of the lumen. If the restriction reaches a stage where the oxygen supply to the myocardium becomes insufficient, this may lead to chest pain (angina). Severe ischemia can lead to infarction and death of myocytes. An example of coronary atherosclerosis is shown below (Figure 1.3).

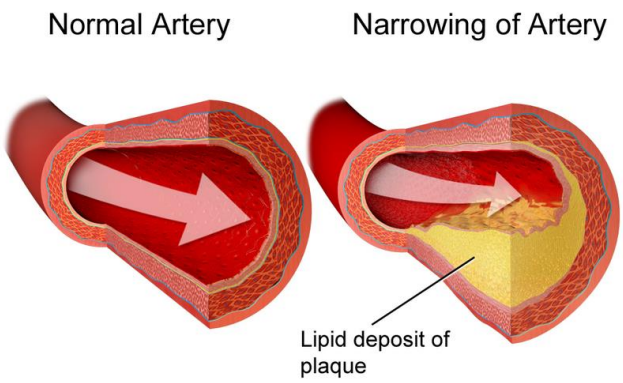

Figure 1.3: Coronary atherosclerosis.
Blausen.com staff (2014). Figure from "Medical gallery of Blausen Medical 2014". WikiJournal of Medicine 1 (2). DOI:10.15347/wjm/2014.010. ISSN2002-4436. CC BY-SA 3.0 - https://commons.wikimedia.org/w/index.php?curid=9967381

In order to investigate the presence of CAD, several imaging-based assessments are used clinically, these tests include invasive coronary angiography (ICA) and computed tomography (CT) coronary angiography (CTCA).

1.2.2 Coronary circulation

The coronary circulation provides nutrients to the heart muscle (the myocardium) [5]. The blood flow in the coronary arteries differs from that in the systemic arteries, because the phases of cardiac contraction generate myocardial extravascular compression. During systole (the ventricular contraction and ejection phase), blood is ejected through the aortic valve into the aorta and systemic arteries and pressure and flow in the main systemic circulation reach a maximum. In contrast, in the coronary arteries during systole, the myocardium is contracted and the coronary microvasculature is compressed thus impairing coronary flow. This explains the diastolic predominance of the coronary flow, an effect which is more pronounced in the left coronary system than the right due to relatively higher left ventricular pressures [6].

While other tissues extract about 25% of oxygen from the blood at rest, because of the high density of capillaries (with more or less one capillary for each cardiomyocyte) the myocardial tissue extracts 70% of the oxygen from the blood [7]. This high rate of extraction explains why, when the heart needs to increase its output, during exercise for example, the myocardium will need more oxygen and nutrients. The only way to achieve this is to increase coronary blood flow.

1.3 Diagnostic process for CAD

Patients with coronary artery disease (CAD) undergo a clinical test called coronary angiography which is used to diagnose the extent and seriousness of the disease [8], [9]. Coronary vessels are investigated during angiography using a catheter that is inserted into the aorta via the femoral or radial artery and advanced along until it reaches one of the main coronary arteries. Once a coronary is reached, a special 'dye' is released into the coronary bloodstream [10], [11]. This 'dye' is a radio-opaque contrast agent which makes the coronary arteries visible radiographically and a series of X-ray images are acquired (Figure 1.4).

These images are 2D projections of the lumen of the coronary artery taken from multiple directions (projection angles) allowing the operator to mentally reconstruct the 3D anatomy of the vessel (a process that is not without difficulty even for an expert operator).

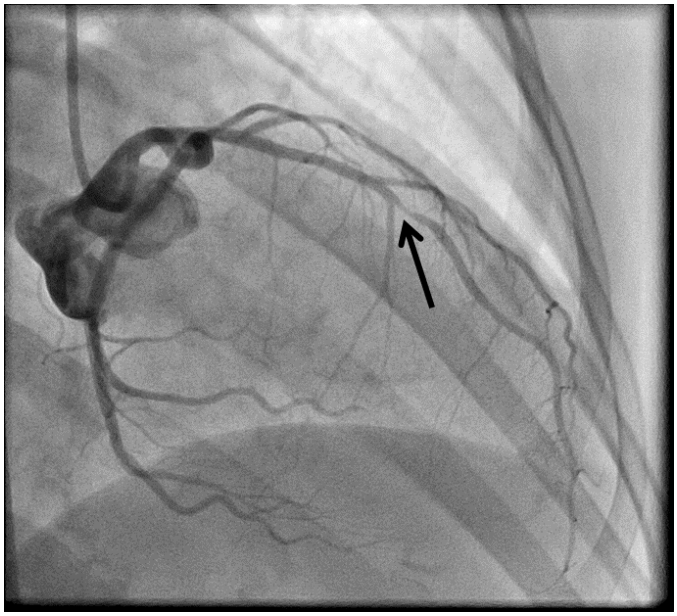

Figure 1.4: An example of angiographic image.
The black arrow shows the stenosis along the coronary vessel. (Courtesy of Dr. Julian Gunn, Northern General Hospital, Sheffield)

Based on the visual representation of the stenosis a decision on its severity and the need for intervention can be made. It is important to highlight that this process is a purely anatomical measure rather than a physiological one. However, using a pressure wire passed through the catheter during angiography it is possible to complement the anatomical measurements with a physiological one, the Fractional Flow Reserve (FFR) [12]–[17].

FFR measures the pressure difference along the coronary stenosis, and is defined as the ratio between the maximum coronary flow in the presence of the stenosis, Q_S^{max}, and the maximal flow in the absence of the stenosis Q_N^{max}. The calculation is based on a simple electrical

analogue, assuming that the resistance is constant and applying Ohm's Law: details of the derivation are presented in section 1.3.1.

$$FFR = \frac{Q_S^{max}}{Q_N^{max}} \cong \frac{P_D}{P_A} \quad \text{(Eq.1.1)}$$

To obtain a measurement of the FFR, cardiologists use an invasive pressure wire to measure the pressure upstream and downstream of the stenosis. The result obtained is a number between 0 to 1 and is helpful to cardiologists in their decision-making. A value higher than 0.8, is taken to indicate a physiologically non-significant stenosis (impairing the flow by only 20%), whilst a lower value indicates a significant stenosis [14], [17], [18]. The measurement of FFR is very important because it is an objective physiology-based parameter and thus better than the visual assessment of the stenosis most frequently made by clinicians in current practice. A potential criticism of FFR is that it measures only the capacity to reinstate a relative flow, but it says nothing about the absolute flow in the artery. Nevertheless it has proven to be a very reliable clinical measure of the likely effectiveness of intervention [17], [19].

Despite its proven clinical value, in the UK, clinical evaluation of FFR is used in less than 15% of cases [1], [9]. The main reason for this is that measurement of FFR is expensive. This is, in part, due to the cost of the wire (≈ £600 per patient), and in part due to the increased Cath Lab time required [20].

A number of different techniques (as described in the next sections) can be used to acquire angiography images, the most common being multiple single plane coronary angiography (MSPCA). Other imaging protocols available include rotational coronary angiography (RoCA) and biplane angiography. MSPCA images are obtained from a series of single plane acquisitions whilst the biplane technique uses two independent acquisition systems to acquire two coronary images simultaneously. Finally, in the RoCA technique, the camera rotates around the patient while acquiring a series of images.

Several authors [9], [21]–[26], have shown that it is possible to estimate FFR using computational fluid dynamics (CFD) starting from a description of the anatomy. The first challenge addressed in this thesis is to obtain a full and fast 3D reconstruction of the whole coronary tree starting from 2D images (at least two projection images) obtained from MSPCA in order to define the 3D surface of the coronary artery. A virtual Fraction Flow Reserve (vFFR) can then be calculated, using a computational model, to help the cardiologist in the clinical decision making [9]. This thesis is based on the use of MSPCA and not biplane or RoCA images because MSPCA is both widely used and more common than the other two techniques [27].

Once the 3D surface of the coronary tree is obtained, there are several advantages in applying a computational FFR. For example: cost and time savings, no need to use a pressure catheter in patients and last but not least, multiple lesions can be included in the computational analysis.

1.3.1 Derivation of the FFR index

Fractional Flow Reserve (FFR) is defined as: "the maximal myocardial perfusion during hyperaemia in the presence of a stenosis in the epicardial artery, expressed as a fraction of its normal maximal expected value" [28]. FFR is a physiological index which describes the pressure drop across the stenosis giving an objective information about the severity of the coronary lesion. Ohm's law can also be described with a hydraulic analogy; the pressure of the fluid is the analogy of voltage. A pressure difference between two points in a pipe (horizontal) drives the fluid flow in the same way as a voltage difference drives the current flow. Therefore, we have:

$$V = RI \qquad \text{(Eq.1.2)}$$

$$P = RQ \qquad \text{(Eq.1.3)}$$

A simple electric circuit of the coronary circulation (Figure 1.5) can be represented as:

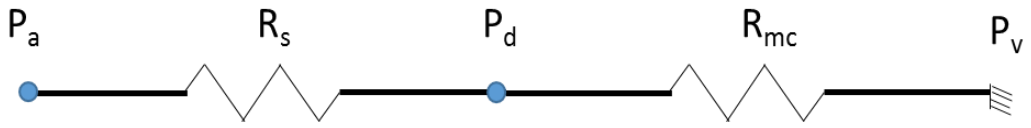

Figure 1.5: Circuit analogy for coronary circulation.
Rs defines the resistance given by the stenosis whilst Rmc is the resistance given by the coronary microcirculation.

Considering the figure above P_a is the aortic pressure, P_d indicates the distal pressure downstream of the stenosis (or multiple stenoses if present in the vessel), P_v is the venous pressure (considered to be equal to zero for small vessels), R_s is the resistance due the stenotic vessel and R_{mc} is the physiological resistance in the coronary microcirculation.

The FFR index can be expressed as the ratio between the distal and the proximal blood pressure, noting that although it is derived from a pressure measurement, it is an index of flow:

$$FFR = \frac{Q_S^{max}}{Q_N^{max}} = \frac{\frac{(P_A - P_V)}{(R_S + R_{mc})}}{\frac{(P_A - P_V)}{R_{mc}}} = \frac{R_{mc}}{R_{mc} + R_S} = \frac{P_D - P_V}{Q} \cdot \frac{Q}{P_A - P_V} \cong \frac{P_D}{P_A} \qquad \text{(Eq.1.4)}$$

Where the maximum coronary flow in the presence of the stenosis is Q_S^{max}, and the maximal flow in the absence of the stenosis is Q_N^{max}. During angiography, the FFR is calculated as the ratio between distal and proximal pressures across the stenosis based on measurements obtained from a pressure wire. The pressure difference is measured in both rest and hyperaemic conditions, but FFR is defined as the pressure ratio under hyperaemia. Vasodilation of the myocardial microcirculation is necessary to emulate the exercise condition (hyperaemia). Adenosine is administered to induce a relaxation of the vessels, a decrease of the myocardial resistance and thus an increase in coronary blood flow.

As indicated previously the FFR value is always within the range [0, 1] and a value below the threshold of 0.8 is take to indicate myocardial ischemia. There are different theories about the influence of haemodynamic conditions on FFR.

According to Pijls and De Bruyne [15], haemodynamics and FFR are independent, because of the linear relationship between pressure and flow (Poseuille's law). Other scientists [29] have demonstrated that in stenotic conditions, the relationship between pressure and flow is not linear:

$$\Delta P = K_1 Q + K_2 Q^2 \qquad \text{(Eq.1.5)}$$

The first term ($K_1 Q$) is related to the viscous losses, often described by Poiseuille's law. The second term ($K_2 Q^2$) is related to the Bernoulli losses, or the reduction of static pressure due to convective acceleration through the stenosis, and a lack of pressure recovery due to viscosity, flow disturbances and sometime turbulence. As it can be seen, the second term in the equation increases with the square of the flow and the Poiseuille part often becomes negligible in comparison. This means that if the fluid flow in the coronary is increased the associated pressure gradient increases in a quadratic manner. If there is no stenosis along the coronary the quadratic term vanishes from the ΔP equation and the pressure loss follows a linear trend, considering only the pressure losses given by the Poiseuille term.

FFR is based on the pressure drop when blood flows across a coronary stenosis. The two terms described above can be approximated using the standard engineering equations:

- **Bernoulli losses**:

$$\Delta P = \frac{1}{2}\rho(v_2^2 - v_1^2) \qquad \text{(Eq.1.6)}$$

or in a second form: considering the continuity equation:

$$\Delta P = \frac{1}{2}\rho Q^2\left(\frac{1}{A_s^2} - \frac{1}{A_{in}^2}\right) \quad \text{(Eq.1.7)}$$

where for the first equation v is the velocity, and ρ is the density of the fluid under consideration. In the second equation Q is the flow, A_s and A_{in} are the cross-sectional areas for the stenosis and the inlet for the geometry under consideration.

- **Poiseuille losses**: every fluid has a viscosity, meaning that it has an internal friction that is a result of the electric forces between the molecules of the fluid. Moreover, to overcome fluid viscosity a pressure difference is required between the inlet and the outlet of a tube or a pipe for the fluid to flow. The Poiseuille equation (Eq. 1.8) explains the viscous losses, which are the pressure losses in a straight tube, associated with a fully developed parabolic flow (Figure 1.6). The equation holds under two conditions: first the fluid has to be incompressible (the volume has to remain constant) and second, the flow has to be laminar.

$$\Delta P = P_{inlet} - P_{outlet} = \frac{8\mu QL}{\pi R^4} \quad \text{(Eq.1.8)}$$

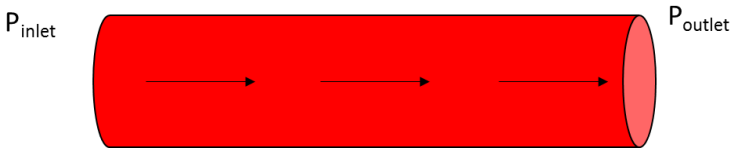

Figure 1.6: Example of blood flow on a straight tube representing the Poiseuille flow.

It is possible to notice that, in the Poiseuille equation, pressure losses increase linearly with flow, viscosity and the length of the tube. Furthermore, they are critically dependent on the fourth power of the radius.

Coronary blood flow is one example of application of these two equations. However, the Bernoulli and Poiseuille laws are very basic haemodynamic laws that do not describe the reality exactly but, rather, approximate the behaviour of the blood flow in the vessels. Furthermore, they have some constraints, for example, as already mentioned above, the Poiseuille equation assumes fully developed flow along a cylindrical pipe and is based on the balance between the pressure gradient and viscous stresses.

On the other hand, the Bernoulli equation, whilst able to predict the pressure loss in a coronary stenosis (vena contracta), has no information about the degree of pressure recovery distal to

the lesion. Both of these equations are based on very simple geometrical approximations they are unable to capture complex haemodynamic behaviour associated with vessel shape and tortuosity. Whilst they may give important information relating to a 1D model with a single stenosis [30]–[33], they cannot describe the haemodynamic interactions between two or multiple stenosis in series. All this suggests that CFD might be required in order to describe adequately all the characteristics of the blood flow in coronary arteries and more generally for physiological simulation. This hypothesis is examined in the context of coronary geometry in chapter 3.

1.3.2 Energy loss in coronary stenosis

The blood flow through our body is driven by pressure but, in contrast to other regions of the circulation, coronary flow increases during the diastolic phase of the cardiac cycle and decreases during the systolic phase. Furthermore, the resistance to flow increases during systole and reduces to a baseline during diastole. It is the pressure gradient that drives the flow. Since it is widely accepted that coronary venous pressure is sufficiently low that it can be regarded as zero [1], [9]; the relative influence of the two resistances is key to understanding and interpreting physiological indices of coronary flow such as FFR.

In the vena contracta or just beyond the occlusion, the flow accelerates increasing the kinetic energy and since total energy must remain constant, the fluid pressure must decrease. Formally the Bernoulli equation is derived by a reduction of the momentum equation, but it is useful to think about its elements in terms of potential and kinetic energies. In general, the Bernoulli equation gives a good estimation of the static pressure drop between the inlet and the coronary stenosis. Furthermore, distal to the vena contracta, the fluid flow starts to decelerate; in this case kinetic energy is lost which corresponds to an increase in pressure and distal to the lesion the Bernoulli equation predicts an increase in hydrostatic energy i.e. pressure. However, the conversion between kinetic energy and pressure is not efficient and, for multiple factors, the static pressure does not recover completely; just beyond the vena contracta the flow starts to rotate producing vortices, a major component of turbulent flow, furthermore it is possible to notice flow separation. Due to these factors pressure will never reach a full recovery. Moreover, there are also viscous losses due to viscous friction between laminar layers of fluid to consider, although these play a less important role.

1.3.3 Factors influencing pressure drop across a stenosis

The most important factor influencing the pressure drop along a coronary artery is the ratio between the minimum radius of the stenosis and that of the undiseased vessel. As it can be seen from equation 1.9, the pressure gradient is inversely proportional to the fourth power of the radius ratio.

$$\Delta P = \frac{1}{2}\rho v_{inlet}^2 \left(\left(\frac{r_{inlet}}{r_{sten}} \right)^4 - 1 \right) \quad \text{(Eq.1.9)}$$

Typically, clinically important pressure drops are associated with radius reductions of 50% or greater. However, as shown in eq. 1.5, the pressure-flow relationship is not linear, the shape of the curve depends by the stenosis resistance.

1.4 Coronary reconstruction in 3D: different models and approaches

Coronary artery disease (CAD) is the most common cause of cardiovascular death in the world [34]. Currently, diagnosis and assessment of CAD relies on invasive techniques such as angiography. Fractional Flow Reserve (FFR) is considered to be the gold-standard for assessment of the physiological significance of coronary artery disease [35]. Several different angiography techniques can be used to detect CAD; biplane, rotational or multi-single plane angiography. All these techniques produce a series of projection images from where it is possible to start a 3D coronary reconstruction. These techniques and the different models employed to achieve 3D coronary reconstruction are described in the next sections.

1.4.1 Biplane technique

Biplane devices have two X-ray source systems, these two systems can rotate independently from one another [36]. Thus, they have a frontal and a lateral view with a global coordinate system in common. The origin of this coordinate system is called the isocentre and is taken as the point of intersection between the lateral and the frontal system. Using biplane angiograms we can obtain two images, acquired at the same time, or better, at the same phase of the cardiac cycle. This could be of particular help in the reconstruction process; acquiring two images at the same time allows us to eliminate the influence of cardiac and respiratory movement on the heart. It is important to emphasise that there should be no table movement or panning during the acquisition. A large number of studies in 3D reconstruction have been carried out starting from biplane images [31, 32], [36-41].

Hoffmann *et al.* [39] produced a tool which determines the 3D vessel tree centreline starting from biplane angiography images. According to them, the first problem to be resolved is the determination of the imaging geometry, i.e. evaluation of transformation matrices relating to the entire system. However, all this information is expressed in terms of Left Anterior Oblique (LAO), Right Anterior Oblique (RAO) and Cranial-Caudal (CC) angles and distances from the source to the X-ray intensifier plane. End-diastolic images were chosen, and points along the centreline marked manually by the user (5-10 points). These points were interpolated with a vessel tracking algorithm. Considering the two planes of projection, the correspondence of points along the two centrelines has been computed using the epipolar technique [42]–[45]. Every matched point from the two planes is used to calculate the 3D position of the point. This position in the three-dimensional space is computed as the interception point retracing the X-ray source beams. Thus, the 3D centreline is obtained repeating the procedure for each point along the centreline in both planes.

In Tu *et al*.[36], the workflow for the reconstruction is composed of several steps. The first step is the correction of the isocentre offset. In a biplane device the isocentre offset is defined as the spatial difference between the two isocentres (frontal and lateral). These should intercept each other, but due to system distortion, the isocentre is not a stable point. Correcting the offset and the epipolar geometry, they wanted to develop a robust tool for the coronary tree reconstruction. This offset leads to inaccurate 3D reconstruction, due to the uncertainty of the correspondence of points between the two projections planes which has to be eliminated before starting the reconstruction process. Their solution to resolving this offset error is to choose one or three pairs of points (usually bifurcations) and then approximate the total distance from the chosen points to the corresponding epipolar lines. The resultant error is a function of the isocentre. They must then minimise this error function to obtain, and eliminate, the offset between the two views. The second step is to mark manually the proximal and the distal point along the coronary vessel in one view, and then the coronary centreline is computed automatically. The proximal and the distal points on the second project plane are calculated once again from the epipolar geometry. Knowing the correct position of corresponding points from the two views, the 3D centreline is computed, calculating the position of each point in 3D as the point of intersection derived from the two X-ray sources beams. According to Tu et al [36], even if two images in biplane device are acquired simultaneously, reproducing an accurate coronary tree in three dimensions is challenging.

Biplane angiography has a great advantage in terms of accuracy of reconstruction because there is no extraneous movement, but a major disadvantage of the biplane technique is that is not widely used in routine cardiological procedures.

1.4.2 RoCA Technique

Rotational coronary angiography (RoCA) is characterised by a single C-arm which collects a series of coronary images during a single rotation. The RoCA technique covers an angle of approximately 120 degrees; the C-arm starts typically from 60 degrees right anterior oblique (RAO) and ends at 60 degrees left anterior oblique (LAO). Depending on the choice of the operator, the C-arm can begin its rotation with a caudal (CAU) or cranial angulation (LAO).

The RoCa technique is very limiting in the sense that, since the heart is moving continuously, and 3D reconstruction has to start from same cardiac phase (usually end-diastole) there are very few images across a single acquisition which are useful for 3DR in any particular cardiac phase, even without respiratory motion.

Hansis *et al*. [74] described a workflow for 3D reconstruction using 2D RoCA projection images. Their aim was to improve the consistency of the projected images with respect to the heart motion. The procedure for 2D motion compensation starts with an initial coronary artery reconstruction; the reconstructed vessel centreline is then projected back on the forward projections. The projected centrelines are then transformed to obtain the best possible match with the centrelines of the forward projections. The group in Sheffield [1, 9, 13] originally used RoCA images and a reconstruction supported on the Philips clinical imaging equipment, but this was only applicable to a small research cohort on which RoCA was performed, and one of the aims of this thesis was to develop a software solution usable by members of the research team on standard MSPCA images.

1.4.3 Reconstruction starting from MSPCA images

Andriotis *et al*. [48] presented a 3D reconstruction workflow of coronary arteries from conventional monoplane angiograms (MSPCA). Their reconstruction approach is based on the epipolar geometry concept. Their model was validated initially against a virtual phantom coronary and then against a reconstructed CT coronary artery. The reconstruction output was a surface grid that could be used as a further step for computational fluid dynamics. In their

paper the group does not mention the presence of artefacts or errors on the reconstruction given by heart motion or table movement during image-acquisition.

One model that is still representative of the state of art in reconstruction from MSCPA images is that of Messenger *et al.*[49]. Their algorithm is composed of a number of steps to achieve the coronary reconstruction. The first step is to acquire images and register the gantry parameters. Gantry parameters are as always: angles (RAO/LAO, Caudal/Cranial), distance source-detector, distance source isocentre and distance between each X-ray source which are important to compute the epipolar geometry.

The second step is the manual extraction of the centerline in one view. Knowing the spatial relationship between the two views, they can compute the third step which is based on matching centerline points from the first view to the second one. In this algorithm correspondence points are computed following the epipolar geometry constraints for the computation of the 3D centreline. The skeleton of the coronary is then computed as sequence of cross-sectional circular disks. The method described in chapter 2 of this thesis follows a similar approach.

1.5 Computational Fluid Dynamics and Reduced Order Methods

Computational fluid dynamics (CFD) is a branch of fluid mechanics and a special area of mathematics [50]. CFD is essential nowadays for engineering applications such as the design of aircraft or in the automotive industry. However, over the last few years, CFD is becoming increasingly important in medical applications dealing with complex flow such as in cardiovascular modelling because it can measure haemodynamic parameters and predict physiological responses which were not possible previously [51]–[54].

CFD is based on the computation of solutions of the continuity and momentum (Navier Stokes) equations which govern fluid motion. These equations are non-linear partial-differential equations, based upon the conservation of mass and momentum. These equations are presented below for an incompressible fluid (density does not change in time). In most cases it is not possible to derive analytical solutions, and they are solved numerically.

$$\rho\frac{\partial u}{\partial t} + \nabla\cdot(\rho u U) = -\frac{\partial p}{\partial x} + \frac{\partial \tau_{xx}}{\partial x} + \frac{\partial \tau_{yx}}{\partial y} + \frac{\partial \tau_{zx}}{\partial z} \qquad \text{(Eq.1.10)}$$

$$\rho\frac{\partial v}{\partial t} + \nabla\cdot(\rho v U) = -\frac{\partial p}{\partial y} + \frac{\partial \tau_{xy}}{\partial x} + \frac{\partial \tau_{yy}}{\partial y} + \frac{\partial \tau_{zy}}{\partial z} \qquad \text{(Eq.1.11)}$$

$$\rho \frac{\partial w}{\partial t} + \nabla \cdot (\rho w U) = -\frac{\partial p}{\partial z} + \frac{\partial \tau_{xz}}{\partial x} + \frac{\partial \tau_{yz}}{\partial y} + \frac{\partial \tau_{zz}}{\partial z} \quad \text{(Eq. 1.12)}$$

$$\tau_{xx} = 2\mu \frac{\partial u}{\partial x} + \lambda \, div \, \boldsymbol{u} \quad \tau_{yy} = 2\mu \frac{\partial v}{\partial y} + \lambda \, div \, \boldsymbol{u} \quad \tau_{zz} = 2\mu \frac{\partial w}{\partial z} + \lambda \, div \, \boldsymbol{u} \quad \text{(Eq. 1.13)}$$

$$\tau_{xy} = \tau_{yx} = \mu \left(\frac{\partial u}{\partial y} + \frac{\partial v}{\partial x} \right) \quad \tau_{xz} = \tau_{zx} = \mu \left(\frac{\partial u}{\partial z} + \frac{\partial w}{\partial x} \right)$$

$$\tau_{yz} = \tau_{zy} = \mu \left(\frac{\partial v}{\partial z} + \frac{\partial w}{\partial y} \right) \quad \text{(Eq. 1.14)}$$

$$\nabla \cdot U = 0 \quad \text{(Eq.1.15)}$$

where *u*, *v* and *w* are the three velocity components along the three directions *x*, *y* and *z*. ρ is the density which characterize the fluid, *p* is the pressure, U is the velocity vector and τ is the shear stress. Applying Newton's second law to the principle of fluid dynamics it is possible to derive the momentum equations. The convective acceleration described by the term uU **(**for the *x*-direction) is non-linear and makes the analytical solution of the Navier-Stokes equations extremely challenging. The first term in each equation accounts for the acceleration in the three dimensions. The second term $\nabla \cdot (\rho u U)$ is the velocity vector accounting for convective acceleration in the appropriate direction. In a simple 1D model, this term can be simplified into the Bernoulli equation. The third term $(-\frac{\partial p}{\partial x})$ is the pressure gradient in the direction specified by the denominator, and finally the last three components $(\frac{\partial \tau_{xx}}{\partial x} + \frac{\partial \tau_{yx}}{\partial y} + \frac{\partial \tau_{zx}}{\partial z})$ account for viscous losses which in a 1D model they can be seen as the Poiseuille equation.

In a Newtonian fluid the viscous stresses are proportional to the rates of deformation (Eq. 1.13 and Eq. 1.14). The dynamic viscosity μ relates stresses to linear deformations, and the second viscosity λ relates stresses to the volumetric deformation. The effect of the second viscosity λ is small in practice and can be thought as $\lambda = -\frac{2}{3}\mu$.

The first three equations account for the conservation of momentum in the *x*, *y* and *z*-direction, while the last equation accounts for the conservation of mass.

The Navier-Stokes equations which are partial differential equations have to be transformed into a system of non-linear algebraic equations which can be solved iteratively. In order to have a full system of equations, the ROI (region of interest) has to be temporally and spatially discretised, furthermore boundary conditions have to be applied to any inlet, outlet and walls. There are several spatial discretisation methods, but the principal are: Finite Difference (FDM),

Finite Volume (FVM) and Finite Element method (FEM). The spatial discretisation consists in dividing the computational mesh in a finite number of areas for 2D or volumes in 3D where the equations are solved. Regarding the temporal discretisation, a time-marching scheme is applied and the end of the solution is achieved incrementally. ANSYS-Fluent is based on the FVM.

For complex transient flows, sometimes with millions of degrees of freedom, large computational resources are often necessary and execution times can still be of the order of days or weeks. Furthermore, if we are interested in having results of the fluid equations for different value(s) of model parameters, we have to repeat the simulation for each value requiring more computational time and effort.

The increasing interest in solving complex multidisciplinary systems has led to the development of model reduction strategies. ROMs gained attention and popularity in different engineering and scientific applications, specifically in different areas: optimisation and design, treatment of high dimensional space, real-time computing (especially in biomedical engineering) and interaction between different model reduction techniques.

ROMs are computationally cheaper than the full order systems; however, they are capable of collecting the most important features of the model [111, 116].

The following section is a brief overview of the state of the art and of the challenges for ROMs applied to computational fluid dynamics problems. ROMs have been applied to different fluid dynamic applications such as: medical, nautical, mechanical and automotive engineering; furthermore, they have been applied to biology and geophysics.

Progress in computational power and capabilities of modern computers have led to a more accurate numerical analyses and advances in simulation modelling. However, even with advancements of technology, there are still unsolved challenges [59, 90, 91, 96] summarised below:

- Models defined in a high dimensional space are very difficult to handle and they encounter what is called “course of dimensionality”. Many parametric problems fall in this class;
- Complex systems which require a fast or close to real time computation are difficult to solve and to control;

- ROMs, which include geometrical parameterisation (difficulties in dealing with large deformations). A clear example is the goal of this thesis, where a fast computation of the haemodynamic in coronaries is required.

Introducing idealising assumptions to the model could be a possible solution to solve these challenges, however this will make the model less accurate. A second solution could be using High Performance Computing or HPC where the great computational power can solve highly complex problem reducing the computational time. The drawback of using HPC is that they are expensive to install, they are not mobile and lack of accessibility.

A more feasible solution is to develop ROMs which aim to maintain high accuracy with less computational cost, allowing researchers and engineers to solve complex problems in real-time or close to real-time. As already discuss, introducing parameters (for parametric problems) into the model increases the dimensional space. In these cases solving parametric PDEs, such as Navier-Stokes equations, requires the collection of multiple full CFD solutions with different values of the parameters [90, 91].

In order to solve fluid flow problems robustly and efficiently, different ROMs techniques have been developed, such as the Proper Orthogonal Decomposition (POD) and Reduced Basis Methods (RB). Both methods are used in academia and for industrial engineering problems; however in this thesis focus will be given to the POD method and it will be described in details in the next section.

In the last few years research in the medical field has moved towards a patient-specific characterisation of the blood flow. This has the aim of improving the diagnosis helping clinical decision making. In order to compute a close to real time simulation, often demanded in a clinical application, and an accurate result we need to rely on ROMs. By usage of the ROMs a huge acceleration in the computation of the variables we are interested in can be achieved, and at the same time reducing the CPU and memory demands (RAM).

1.5.1 The Proper Orthogonal Decomposition and the Singular Value Decomposition Approach

In any scientific field, collecting very large amounts of data by numerical simulations or experimental approaches is a common situation. There is a great need to have specific post-processing techniques able to extract from these large quantities of high dimensional data,

synthetic information essential to understand and eventually to model the process under study. One of the most powerful methods of data-analysis for multivariate and non-linear phenomena is the Proper Orthogonal Decomposition (POD). The POD procedure is a linear procedure that takes a given collection of input data and creates an orthogonal basis constituted by functions estimated as the solutions of an eigenvalue problem. The POD can be approached as an application of the Singular Value Decomposition (SVD).

The SVD provides a basis for the modal decomposition of an ensemble of functions, such as data obtained from experiments or numerical simulations. The beauty of the SVD method is its optimality in the sense that it provides the most efficient way of capturing the dominant components or dominant features with only a finite number of "modes" [55], [56]. In terms of CFD analysis, the SVD allows to capture the most significant fluid flow patterns in the dataset. The SVD then, provides a linear approximation of a set of functions that enable an easier characterization of the complex original input data as a sum of weighted modes. Furthermore, the mathematical fundamental idea of the SVD approach is to decompose any quantity distribution into a linear combination of modes coefficients and modes [57]–[59].

Therefore, we have:

$$S^{(k)} = \sum_{m=1}^{M} \alpha_m^{(k)} \varphi_m \qquad \text{(Eq.1.16)}$$

Where $S^{(k)}$ is the recomputed solution given by the linear combination, the index *k* defines the *k-th* recomputed solution, $\alpha_m^{(k)}$ are the modes coefficients for the solution *k* and φ_m are the modes. In order to construct the SVD all the mesh nodes values for each simulation is reordered into a row and put into a matrix. For a 2D example we have:

$$S = \begin{bmatrix} S^1 \\ S^2 \\ S^3 \\ \vdots \\ S^K \end{bmatrix} = \begin{bmatrix} s^1_{i=1,j=1} & s^1_{i=1,j=2} & \cdots & s^1_{i=1,j=J} & s^1_{i=2,j=1} & \cdots & s^1_{i=I,j=J} \\ s^2_{i=1,j=1} & s^2_{i=1,j=2} & \cdots & s^2_{i=1,j=J} & s^2_{i=2,j=1} & \cdots & s^2_{i=I,j=J} \\ \cdots & \cdots & \cdots & \cdots & \cdots & \cdots & \cdots \\ s^K_{i=1,j=1} & s^K_{i=1,j=2} & \cdots & s^K_{i=1,j=J} & s^K_{i=2,j=1} & \cdots & s^K_{i=I,j=J} \end{bmatrix} \qquad \text{(Eq.1.17)}$$

where *S* is the matrix constructed (for a 2D mesh grid) with all the full CFD simulations for the quantity or quantities of interest; *K* is the total number of CFD simulations, called snapshots, considered to build the ROM and *IxJ* is the total number of nodes values in the considered geometry. The s_{ij} define the solution value at the mesh nodes. It can be deduced from the rectangular form of the matrix *S* that all the meshes which form the dataset have to be isotopological, which means they have to have same number of nodes and elements [60].

Once all the data are saved in the *S* matrix, the correlation matrix is computed as:

$$C = \frac{1}{K} SS^T \qquad \text{(Eq.1.18)}$$

The aim of the SVD is to find a sequence of modes in order to minimise the following function:

$$\sum_{k=1}^{K} \| S^k - \sum_{m=1}^{M} \alpha_m^{(k)} \varphi_m \|^2 \rightarrow min \qquad \text{(Eq.1.19)}$$

where $\| \cdot \|$ denotes the L^2 norm. *K* is the total number of snapshots considered to construct the correlation matrix, *M* is the number of modes considered to build the low-order model where $M \ll K$. The S^k term in eq. 1.17 is the full CFD solution and the second term represents the recomputed solution as linear combination of modes coefficient and modes.

The minimisation problem is resolved by computing a singular value decomposition on the correlation matrix. The problem is of the form:

$$C = U \sum V^T \qquad \text{(Eq.1.20)}$$

where *C* is the correlation matrix, *U* is an *NxN* orthogonal matrix formed by the left singular vectors, *V* is an *m*x*m* orthogonal matrix formed by the right singular vectors and $\sum$ is an *Nxm* matrix with all element zero except the diagonal. The non zero diagonal elements, are arranged in decreasing order and are called the singular values. The modes represent the extracted flow pattern, however they do not necessarily reflect a real flow structure that can be observed in a flow field. Instead, every mode represents a component of a flow field that is reconstructed by summing over all modes coefficients ($\alpha_m^{(k)}$).

The modes coefficients are computed by projecting the original solution fields (S matrix) onto the computed modes (φ_m); every coefficient represents a weight, which is telling us how much that particular mode is contributing to a particular snapshot. However, when the full CFD solution is not known, the modes coefficient $\alpha_m^{(k)}$ are computed by interpolation.Aim of the project and thesis workflow

The primary aim of the project "*Effective computational coronary heamodynamics for clinical application*" is to construct and validate a computational model which combines segmentation of coronary arteries and Reduced Order Methods to achieve a fast (close to real time), accurate computation of the FFR index. Achievement of this aim will underpin the development of a software solution to help clinicians in their decision making. The overall workflow (Figure 1.7) to achieve the computational model is composed of several major blocks:

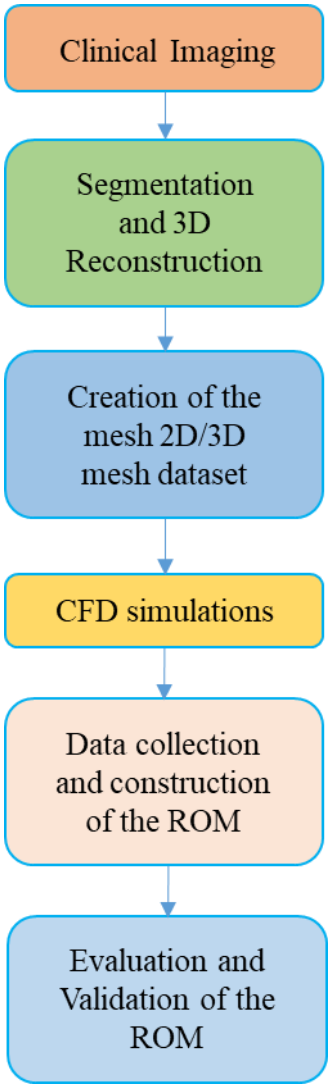

Figure 1.7: Overall Thesis workflow with the different steps.
The workflow starts from the acquisition of clinical images. Coronaries are then reconstructed in 3D to create volumetric meshes. CFD are run for every geometry and CFD solutions are collected in order to build and train the ROM.

The different blocks are briefly explained:

- **Clinical Imaging**: In this thesis MSPCA images acquired with a Philips Allura Xper Swing C-arm system (Philips Healthcare, Best, NL) are used in the segmentation tool for the reconstruction. Images should provide sufficient anatomical and physiological details, in an appropriate format (DICOM) and quality. In addition, geometries reconstructed with Philips 3DCA (RoCA images) segmentation tool have been used as well in order to extract the parameters to develop and build the clinical parameterised ROMs.

- **Segmentation and 3D Reconstruction**: The segmentation and the reconstruction step is a key point in the workflow, but also the most error prone and subjective. The segmentation identifies the coronary geometry from the angiography images and, starting from at least two projection images, a three dimensional geometry is computed. The 3D geometry has to be an accurate reconstruction and has to maintain the most important geometrical features (radii dimensions, shape, curvature etc etc.) of the projected coronary. Furthermore, if the reconstructed geometry is not accurate, one can end up with completely different value of the FFR index (true FFR vs vFFR) resulting in the wrong clinical decision.

- **Mesh creation**: The output of the segmentation step is a 3D mesh surface (.stl file), which is necessary but not sufficient to compute a CFD analyses. For a CFD study a volumetric mesh is necessary. The action of creating a volumetric mesh is called spatial discretisation and the aim is to divide (or discretise) the geometry into little discrete volumetric cells (FVM). Temporal discretisation is also available, it allows to divide the solution into discrete time steps. However, since in this thesis steady state simulations will only be taken into consideration, temporal discretisation will not be applied. The mesh creation is the most time consuming time step in setting up the CFD analysis. The accuracy and the numerical stability of the solutions are influenced by the mesh, the spatial discretisation must be refined enough to capture the haemodynamic behaviour in the entire domain. However, much refinement of the spatio-temporal discretisation will not lead to an improvement of the solution and furthermore will impact on CPU memory and solution time. In order to build the ROM several thousands of simulations are necessary to construct the training dataset.

- **CFD simulations**: As stated above, in order to build the Reduced Order Method, many CFD simulations have to be run. Every simulation is characterised by its own journal file, a journal file contains a sequence of Ansys Fluent commands. These commands could be typed in the Fluent GUI, however to automate the process these files have been created automatically in MATLAB and then saved as a text file (.scm). The purpose of a journal file is to automate a series of commands instead of entering them in the command line or selecting the same commands from the Fluent GUI. The journal

file contains all the information necessary to compute a simulation i.e. all the settings defining the physical parameters of the model.

The journal file must include following information:

- units of the mesh;
- the fluid properties as density and viscosity;
- boundary conditions;
- model to use;
- the discretisation method;
- convergence criteria.

Regarding boundary conditions, in order to compute a CFD analysis the user has to define at least one inlet, one outlet and the wall region. Boundary conditions are required component to solve the mathematical model. Since a clinical problem is considered, boundary conditions should be as close as possible to the reality (which is physiological) i.e. the user has to specify an initial boundary condition value as a pressure, a mass flow rate or a velocity. Boundary conditions are really important in CFD analyses, it might be common to analyse a very difficult problem with a very high refined mesh, but with a poor description of boundary conditions. In this case the user ends with a very accurate solution, however that solution does not represent the physiological problem taken into consideration.

The Navier-Stokes equations are a non-linear system of partial differential equations. The CFD solutions are achieved iteratively where an algorithm leads to a reduction in error at each iteration until the equations are satisfied with some defined tolerance (convergence criteria). If the CFD analysis is a transient simulation, once the convergence has been achieved for the first time step, the time is incremented and the iteration process starts again. However, even if the solution has converged, there is still the possibility the solution is not accurate; the convergence criteria in fact could be misleading. The user should define a solution monitor in order to check the variable of interest in is not changing of value during the iteration process.

A CFD simulation could take several hours of computational time and thus CPU memory depending on the number of elements and on the temporal discretisation. This is why in this thesis a method to achieve a fast and accurate computation of the pressure field in coronary arteries using a ROM is presented. All the CFD simulations presented in this thesis have been run with a steady state laminar model, since the Reynolds numbers were below the turbulent threshold.

- **Building the ROM:** Once all the designed CFD simulations have been computed, the following step is the collection of the data. The output data we are interested in for the purpose of this thesis is the pressure field for every coronary artery. It should be noted that the user could save and build a ROM for any/every variable. Since all the CFD solutions depend on a pre-defined number of parameters such as geometrical parameters (e.g. shape and curvature parameterisation) and fluid dynamic parameters (e.g mass flow), the ROM is also parameterised by these. To build a ROM two different steps are needed: the *offline mode* and the *online mode*. The offline mode is the step in which many CFD simulations have to run to build the reduction order method, and is therefore the most time consuming. However, the *offline* step has to be computed only once. The second step is the online mode which is based on the computation of the pressure profile for a completely new set of parameters. The *online* step is very fast, close to real time and has great benefits in terms of time and computational requirements.

In the *online* mode, there are two major steps: the evaluation step and the validation step. Important in these steps is the computation of two errors: the projection error and the interpolation error which describe the goodness of fit of the ROM. The full process for building a ROM will be detailed in Chapter 3 and Chapter 4.

1.6 Thesis Outline

This PhD project has been organised into four main chapters plus introduction and conclusions. This first chapter, *Introduction*, provides a contextual overview of the relevant anatomical and physiological concepts of the cardiovascular system, of the clinical problem and of the state-of-the-art in 3D algorithms for coronary artery reconstructions and an introduction for Reduced Order Method in Computational Fluid Dynamics.

Chapter 2, *3D Coronary Reconstruction software: towards a clinical tool*, provides a description of the developed tool written in MATLAB to achieve a 3D reconstruction of coronary arteries starting from 2D multi-single plane coronary angiography projection images.

Chapter 3, *2D ROM generation and fluid flow interactions between multiple stenosis*, describes the right ingredients and the most important steps necessary to build a ROM. Different ROMs have been created in idealised coronary geometries, i.e. straight axisymmetric tubes in 2D with a single or multiple stenosis. Pressure gradients have been computed and compared using different methods.

Chapter 4, *Shape parameterisation and ROM in 2D patient-specific coronary geometries*, is focused on shape parameterisation in order to extract geometrical parameters which describe the variation of the radius along the length for any patient-specific coronary geometry. Furthermore, multiple ROMs have been created, evaluated and tested against a clinical coronary dataset.

Chapter 5, *3D CFD coronary arteries simulations: towards a Reduced Order Method for fast haemodynamic prediction*, illustrates a comparison between multiple models to compute pressure gradients. It also introduces a 3D coronary centreline parameterisation in order to develop 3D ROMs applied to 3D coronary arteries.

In Chapter 6, *Conclusions and future work*, a final overview of the limitations and conclusions of this project in terms of results obtained is reported. Also future work and ideas for improvement are presented.

Chapter 2

3D Coronary Reconstruction software: towards a clinical tool

In this chapter, the development of a coronary segmentation tool will be presented. The chapter addresses the problem of accurate reconstruction of the anatomy from multiple single plane coronary angiography (MSPCA), which is the most readily-available, and universally used, standard imaging protocol [27]. The development of the segmentation tool is the first step in order to achieve the computation of the FFR with a CFD software and for using the ROM method [13], [26], [1]. The segmentation process and the segmentation tool are based on MATLAB. Furthermore, a GUI has been developed in order to allow the user easier use of the research tool. The first output of the presented tool is a 3D single coronary vessel reconstruction in the form of a surface mesh (.stl) which can be imported into any CFD solver to compute a full fluid flow simulation after creating a volumetric mesh. The computed surface meshes are used both to compute standard CFD analyses for the calculation of the vFFR index and to feed the clinical dataset used for training the ROM. A virtual Fraction Flow Reserve (vFFR) can then be calculated in order to help cardiologists with their clinical decision making [9], [22], [48], [61].

Furthermore, the tool can be used as an offline standalone software helping clinicians to visualise the coronary in 3D in a computer screen. Due to time constraints, during clinical operations it is not possible to reconstruct the coronary tree (unless this is done mentally based on experience) since the coronary arteries are projected as a series of 2D images [45], [62], [63]. The workflow for the 3D coronary reconstruction is presented in Figure 2.1 below.

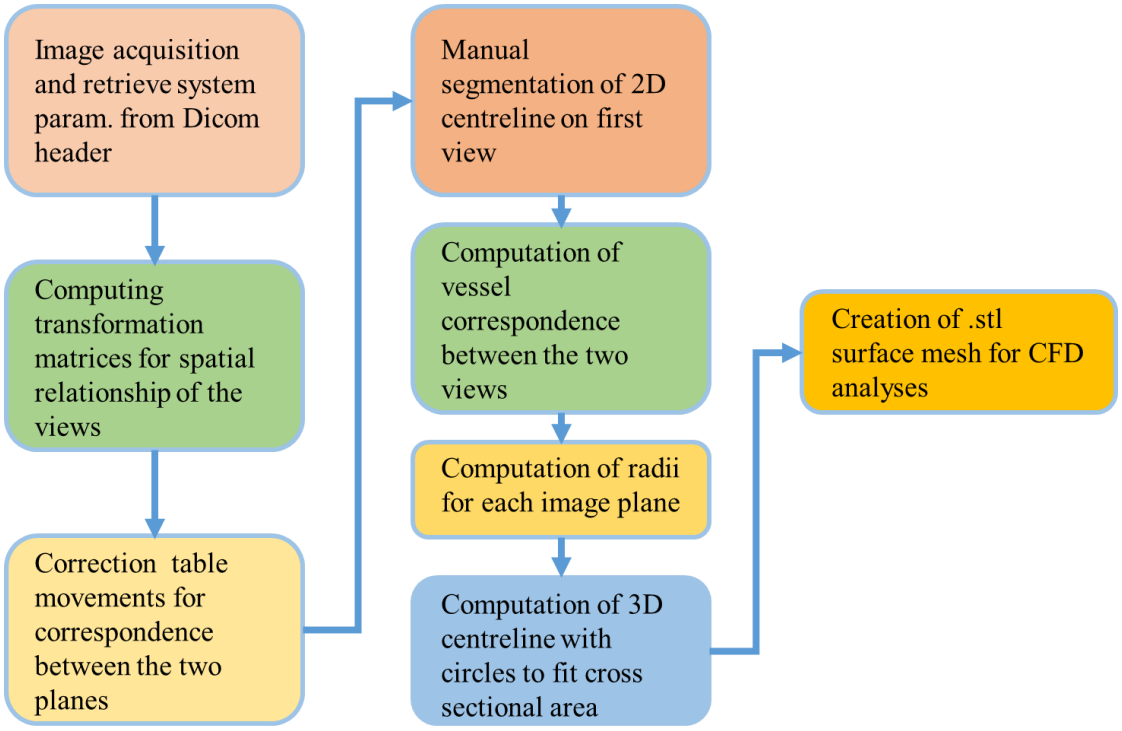

Figure 2.1: 3D Coronary Reconstruction Workflow with the different steps.

2.1 3D Coronary Reconstruction: main features and goals

In recent times, a lot of attention and research has been given to achieve predictive medicine ([64]–[69]) . However, predictive medicine requires accurate models and accurate models require time ([70]–[73]). Therefore, one of the biggest challenges is to achieve a fast, effective and robust patient specific simulation close to real-time for predictive medicine, which could improve the clinical decision making.

The first step of the workflow to compute a virtual FFR (vFFR) is to reconstruct the coronary geometry in 3D to have a clear view of the diseased vessel.

There are five catheterisation laboratories in Sheffield. Many of the images on which the current analysis is based were captured in a laboratory equipped with an Allura Xper Swing C-arm system (Philips Healthcare, Best, NL). The C-arm is capable of acquiring MSPCA images, and includes the facility to acquire rotational coronary angiography (RoCA) images [74], [75]. In a RoCA system, the C-arm rotates around the patient acquiring 121 images in a 120° arc with a rate of 30° degrees per second; with the RoCA technique the table on which the patient lies is not moved during the acquisition and this strongly improves the accuracy and stability of the reconstruction process. However, MSPCA is the normal clinical protocol, the spatial correspondence between the multiple images is uncertain [27]. Here the camera angles and

distance are known and recorded, but arbitrary table movements are made to present the clinician with the best views to see the culprit arteries. In the most modern systems these movements might be recorded, but for the data available to the current study, and indeed still generally in clinical practice, they are not. Therefore, the software development described in the current chapter is for MSPCA image data.

2.2 Implementation of the workflow

To obtain angiography images a C-arm is needed, which carries an X-ray tube plus an image intensifier. The C-arm has two degrees of freedom: independent rotations are made about the global axis *X* and the global axis *Y* (Figure 2.2) [76]–[78]. Most of the 3D reconstruction models taken into account in this section provide a coronary reconstruction knowing some geometrical parameters such as the positions of the focuses (F_A in Figure 2.2), distances from the X-ray sources to projection planes (F_A - O_A in Figure 2.2), gantry angles (ϕ_x and ϕ_y in Figure 2.2) and ECG data. Gantry angles are described in terms of left/right anterior oblique (LAO/RAO) and Caudal/Cranial (Caud/Cra) angle. All these parameters which are necessary to provide a 3D reconstruction, are usually written into the header of the DICOM file that describes the image [79]. At least two 2D projection images are needed to compute a 3D reconstruction.

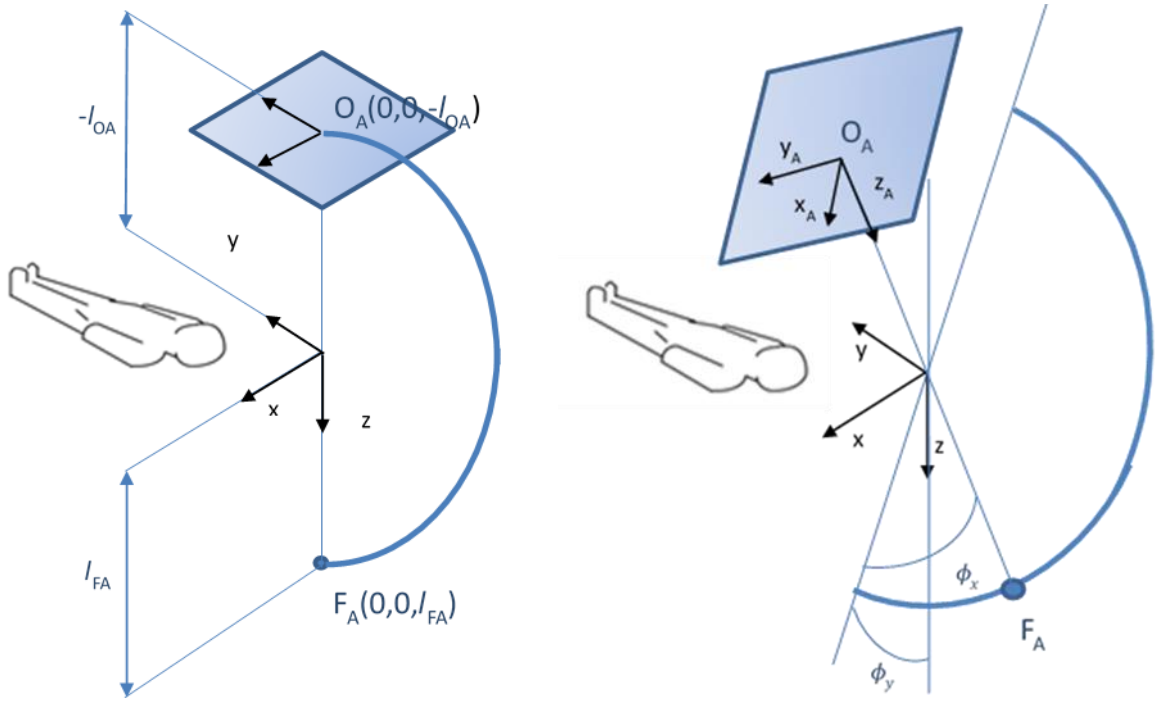

Figure 2.2: Degrees of freedom for the C-arm.
A) No rotations are applied to the system. B) Two rotations are applied; the first one along the global x-axis ϕ_x, and the second rotation along the global y-axis ϕ_y.

With the C-arm we can obtain projection images in 2D which are captured on a projection plane by an X-ray intensifier. Figure 2.2A shows the initial position of the C-arm. Fixing a coordinate system, the X-ray source is positioned at a distance equal to l_{FA} whilst the centre of the X-ray intensifier plane is positioned at $-l_{OA}$. The C-arm has two degrees of freedom, one rotation about the x-axis expressed as ϕ_x and a second rotation about the y-axis expressed as

ϕ_y. An experienced cardiologist might be able to mentally reconstruct a 3D coronary starting from coronary images taken from different angles and positions. However, in most cases, images are not easy to interpret. Image properties such as noise, low levels of contrast, foreshortening and overlapping make it difficult to identify the various coronary arteries in the image (https://rpop.iaea.org/) [79]. In normal practice, it is already a challenge to find images which do not contain artefacts including the ones described above. For example, foreshortened vessels are very difficult to reconstruct since they are not in the longitudinal alignment necessary for the evaluation (as an effect of the angle vision), and overlapping can obscure regions of interests.

For all these reasons an accurate three-dimensional reconstruction is necessary to give a geometrical representation and furthermore to make a CFD analysis possible and meaningful.

Most of the 3D recontruction models are based on biplane angiography images [39], [41] which differ from MSPCA in terms of both the images and the technique, but the ideas to reconstruct the coronary tree are very similar. The downside of the biplane and RoCA technique is that they are not widely used [27] in interventional cardiology. Moreover, even if those two techniques are used in combination with the ECG signal to obtain the same heart phase, they may give higher errors in correlating the two views due to table movement or panning than the MSPCA technique.

2.2.1 Image Acquisition and Epipolar Lines Method

Over time, several different models have been developed for 3D reconstruction starting from multiple single plane images [49], [62], [82], [83], [84]. Acquiring multiple single plane images (MSPCA) (Figure 2.2), uses a slightly different protocol to the biplane technique. Whilst in the biplane device two images are acquired at the same time and thus at same heart phase, coronary artery cine-images are independently acquired from different views, i.e. different projection angles [37]–[40], [80]. The gantry position to obtain different projections is decided by the cardiologist's experience and it is possible that some images will be inadequate for analysis due to non-optimal angle view. With MSPCA images we must correlate the ECG data in order to choose images at the same point in the heart motion [81]. Respiratory motion might also be an issue but there is no simple way to compensate for this, and for the current wotk it is treated just as part of a general movement between acquisitions.

One of the most difficult challenges of working with MSPCA images is that, during acquisitions, in order to have a better view of the culprit artery on the X-ray intensifier screen, the view might be magnified by panning the screen along the projection axis. Furthermore,

often one image of the coronary tree is captured in one view, and then the table is moved before acquisition commences from a different angulation. Although in some modern imaging systems the table movements are recorded, historically this has not been the case. Table movements are very difficult to evaluate *a posteriori*, and they can lead to important reconstruction errors and inaccurate geometry which do not represent the real vessel.
These table movements lead to a non-correspondence of points between planes and then to an inaccurate reconstruction.

The workflow to compute a 3D reconstruction is composed of several steps, outlined in the abstract and illustrated graphically in Figure 2.1.
The first step is the choice of the pair of images that the user would like to segment. Usually end-diastole is chosen as the heart phase in which to perform the segmentation. The consistent identification of the same phase in multiple projections is much simpler when ECG data is available.

The acquisition process for an X-ray angiography is similar to the pinhole camera model used in computer vision and both of them are based on perspective projection. The main difference between the two systems is that using cameras the image is inverted. A single-plain digital angiographic system (Allura Xper FD10 System, Philips Medical Systems) was used for image acquisitions. A single run is composed of several image frames, in order to record different heart phases, and the gantry angles are selected by the individual operator. There was no restriction for table movement or panning during acquisitions since the software had to cope with images acquired from the standard clinical protocol. The information needed to compute the 3D reconstruction are all stored in the DICOM header. However, within the header the coordinates of the table movement are not stored. The data strictly needed for the 3DR are the following: gantry angles, distance source to detector, distance source to patient, image pixel scaling in terms of pixel size (e.g. 0.25 [*mm/pixel]*) and ECG data. The gantry angles are described in terms of right/left anterior oblique (Rao/Lao) and Caudal/Cranial (Caud/Cran).
The second step of the workflow is the computation of the transformation matrices which describe the relationship between the two views. The relationship between global co-ordinates and local coordinates (x_{Ap}, y_{Ap}, z_{Ap}) are described by rotation and translation matrices, which can be combined into a 4x4 matrix operator (Eq.2.1). The rotation matrix in 3D is composed of two rotations R_x and R_y, dictated by the degrees of freedom of the C-arm: the first rotation

is about the global *x* axis, and the second rotation is about the global *y* axis. The description of the total rotation is:

$$\begin{bmatrix} x'' \\ y'' \\ z'' \end{bmatrix} = [\mathrm{R_y}][\mathrm{R_x}] \begin{bmatrix} \mathrm{x} \\ \mathrm{y} \\ \mathrm{z} \end{bmatrix} = \begin{bmatrix} \cos\phi_y & 0 & -\sin\phi_y \\ 0 & 1 & 0 \\ \sin\phi_y & 0 & \cos\phi_y \end{bmatrix} \begin{bmatrix} 1 & 0 & 0 \\ 0 & \cos\phi_x & \sin\phi_x \\ 0 & -\sin\phi_x & \cos\phi_x \end{bmatrix} \begin{bmatrix} \mathrm{x} \\ \mathrm{y} \\ \mathrm{z} \end{bmatrix} \quad \text{(Eq.2.2)}$$

$$\begin{bmatrix} x'' \\ y'' \\ z'' \end{bmatrix} = \begin{bmatrix} \cos\phi_y & \sin\phi_x \sin\phi_y & -\cos\phi_x \sin\phi_y \\ 0 & \cos\phi_x & \sin\phi_x \\ \sin\phi_y & -\sin\phi_x \cos\phi_y & \cos\phi_x \cos\phi_y \end{bmatrix} \begin{bmatrix} \mathrm{x} \\ \mathrm{y} \\ \mathrm{z} \end{bmatrix} \quad \text{(Eq.2.3)}$$

Adding the translation:

$$\begin{bmatrix} x'' \\ y'' \\ z'' \\ 1 \end{bmatrix} = \begin{bmatrix} \cos\phi_y & \sin\phi_x \sin\phi_y & -\cos\phi_x \sin\phi_y & T_x \\ 0 & \cos\phi_x & \sin\phi_x & T_y \\ \sin\phi_y & -\sin\phi_x \cos\phi_y & \cos\phi_x \cos\phi_y & T_z \\ 0 & 0 & 0 & 1 \end{bmatrix} \begin{bmatrix} \mathrm{x} \\ \mathrm{y} \\ \mathrm{z} \\ 1 \end{bmatrix} \quad \text{(Eq.2.4)}$$

In Figure 2.3 a point on the centreline of the coronary artery is projected to the image plane. The point has coordinates $= [x, y, z]^T$, while the coordinates of P_A are naturally expressed in terms of the position in projection plane A so $P_A = [x_{APA}, y_{APA}]$ where x_{APA} and y_{APA} describe the projected x-coordinate and y-coordinate of point P into plane A.

To derive the coordinates of the point P in the projection plane the following equations are used:

$$\mathrm{x}_{\mathrm{A_{P_A}}} = \frac{(\mathrm{L_{OA}} + \mathrm{L_F})}{\mathrm{L_{OA}} + \mathrm{L_F} + \mathrm{z}_{\mathrm{A_P}}} \mathrm{x}_{\mathrm{A_P}} \quad \text{(Eq.2.5)}$$

$$\mathrm{y}_{\mathrm{A_{P_A}}} = \frac{(\mathrm{L_{OA}} + \mathrm{L_F})}{\mathrm{L_{OA}} + \mathrm{L_F} + \mathrm{z}_{\mathrm{A_P}}} \mathrm{y}_{\mathrm{A_P}} \quad \text{(Eq.2.6)}$$

$\mathrm{L_{OA}}$ defines the distance between the centre of projection plane A and the patient, $\mathrm{L_F}$ describes the distance between the patient and the X-ray source. $\mathrm{L_{OA}}$ and $\mathrm{L_F}$ are data stored within the Dicom file. The dimensions $\mathrm{x}_{\mathrm{A_P}}$ and $\mathrm{y}_{\mathrm{A_P}}$ describe the local coordinate of point P into plane A. Furthermore, the dimension z_{AP} is always negative and so there is always a magnification of the object to consider.

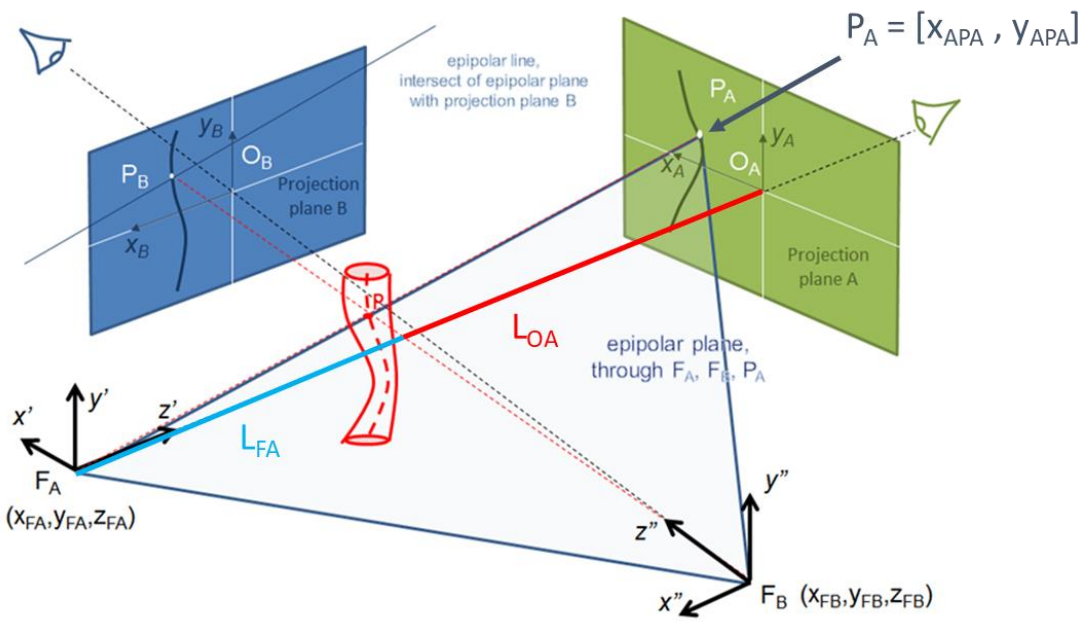

Figure 2.3: Coronary centreline point projected onto the two planes.
A 3D point (point P) is projected into two planes starting from two different positions of the focus (Fa and Fb). Pa is the projection of point P onto plane A. Pb is computed as intersection point between the projected coronary centreline onto plane B and epipolar plane computed from Fa, Fb, and Pa.

As already described, the coordinates of the point which has to be projected into the projection planes are given in the global coordinate system and so to apply the above equations the Q transformation is needed first in order to transform global to local coordinates (Eq.2.6).

$$\begin{bmatrix} x_{A_P} \\ y_{A_P} \\ z_{A_P} \\ 1 \end{bmatrix} = \begin{bmatrix} Q_{11} & Q_{12} & Q_{13} & Q_{14} \\ Q_{21} & Q_{22} & Q_{23} & Q_{24} \\ Q_{31} & Q_{32} & Q_{33} & Q_{34} \\ Q_{41} & Q_{42} & Q_{43} & Q_{44} \end{bmatrix}_{\mathrm{GA}} \begin{bmatrix} x_P \\ y_P \\ z_P \\ 1 \end{bmatrix} \qquad \text{(Eq.2.7)}$$

The **Q** matrix describes a rotation plus a translation (see Eq.2.8), the subscript GA defines that the operation transforms the global coordinates of a 3D point (x_P, y_p, z_p) to local coordinates on plane A $(x_{A_P}, y_{AP}, z_{AP})$.

Before starting with the third step which is the table movement correction, the image coordinate reference in MATLAB are moved to be in the middle of the image as shown in Figure 2.4,this is done in order to have a consistent coordinate reference with the whole system.

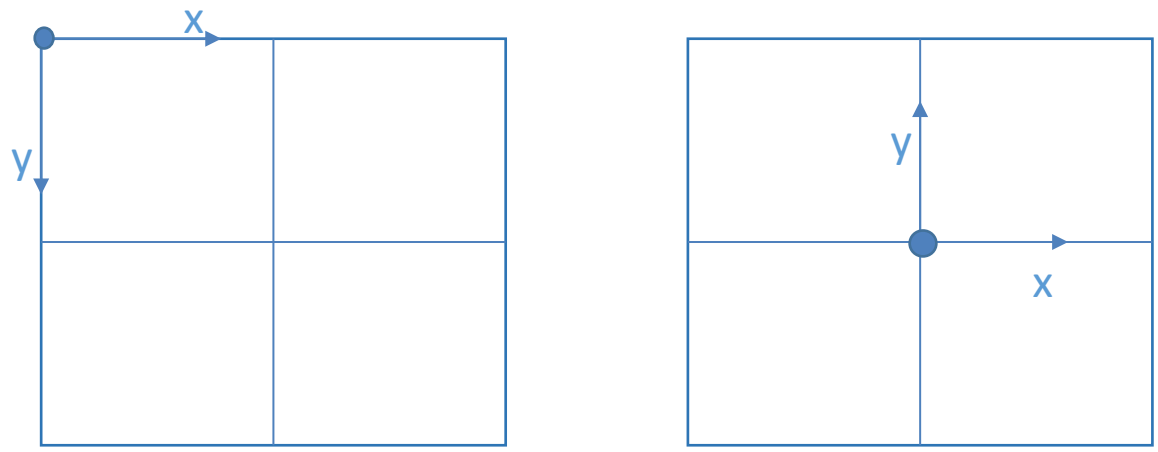

Figure 2.4: Moving Coordinate reference in MATLAB for table correction.
A) Initial coordinate system. B) The coordinate system moved to the centre of the image in order to reflect the C-arm coordinate system.

2.2.2 Novel Click to Correct Algorithm

Between and during acquisitions of MSPCA images, the table position is often changed based on the clinical operator's clinical need. Furthermore, the movement in terms of translation is not known or predictable which makes the 3D reconstruction a non-trivial process. Since these movements may introduce large errors, they have to be eliminated before starting the reconstruction process. The approach for table movement correction implemented for this thesis is based on the application of an affine transformation between the two planes, based on the hypothesis that the motion of the coronary system produces a projection image that is an affine transformation of the image that would have been produced without motion [79]. This is not strictly true, but might be a good starting point for the motion correction. The accuracy of reconstructions under table movement using this model has been investigated separately. The affine transformation matrix has six parameters (α_{ij}), and in principle these could be computed if six correspondence points (features points) were selected in two images.

$$\begin{bmatrix} x_{PA} \\ y_{PA} \\ 1 \end{bmatrix} = \begin{bmatrix} \alpha_{11} & \alpha_{12} & \alpha_{13} \\ \alpha_{21} & \alpha_{22} & \alpha_{23} \\ 0 & 0 & 1 \end{bmatrix} \begin{bmatrix} x_{PA'} \\ y_{PA'} \\ 1 \end{bmatrix} \quad \text{(Eq.2.9)}$$

However, in practice the computation is unstable, for reasons that will be discussed later, and in this thesis a simpler transformation matrix with only 3 parameters is adopted (Eq.2.8).

$$\begin{bmatrix} x_{PA} \\ y_{PA} \\ 1 \end{bmatrix} = \begin{bmatrix} \alpha_{11} & 0 & \alpha_{13} \\ 0 & \alpha_{11} & \alpha_{23} \\ 0 & 0 & 1 \end{bmatrix} \begin{bmatrix} x_{PA'} \\ y_{PA'} \\ 1 \end{bmatrix} \quad \text{(Eq.2.10)}$$

The three parameters describe a scaling, associated with the movement of the coronaries along the line from the source and orthogonal to the projection plane and a translation parallel to the projection plane. Since the affine transformation matrix has three unknown parameters, the user must choose at least three points which are visible in both views (usually feature points such as bifurcation are chosen or stenosis), which will be moved into correspondence in the correction operation. However, the user can choose as many points as required to correct table movement during acquisition. Corrections are not just necessary for table movements and heart or respiratory motion, but the gantry parameters stored in the DICOM header may not accurately describe by the system. The main reasons why these data are not accurately described are related especially to mechanical errors (manufacturing) in the device, and intrinsic parameters such as the skew parameter. Examples of errors and correction of the latter ones between the two views is shown in Figure 2.5.

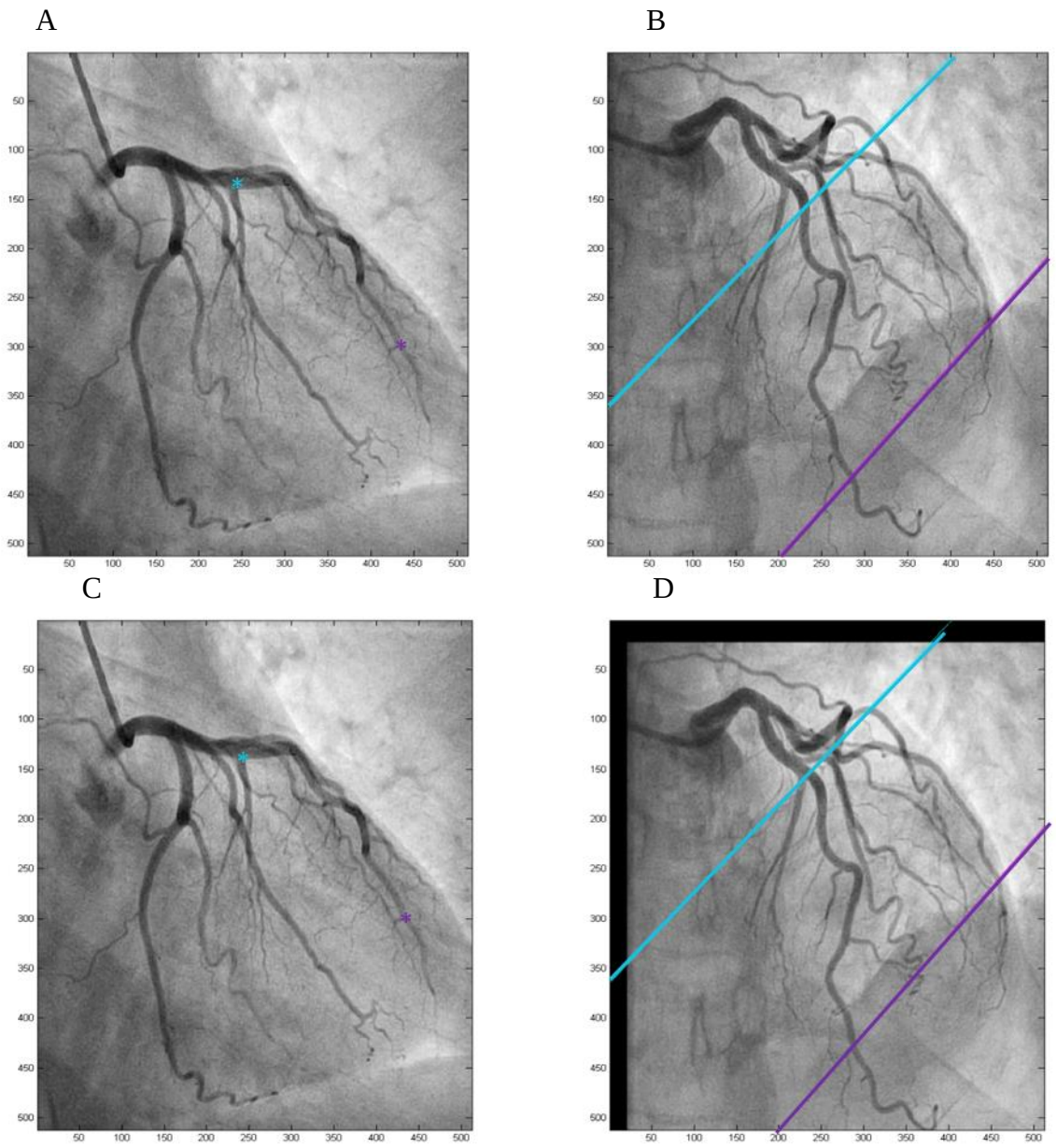

Figure 2.5: Steps for table movement correction.
A) Featured points (e.g. branches, stenosis) are marked onto the first view. B) Epipolar planes are projected on second view to form epipolar lines. C) Affine matrix is computed. D) Table movement correction applied to second view.

Epipolar geometry is the term used to describe the geometry of reconstruction of the shape of a body from stereoscopic views. The concept of epipolar geometry is to correlate points between two or more different views in different projection planes [43], [44], [89]. If the projection of a point in 3D onto any particular imaging plane is known and the locations of the X-ray source are known for that and any other projection are known then the epipolar plane is defined as that which includes these three points (Figure 2.3). The projection of the point into the second projection plane lies on a line that is the intersection between the epipolar plane and

the second projection plane. In order to find the correspondence of points between the two views, epipolar lines are computed [44], [63], [85]–[88]. The epipolar lines are the lines in the second projection that a selected point in the first projection must lie, given the position of the camera for the two projections. In Figure 2.5 the point at the blue cross in image A must lie on the blue line in image B, and similarly for the magenta. Note that the epipolar lines for the two points are almost parallel to each other, and this is responsible for a lack of robustness to error in the identification of corresponding points since large translations parallel to the lines is required to compensate for small errors in distance between the points

The general equation of a plane is c1x+ c2y+ c3z+ c4=0. The equation can be multiplied by an arbitrary constant. Choosing this constant as $-1/c_4$ (providing $c_4 \neq 0$) and writing $a_i = -c_i/c_4$ we obtain:

$$a_1 x + a_2 y + a_3 z - 1 = 0 \qquad \text{(Eq.2.11)}$$

or, in matrix algebra,

$$\begin{bmatrix} x \\ y \\ z \end{bmatrix}^{\mathrm{T}} \begin{bmatrix} a_1 \\ a_2 \\ a_3 \end{bmatrix} - 1 = 0 \qquad \text{(Eq.2.12)}$$

This equation must be satisfied at each of the known points, F_A, F_B and P_A, in the epipolar plane, and so:

$$\begin{bmatrix} x_{FA} & y_{FA} & z_{FA} \\ x_{FB} & y_{FB} & z_{FB} \\ x_{PA} & y_{PA} & z_{PA} \end{bmatrix} \begin{bmatrix} a_1 \\ a_2 \\ a_3 \end{bmatrix} = \begin{bmatrix} 1 \\ 1 \\ 1 \end{bmatrix} \qquad \text{(Eq.2.13)}$$

$$\begin{bmatrix} a_1 \\ a_2 \\ a_3 \end{bmatrix} = \begin{bmatrix} x_{FA} & y_{FA} & z_{FA} \\ x_{FB} & y_{FB} & z_{FB} \\ x_{PA} & y_{PA} & z_{PA} \end{bmatrix}^{-1} \begin{bmatrix} 1 \\ 1 \\ 1 \end{bmatrix} \qquad \text{(Eq.2.14)}$$

Thus, the equation of the epipolar plane in any coordinate system can be determined by computing the co-ordinates in that coordinate system.

To determine the equation of the epipolar line in projection plane B that is the intersection of this plane with the epipolar plane, it is simplest to describe the epipolar plane in co-ordinate system B. Then:

$$\begin{bmatrix} a_{1_B} \\ a_{2_B} \\ a_{3_B} \end{bmatrix} = \begin{bmatrix} x_{FA_B} & y_{FA_B} & z_{FA_B} \\ x_{FB_B} & y_{FB_B} & z_{FB_B} \\ x_{PA_B} & y_{PA_B} & z_{PA_B} \end{bmatrix}^{-1} \begin{bmatrix} 1 \\ 1 \\ 1 \end{bmatrix} \qquad \text{(Eq.2.15)}$$

The equation of the epipolar line in projection plane B is simply the equation of the plane when $z_B=0$, or:

$$a_{1_B} x_B + a_{2_B} y_B - 1 = 0 \qquad \text{(Eq.2.16)}$$

The intersection between projection plane B and the epipolar plane is the epipolar line. The projection of the point to be reconstructed in 3D must lie along the epipolar line. The intersection between the projection of the vessel centreline in plane B and the epipolar line yields the position of point B in projection plane B.

An example of the epipolar concept applied to clinical coronary artery images is given in Figure 2.6.

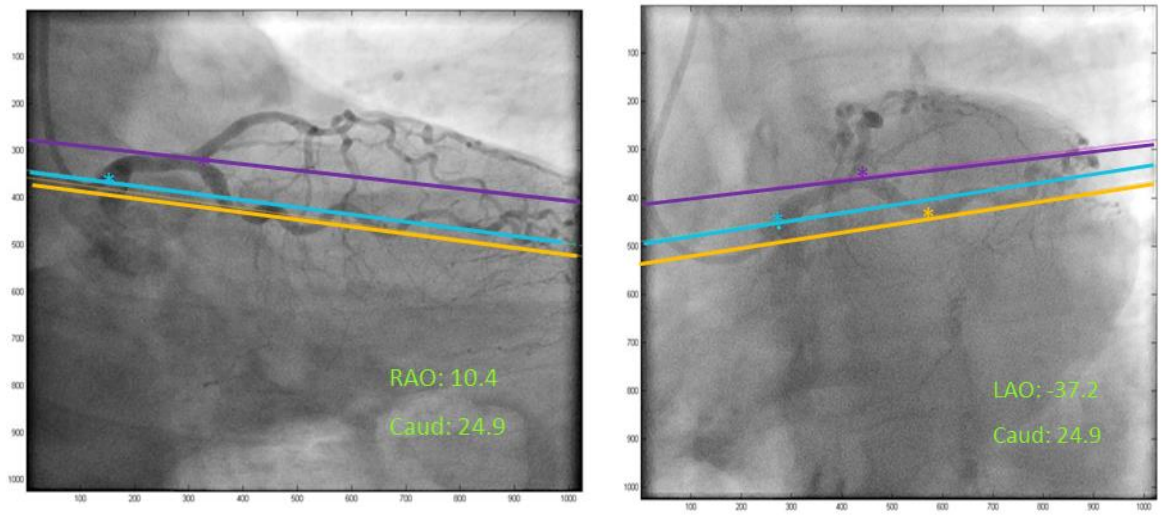

Figure 2.6: Example of Epipolar lines concept applied to angiography images. For this example it can be noticed the near parallel nature of the epipolar lines.

It is clear from these test images that the epipolar lines are almost parallel to the coronary centreline, and this introduces a complication in the correction for motion artefact. Although it is possible to find the parameters in the transformation matrix that bring three user-selected points onto the epipolar lines, the near parallel nature of the epipolar lines means that small errors in the selection of corresponding points can lead to unrealistically large translations. The actual transformation computed is:

$$\begin{bmatrix} x_{PA} \\ y_{PA} \\ 1 \end{bmatrix} = \begin{bmatrix} \alpha_{11} & 0 & -m\alpha_{23} \\ 0 & \alpha_{11} & \alpha_{23} \\ 0 & 0 & 1 \end{bmatrix} \begin{bmatrix} x_{PA'} \\ y_{PA'} \\ 1 \end{bmatrix} \qquad \text{(Eq.2.17)}$$

where m is the mean slope of the epipolar lines for the selected points used for the correction. This change in the transformation is more stable in practice.

2.2.3 Manual segmentation and the 3D Reconstruction process

To achieve a 3D reconstruction, the next step of the workflow is the centreline segmentation in the first view where the 2D coronary is extracted manually from the image. In the developed workflow, the centreline segmentation process and table movement correction require user

input. Although it is possible to identify the centreline automatically, experience gained during the development and testing of the workflow indicated that manual identification in each view gives to the user more control and is less error prone. There is a balance between the interaction demanded of the user, which should be minimal, and the robustness of the process. It can be very frustrating when an automated process detects the wrong line unless correction is easy. For this thesis manual assistance was chosen to maximize the number of vessels that could be segmented by the software in normal operation. An example of coronary segmentation in the first view (Plane A) and the corresponding proximal and distal point in the second view using epipolar lines is shown in Figure 2.7.

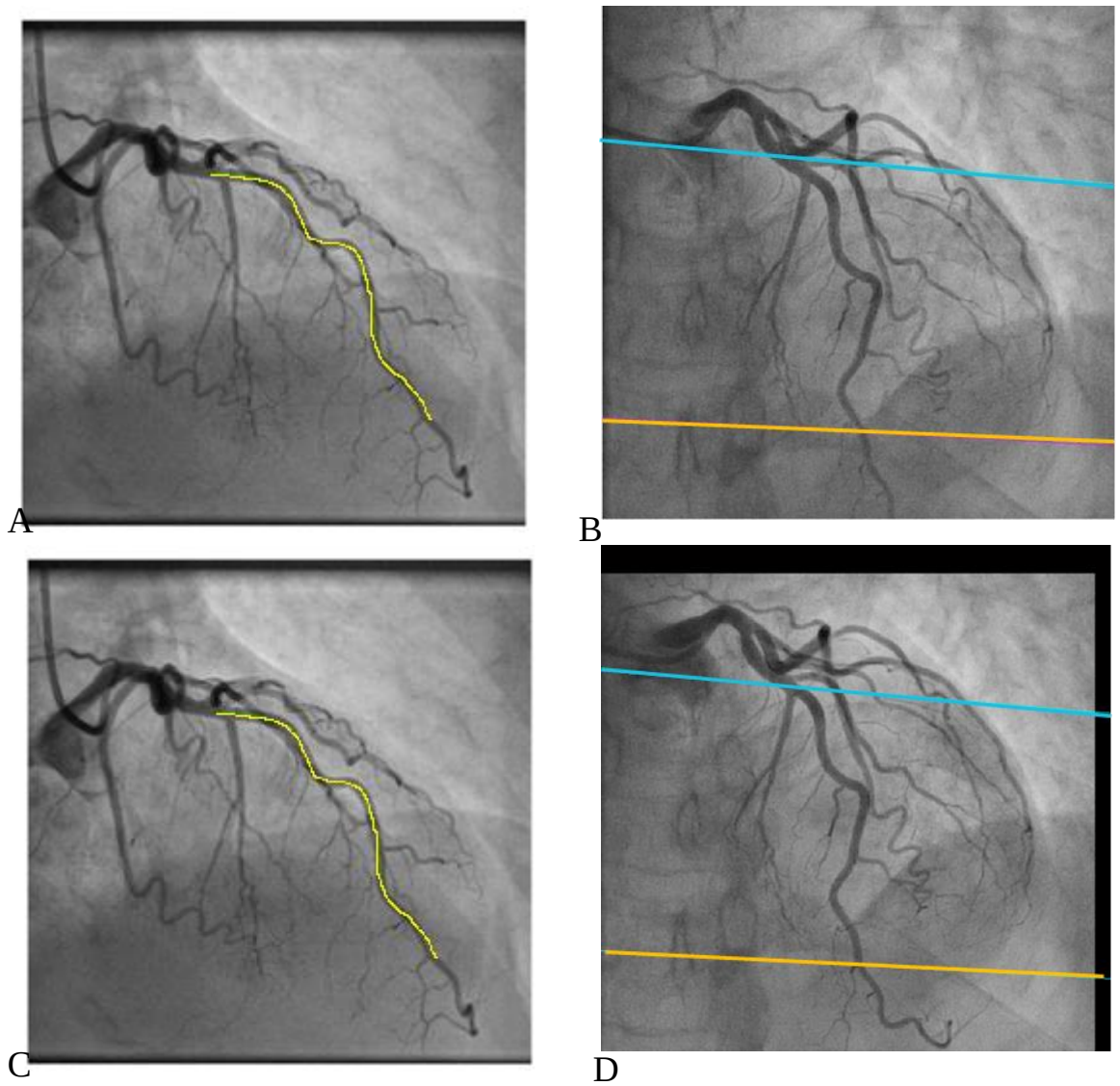

Figure 2.7: A) Manual segmentation in the master view (Plane A).
B-C) The proximal and distal point have been projected into the second view (Plane B). D) Segmentation with table correction can start on the second view.

The computation of the two transformation matrices which define the relationship between the two views in conjunction with the epipolar constraints are employed for establishing the point correspondences on the vessel centrelines based on the two 2D coronary artery identified manually on the two views. The centreline is then discretised into equally spaced points. Starting from several points along the first 2D segmented centreline epipolar planes from each point taken from the first view are computed and then projected onto the second view. The position in plane B of points identified in plane A are given by the epipolar line intersections with the 2D centreline in the second view.

The reconstruction operation is the computation of the 3D position of point P given the coordinates of its image in the two projection planes. Equations presented in section 2.1.1 are re-arranged to give:

$$(\mathrm{L_F} + \mathrm{L_{OA}})\mathrm{x_{A_P}} - \mathrm{x_{A_{P_A}}}\mathrm{z_{A_P}} = (\mathrm{L_F} + \mathrm{L_{OA}})\mathrm{x_{A_{P_A}}} \quad \text{(Eq.2.18)}$$

$$(\mathrm{L_F} + \mathrm{L_{OA}})\mathrm{y_{A_P}} - \mathrm{y_{A_{P_A}}}\mathrm{z_{A_P}} = (\mathrm{L_F} + \mathrm{L_{OA}})\mathrm{y_{A_{P_A}}} \quad \text{(Eq.2.19)}$$

And in matrix representation:

$$\begin{bmatrix} (\mathrm{L_F} + \mathrm{L_{OA}}) & 0 & -\mathrm{x_{A_{P_A}}} & 0 \\ 0 & (\mathrm{L_F} + \mathrm{L_{OA}}) & -\mathrm{y_{A_{P_A}}} & 0 \end{bmatrix} \begin{bmatrix} x_{A_P} \\ y_{A_P} \\ z_{A_P} \\ 1 \end{bmatrix} = \begin{bmatrix} (L_F + L_{OA})x_{A_{P_A}} \\ (L_F + L_{OA})y_{A_{P_A}} \end{bmatrix} \quad \text{(Eq.2.20)}$$

Substituting $\{x_{AP}, y_{AP}, z_{AP}, 1\}^T$ with the Eq. 2.6 we have

$$[\mathrm{H}]_\mathrm{A}[Q]_\mathrm{GA}\{x\}_\mathrm{P} = \begin{bmatrix} (L_F + L_{OA})x_{A_{P_A}} \\ (L_F + L_{OA})y_{A_{P_A}} \end{bmatrix} \quad \text{(Eq.2.21)}$$

with:

$$[\mathrm{H}]_\mathrm{A} = \begin{bmatrix} (\mathrm{L_F} + \mathrm{L_{OA}}) & 0 & -\mathrm{x_{A_{P_A}}} & 0 \\ 0 & (\mathrm{L_F} + \mathrm{L_{OA}}) & -\mathrm{y_{A_{P_A}}} & 0 \end{bmatrix} \quad \text{(Eq.2.22)}$$

Similarly, from the second view:

$$[\mathrm{H}]_\mathrm{B}[Q]_\mathrm{GB}\{x\}_\mathrm{P} = \begin{bmatrix} (L_F + L_{OB})x_{B_{P_B}} \\ (L_F + L_{OB})y_{B_{P_B}} \end{bmatrix} \quad \text{(Eq.2.23)}$$

Taking the two equations together:

$$\begin{bmatrix} [\mathrm{H}]_\mathrm{A}[\mathrm{Q}]_\mathrm{GA} \\ [\mathrm{H}]_\mathrm{B}[\mathrm{Q}]_\mathrm{GB} \end{bmatrix} [x]_\mathrm{P} = \begin{bmatrix} (L_F + L_{OA})x_{A_{P_A}} \\ (L_F + L_{OA})y_{A_{P_A}} \\ (L_F + L_{OB})x_{B_{P_B}} \\ (L_F + L_{OB})y_{B_{P_B}} \end{bmatrix} \quad \text{(Eq.2.24)}$$

Having four equations in three unknowns (i.e. an overdetermined system in the *x*, *y*, *z* global coordinates) the linear system can be solved using a standard linear least squares approach which minimises the sum of squared differences.

The best approximation is computed using the general formula:

$$[A]^{\mathrm{T}}[A]\{\mathrm{u}\} = -[A]^{\mathrm{T}}\{b\} \qquad \text{(Eq.2.25)}$$

where $\{\mathrm{u}\}$ is equal to $[x, y, z]_P^T$. Once the **u** matrix is computed the skeleton of the segmented coronary is produced in terms of 3D vessel centreline. An example of 3D vessel centreline is shown in **Figure 2.8**.

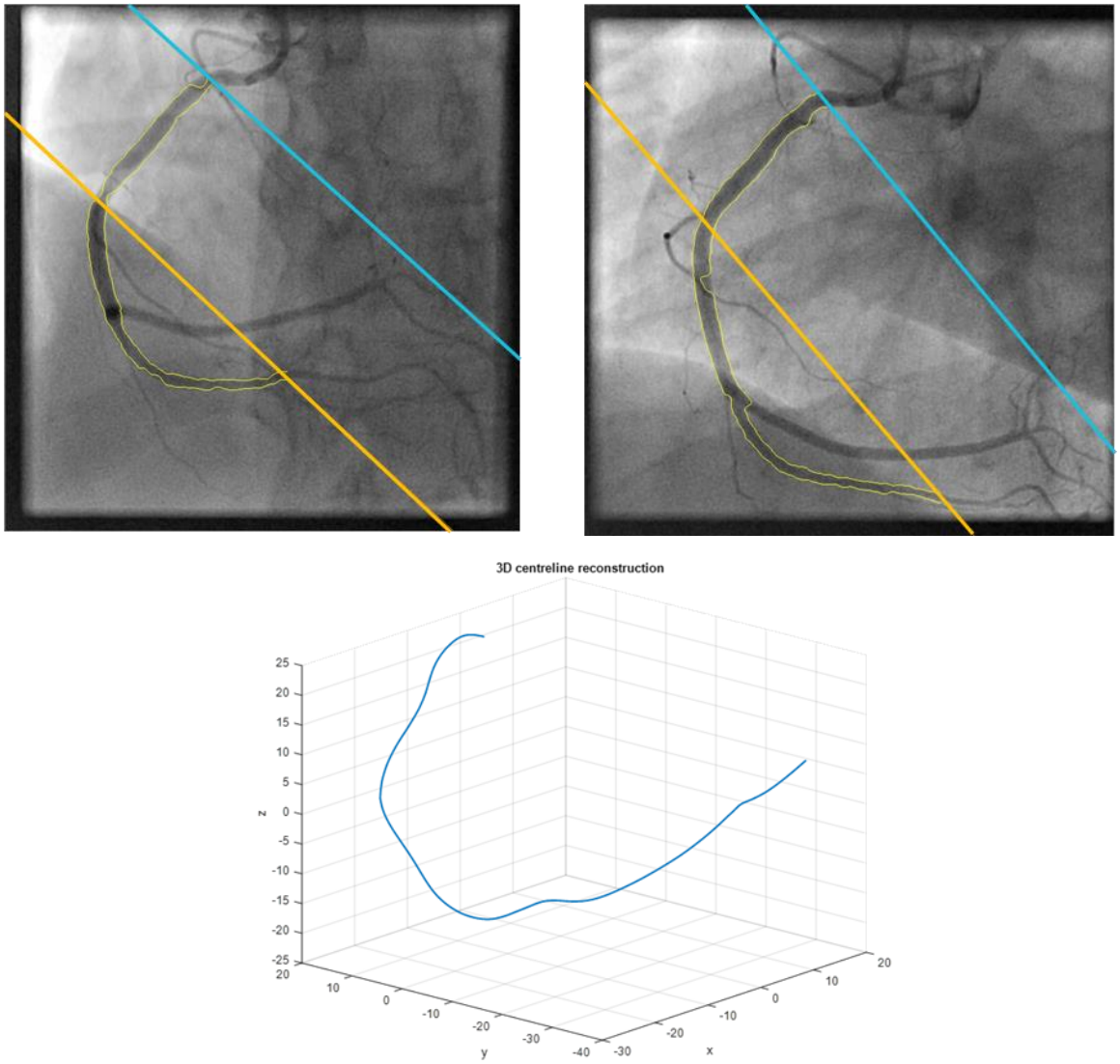

Figure 2.8: Top) Images of a right coronary artery from two different angiographic views. Bottom)3D Centreline reconstruction example from the two images. The centreline is defined with a series of 3D points with their coordinates x, y and z.

Once the 3D centreline is constructed, the next step is the computation of the vessel borders in order to achieve information about the vessel radius for each location along the 2D centreline. Since edge detection is very sensitive to noise, a prior operation of smoothing is performed in both views. The smoothing is performed with a convolution between the image and a Gaussian blur kernel, given by Eq. 2.24 in order to obtain a smooth grayscale digital image as shown in **Figure 2.9**.

$$G(x,y) = \frac{1}{2\pi\sigma^2} exp^{-\left(\frac{x^2+y^2}{2\sigma^2}\right)} \quad \text{(Eq.2.26)}$$

Following the smoothing operation, the normal along each location is computed. To compute the normal for every point the derivative has to be computed first.

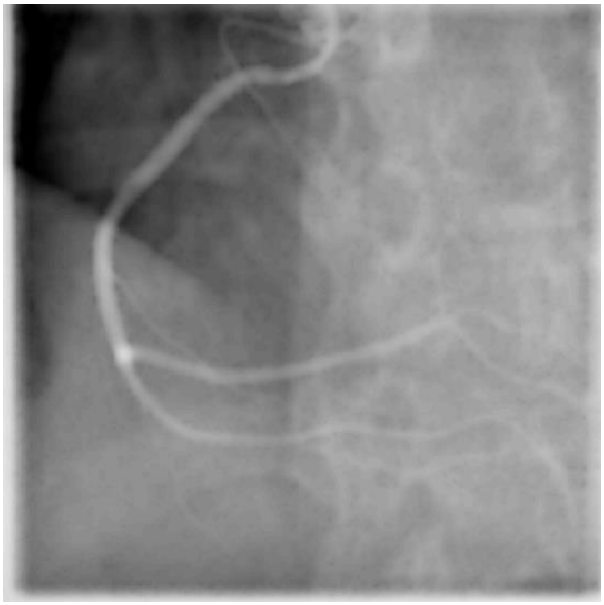

Figure 2.9: Smooth grayscale digital image. The original image is convoluted with a 2D Gaussian kernel.

The considered derivative is the central difference:

$$f'(x_i) = \frac{(y_{i+1} - y_{i-1})}{(x_{i+1} - x_{i-1})} \quad \text{(Eq.2.27)}$$

Thus, starting from the centreline, the normal is computed for every point and the values of the pixel intensity along the normal is registered. Border locations are where the derivative reaches the highest and lowest values. Ideally, if we would have had a binary image (black background equal to 0 white vessel equal to 1) as input the derivative would have the form of **Figure 2.10**.

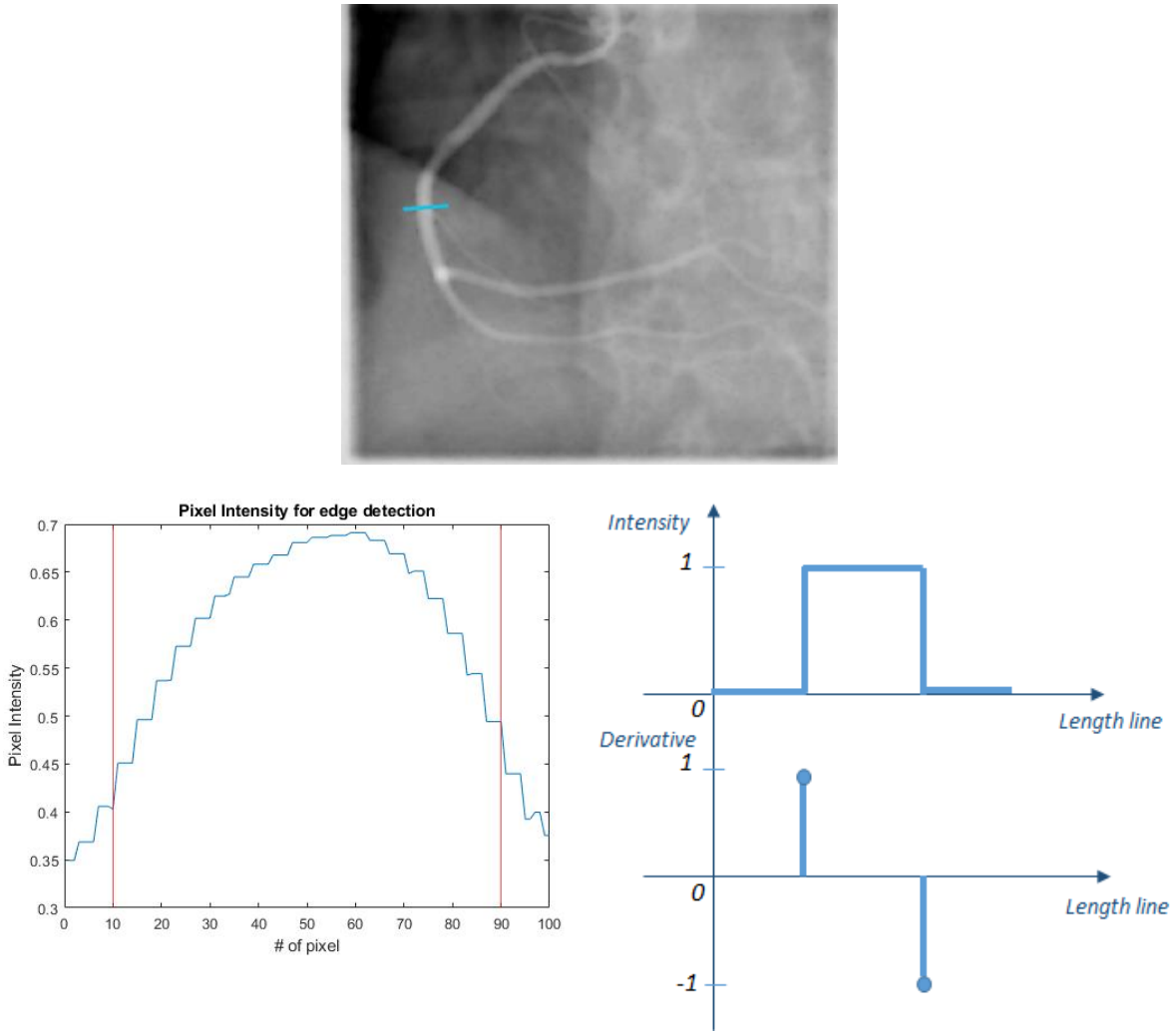

Figure 2.10: Example of computing borders on a greyscale coronary image.
Top Image) Greyscale image of a coronary, along the blue line values of pixel intensity are saved. Bottom left) Plot of the pixels intensity values along the blue line; the two red vertical lines represent the location of the borders for the coronary. Bottom right) Idealised coronary edge detection for a binary image (black and white pixels).

Once the radius for each centreline location is computed on the image plane, to recover the real dimension (since radius on the image plane is magnified) the following formula has been used:

$$r_{3D} = r_{image} * \frac{distSP}{distSD} \qquad \text{(Eq.2.28)}$$

Where r_{3D} is the radius dimension for the 3D reconstruction, r_{image} is the radius computed on the 2D projection images, $distSP$ and $distSD$ are the distance between the source (X-Ray source) and the patient and the distance between the source and the detector (X-Ray panel). The ratio $\frac{distSP}{distSD}$ is always < 1 so r_{3D} is always smaller than r_{image} as it should be when working with projected images. Note that this is an approximation, and *distSP* could be replaced using the computed local z-co-ordinate in 3D. In practice this produces a relatively small change, but

it has been implemented in later versions of the software. It is important to mention that all the dimensions taken from the image plane have to be transformed from *pixel* to *mm*, this is achieved multiplying the pixel dimension for the image pixel ratio which is a parameter within the DICOM header. Once the 3D centreline is reconstructed starting from the two projection planes, the 3D lumen of the vessel has to be computed. The coronary lumen is approximated on the basis of a sequence of circular cross-section contours. Each circular disk along the vessel is centred at and perpendicular to the 3D centreline at each location $(x_i, y_i, z_i \quad with\, i = 1, \dots, n)$ in order to form the coronary skeleton. Every circle which forms the skeleton has been arbitrarily chosen to have 128 nodes called vertices, the conjunction between three vertices form a closed domain called a face. Since from the reconstruction process two different values of r_{image} are obtained for every point along the centreline (one from each projection), the mean value for every pair of points has been chosen to compute the circle in 3D. It is a limitation of the reconstruction that the vessel is considered circular at every cross-section. Superficially it might appear that there is sufficient information from the two projections to define the two principal radii of an ellipse, but in fact the orientation about the axis would not be determined from just two projections.

Triangular patches formed by vertices and faces have been computed to create the surface and to connect every pair of consecutive disks in order to have a 3D rendering of the segmented vessel Figure 2.11. The computed .stl file is a closed domain with inlet, outlet and wall (Figure 2.12).

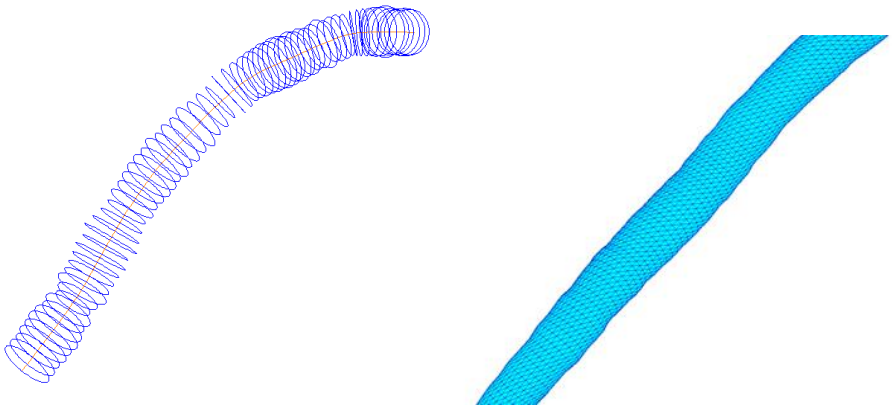

Figure 2.11: A)Skeleton of a coronary artery formed by circles normal to the centreline. B) Zoom of coronary surface mesh (.stl) formed by triangular patches.

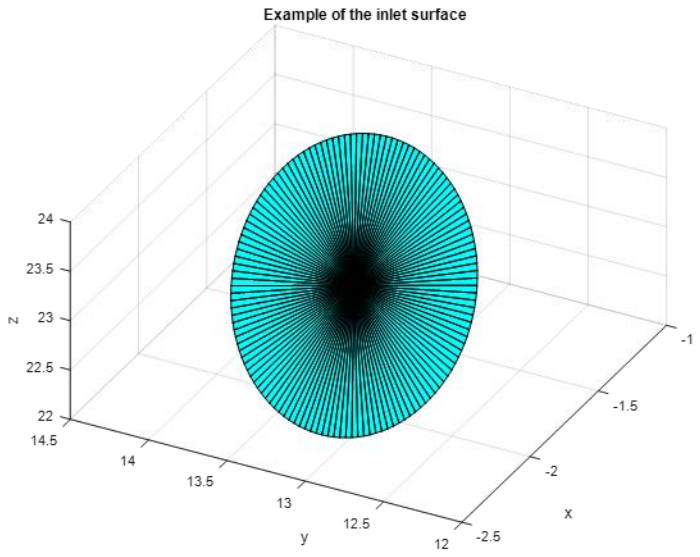

Figure 2.12: Example of the inlet surface for the surface mesh.
The surface is created with triangular patches, the base of every triangle is formed connecting two consecutive points on the circle edge.

The creation of a 3D surface mesh is the first step to computed CFD analyses on the reconstructed geometries.

2.3 Creation of a Graphical User Interface (GUI) to achieve the segmentation

A MATLAB GUI (graphical user interfaces) has been created in order to allow users to use the 3D Reconstruction tool more easily without the need to learn how to code in MATLAB. Furthermore, it is also possible to export into, and to use the application in another computer as a standalone project without the need to have MATLAB installed.

The GUI contains several windows such as buttons and sliders to visualize the angiography images. An image of the developed GUI is shown in Figure 2.13.

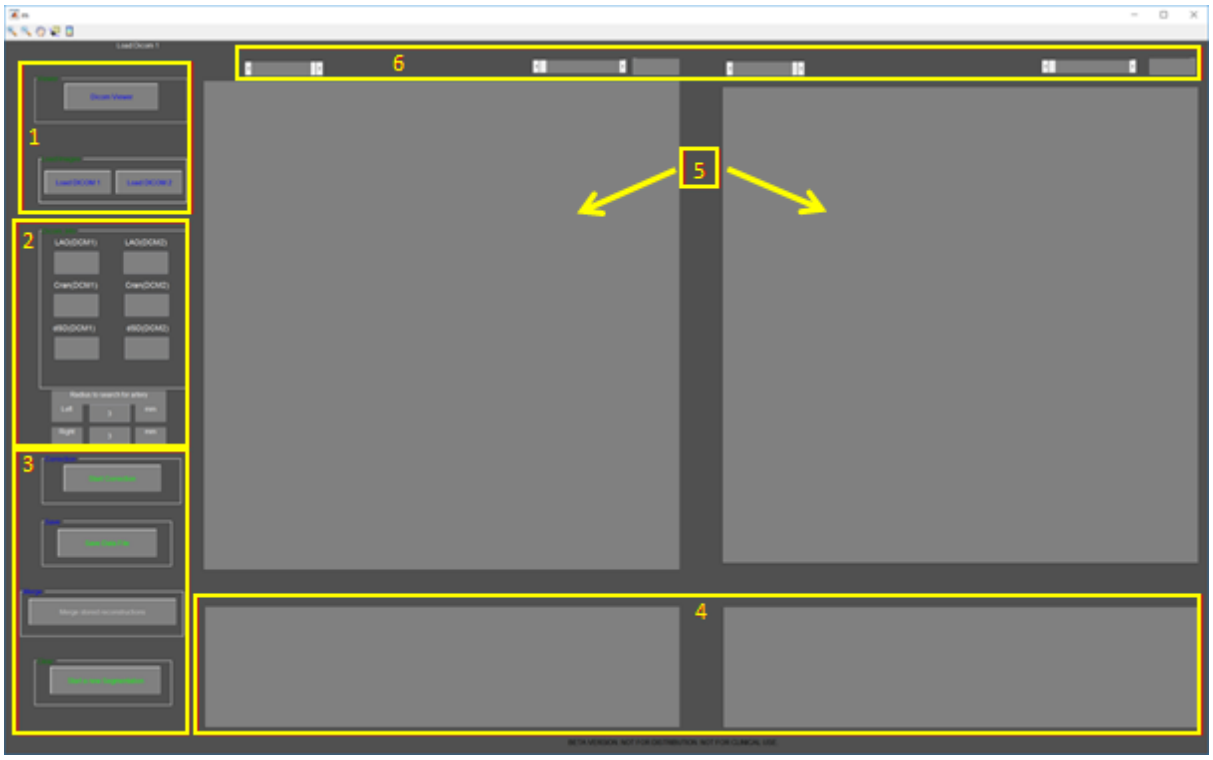

Figure 2.13: Skeleton of the developed GUI with push buttons to perform coronary segmentation. The left hand side is formed by push buttons and system information. Central panels (4-5) are for ECG data and 2D coronary images

First Step Segmentation

The segmentation process starts with the DICOM viewer (Figure 2.13 box n 1). The DICOM file name is a numeric and letter code which is not linked to the angiography run number, so it is impossible to recognize the run from the DICOM name. This is important for clinicians since they are not able to remap the DICOM code to the right angiography run. The viewer gives the user the opportunity to have a pre-view of the file to support the choice of the best runs for the segmentation. Once the choice is made the user needs to load the two views pressing the two

buttons on the left hand side (Load DICOM 1 and DICOM 2). Information regarding the position of the C-arm in terms of angles (LAO/RAO Caud/Cran) and the distance between the source to the detector are printed in the boxes on the left hand side (Figure 2.13 box n 2). These data are important for two reasons: first of all the geometrical data are important for the reconstruction process, if these data are not saved within the DICOM header the reconstruction cannot start, and secondly the angles give a spatial information to the user about the position of the C-arm while the acquisition was done. If the difference between the angles is less than 30° a warning window pops up telling the user the reconstruction can be achieved although it might be less accurate than using a bigger angle difference between the two images. Showing a warning message regarding the low angle is a reasonable choice, in fact even if the coronary with its stenosis is displayed successfully on the screens, the stenosis severity assessment from the 2D views could be unreliable. Furthermore, 2D images are unable to collect the right cross sectional area of the stenosis (Figure 2.14).

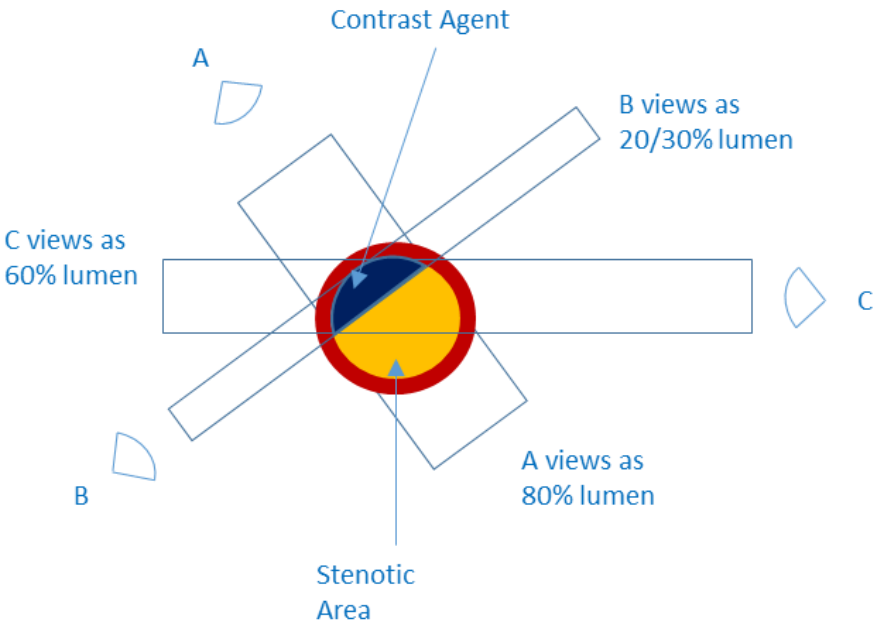

Figure 2.14: Percentage of coronary lumen view from different angulations.
A section of a stenotic vessel is represented with a stenotic area in yellow, contrast agent in blue, indicating where the blood is flowing and vessel wall in red. Images of the vessel from different angulations/perspectives (A, B, C) can show a different stenosis severity (80%, 60%, 20/30%).

There is the option to give a first estimation of the coronary radius on a box on the left hand side, usually the values of the first estimation varies between 2-3mm (Figure 2.13 box n 2). A process starts in background for the coronary edge detection, the radius initialization is helpful

especially in coronaries with branches. Close to the region of a branch the edge detection algorithm is likely to fail and manual corrections are needed.

On the top part of the GUI, two sliders allow the user to move through the runs and allow for an accurate selection of the best frame to use for the segmentation, trying to avoid overlapping of the vessels (Figure 2.13 box n 6). The movement of the slider is paired with the ECG graph; the user needs to know the exact cardiac phase of the projected image.

On the bottom part of the GUI ECG curves are plotted underneath the correspondent run in order to choose a frame in both view which are in the same cardiac phase (Figure 2.13 box n 4). Usually the chosen cardiac phase is end-diastole since the heart is at its maximum expansion. On these two plots a red marker is moving accordingly with the motion of the slider.

Once the two MSPCA images have been chosen, the two images are displayed on the two windows (Figure 2.13 box n 5 and Figure 2.15) and the user starts to segment manually the centreline in the first image, a manual segmentation gives more control to the user and is quick. If the user clicks accidentally a wrong point, there is the option to undo the last action clicking the right mouse button.

Centreline Computation

The computation of the centreline is achieved by a piecewise cubic interpolation which produces a cubic polynomial $P(x)$ where on each subinterval $x_k \leq x \leq x_{k+1}$ the polynomial is a cubic Hermite interpolating polynomial with specified derivatives at the interpolation points. Moreover, the centreline is discretized with equally spaced points which are saved in a MATLAB matrix as points coordinates *(x,y)* in the projection plane.

Manual corrections are necessary regarding the edge detections, the variation of the radius along the length for every coronary artery is the most important factor for the FFR computation. For this reason, it is fundamental to maintain the coronary shape and more important to capture correctly the physiological radius variation along the stenosis. Using a simple Bernoulli calculation is easy to show that a small variation in the minimum radius (r_{sten}) for the stenotic area leads to large errors for the FFR index (eq. 1.9), and so it is critical that the user checks the segmentation and ensures that the radii are adequately captured especially in the region of the stenosis.

Surface Mesh Creation

When the user has completed the segmentation, the 3D surface mesh can be saved in *.stl* format plus it is also possible to save the coordinates of the centreline in *.vtk* format (Figure 2.13 box n 3). The output *.stl* file is a concatenation of three *.stl* files; the 3D surface mesh is a closed surface connecting inlet, wall and outlet to facilitate the process of creating a volumetric mesh when the *.stl* file is exported to a meshing software.

As it can be seen in Figure 2.15 the user is computing the table movement corrections. Three points (or at least) are marked on the first view; then the points are projected on the second plane for correction. In Figure 2.16 the user had segmented the vessel from the first view and borders are computed starting from each point of the centreline. The segmentation process ends when the vessel is segmented in both views (Figure 2.17). The created surface mesh can be imported and visualized within the VIRTUheart™ research tool (Figure 2.18). After creating the volumetric mesh, it is possible to apply CFD to the geometry and to compute the vFFR index (Figure 2.19,Figure 2.20).

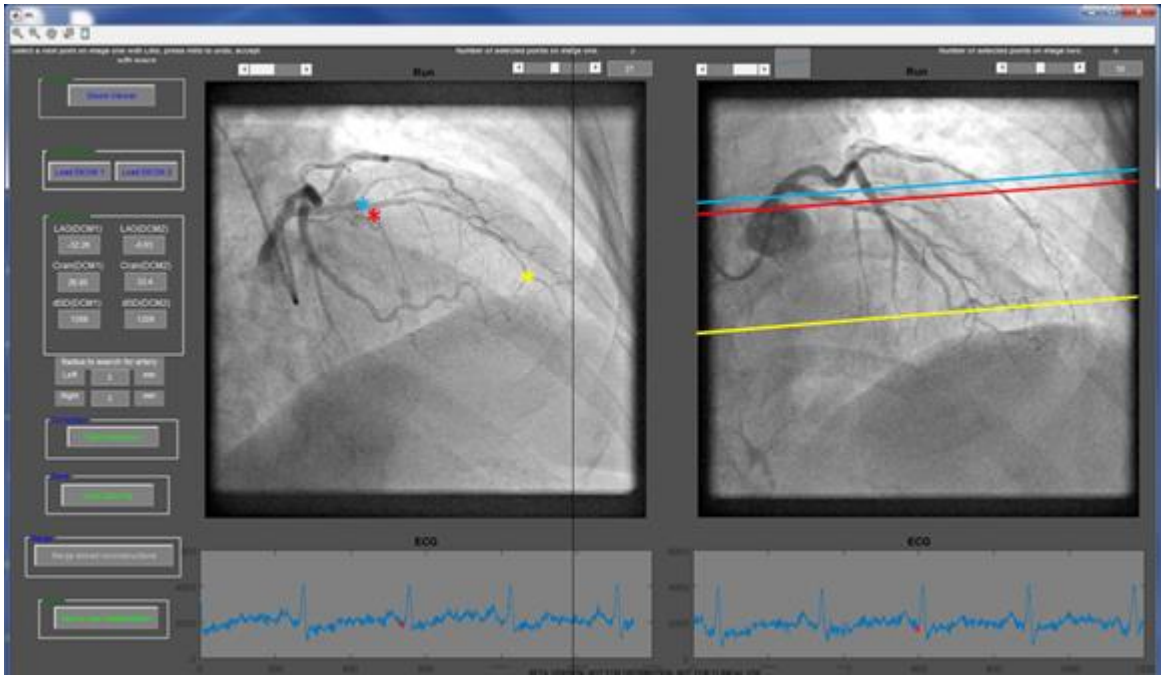

Figure 2.15: Table movement correction process.
A) Three points are marked on the first plane. B) Epipolar lines are computed on second plane.

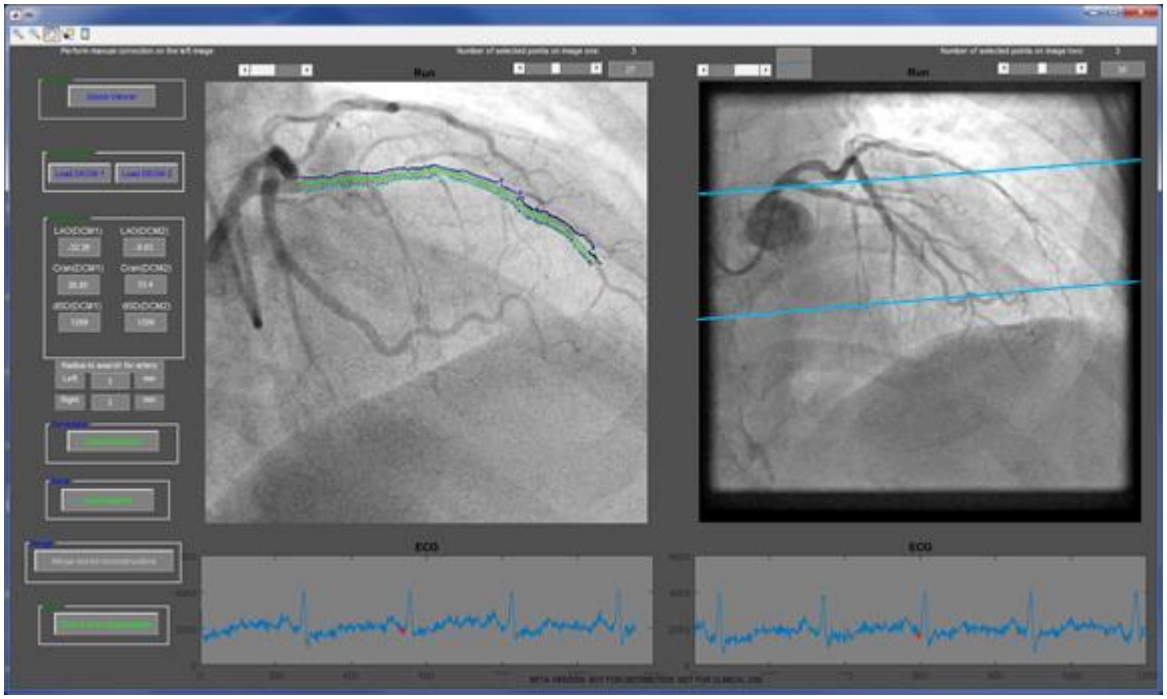

Figure 2.16: The vessel has been segmented in the first view (Left).
The start and end points of the vessel are marked by the epipolar lines on the second view (Right).

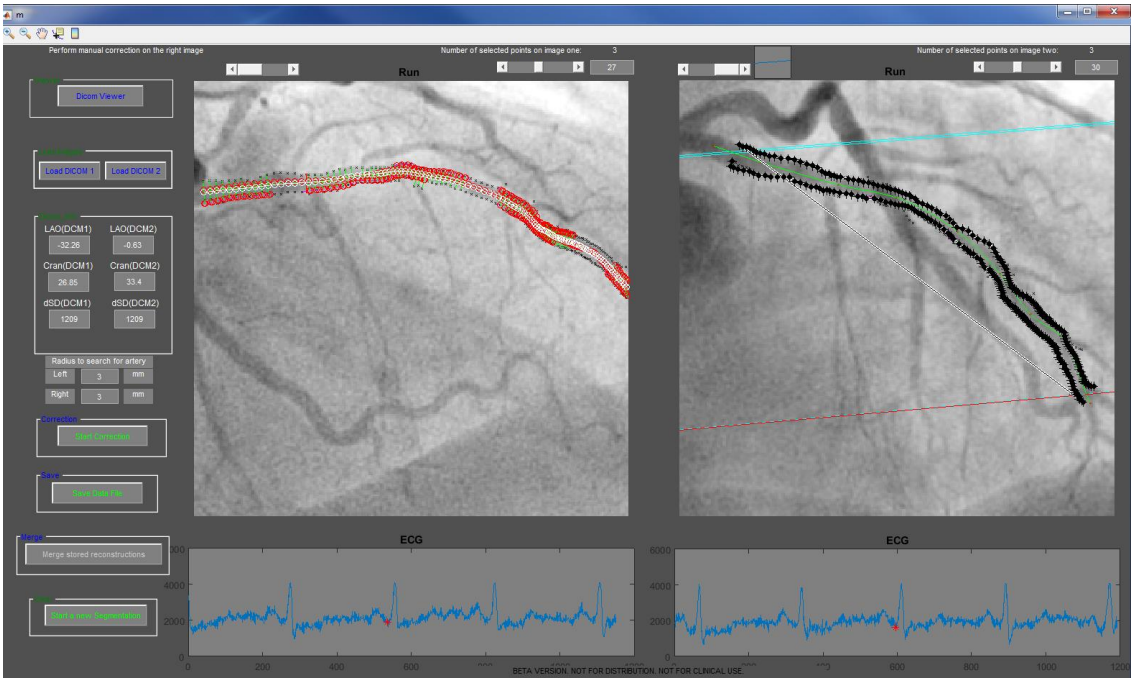

Figure 2.17: The vessel is segmented on the two views. Coronary edges are computed in both images.

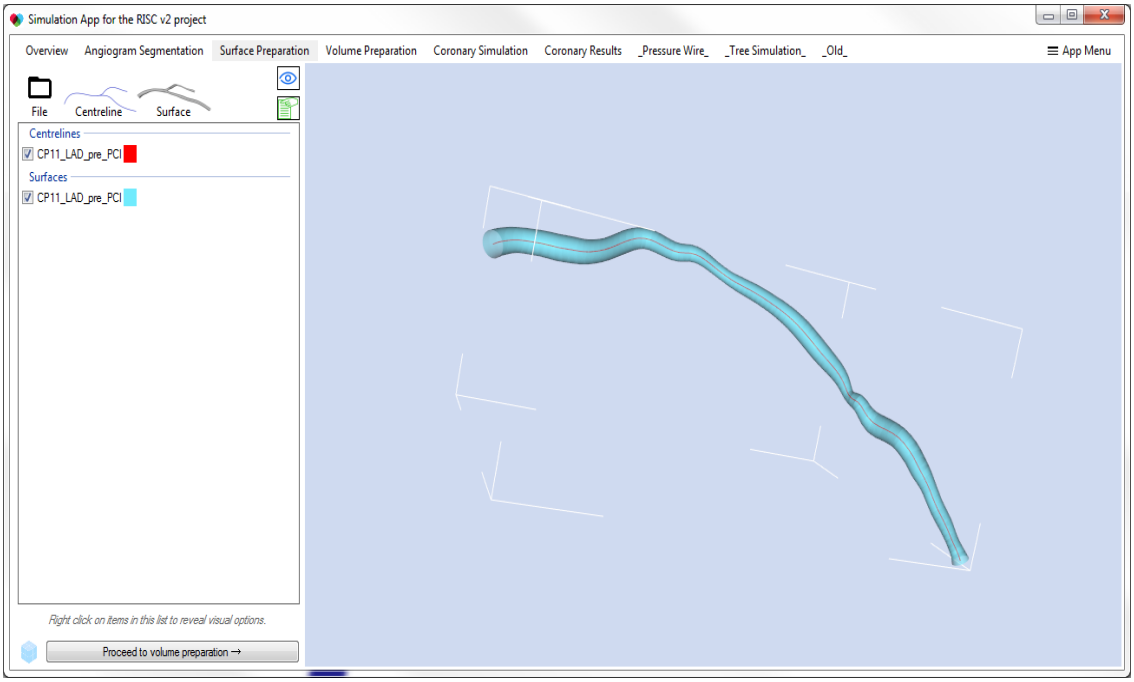

Figure 2.18: Visualisation of the coronary geometry within the VIRTUHeart tool. The user can create a volumetric mesh and run a full CFD analyses within the tool.

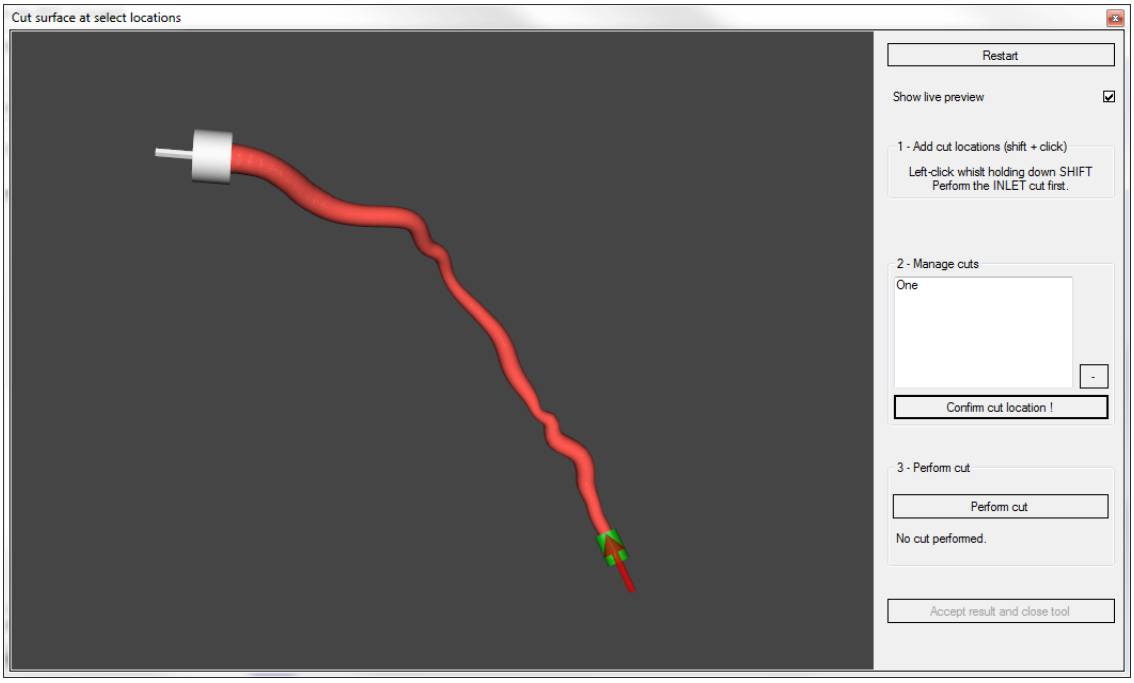

Figure 2.19: The user can cut the geometry (decide location for input and ouput along the centreline) and apply boundary conditions.

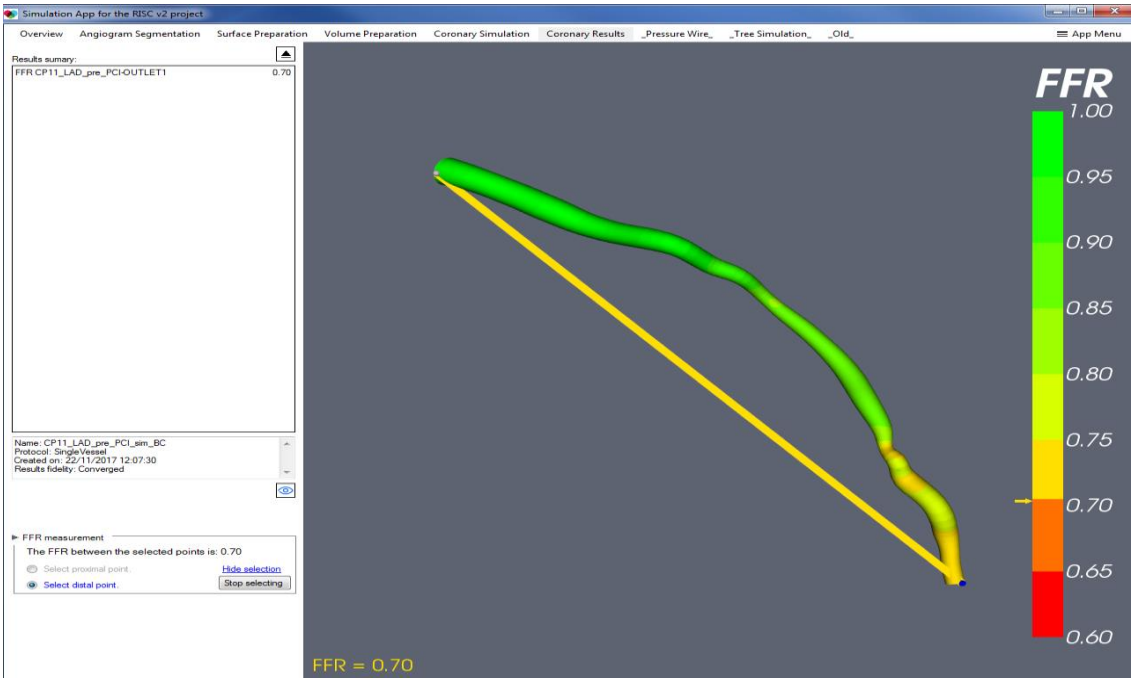

Figure 2.20: Result of the full 3D simulation, where the FFR is computed as pressure ratio between inlet and outlet.

2.4 Validation of the tool

One 3D printed geometry has been used to validate the 3D reconstruction tool. The model is a straight tube with a narrow part in the middle of the geometry. The phantom has been mounted in a rigid structure in order to not allow translations and rotations during acquisitions in the CathLab. Before starting the acquisitions, the model had been filled with contrast agent.

2.4.1 Straight tube geometry with a stenosis

The straight tube geometry is shown in Figure 2.21. Several projection images have been taken for the geometry following a protocol i.e. standard acquisitions without and with table movement in the three global directions, rotational angiogram, acquisitions with panning and finally acquisitions with different magnification factor.

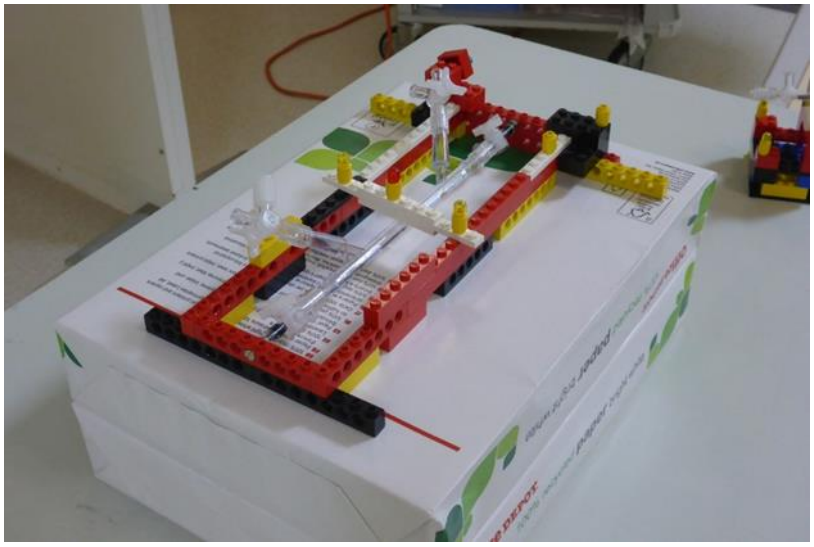

Figure 2.21: Straight 3D printed tube used for validation attached on LEGO frame.

The first step to validate the MATLAB workflow for 3DR has been to check whether the epipolar lines were intersecting marked objects. Along the Lego scaffold, some ball bearings have been positioned along the frame during image acquisition, allowing the presence of reference points onto the 2D projection images.

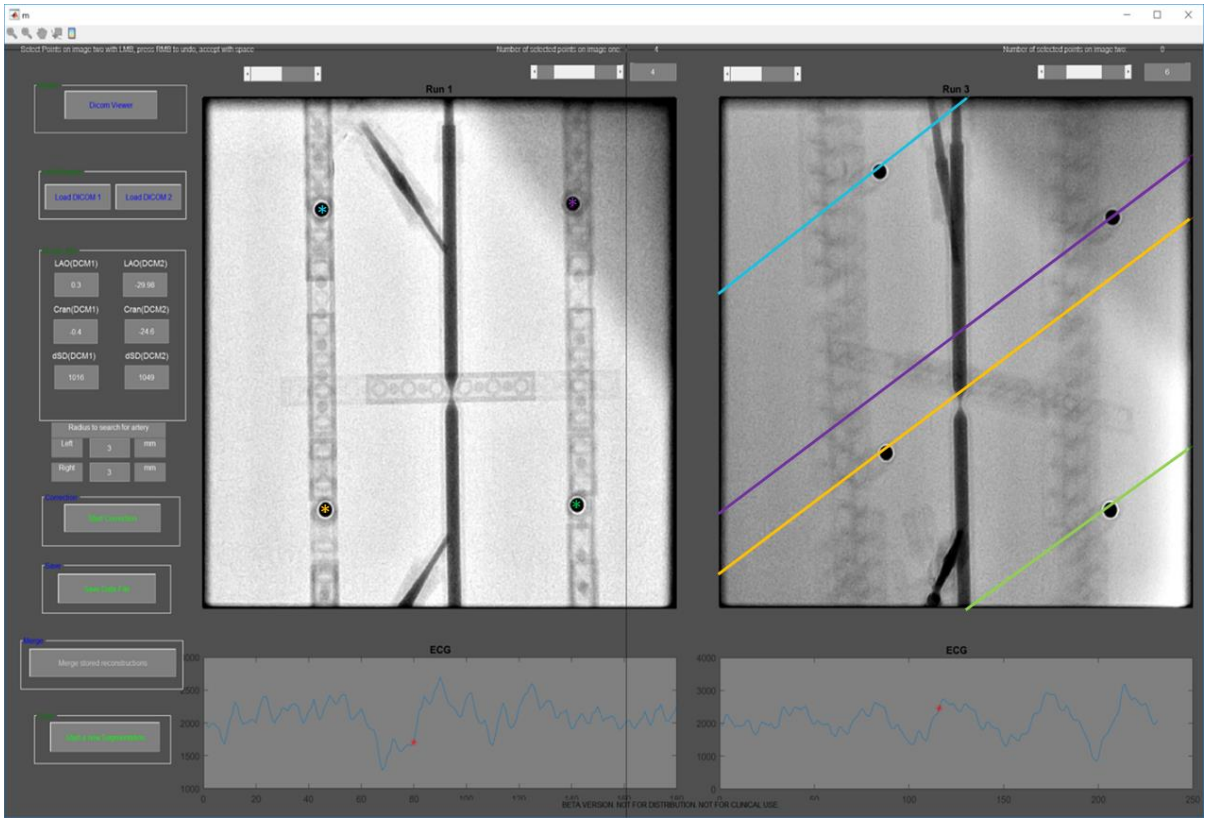

Figure 2.22: Validation step for the epipolar lines.
The four ball bearings are marked on the first image, the correspondent epipolar lines are not passing through the centre of the ball bearings on the second image.

Figure 2.22 is showing the correction step, the centre point of the four ball bearings on the left image have been marked. The four pairs of *x*, *y* coordinates are saved in a matrix and used to compute four epipolar planes to be projected to the second view on the right. The four epipolar lines on the right image should pass exactly through the centre points of the four ball bearings. However, this is not the case here because although the 3D model attached to the frame is not moving as a real heart would do during acquisitions, there are still intrinsic errors introduced by the system (mechanical errors). In fact, it is possible to notice that the four epipolar lines are moved towards the upper part of the ball bearing centres. To correct this error, the affine matrix described Section 2.2.2 has been computed and applied, the result of the computation is shown in Figure 2.23.

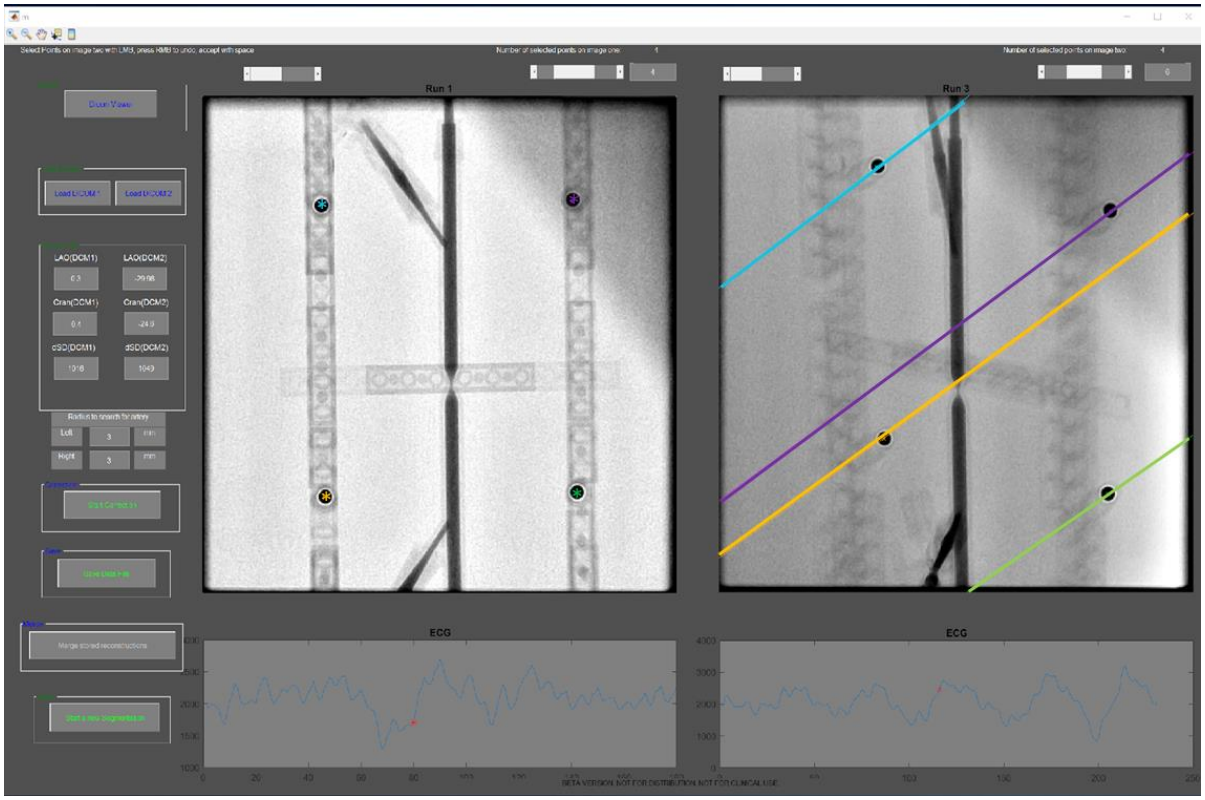

Figure 2.23: Epipolar lines passing exactly through the centre of the ball bearings.

As it can be seen, following the affine matrix calculation, the four epipolar lines on the right projection pass exactly through the marked centre of the ball bearings.

Measurements on the mean radius have been performed on the 3DRs compared with the real phantom data and also with a second segmentation tool available in our laboratory, the Philips 3DCA which works just on rotational angiography images (Figure 2.24).

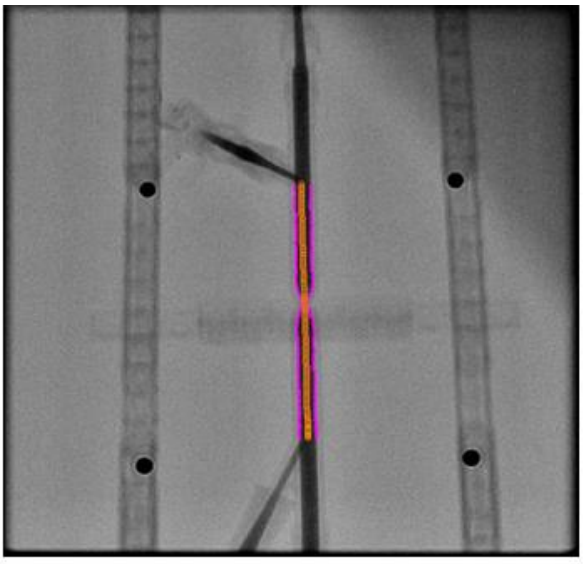

Figure 2.24: Coronary centreline segmented and computed edges for the straight tube.

The segmentation and radius detection has been performed in both planes and the corresponding image reconstruction from different views is shown in Figure 2.25. To validate the reconstruction of the straight tube with our MATLAB tool, the reconstruction is compared with that obtained from RoCA reconstruction of the same geometry using the Philips 3DCA tool. From the two 3D results in Figure 2.25 it is possible to see that the two geometries are overlapping, confirming the ability of the software described in this chapter to reconstruct these two phantom geometries. As can be seen in the radius variation along the length for the CAD file geometry is a straight tube of radius 2 *mm* plus a stenosis (Figure 2.26 left panel).
The minimum radius of the stenosis is 0.5 *mm* which corresponds to 75% radius reduction. Figure 2.26 and Figure 2.27 show a comparison between three geometries, the original CAD geometry, and the two geometries reconstructed with the Philips tool and the MATLAB tool described in this chapter. It can be seen that the professional tool, based on RoCA images, better reconstructs the diameter of the normal artery, whilst the diameter of the stenosis is similar in the two reconstructions. Furthermore, it has to be said that at the stage when the validation for the straight tube had been done, manual corrections had not yet been implemented in the current tool: later modifications have further improved the accuracy of the segmentations. The average error in the radius reconstruction relative to CAD from the developed software was 0.27 *mm*. Given that each pixel in the image is approximately 0.21 *mm*, the error is of the order of a pixel. A comparison of the computed errors is shown in Figure 2.28.

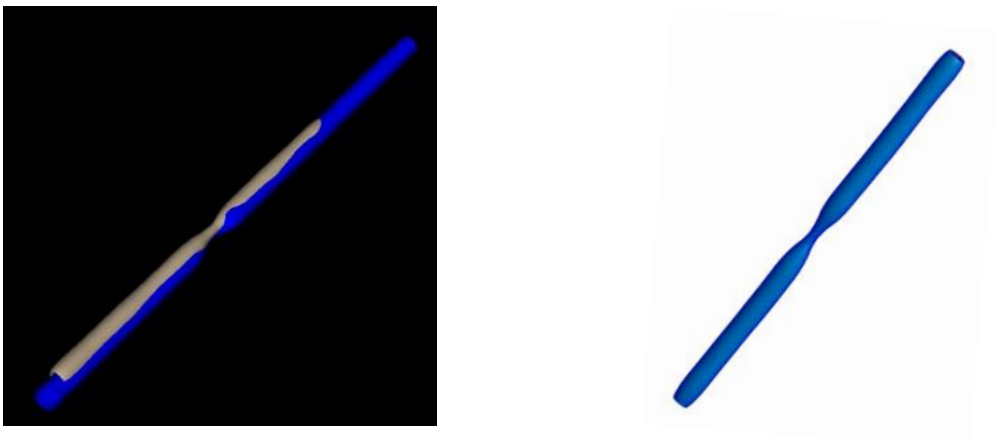

Figure 2.25: Left) Comparison of two 3D reconstruction.
Left) Philips 3DCA tool (Blue geometry) and the MATLAB tool (Grey geometry). Right) 3D Reconstruction with the MATLAB tool of the straight tube.

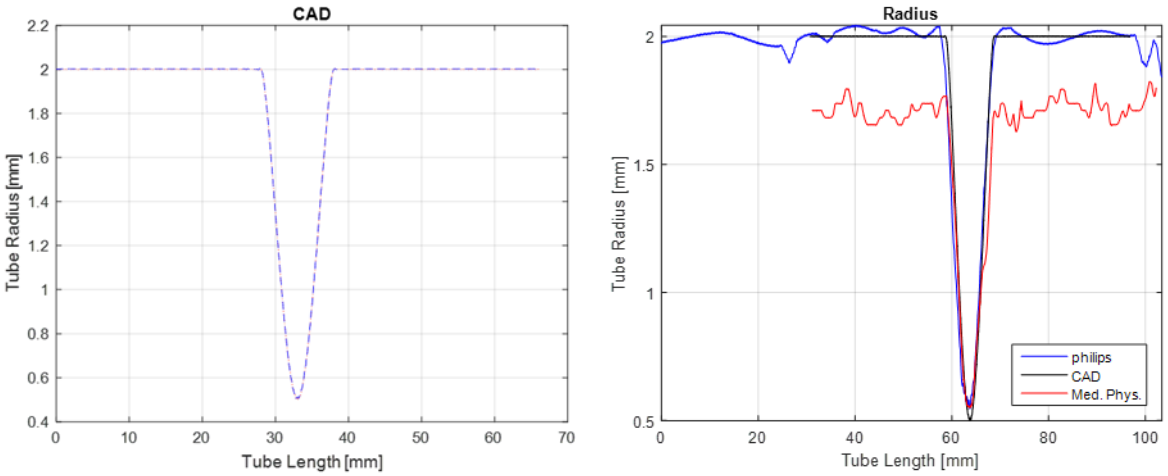

Figure 2.26: Plots of the CAD geometry.
CAD geometry radius variation along the length (Left). Comparison of the two segmentation tools (Philips and VIRTUHeart MATLAB tool) with the CAD

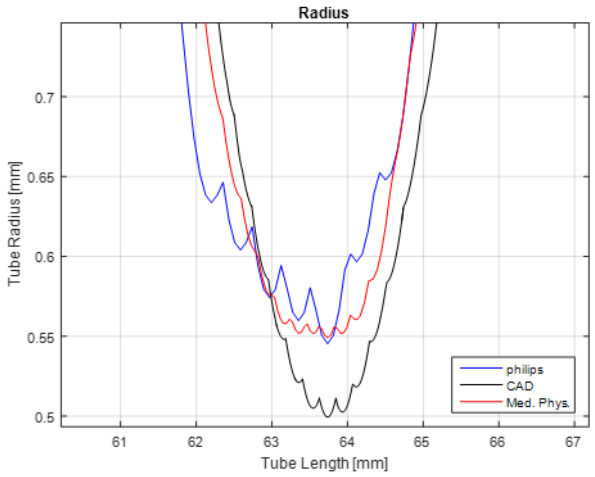

Figure 2.27: Zoom onto the minimum radius for the three geometries (CAD, Philips and Med. Physics).

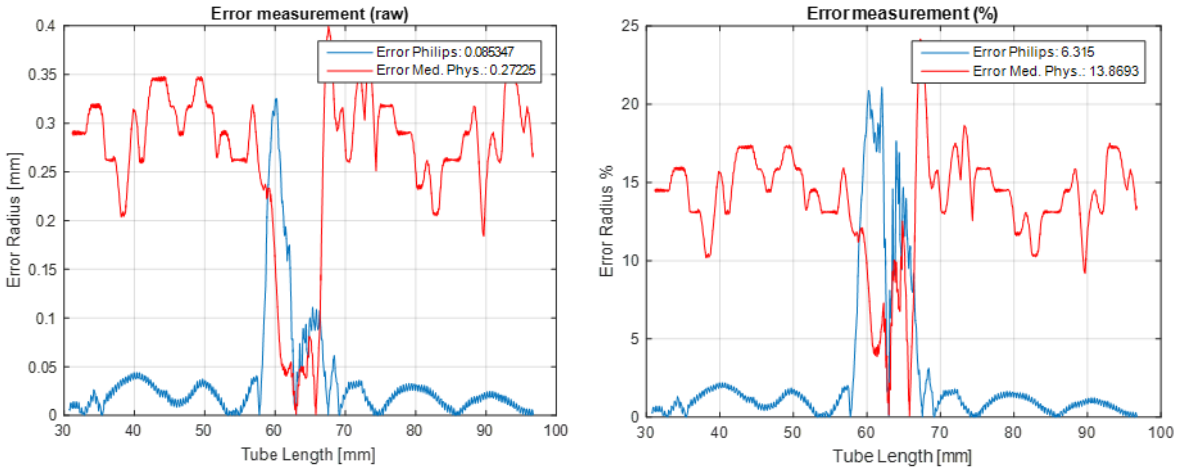

Figure 2.28: Comparison of the reconstruction errors with the Philips and the MATLAB tool. Left) Raw Errors. Right) Percentage Errors.

From Figure 2.28 it is possible to notice how the Philips tool is performing better in segmenting the straight geometry than the VIRTUHeart segmentation tool. This is not surprising since the Philips tool already has some important features implemented such as manual corrections for a better border extraction. However, the results obtained with the VIRTUHeart segmentation tool are really promising.

2.5 Conclusions and limitations

Segmenting coronary arteries is not a trivial task; foreshortening, overlapping, heart motion and table movement lead to a very complicated reconstruction process. One limitation is that the orientation of the coronary should remain unchanged while the C-arm is going to be repositioned to another angulation, however this condition is never respected due to patient, cardiac and respiratory motion. Even using ECG gating, patients need to hold their breath to avoid respiratory motion. Regarding the table movement correction, the user might find difficult to correct images where chosen points have different distances between their correspondent epipolar lines. This situation could happen especially when the user would like to correct a point near the catheter tip which usually is quite fixed and a point in the bottom part of the coronary which is really affected by cardiac and diaphragm motion. The result of the application of the computed affine matrix applied to the image might be a strong magnification or a shrinkage of the image itself. In these cases, the reconstruction process described in this chapter can produce significant errors, and the selection of points that might be subjected to strong relative deformations as opposed to pure translations is not recommended. The reconstruction process using epipolar lines sometimes is not possible, difficult situations arise where epipolar lines are parallel or nearly parallel to the vessel centreline. To avoid these reconstruction problems a script has been written in order to use more than two images to compute the 3D coronary vessel reconstruction, although the code has not been optimised yet. Having more than two views allows the user to segment different parts of the vessel and then once the segmentation is terminated merge the segmented parts in one total vessel. Using multiple views would also benefit the edge detection for the reason explained in Figure 2.14.

In conclusion the software developed and implemented in MATLAB is able to compute a 3D coronary reconstruction and to obtain geometry meshes which are useful to compute CFD studies and to compute important coronary parameters such as the FFR. Once the 3DR has been computed, information can be used to help cardiologists' clinical decision making. To correct for cardiac motion and table movement between acquisitions a novel click to correct algorithm has been introduced. The advice is to choose bifurcation points as correction points, however sometimes there might be no or few bifurcations visible in the two views, so the catheter tip and small branches with little clinical value can be used to compute the affine matrix. The computation of the affine transformation requires at least three pairs of feature points. Theoretically more pairs of points would improve the accuracy of the system. However,

three or four pairs of points may be sufficient to determine an accurate correction. A further development would be to fit elliptical cross sections instead of circles in order to define more accurately the artery shape, especially in the region of stenoses.

Chapter 3

2D ROM generation and fluid flow interactions between multiple stenosis

Nowadays, numerical analysis is playing a very important role in every engineering field where complex physical phenomena are involved. These models quite often require large amount of time and furthermore CPU power and memory leading to a non-feasible process. Moreover, in a general CFD study, if we are interested in changing even only one parameter within the model we are required to repeat the whole full order simulation. However, in the last decade the aim of computer simulations applied in the medical fields is pushing towards a patient-specific analysis for personalised decision support. Reduced order methods (ROMs) aim to reduce the computational demand, to achieve an acceptable level of accuracy compared to the full order system and last but not least they provide a huge acceleration on the computation of the reduced solution demanding much less CPU power and RAM memory [59],[90]. In this chapter and in general in this thesis the fundamental principles and all the ingredients necessary to build a parameterised ROM will be presented and described. In these systems the full order equations which govern the model and their correspondent solutions depend on a set of parameters, i.e. a parametric approach. The first aim of these ROMs is to build a low order but sufficiently accurate model which is able to describe every solution for a completely new set of numerical values of these parameters. The parameterised ROM should approximate the full order model with sufficient level of accuracy, which will depend on the application, on sensitivity and on the interpretation of the model outputs. To achieve this, in order to train the model, it is required to compute multiple full-order solutions for different values of the parameters (*off-line* mode). In the next sections of this chapter, the most important steps to build a ROM plus some examples of ROMs applied on straight tubes are presented with single and multiple lesions in series [91]. The aims of this chapter are firstly, to highlight the basic principles of ROMs applied to simple models and secondly to describe the fluid flow interactions between multiple lesions. Furthermore, the pressure drop in different coronary geometries will be considered using different methods of computation: Bernoulli pressure drops vs 1D vs 2D CFD vs 2D ROMs pressure drops.

3.1 Building the ROM (the off-line mode)

The first step to build a reduced order method is to construct a fluid flow full order computational model dataset. In the current application in coronary haemodyamics, this means using Fluent or any other CFD solver to compute the full CFD simulation on the given mesh with the right boundary conditions to achieve a high fidelity solution. As already mentioned in Chapter 1, considering a practical approach, the user needs to collect the steady state solutions of the full dataset, called snapshots, into one matrix (the correlation matrix), and perform a singular value decomposition of this matrix [55], [92]–[94]. Every snapshot is a vector stored as a row in the matrix. If the model can be parameterised, including the geometrical description and the boundary conditions (it is assumed that the rheological properties are fixed in this application), every full order solution depends upon the numerical values of the parameters [59], [95], [96].

The workflow to construct a ROM consists of two steps: the *off-line*, and the *on-line* mode. The *off-line* mode is based on the design of the whole dataset; it is not possible to compute a full order simulation for every change in the parameter values. Thus, we need to sample the parameter space in a smart way. In designing the process for sampling of the parameter space we are interested in the full order solution over a range of parameter values, for example a change in the coronary shape and/or a change in the mass flow rate. However, when creating the design of experiments (DOE), the variation range for every parameter has to reflect the physiological model. It is possible to sample a larger parameter space, however this is inefficient since some regions of the space will not correspond to practically-occurring variations of coronary artery geometry or boundary conditions. The *off-line* process is the step within the ROM, which takes most of the time (weeks), although it needs to be completed only once, assuming that the space is adequately sampled.

The *on-line* mode consists on the evaluation and validation of the built ROM. At this stage the user can change one or all the parameters within the applicable domain of the ROM to have a quasi-real time solution.

3.1.1 2D Mesh Generation

For the work described in this chapter and the next, the ROM is constructed using the ROMBuilder tool developed and supplied by the research team at ANSYS in France, with their industrial collaborators. The ROMBuilder tool is an add-on package which can be loaded

within the Fluent environment. As already mentioned with the ROMBuilder tool it is possible to store all the CFD simulations taken into consideration in a binary format. Once all the CFD simulations have been computed it is possible to start the process of building the reduced order model.

The use of the ROMBuilder tool requires all of the meshes in the training and validation dataset to be isotopological [57], [58] and to contain the same number of nodes and elements. It has been found difficult to create isotopological meshes using ANSYS products, for this reason, a 2D mesher was written in MATLAB (https://uk.mathworks.com/), saving the text file describing every mesh as a .msh and then importing the mesh into Fluent for the 2D CFD analyses. In order to create all the .msh files, the ANSYS mesh file format documentation has been followed. Furthermore, the MATLAB environment has been exploited to launch simulations in parallel exploiting the parallel toolbox.

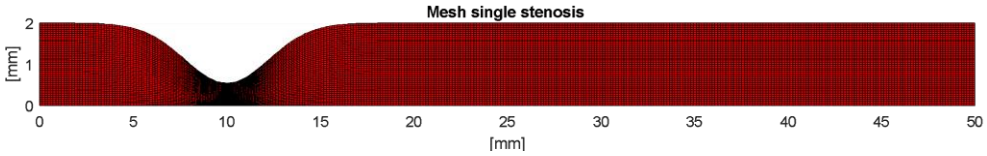

Figure 3.1: Example of computed 2D axisymmetric mesh developed in MATLAB.

3.1.2 Generation of a 2D phantom training dataset

To use the ROMBuilder tool, first of all a design of experiments (DOE) of the Fluent cases has to be designed. A DOE is a structured set of tests for a system or process. Since thousands of simulations have to run for the training dataset in the *off-line* mode, sampling the parameters space become important. The challenge is to explore the multi-dimensional space in an effective and computationally efficient way. The first sampling method which has been employed in this thesis was to randomly sample the space, however this proved sub-optimal case since one could end with some regions of the space which are barely sampled or not sampled at all.

To improve on the random sampling, a Latin hypercube sampling (LHS) was implemented. The LHS design is a strategy for generating random sample points ensuring that all portions of the parameter space is represented [97] [98], [99].

Furthermore, the size of the training dataset is also very important. The essential process of the ROM can be summarised into four main steps:

1. In order to characterise the solution space, to perform sufficiently many CFD simulations of points in the space;

2. Computing the modes, the aim is to identify a more concise representation of the solution space;
3. Reconstruct the low order solution using the modes computed at step 2;
4. Interpolation is used to compute the modes coefficients for intermediate values of the input parameters which were not included in order to characterise the solution space at step 1.

It might be expected that the number of points needed in the training set might depend on the number of parameters in the input and on the form (nonlinearity or flat regions of the space) of the relationship between the input parameters and the outputs. However, it is still not clear exactly how many points in the training dataset are needed so it is a matter for experimentation to establish the minimum size of the training set for any particular problem. It might be expected that too few points in the training set might manifest itself by high errors in the interpolation step, but it is also possible that the first transformation step may not inadequately capture the overall fundamental behaviour of the system.

In summary, for a given new coronary geometry which is characterised by some input parameters, ROM is applied on the output pressure profile of the Fluent solver [58].

Several CFD simulations are necessary for the *off-line* learning step where saved pressure profiles are compressed into a small number of modes using a Singular Value Decomposition. SVD allows each pressure profile to be described by a linear combination of modes coefficients and modes. Once the ROM has been built, it can interactively give an accurate approximation of the full order solution for a new set of input parameters (*on-line* mode).

To maximise the power of the current study to explore the application in large parameter spaces, the *off-line* mode has been computed on Prometheus, an HP computer based in Krakow (Poland, http://www.cyfronet.krakow.pl/komputery/15207,artykul,prometheus.html) plus a local desktop machine with 12 cores.

3.1.3 Extracting modes with SVD approach

Once all the CFD simulations have run, and the correlation matrix has been populated, the next challenge is to choose the dimension *D* of the sub-space (number of modes to recompute full CFD solutions). Here, the purpose is to describe a more compact combination of the solution vectors which supports the assembly of the full solutions so it is possible to interpolate in this low order space.[58]. In order to decide the right dimension for the low-order system we need

to study the singular values, which are the output values from the singular value decomposition of the correlation matrix (Section 1.5.1).

3.2 Tuning the ROM (the on-line mode): the ROMbuilder tool

The second step in building the ROM is the *on-line* mode. The *on-line* mode is the step where the user exploits the built ROM to compute a low order solution for a new set of parameters (new coronary geometry and mass-flow rate) which were not used for the *off-line* mode.

The on-line process is composed of two steps: the evaluation and the validation of the ROM.

3.2.1 Evaluation of the ROM

To evaluate the ROM for a specific value of the input parameters, the first step to do is to configure the *evaluation.conf* which is a .json configuration file. The configuration file contains different fields:

- **Read ROM** from: in this field the user gives the name (and the path if necessary) of the input file that contains the ROM. Usually the ROM is the last created in the previous step, with the reduce configuration file.
- **Vector type**: in this field the user has to specify the type of format of the output file of the solution vector. The ROM is built with binary input files, so the suggested field is “binary”.
- **Parametric configuration**: this field is the most important one respect to the above fields. The user has to specify the parameter values where to evaluate the ROM, so instead of running a full CFD simulation, we can exploit the ROM and obtain an accurate and low order solution in few seconds.

3.2.2 Validation of the ROM

The last step is the verification and validation of the computed ROM. At this stage it is possible to have information about the projection and interpolation errors since the user has to compute the CFD simulations for the cases evaluated at the former step. The validation step is necessary since it allows the user to check if the ROM is performing as expected. The built ROM can be validated against the simulations used for training the ROM and against simulations which were not part of the training dataset. The two methods and the error estimation step are explained in details in the next section.

3.2.3 Output errors estimation

Once the validation step has been run it is possible to post-treat the solutions. The quality of the ROM is estimated by comparing in the validation points the exact solutions (full-order) computed by Fluent and the rebuilt solutions from the ROM. The whole error for the ROM is composed of two parts: the projection error and the interpolation error.

- **Projection Error**: is the output error obtained from the projected field. Once the ROM is built, we can validate the ROM against the full order solutions used to build the ROM itself. The projection error is a measure of how good is the description of the exact fields which are projected into the basis of modes. In the next sections it will possible to notice how the projection error decreases if we increase the number of modes. The former trend is expected; in fact if we continuously increase the number of modes we should expect to obtain the same level of accuracy of the full order solution. The projection error for every case is computed as:

$$err = \frac{\|X_i - P_i\|}{\|X_i\|} \qquad \text{(Eq.3.1)}$$

  where X_i is the full order CFD solution for case *i*, P_i is the projected solution and $\|\bullet\|$is the 2-norm error.

- **Interpolation Error**: is the output error computed as a difference between the full order solution and the predicted solution; the latter one is the low-order solution which has been evaluated with a complete new set of numerical parameters. Furthermore, the modes coefficients have been computed with interpolation. However, it has to be clear that for a complete new coronary geometry parameterised by a new set of parameters, is not possible to compute both the projection and the interpolation error if the full CFD solution has not been computed. To compute the norm of the interpolation error the full CFD and the decomposition of the solution into the mode space are needed. The interpolation error is described as:

$$err = \frac{\|X_i - R_i\|}{\|R_i\|} \qquad \text{(Eq.3.2)}$$

  where R_i is the predicted solution computed with the ROM.

3.3 2D axisymmetric straight tube model with a single stenosis

Introduction

In this section (divided into Introduction, Methods and Results), a ROM is constructed for an axisymmetric straight tube with one stenosis. The tube is $L = 70mm$ long, inlet and outlet radius are $R = 2mm$, the stenosis is centred at $x = 10mm$. In order to construct the training dataset, two parameters are varied: the severity of the stenosis and the inlet mass-flow rate Q_{in} $\left[\frac{Kg}{s}\right]$. The severity of the stenosis is measured as a radius reduction percentage and this reduction can vary between 55% and 80%, the minimum radius that can be achieved is equal to $R_{min} = 0.4mm$, which is still within the ROI (region of interest) for real stenosis in which FFR might be measured (tighter stenoses would generally be treated irrespective of FFR).

The axial variation of the radius is described by the following equation:

$$R(x) = 2 - S_r e^{\left(-\frac{(x-10)^2}{2\sigma^2}\right)} \qquad \text{(Eq.3.3)}$$

where S_r is the stenosis radius and σ represents the width of the stenosis.

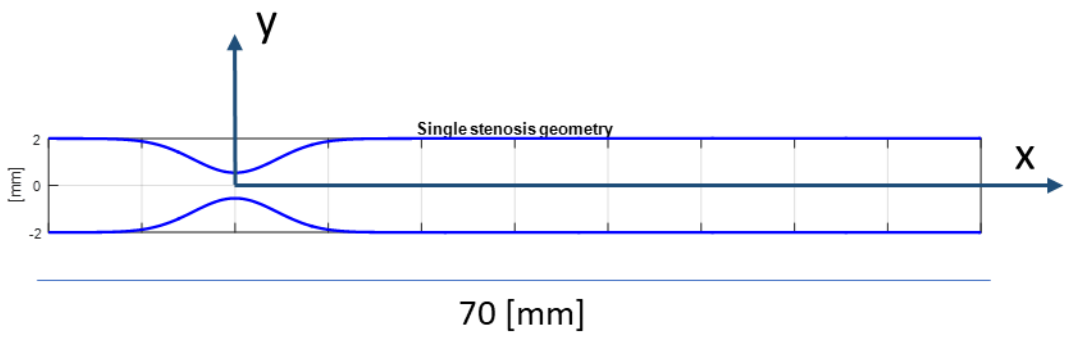

Figure 3.2: Single stenosis geometry.

In order to obtain values of mass-flow rate within the clinical range, a first estimation of the mass flow has been computed resolving the electrical-hydraulic circuit coupling the 2D tube model with a 0D model characterised with a downstream resistance R_{mc}. The inputs to the problem are: P_a (inlet pressure = arterial pressure), P_v (venous pressure = 0), R_{mc} (downstream resistance), A_{inlet} and A_s (Area inlet and area stenosis).

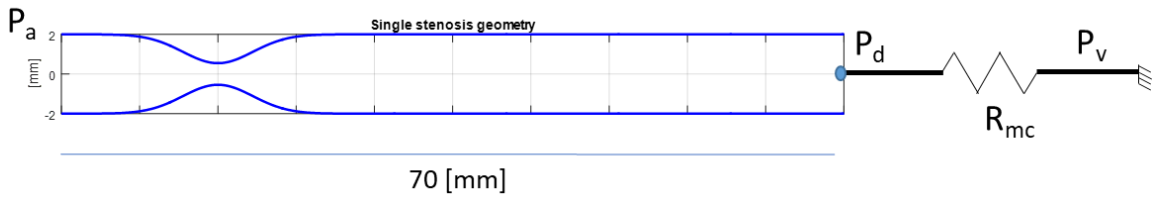

Figure 3.3: 2D model coupled with 0D model.
The coupling is made in order to compute a first estimation of the mass flow rate to use as inlet boundary condition.

Considering the Bernoulli equation between the inlet and the stenosis, the venous pressure (P_v) equal to 0 and moreover assuming no pressure recovery downstream the vena contracta we obtain the following quadratic equation in Q(Eq.3.6):

$$\frac{1}{2}\rho Q^2\left(\frac{1}{A_s^2}-\frac{1}{A_{inlet}^2}\right)+QR_{mc}-P_a=0 \qquad \text{(Eq.3.4)}$$

The values of R_{mc} and P_a are assigned in advance for this study, although of course they could be additional parameters in a ROM. The value of P_a is equal to the aortic pressure of 100$mmHg$ or 13333Pa. The downstream resistance (R_{mc}) is representing the resistance of the microvasculature. The value of R_{mc} is a patient specific value and is changing accordingly to baseline or hyperaemic condition, physiologically its value changes between 50 to 90 *mmHg*s/ml* [26]. For all the numerical simulations, blood has been modelled as an incompressible fluid with density and viscosity values equal to 1066 $\left[\frac{Kg}{m^3}\right]$ and 0.0035 $[Pa.s]$ The partial differential equations were solved iteratively in Fluent, until convergence criteria of 10^{-5} were reached both for the continuity equation and for the momentum equations in the two dimensions.

3.3.1 Generation of the ROM with the single lesion dataset

Methods

Three different training datasets with full order solutions have been used to train the ROM for a total of 300 cases. Each of the dataset consists of 100 geometries. However, these 100 geometries are equal for each dataset and the variable that is varied between the three datasets is the value of R_{mc} (Table 3.1). For obvious reasons we should expect the inlet mass-flow rate to change as we change the value of the downstream resistance (higher values of mass-flow rate for low values of resistance and vice-versa). The two parameters used for the ROM construction are: λ (in percentage) which is defined as the ratio between $r_{stenosis}$ and r_{inlet}; and the mass-flow inlet (Q).

Table 3.1: Single stenosis dataset with ROM.

Dataset	# of geometries	R_{mc} value	ROM
1	[1 : 100]	$50 mmHg * \frac{s}{ml}$	ROM with 2 parameters (Radius reduction λ, Q)
2	[101 : 200]	$70 mmHg * \frac{s}{ml}$	
3	[201 : 300]	$90 mmHg * \frac{s}{ml}$	

Considering the three datasets, the computed flow values varied between $1 \left[\frac{ml}{s}\right] < Q < 2.2 \left[\frac{ml}{s}\right]$ (Figure 3.4).

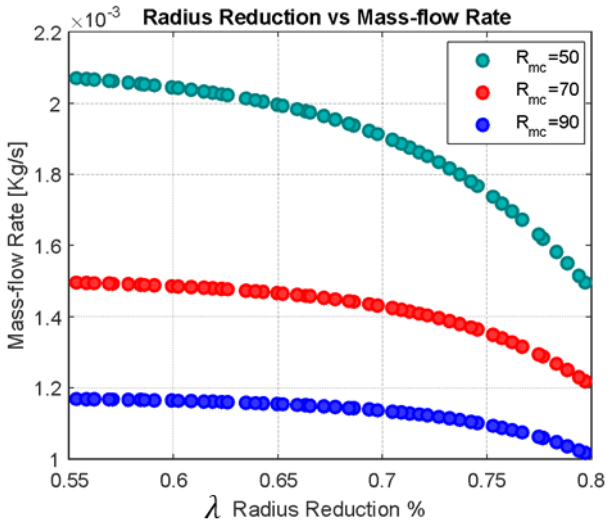

Figure 3.4: Mass-flow rate vs Radius Reduction.
The mass-flow rate is computed for different values of microvasculature resistance [50, 70, 90 mmHg * s/ml].

Once all the 300 CFD solutions have been computed it is possible to store all the snapshots into the correlation matrix and to compute an SVD. The singular values obtained with SVD are shown below (Figure 3.5):

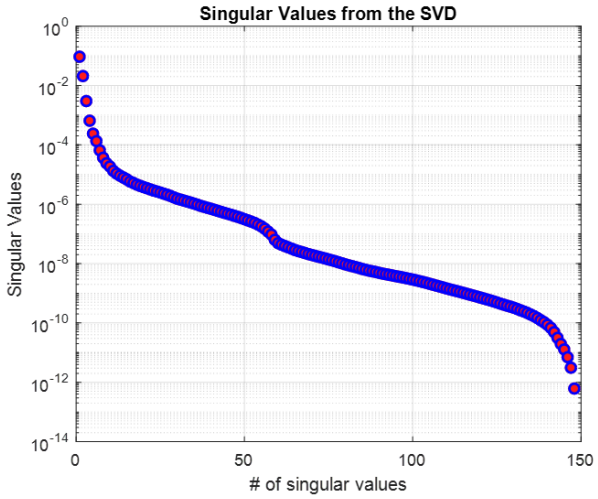

Figure 3.5: Singular Values computed from the SVD algorithm on the training dataset. The x-axis represents the number of singular values, whilst the y-axis represents the value of the singular values on a logarithmic scale.

The training dataset is made up of 150 simulations (50% of the full dataset size), with 50 different geometries and where for every geometry three full order CFD simulations have been computed, with three different values of mass flow rate (each corresponding to a different value of the downstream R_{mc}). From the study of the singular values given by the system (Figure 3.5), it is possible to notice the initial steep decay of these values. This means that the first few modes are collecting the most important behaviour of the fluid flow. Furthermore, a reduced order model was built using just few modes, chosen to ensure that the ROM is capable to describe with a good level of accuracy every full order solution. Different ROMs have been built, with different number of modes. Once the ROMs have been built, the *on-line* mode can start, this means new geometries with new parameters have to be generated in order to evaluate the ROMs.

Since the initial flow computed with the quadratic equation is only a crude estimation of the real flow, another step is necessary for the evaluation step. A recursive loop has been written in MATLAB to check the convergence of the mass-flow rate for every iteration. Figure 3.6 shows the workflow:

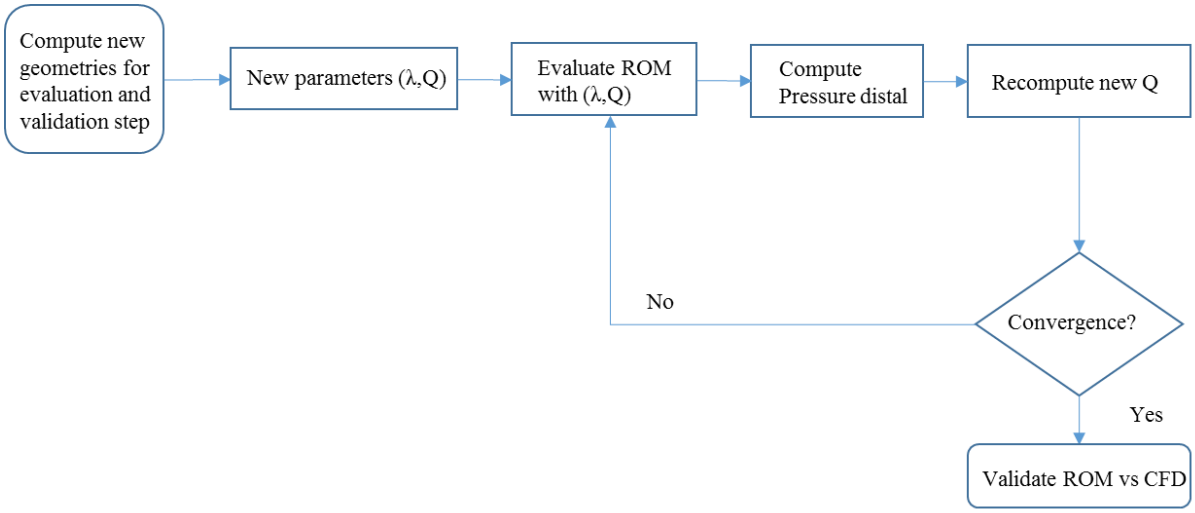

Figure 3.6: Iterative loop for recomputing Q to achieve convergence. The iteration is computed in MATLAB.

Results

The computed ROMs are evaluated with 25 geometries outside of the training dataset. If a solution space for a two parameter model is smooth enough we should expect that the system should be well-represented by 150 points in the space.

The graphs below (Figure 3.7) show the evaluation step for two cases (Table 3-2) outside the dataset exploiting the computed ROM with different number of considered modes (m=1,2,3,4). What should be expected is that, increasing the number of modes, the ROM solutions should converge to the full CFD solutions, achieving a better accuracy for the overall description of the different pressure profiles (and then FFR). Furthermore, a Bland-Altman graph is presented for the 25 cases outside the dataset when m=4 (Figure 3.8).

Table 3.2: Mass flow rate and radius reduction for each simulation.

	Mass-Flow Rate	Radius reduction
Case # 4	0.0018	71%
Case # 8	0.0015	79%

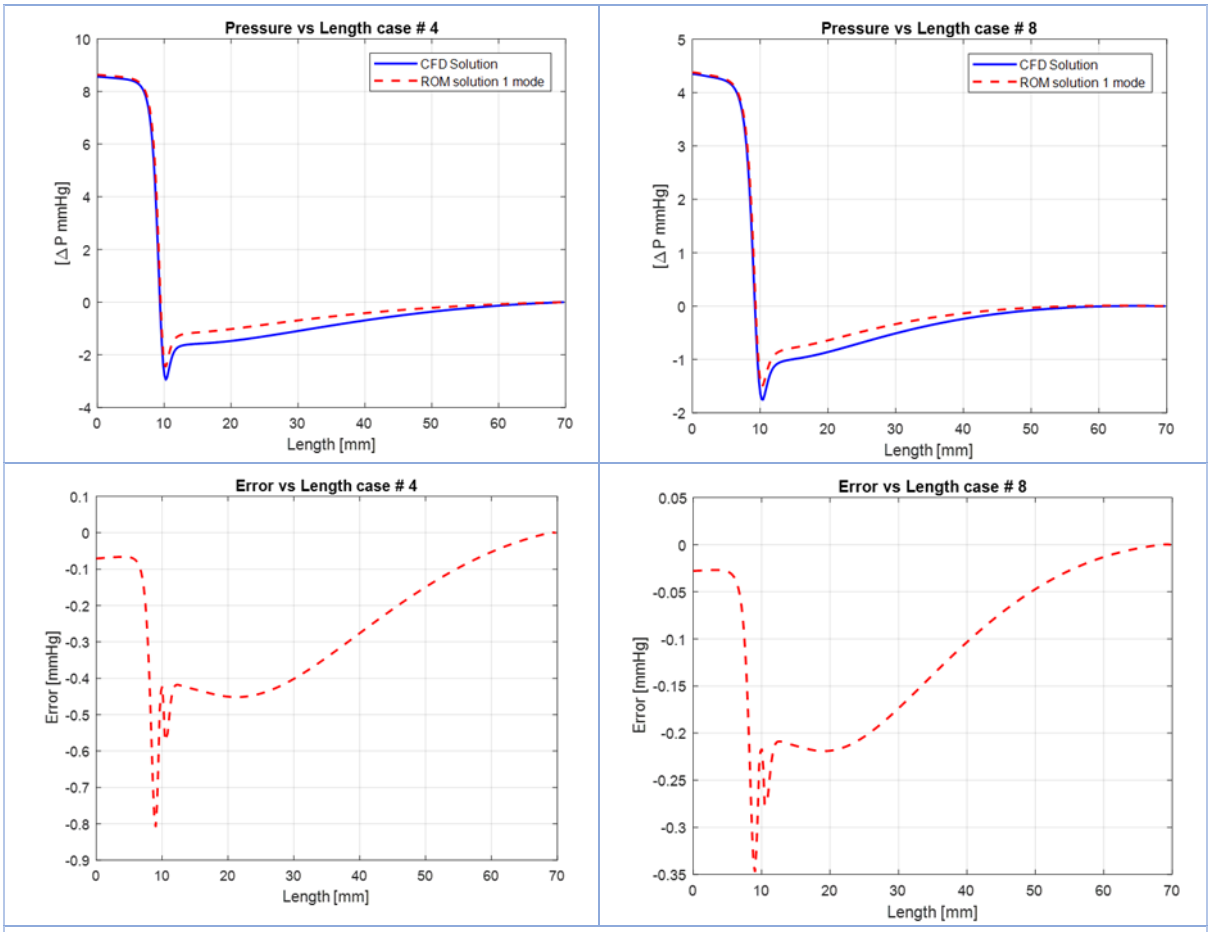

Figure 3.7: Full CFD solutions vs ROM computation for two different cases of the single stenosis dataset described with 1 mode.
Top Row) Pressure profiles along the length comparison for full CFD and ROM. Bottom Row) Error in mmHg between the pressure profiles.

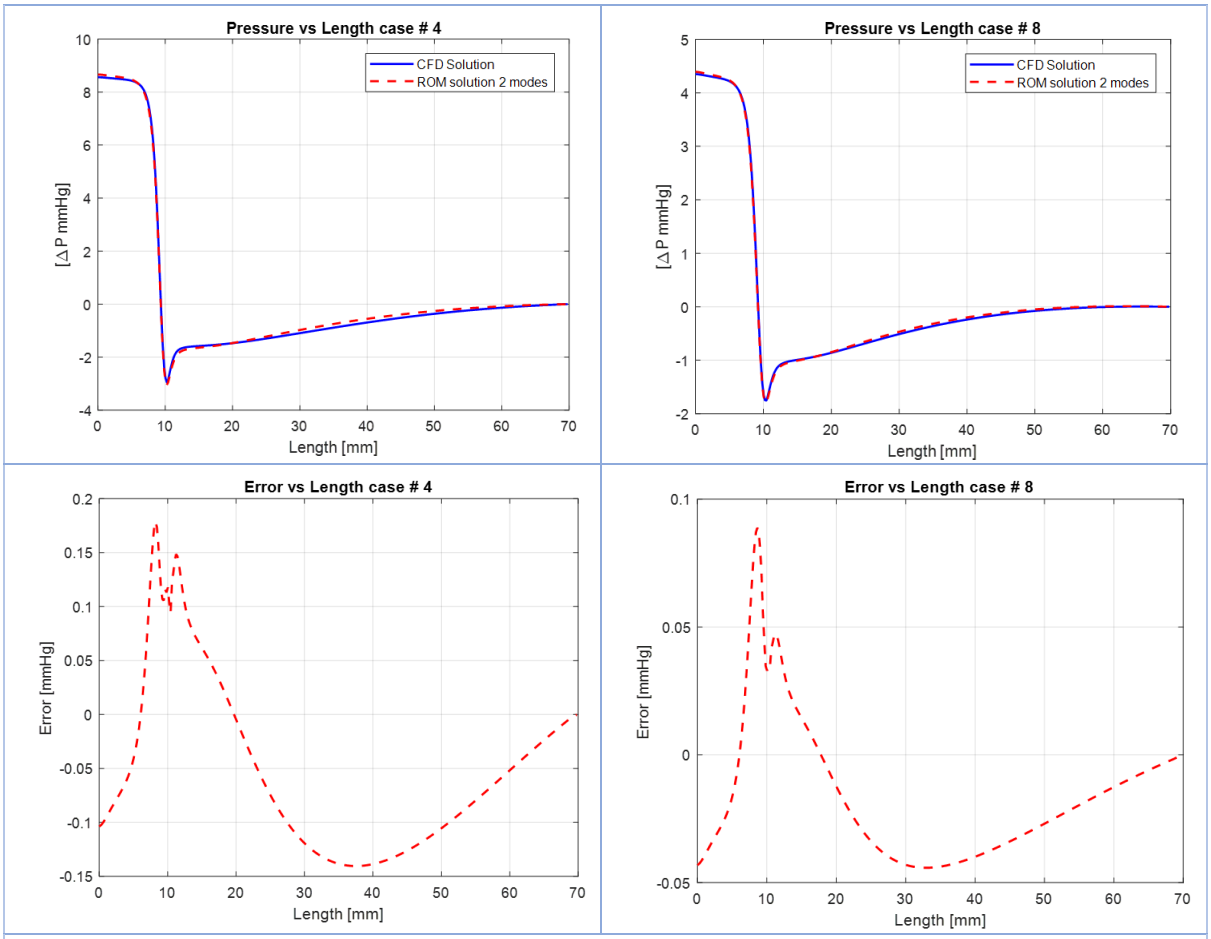

Figure 3.8: Full CFD solutions vs ROM computation for two different cases of the single stenosis dataset described with 2 modes.
Top Row) Pressure profiles along the length comparison for full CFD and ROM. Bottom Row) Error in mmHg between the pressure profiles.

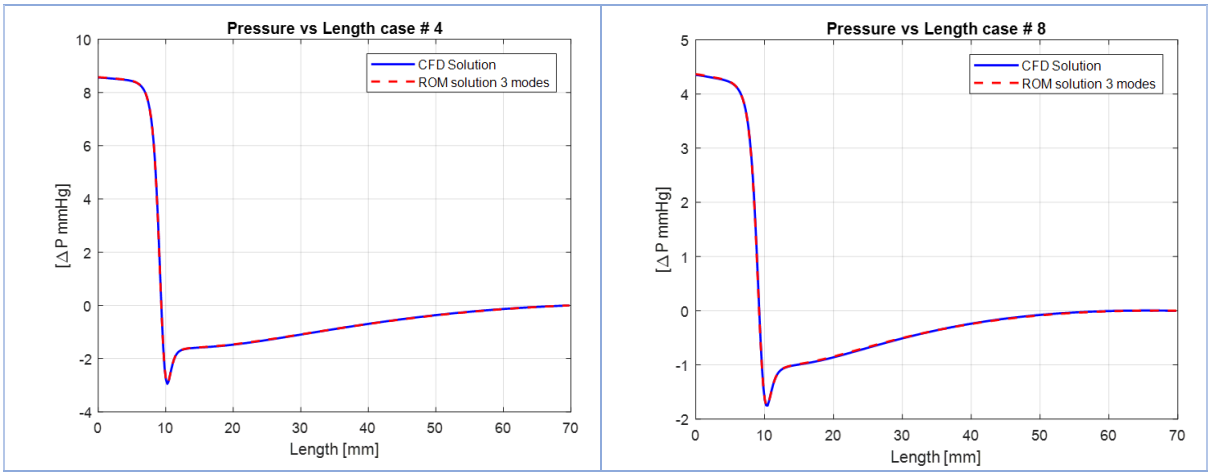

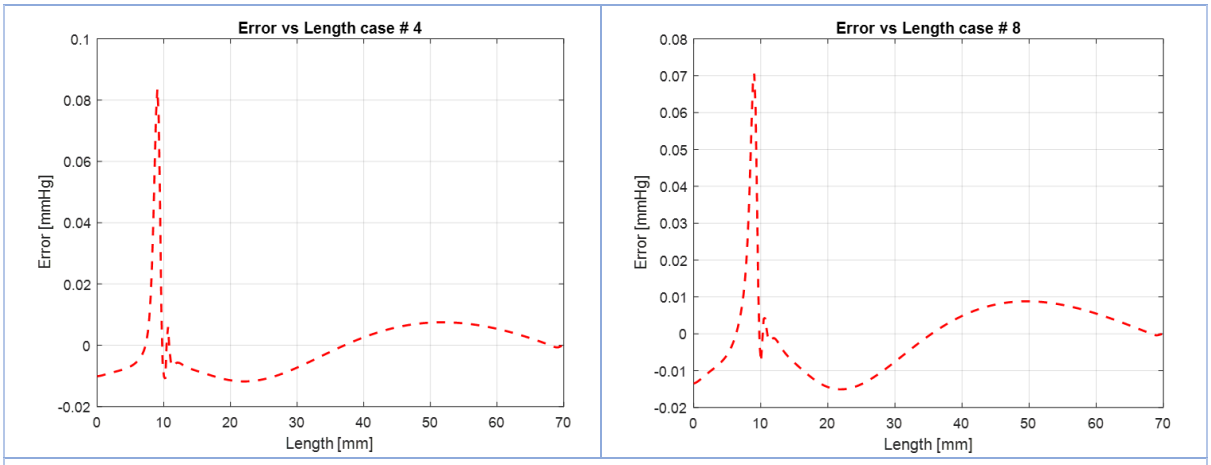

Figure 3.9: Full CFD solutions vs ROM computation for two different cases of the single stenosis dataset described with 3 modes.
Top Row) Pressure profiles along the length comparison for full CFD and ROM. Bottom Row) Error in mmHg between the pressure profiles.

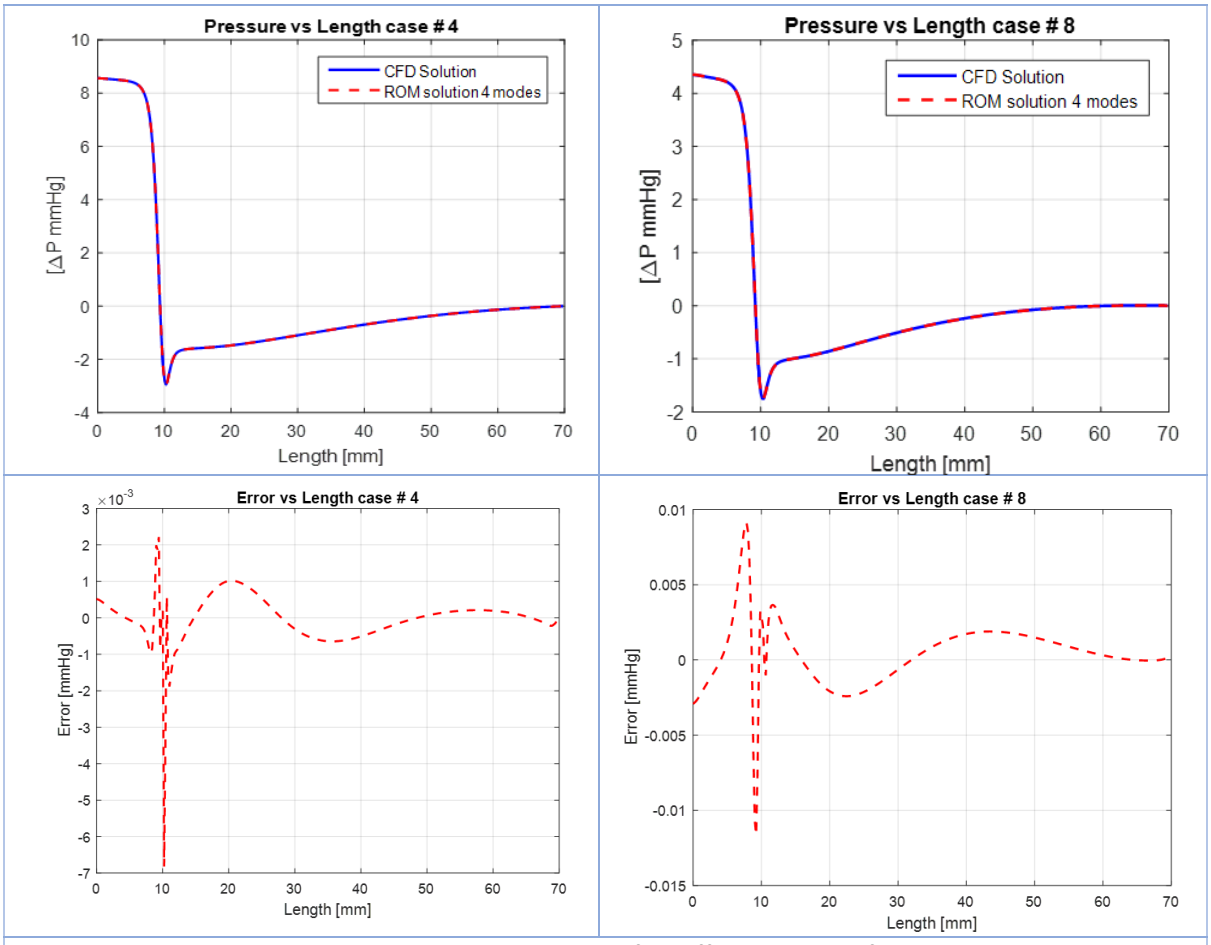

Figure 3.10: Full CFD solutions vs ROM computation for different cases of the single stenosis dataset described with 4 modes.
Top Row) Pressure profiles along the length comparison for full CFD and ROM. Bottom Row) Error in mmHg between the pressure profiles.

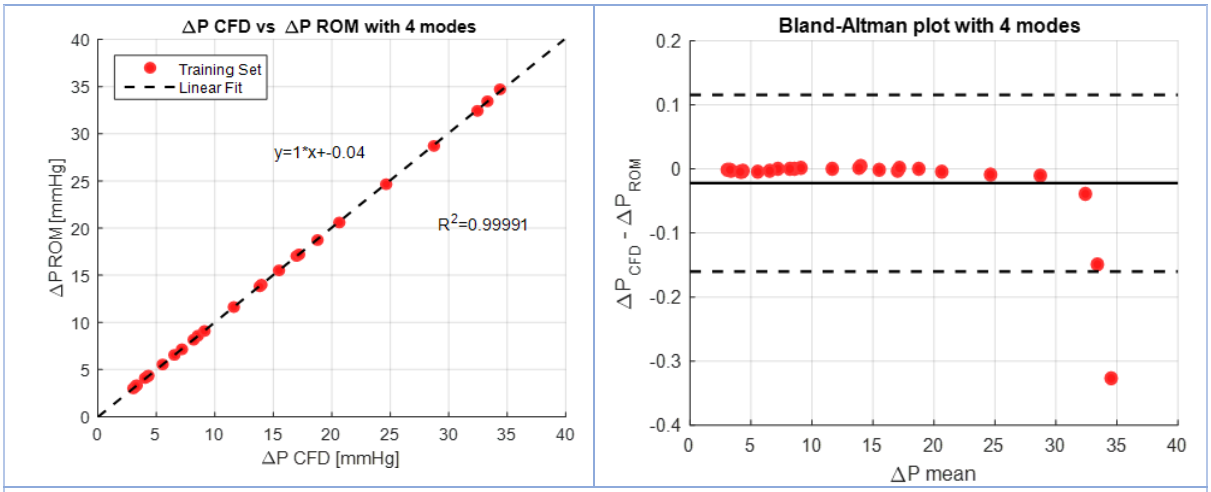

Figure 3.11: Correlation between full order pressure drop and ROM computed pressure drop. Left) Linear correlation; Right) Bland-Altman plot.

Discussion

Although the model is very simple (single stenosis with two parameters), the results obtained are excellent in terms of the computation for the pressure profile. The correlation between full pressure drop and the low order pressure drop obtained a value of $R^2 = 0.99$ when computing the solution with 4 modes. Furthermore, the maximum error shown on the Bland-Altman graph reached a value of $\Delta P_{CFD} - \Delta P_{ROM} < -0.4\, mmHg$ at high values of pressure drop. Errors between full solutions and recomputed solutions with the ROM are very small, reaching a magnitude of 10^{-3} for the cases described by 4 modes. Regarding execution time comparisons, a full 2D steady state CFD simulation takes approximately 2 minutes; the computation of the ROM solution takes 0.2 seconds on a normal laptop Pc.

3.3.2 2D CFD analysis vs Bernoulli pressure drop for single stenosis

In this section, and also for the next examples the simplified Bernoulli equation and a full CFD analyses will be taken into account in order to consider the errors in the computation of the pressure drop. The aim of this section is to consider the computation of the irreversible pressure drop across a stenotic lesion comparing the Bernoulli and 2D CFD straight tube axisymmetric model with a single stenosis. The hypothesis is that even for very simple cases such as a single lesion along the straight tube domain the Bernoulli equation cannot describe accurately the fluid flow behaviour.

We use the geometrical model as described in the former section, i.e. one single stenosis along the fluid domain, followed by a sudden expansion which returns the geometry to the original cross-sectional area. Writing down the energy balance on a particle of fluid travelling on a streamline through this domain, it gives:

$$\left(P+\frac{1}{2}\rho v^2+\rho gh\right)_1=\left(P+\frac{1}{2}\rho v^2+\rho gh\right)_2+f \qquad \text{(Eq.3.5)}$$

where P is the pressure, v is the velocity, g is the gravitational acceleration, h is the height, ρ is the density of the fluid and f is the frictional energy loss. However, the height in a horizontal tube can be eliminated on both sides and the frictional energy loss is negligible, under the assumption of no viscosity. The equation becomes a simplified Bernoulli equation used to translate velocity to a pressure difference:

$$P_1+\frac{1}{2}\rho v_1^2=P_2+\frac{1}{2}\rho v_2^2 \qquad \text{(Eq.3.6)}$$

Pressure drop with Bernoulli has been computed considering mass flow of the fluid, the inlet area and the stenosis area. Applying the continuity equation and writing $v=\frac{Q}{A}$ we have:

$$\Delta P=\frac{1}{2}\rho Q^2\left(\frac{1}{A_s^2}-\frac{1}{A_{in}^2}\right) \qquad \text{(Eq.3.7)}$$

Considering the Bernoulli equation, the energy balance can be applied between any pair of points.

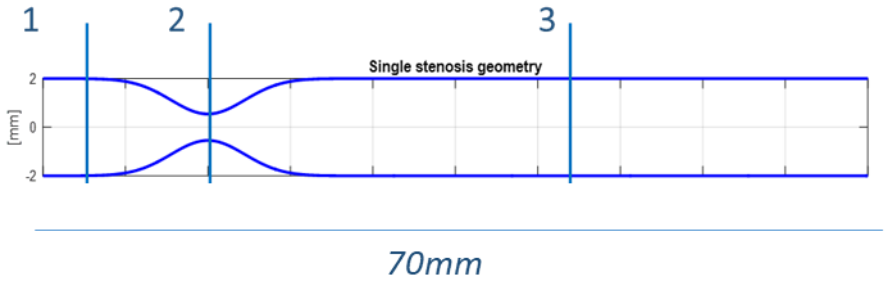

Figure 3.12: Single stenosis geometry for Bernoulli computation.

Looking at Figure 3.9 the type of geometry is a straight tube with a vena contracta, the radius at point 1 is equal to the radius at point 3 and considering the continuity equations the two velocities have to be equal. So according to Bernoulli (and neglecting frictional loss) we have no pressure drop between point 1 and 3. Clearly, in a real system this is not true, the pressure value at point 3 is lower than at point 1 due to frictional energy loss which reduces the pressure recovery between point 2 and 3. Furthermore the stenosis creates disturbances and complex flow fields which contribute to the overall losses.

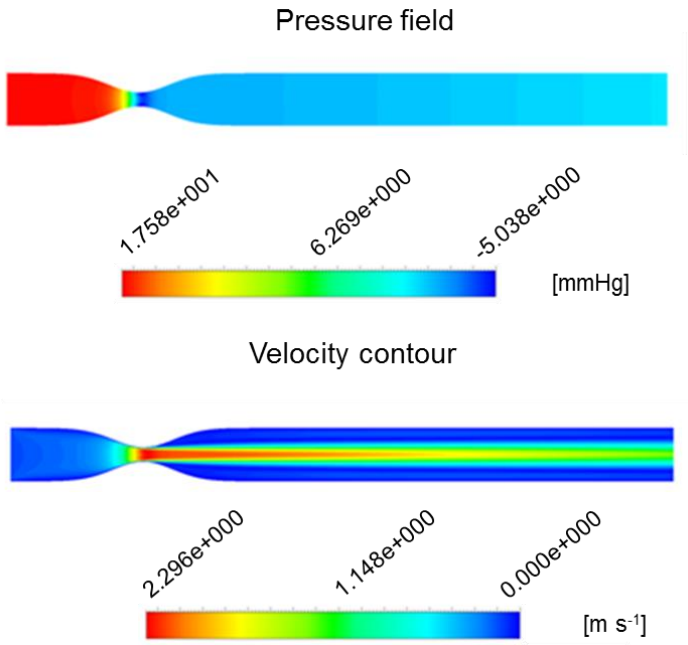

Figure 3.13: Example of pressure contour (top) and velocity contour (bottom) for the single stenosis geometry.

As expected, the blood flow increases its speed significantly as it passes through the vena contracta. The phenomenon of flow separation occurs just after the constriction, since there is a rapid expansion of the geometry. The flow separation causes a change on the fluid motion since the fluid starts to recirculate near the walls. Most important, it is possible to notice from the pressure contour, that the pressure drop is concentrated on the region of the stenosis and that there is a little pressure recovery downstream of the vena contracta which is due to the deceleration of the fluid. In fact, in the direction of the fluid, the pressure is falling on the convergent section of the tube, however the pressure rises as the cross sectional area starts to expand again after the lesion. The fluid jet continues to narrow further downstream of the lesion until it reaches the vena contracta where the velocity of the fluid is at its maximum speed (minimum fluid cross-sectional area). At this stage, the flow starts to expand, filling the whole cross-sectional area of the idealised straight coronary.

Before writing the discussions for these cases, it is important to mention that the idealised coronary domain should be long enough to ensure that pressure recovery effect is complete. However, for the cases taken into consideration, the domain is quite short and pressure is still recovering, meaning that the reported pressure drops are arbitrary since the length of the domain is arbitrary. One should consider the pressure drop once the flow has fully recovered and the pressure profile starts to diminish again following a linear pressure drop given by the Poiseuille law after which the full effect of the stenosis has been accounted for (Figure 3.11).

However, as it can be seen from Figure 3.11 (considering a much longer tube *L=300mm*) the maximum pressure recovery (full recovery), can be far away and not important for coronaries. It can also be said that the coronaries are too short to allow blood flow to develop. The length needed by the flow to develop on a straight tube, is called inlet length; the inlet length l_{inlet}, depends on the Reynolds number as:

$$\frac{l_{inlet}}{D} \approx 0.06\, Re \qquad \text{(Eq.3.8)}$$

If it is considered a $Re = 500$ and an average coronary diameter of 4 mm; the length necessary to the blood flow to become developed is $\approx 120\ mm$.

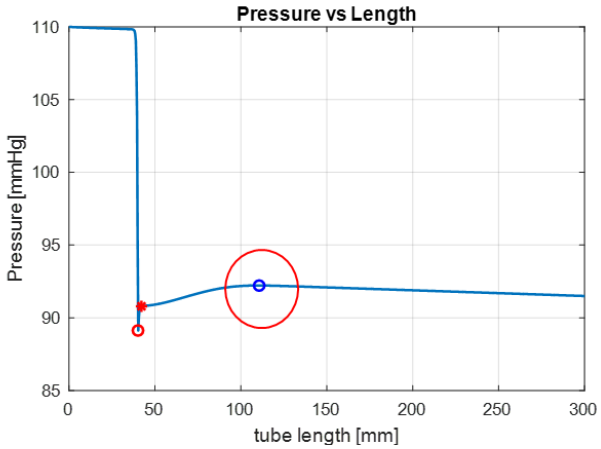

Figure 3.14: Example of pressure recovery for a long straight tube (blue circle).

A Bland-Altman graph has been computed with 50 different geometries where the mass-flow rate was a parameter (Figure 3.12). However, the different mass-flows have been computed starting from different values of the R_{mc} as shown in Table 3.1.

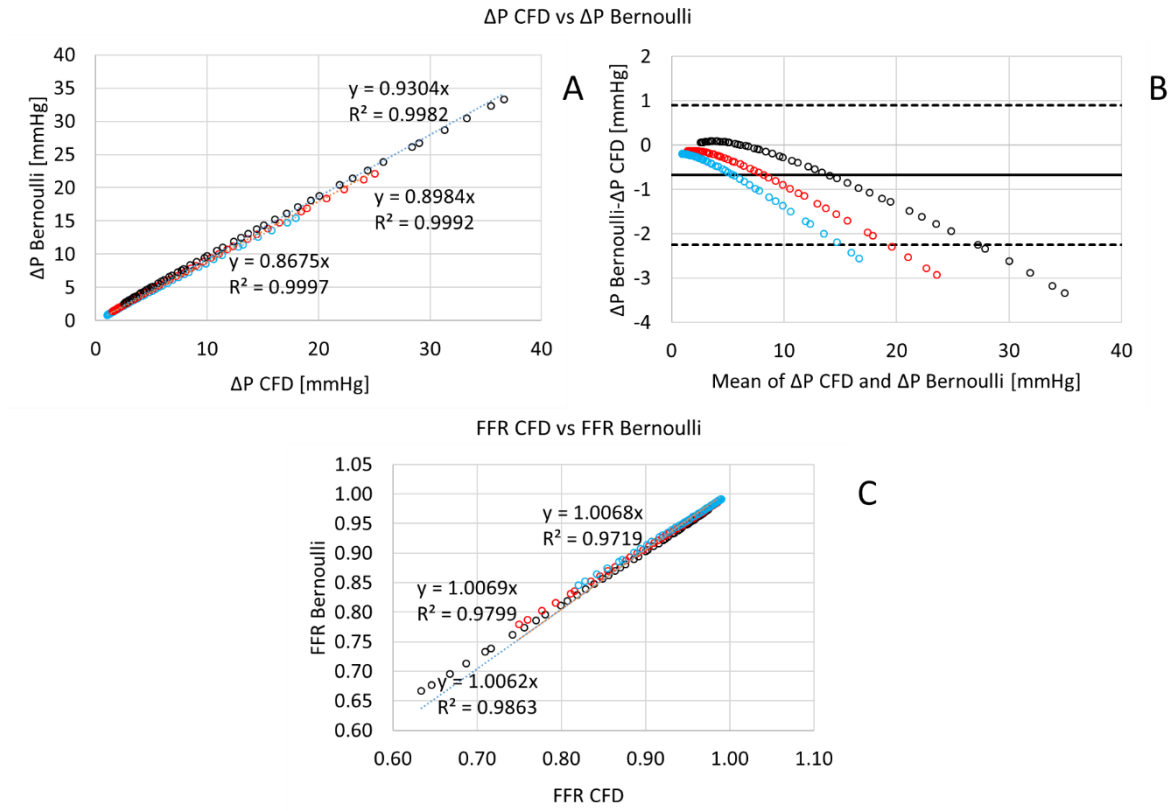

Figure 3.15: Top graphs) Comparison of pressure drops computed with CFD and Bernoulli (A). Bland-Altman plot for the pressure drops (B). Bottom graph) FFR CFD vs FFR Bernoulli for different values of Rmc.

It is possible to notice that using the Bernoulli formula (with the average velocity) the pressure drop is underestimated since the error $\Delta P_{Bernoulli}$-ΔP_{CFD} is negative. Furthermore, the difference between the two ΔP_s is increasing whilst considering higher values of mean ΔP. An underestimation of the pressure drop means that the FFR index computed with Bernoulli is overestimated, moreover low values of FFR are poorly described since for high values of mean ΔP correspond higher errors on the pressure difference. It is perhaps surprising that the Bernoulli loss is smaller than the CFD pressure gradient despite the fact that in the Bernoulli computation it has been assumed no pressure recovery. This is why for the next computations of Bernoulli pressure drops presented in the next sections, it will be taken into account also the maximum velocity reached by the blood flow along the centreline of the coronary. The peak velocity values computed with CFD simulations have been plugged into the Bernoulli formula.

3.3.3 Results CFD vs ROM vs Bernoulli for a single lesion

The ROM has been validated against 90 cases which were out of the dataset, the FFR has been computed with three different methods, CFD, ROM and Bernoulli, in order to compare the accuracy. The FFR value with Bernoulli has been computed twice, the first computation has

been done considering the average value of velocity, instead the second Bernoulli computation is considering the maximum value of the velocity along the coronary centreline. The correlation between the FFR computations is represented with Bland-Altman graphs (Figure 3.15). Some results of the CFD simulations vs ROM solutions are shown in Figure 3.13 and Figure 3.14.

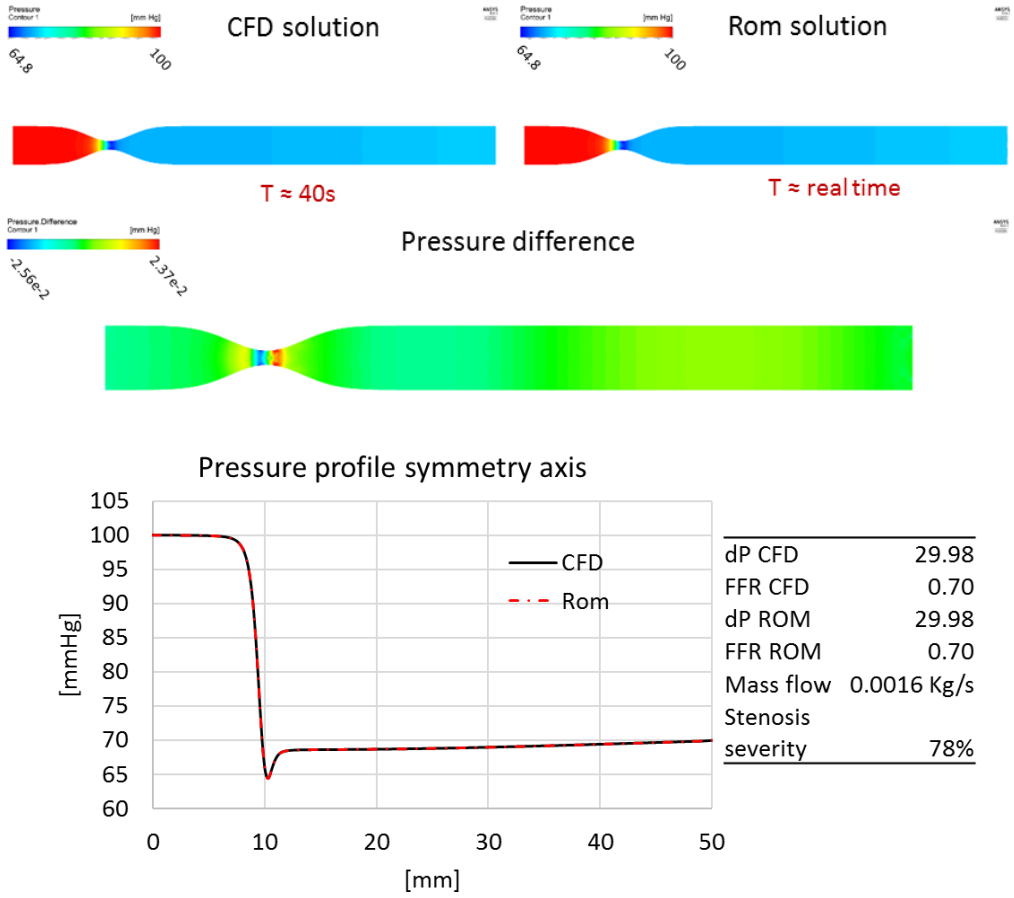

Figure 3.16: Top graphs) Full CFD solution vs ROM solution with 4 modes for the pressure contour. Bottom graph) Axial pressure profile vs coronary length for CFD solution and ROM solution.

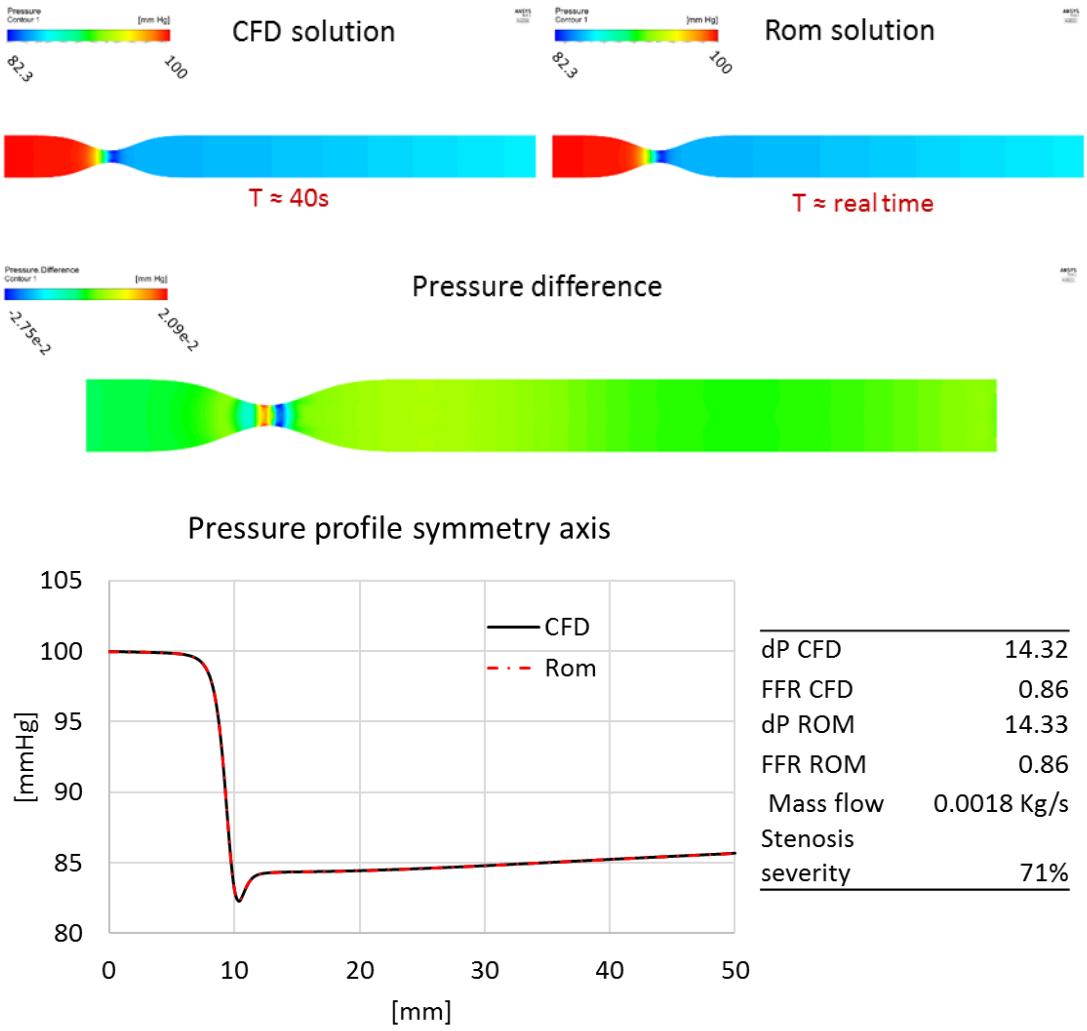

Figure 3.17: Top graphs) Full CFD solution vs ROM solution with 4 modes for the pressure contour. Bottom graph) Axial pressure profile vs coronary length for CFD solution and ROM solution.

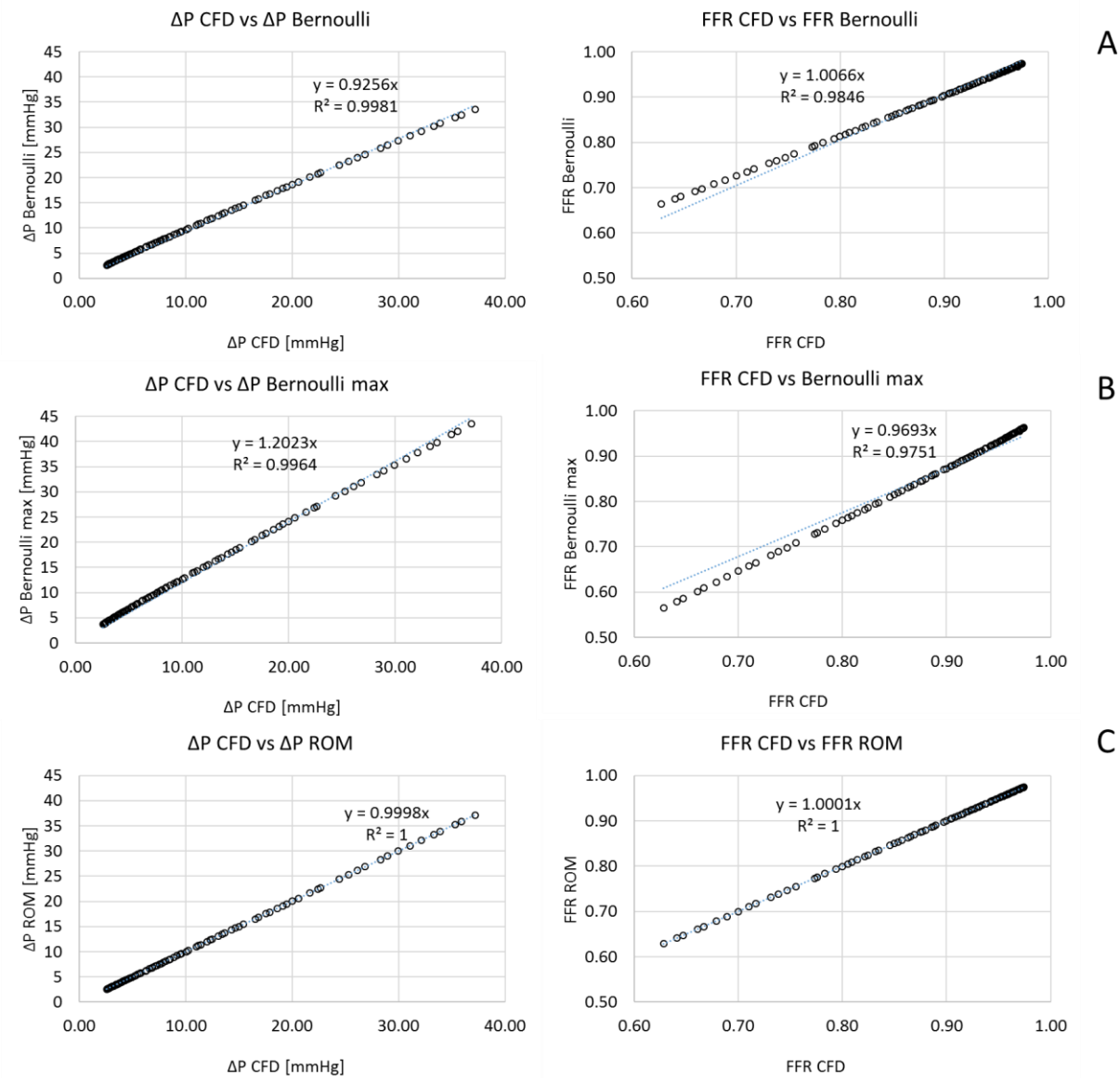

Figure 3.18: Correlation for pressure drops and FFR computed with the different methods. Full CFD vs Bernoulli (top row), full CFD vs Bernoulli max (middle row), full CFD vs ROM (bottom row) The plots are computed for the single stenosis study.

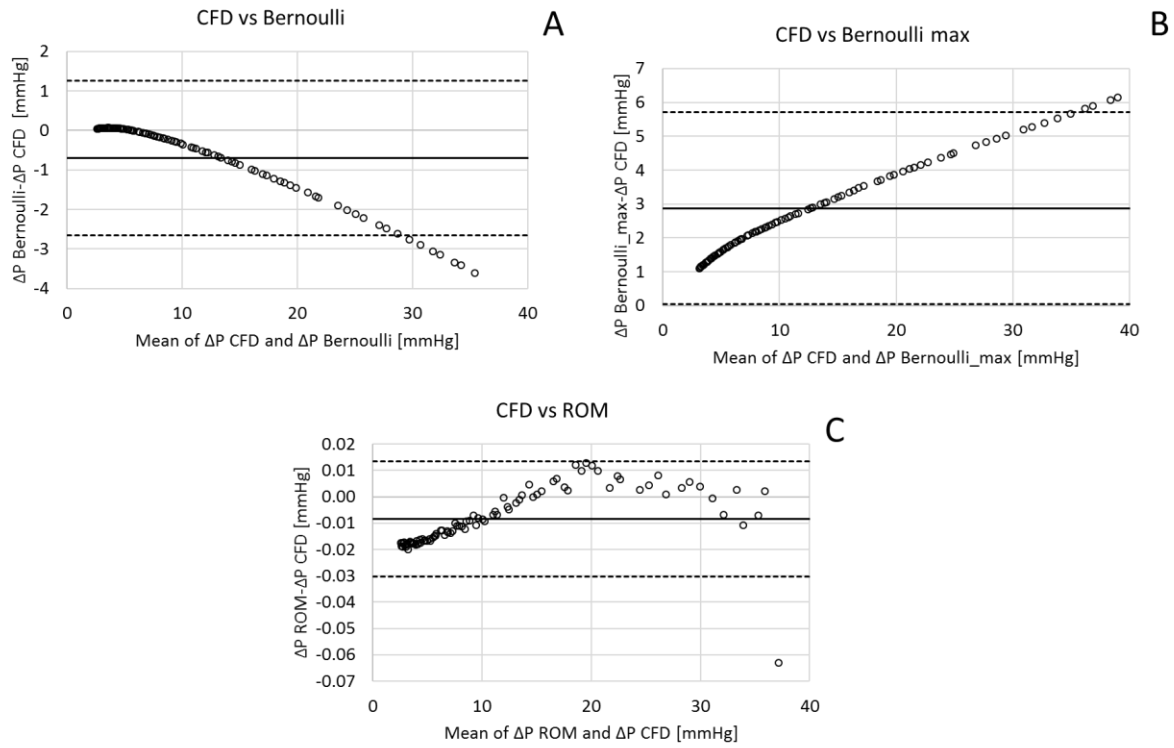

Figure 3.19: Bland-Altman graphs for the different methods.
A) CFD vs Bernoulli; B) CFD vs Bernoulli max; C) CFD vs ROM.

This study is showing how the modified Bernoulli equation is not a very good estimation for the FFR computation, furthermore the graphs are showing that the ROM estimate of the FFR is better than Bernoulli with an excellent correlation (the slope of the linear regression model is equal to 1). However, it has to be said that the ROM is built on the same domain as the CFD, so it is not surprising the errors are very small. The error values computed with Bernoulli are higher compared to the ROM errors. It is interesting to notice how the FFR computed with modified Bernoulli equation using the maximum value of velocity is always overestimating the pressure drop meaning that the computed FFR is always underestimated. This behaviour is opposite to the underestimation of the pressure drop given by Bernoulli with the average velocity. Other studies have highlighted this kind of behaviour as in [100], [101] especially the case of overestimating the pressure drop, using Doppler ultrasound for clinical measurements. However, if considering invasive study, it is common to consider the pressure profiles effectively uniform after the lesion. As already described in the previous sections, the jet of the fluid expands downstream of the vena contracta; moreover, its velocity decreases, and pressure recovers thanks to the conversion of kinetic energy to pressure. The pressure recovery behaviour can lead to overestimation of the pressure gradient so that the measured gradient will

be lower if the distal catheter is positioned downstream from the vena contracta. This can lead to the overestimation of the pressure gradient because of the phenomena of pressure recovery.

3.4 2D axisymmetric straight tube model with a double lesion

A potential question with regard to the analyses of a single stenosis presented in the previous section is whether the pressure behaviour might be captured by a 1D model. In this section a straight rigid tube with two stenoses in series has been analysed. For this system it might be expected that a 1D model might not adequately capture the interactions between the stenoses that are associated with jet expansion and pressure recovery. Multiple CFD studies have been performed for the 2D straight tube axisymmetric study with a double stenosis [12], [102]–[104]. The present numerical study has been developed to understand the haemodynamic and geometrical effects of two stenosis in series since it is quite common to find multiple stenosis in series in a diseased coronary vessel. Although is a simple model, it is useful to understand the different interactions between the stenosis, representing situations which could easily occur in patients with CAD. The hypothesis is that the interaction between the two stenosis depends on the grade of the severity, on the interspacing distance between the two occlusion and on the mass flow rate.

3.4.1 2D CFD interactions between two stenosis in series

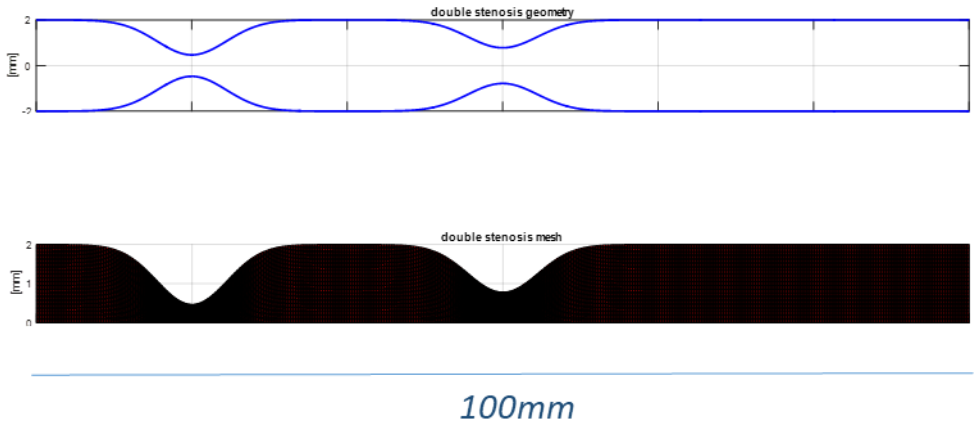

Figure 3.20: Double stenosis geometry with relative 2D mesh.

The geometry of the straight tube is 10 cm long, the dimensions of the inlet and outlet radii are equal (r = 2 mm). The position of the first stenosis has been kept fixed and it is centred at 5r. The position of the second stenosis is varied such that the interspace distance between the two minimum radii of the two constrictions is varied between $5r \leq int_{dist} \leq 35r$ increasing gradually the distance in increments of *2.5r*. Four datasets, consisting of 13 geometries each have been taken into consideration. The fluid flow in each of the 13 different geometries in a

single dataset have been simulated using different mass flow rates, with Q ranging from 1 to3 *ml/s*. Every dataset is formed by 65 simulations, giving a total of 260 steady state simulations (Table 3-3). The interspace distance between the two stenosis, the two radii reductions (severity of the stenosis) and the inlet mass flow rate have been varied for this study ($N = 4\ parameters$). It will become evident in the next sections that the haemodynamic interactions between two stenoses in series is strongly dependant on all four parameters. We demonstrate that the two stenoses do not interact haemodynamically if the fluid flow after the first stenosis has effectively reattached to the wall.

Table 3.3: Summary of the different simulation.
The two lambdas (λ_1 and λ_2) refers to the radius reduction in percentage of the first stenosis and the second stenosis.

Severity λ_1 (%)	**Severity λ_2** (%)	Mass-flow (Q) [1:0.5:3]	Distance [5r:2.5:35r]	Total Simulations
50	50	5 flows	13 geometries	65
70	70	5 flows	13 geometries	65
50	70	5 flows	13 geometries	65
70	50	5 flows	13 geometries	65

We consider axial velocities and axial pressure profiles as our variables of choice to study the geometric and haemodynamic interactions.

Pressure profiles on the centreline

Case-A S1=50% S2=50%

For two stenoses in series of the same degree which are non-interacting (large interspace between them), the pressure drop along the centreline is (almost) double that of the pressure drop on a single stenosis (Figure 3.25 and Figure 3.26). In fact, the two stenoses, even if they are in series, act as two separate stenosis and the total pressure drop along the tube is given by the summation of the two independent pressure drops (case where s1=50% s2= 50% at high value of distance).

In contrast, if we consider interacting stenoses, the total pressure drop along the tube is less than the sum of the pressure loss of each stenosis (graph of pressure profiles Figure 3.23 and Figure 3.24). The closer the two stenoses are, the more the difference increases in the total pressure drop. As the second stenosis get closer and closer to the first stenosis, the pressure drop across the second stenosis tends to be lower (Figure 3.21 and Figure 3.22). Moreover, the

minimum pressure at the throat of the second stenosis increases when the second stenosis is close to the first.

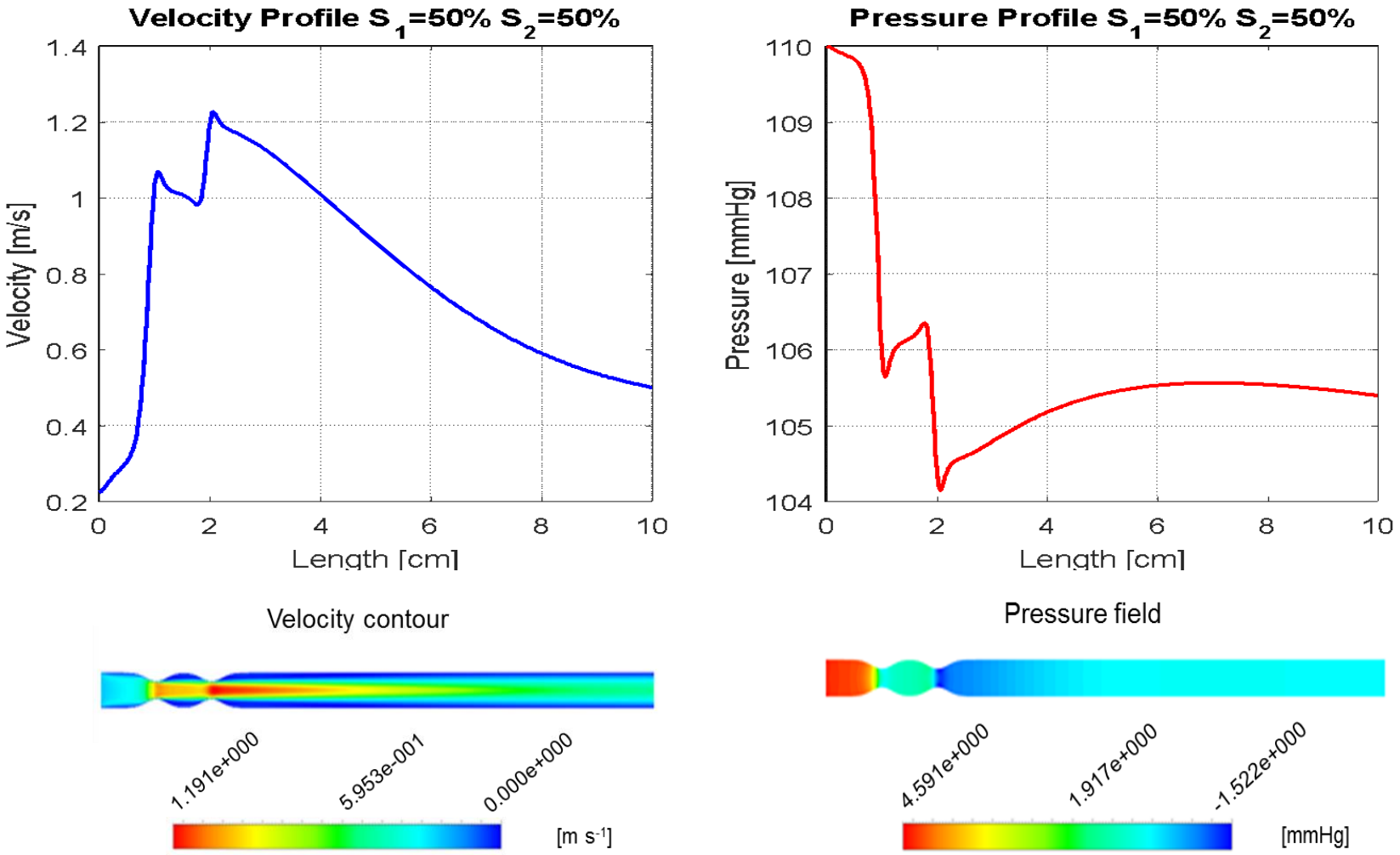

Figure 3.21: Left plot) Axial velocity profile. Right plot) Axial pressure profile.

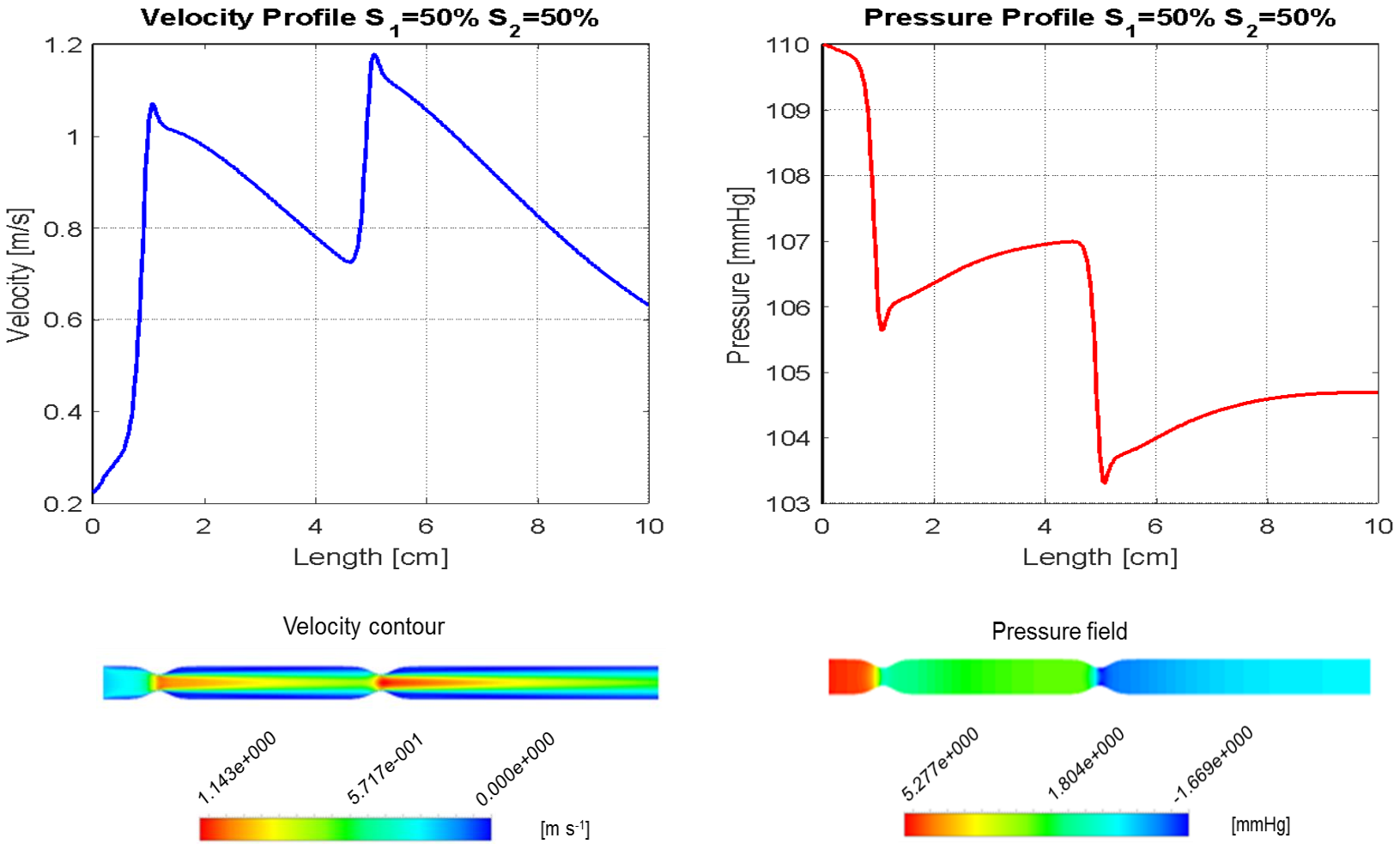

Figure 3.22: Left plot) Axial velocity profile. Right plot) Axial pressure profile.

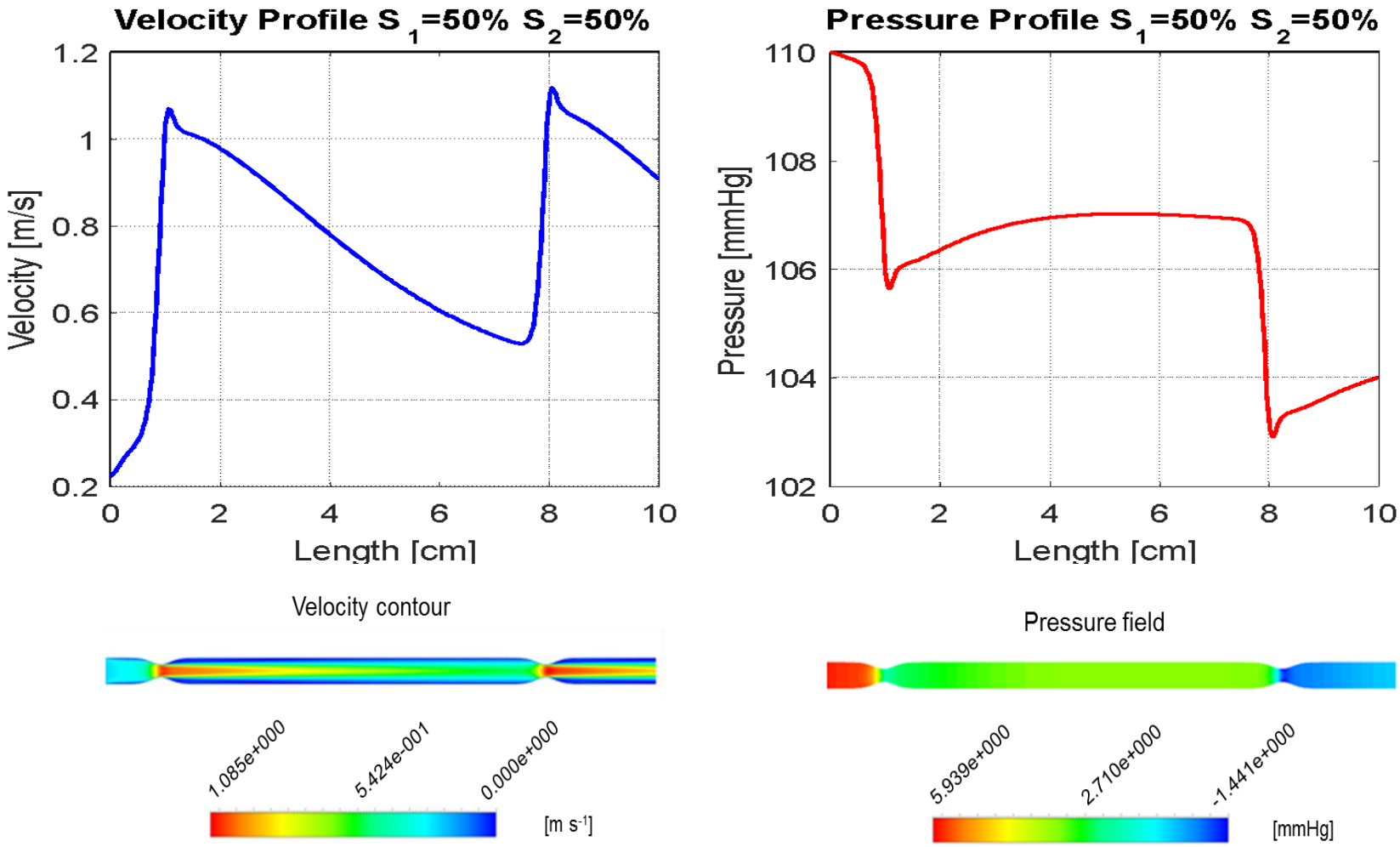

Figure 3.23: Left plot) Axial velocity profile. Right plot) Axial pressure profile.

Case-C S2=70% S2=50%

In case the severity of the two stenoses is different, it is interesting to look at an example where the first stenosis is more severe than the distal one. For interacting stenoses (small interspace distance), the flow accelerates at the first stenosis, pressure is converted into kinetic energy and a big pressure drop occurs. The accelerated fluid flow does not interact haemodynamically with the second stenosis, in fact there is no additional pressure drop at the second vena contracta but surprisingly there is a pressure recovery. This effect means that the second stenosis has a positive impact in helping the pressure recovery [105]. The small radius reduction of the second stenosis does not accelerate the flow any further, on the contrary the distal stenosis decelerates the jet. This behaviour is explained by Figure 3.25, the jet is expanding at the second stenosis and this expansion is causing a reduction in velocity and a concomitant increase in static pressure.

The beneficial effects of the second stenosis disappear when the interspace between the two increases. We note a small acceleration into the second stenosis when the two stenoses are far apart. As result, the less severe distal stenosis adds a small contribution to the total pressure drop, increasing when the distance between the two stenosis increases. It is apparent that, as might be expected, the two stenoses in series tend to act haemodynamically as a single stenosis when they are close together. The jet does not ‘see’ the second stenosis, as it is still narrow when it arrives at the second stenosis.

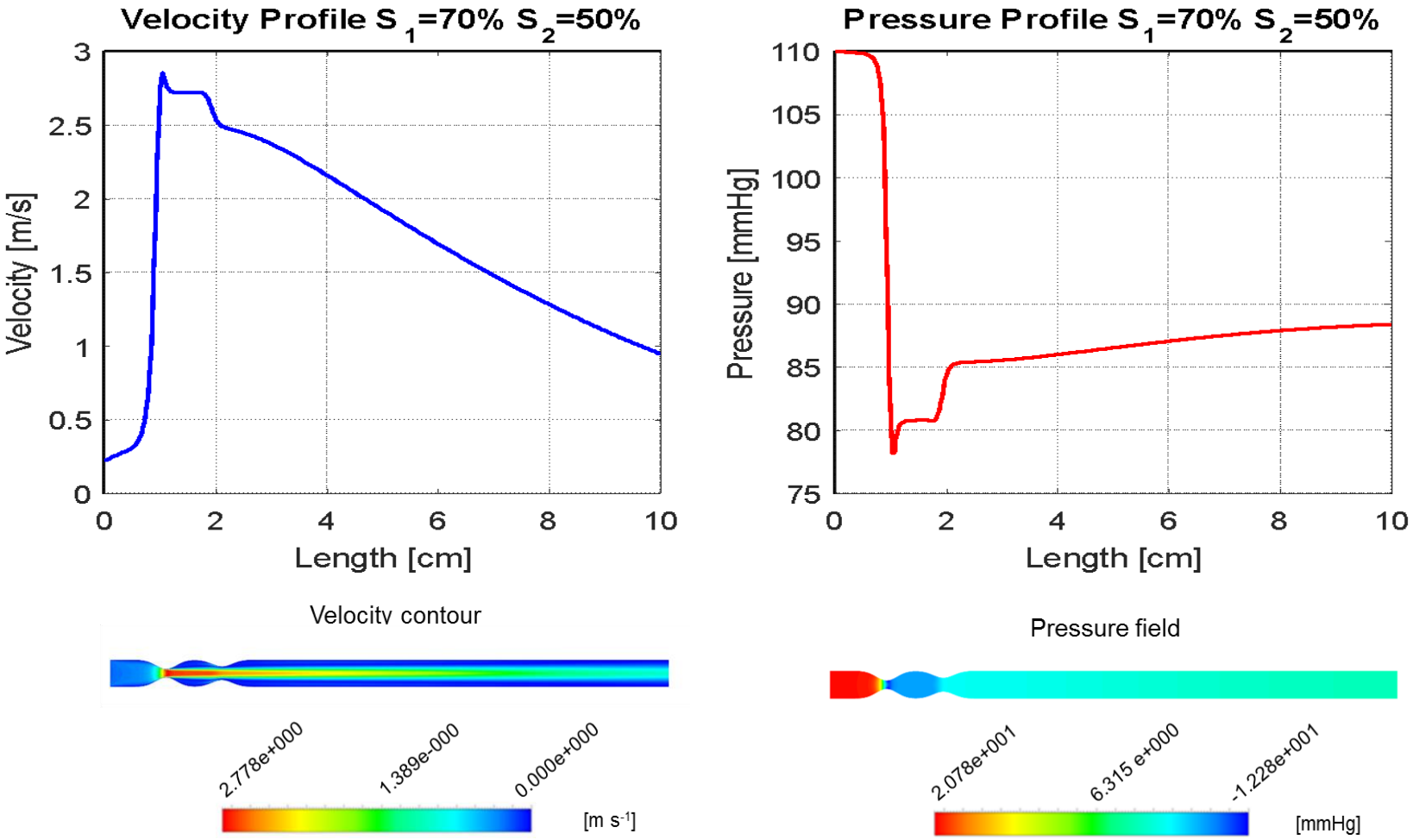

Figure 3.24: Left plot) Axial velocity profile. Right plot) Axial pressure profile.

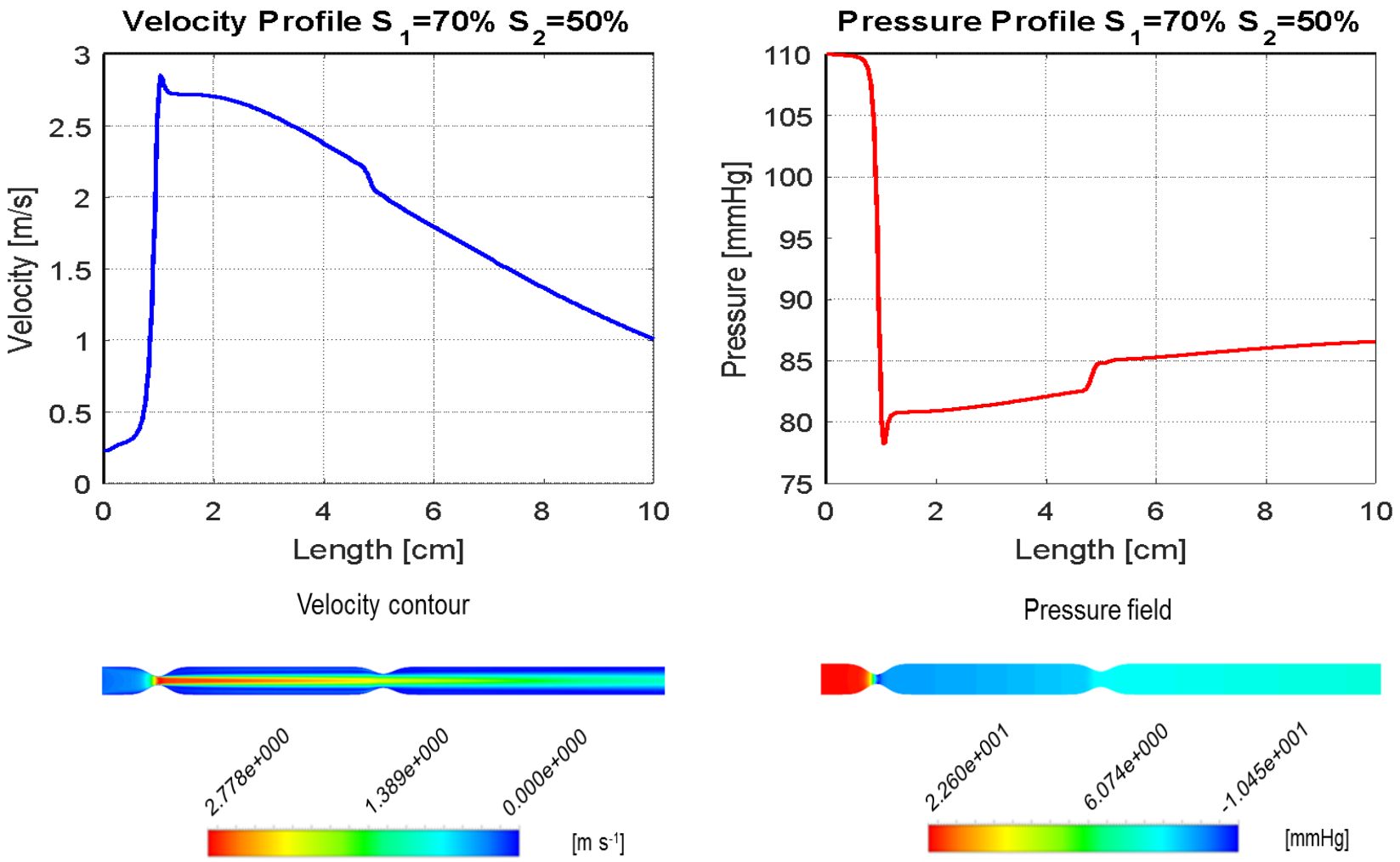

Figure 3.25: Left plot) Axial velocity profile. Right plot) Axial pressure profile.

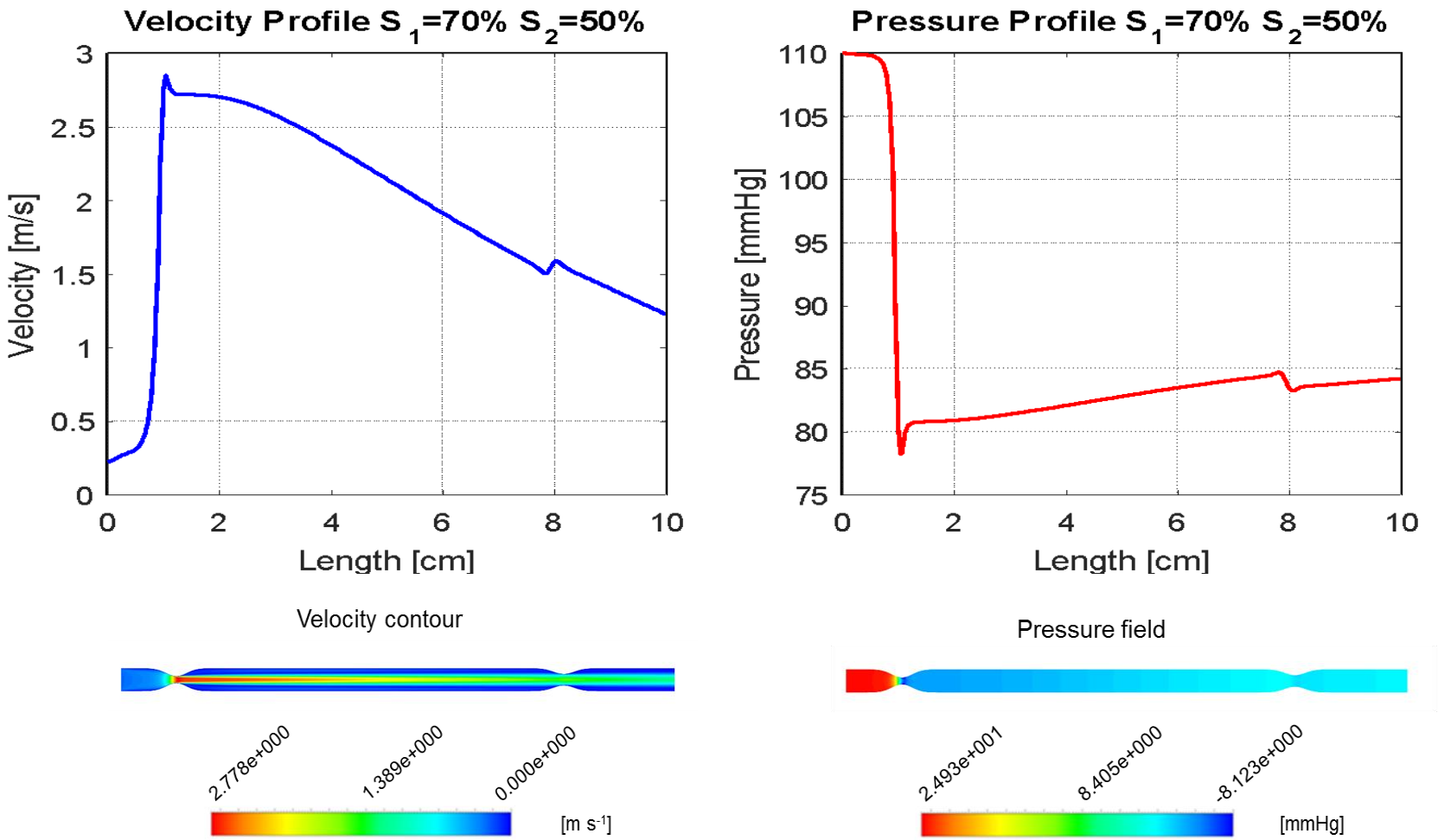

Figure 3.26: Left plot) Axial velocity profile. Right plot) Axial pressure profile.

Case-D S1=50% S2=70%

When the first stenosis is less severe than the distal stenosis, the system behaves as expected. There is pressure drop which occurs at the first occlusion, moreover the fluid flow encounters the second stenosis while it is in recovery in the separation zone. The largest pressure drop occurs at the more severe stenosis where the flow suddenly accelerates.

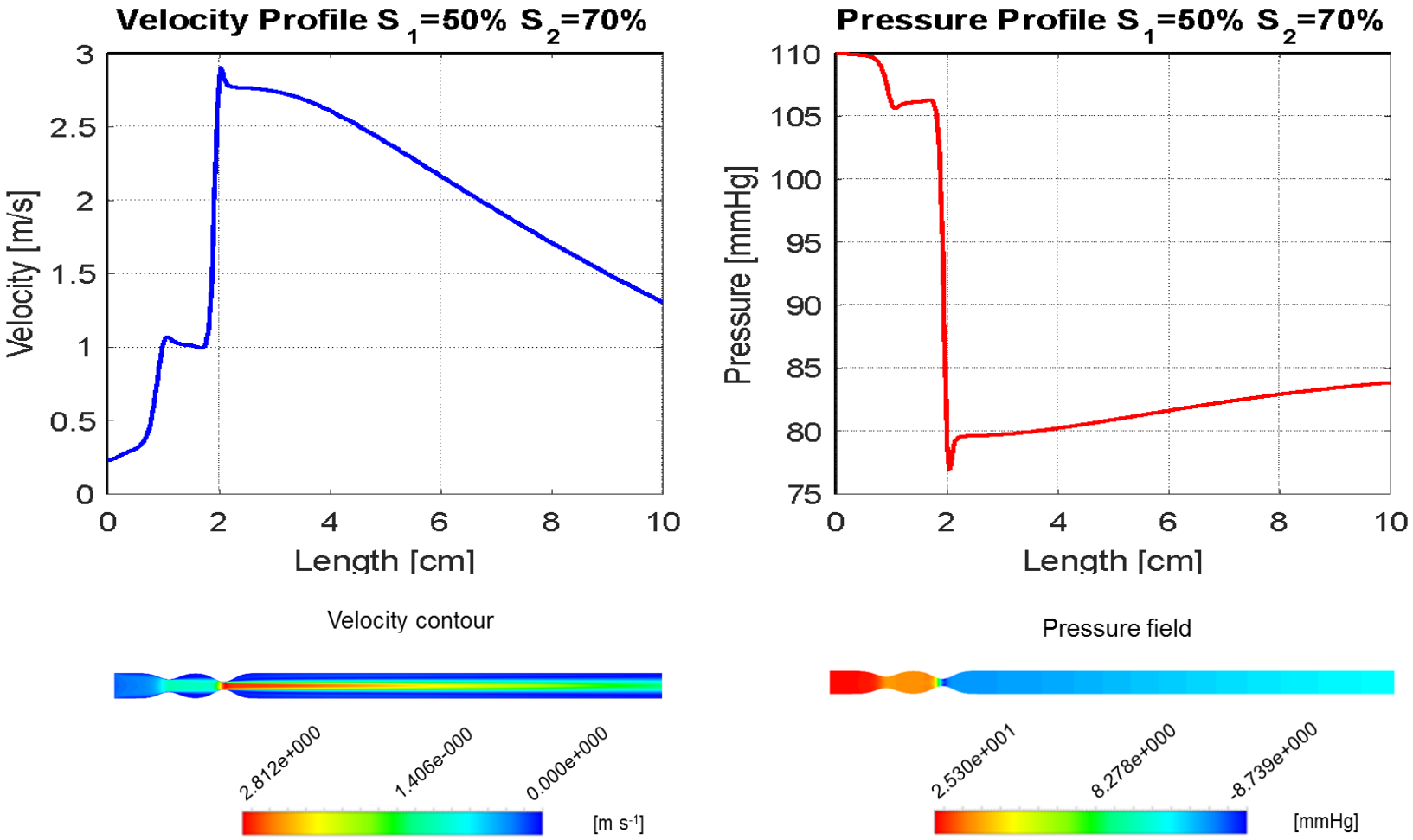

Figure 3.27: Left plot) Axial velocity profile. Right plot) Axial pressure profile.

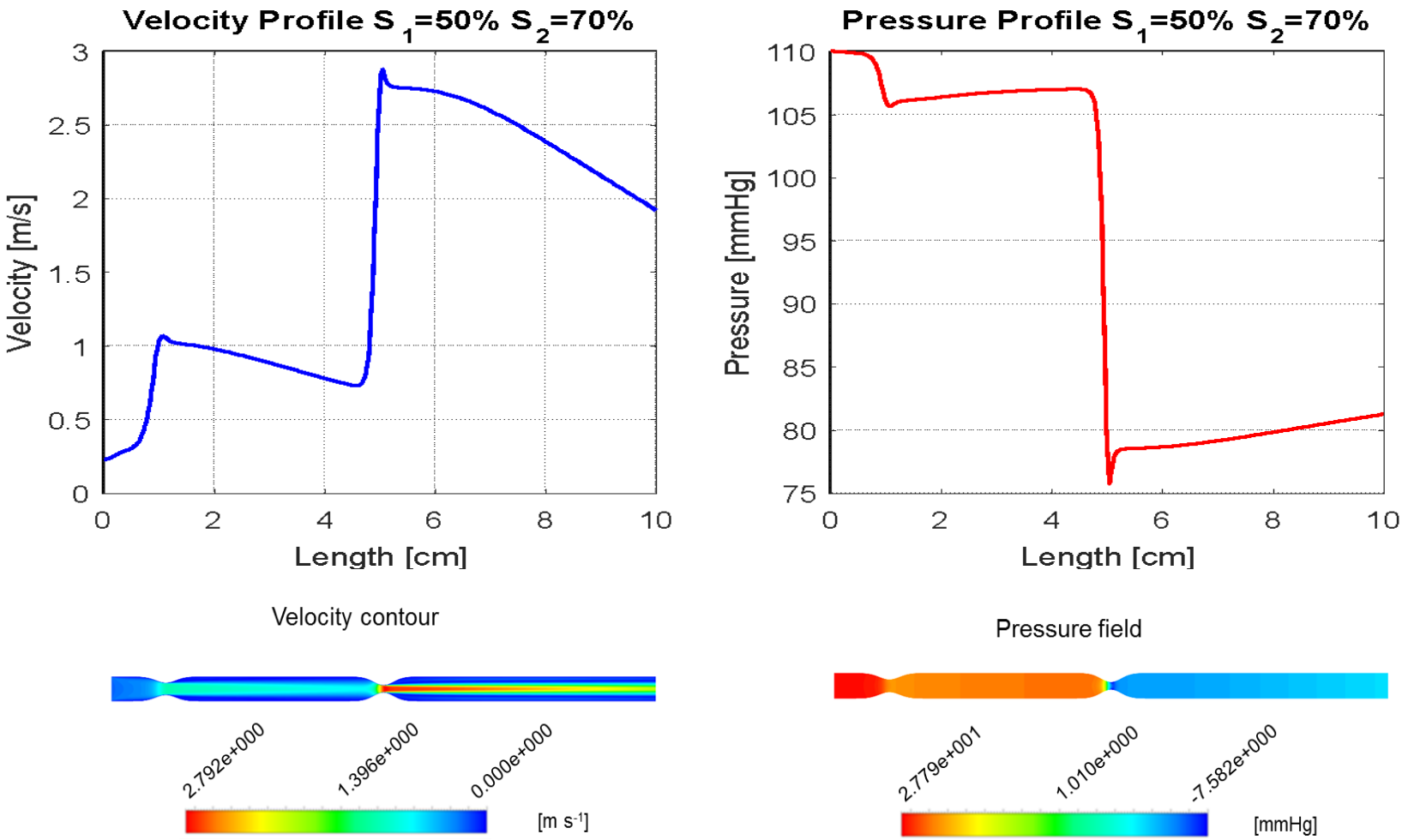

Figure 3.28: Left plot) Axial velocity profile. Right plot) Axial pressure profile.

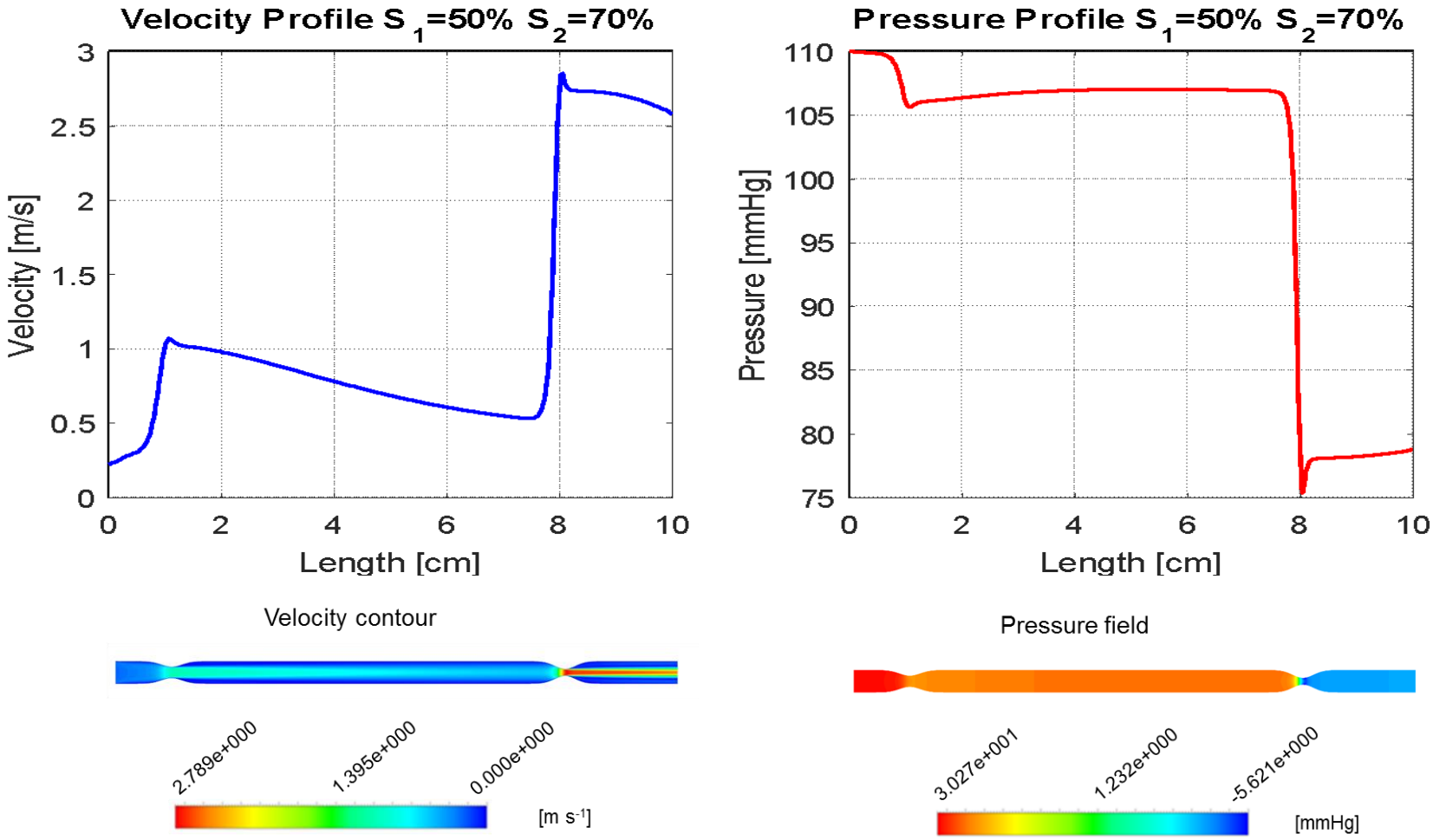

Figure 3.29: Left plot) Axial velocity profile. Right plot) Axial pressure profile.

Pressure Profiles

In this section we present the pressure profiles along the centreline for the dataset case A (S1=50%, S2=50%) in order to visualise the change in pressure with the interspace distance between the stenoses. Figure 3.36 shows that as the interspace distance between the two increases, each stenosis acts as independent. In fact, at 7cm interspace distance the total pressure drop is twice the pressure drop on a single stenosis. Since the Bernoulli formulation does not account for the geometrical and haemodynamic relations between the two stenoses, a decreasing difference between the computation of ΔP CFD and ΔP Bernoulli might be expected as the interspace distance is increased (Table 3-4 and Figure 3.37).

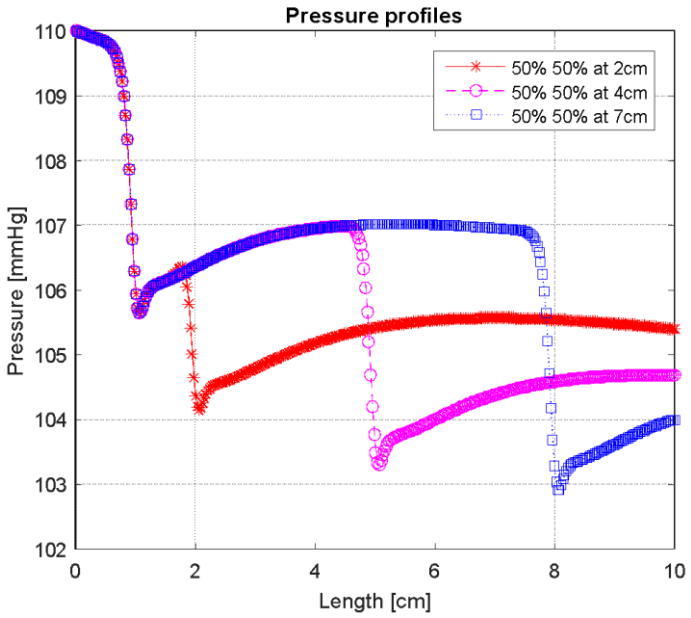

Figure 3.30: Pressure profiles for Case A (S1=50%, S2=50%) at different interspace distances.

Table 3.4: Comparison of CFD and Bernoulli pressure gradient.

$S_1(\%), S_2(\%), Distance$	CFD ΔP [mmHg]	Bernoulli ΔP [mmHg]
50,50,5r	*4.60*	*6.80*
50,50,20r	*5.31*	*6.80*
50,50,35r	*5.99*	*6.80*
70,50,5r	*21.63*	*31.17*
70,50,20r	*23.46*	*31.17*
70,50,35r	*25.79*	*31.17*
50,70,5r	*26.18*	*31.17*
50,70,20r	*28.73*	*31.17*
50,70,35r	*31.23*	*31.17*

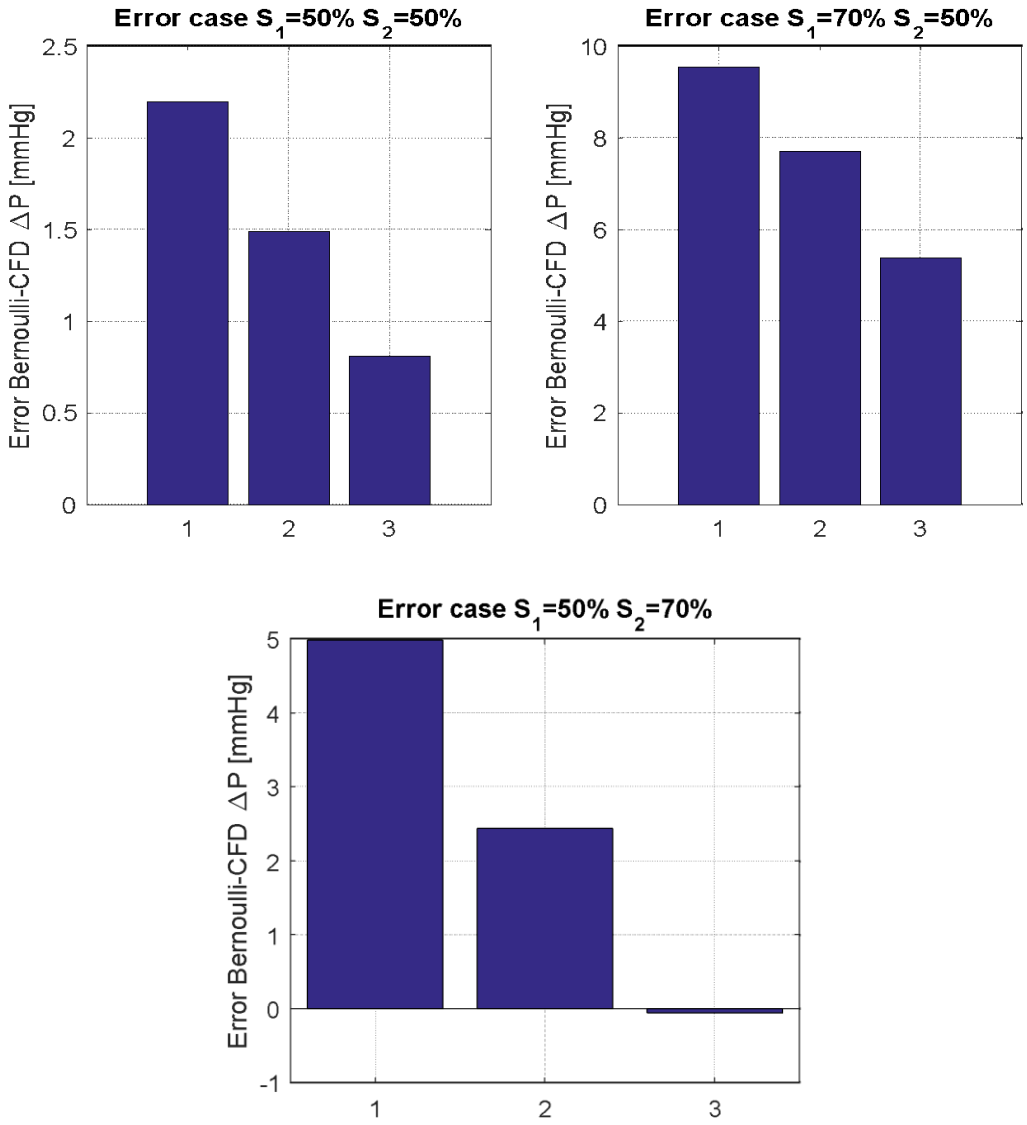

Figure 3.31: Error between Bernoulli and CFD pressure drop for three different cases: (S_1, S_2=50%), (S_1=70%, S_2-50%), (S_1=50%,S_2=70%)

Axial velocity profile (fixed interspace distance, varying severity of stenosis)

Velocity profiles for Case A, B, C, D are shown in Figure 3.38. The centreline velocity profile is shown for the different geometries at fixed interspace distance between the two stenoses of *20r*. The maximum velocities occur along the centrelines and specifically at the location of the vena contracta where we have global maximum values for the most severe stenoses (Case B 70%, 70%). It is clear that after the restrictions the fluid flow decelerates and the pressure gradually recovers. However, the case where the first stenosis is more severe than the distal one (Case C 70%, 50%), velocity at the second stenosis does not increase but decreases instead. The second mild stenosis decelerates the jet causing a reduction in velocity and a concomitant increase in static pressure.

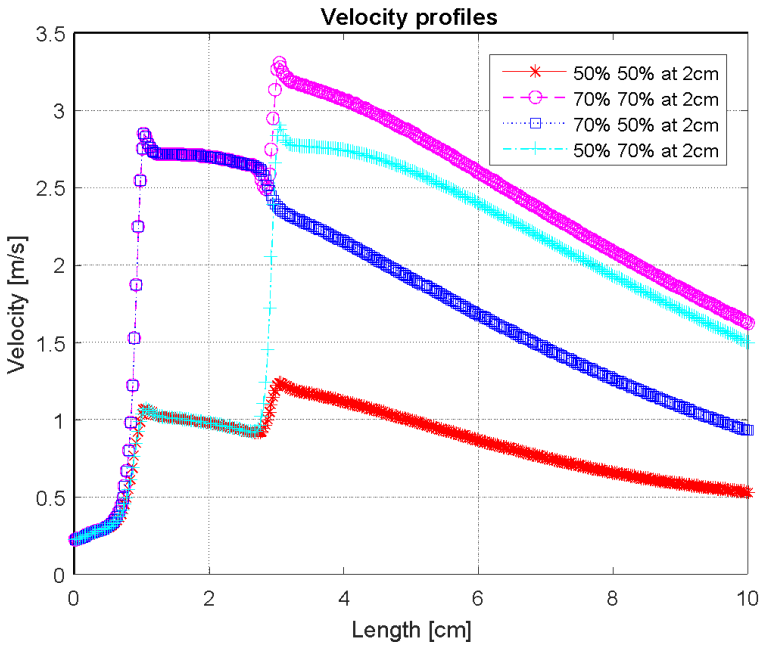

Figure 3.32: Velocity profiles for the four different datasets, keeping constant the interspace distance.

3.5 2D vs 1D vs Bernoulli of the double stenosis interaction model

In the previous section it has been already demonstrated that the error between the ΔP computed with Bernoulli and the computation of the ΔP with an axisymmetric model decreases when the two stenoses have a large interspace distance; this is because the two lesions are no longer interacting haemodynamically. In section 3.3 the single stenosis case has been considered highlighting the difference between the computation of the pressure drop with a simple Bernoulli formula or with CFD for an axisymmetric geometry.

However, what has not been demonstrated is a comparison between a 2D model, a 2D model with ROM and a 1D model. This comparison is a necessary step since if the 1D model will show comparable results with the 2D model, a ROM computation would not be necessary (due to the fact that 1D models require a small amount of CPU and RAM). In this section a similar study with a comparison between axisymmetric CFD vs Bernoulli vs 1D solver has been computed in order to numerically assess the errors in the pressure drop when different methods are deployed [106],[31], [107].

Considering the Bernoulli formula, in a straight tube, with N stenoses in series the total pressure drop is the summation of the pressure drop given by the N_{th} stenosis. Therefore, we would have:

$$\Delta P_{tot} = \sum_{i=1}^{N} \Delta P_i \qquad \text{(Eq.3.9)}$$

where ΔP_i is the pressure drop which occurs at the i_{th} stenosis. Since in this study there are two stenosis in series and the geometry of the tube is known, the total Bernoulli pressure drop is given by:

$$\Delta P_{Bernoulli} = \frac{1}{2}\rho Q^2 \left(\frac{1}{A_{s1}^2} - \frac{1}{A_{inlet1}^2} + \frac{1}{A_{s2}^2} - \frac{1}{A_{inlet2}^2} \right) \qquad \text{(Eq.3.10)}$$

In the 1D model, the fluid flow domain is decomposed into little segments, connected at nodes. The 1D solver used in this section is called OpenBF, the solver is open source (Apache 2.0) and has been developed in INSIGNEO (Sheffield) [30]. OpenBF is a finite volume solver based on a 1D reduction of the Navier-Stokes equations and it is characterised by some model assumptions:

- The blood flows through narrow and circular vessels;
- The vessels are straight and have linear elastic compliant walls;
- Displacements in the radial direction are small;
- The blood is an incompressible Newtonian fluid.

For this study a single vessel is considered and furthermore the vessel must not present bends along the axial direction.

The equations which describe the 1D solver are:

$$\begin{cases} \dfrac{\partial A}{\partial t} + \dfrac{\partial Q}{\partial x} = 0 \\ \dfrac{\partial Q}{\partial t} + \dfrac{\partial}{\partial x}\left(\dfrac{\alpha Q^2}{A}\right) + \dfrac{A}{\rho}\dfrac{\partial p}{\partial x} = -\dfrac{2\mu}{\rho}(\gamma_v + 2)\dfrac{Q}{A} \\ P(A) = P_{ext} + \beta\left(\sqrt{\dfrac{A}{A_0}} - 1\right), \quad \beta = \sqrt{\dfrac{\pi}{A_0}}\dfrac{Eh_0}{1-\nu^2} \end{cases} \qquad \text{(Eq.3.11)}$$

where t is time, x is the axial coordinate, $A(x,t)$ is the coronary cross-sectional area, $Q(x,t)$ is the volumetric flow rate, α is the Coriolis' coefficient, ρ is the blood density, $P(x,t)$ is the blood pressure, μ is the blood dynamic viscosity, γ_v is a parameter defining the shape of the radial velocity profile, P_{ext} is the vessel external pressure, $E(x)$ is the vessel wall Young's modulus, ν is the Poisson's ratio, $A_0(x)$ is the reference cross-sectional area and finally h_0 is the reference wall thickness. The cross-sectional areas $A_0(x)$ for the different cases have been set up to match the variation of the radius of the 2D geometries. Since the 2D geometries considered in the previous sections were not compliant, in order to replicate the same behaviour for the 1D model, it has been chosen a high value of the Young's modulus was used.

52 cases have been used for the comparison between 2D and 1D model, using the same boundary conditions.

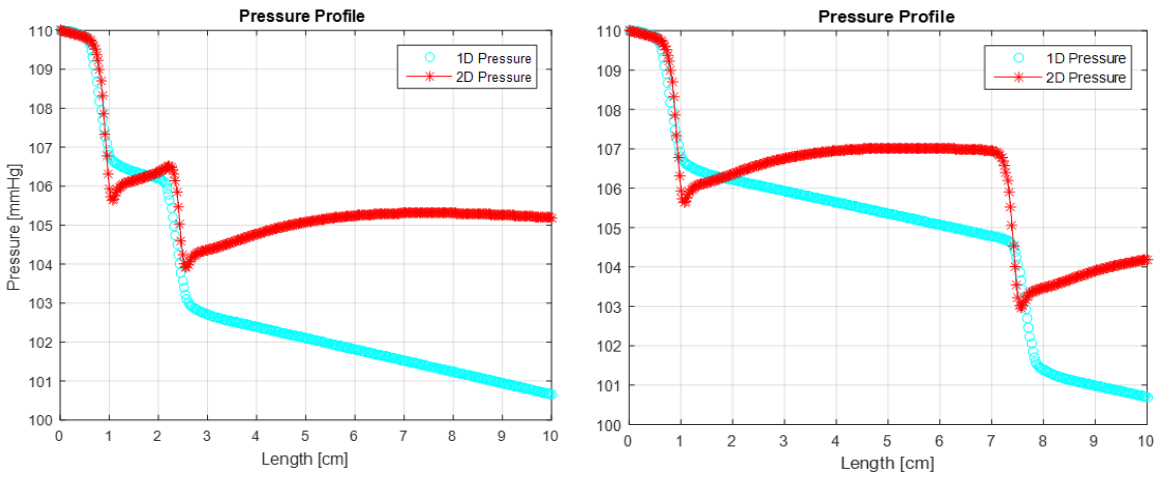

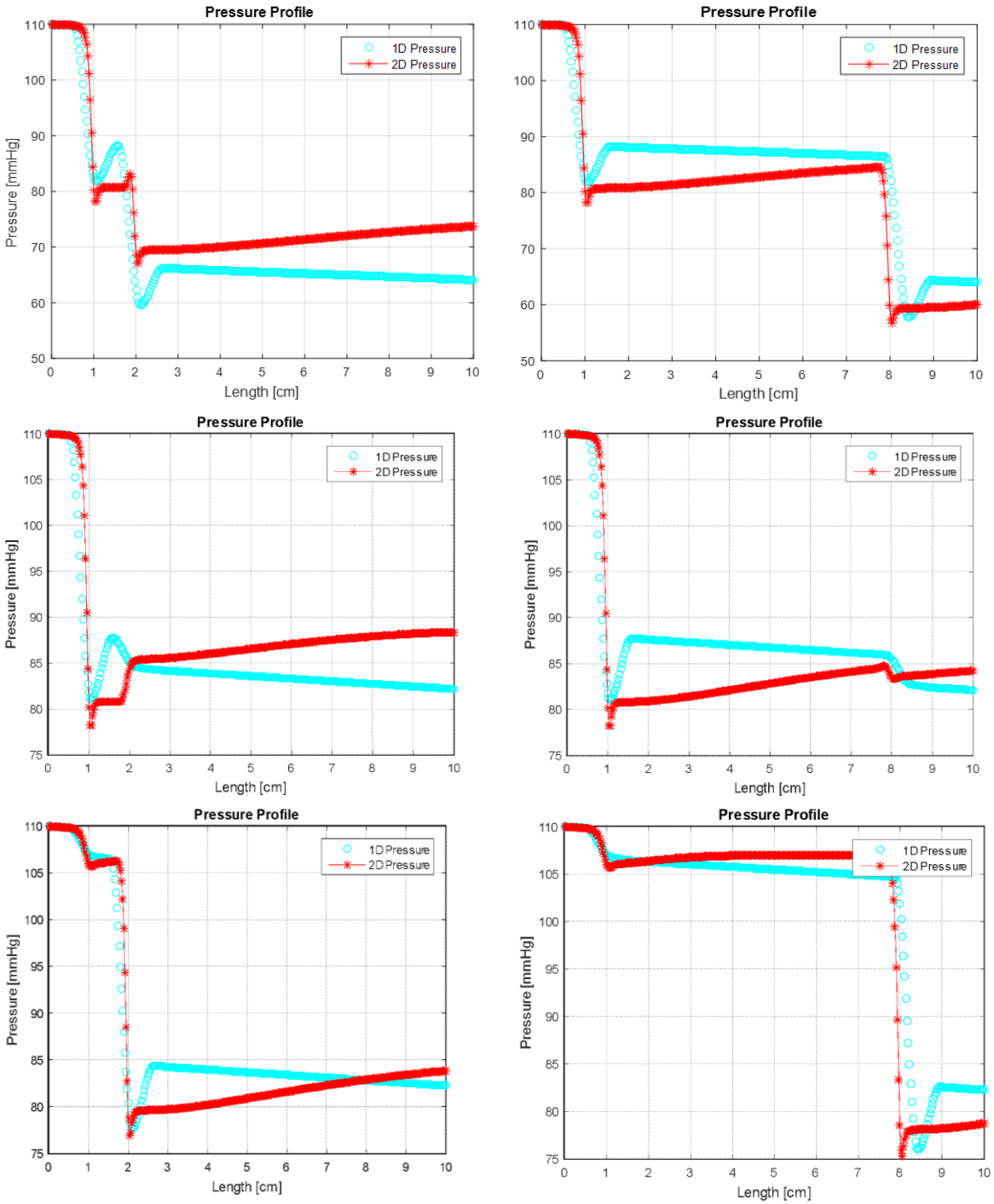

Figure 3.33: 1D vs 2D model comparison for Pressure vs Length for different double stenosis geometries.

In Figure 3.33 it is possible to notice the differences between the computations of the pressure profiles for different geometries. The 1D is capable of collecting the pressure drop at the right locations (minimum radii) however there is no sign of pressure recovery after the lesion in any of the plots. In fact, although 1D models are less computational expensive than 2D models, their drawback resides in the lack of accuracy where recirculation of flow may occur. It is also possible to notice how the pressure drop in the 1D model is following a linear decay just after

the lesion (Poiseuille pressure drop), whilst 2D models are still in pressure recovery mode. In Figure 3.40 it is shown a full comparison of the three different methods for the pressure drop computations. It can be notice that the Bernoulli computation of ΔP is overestimated in the majority of the cases.

Figure 3.34: Bernoulli vs 1D vs 2D pressure drops for 52 double stenosis cases.

3.6 Generation of the ROM with double lesion

In this section a generation of a ROM in a straight tube with double lesion is presented. This study is different from section 3.4, the former was characterised by two stenoses where the first one was kept fixed, varying the interspace distance with the second stenosis. The two stenoses had a fixed radius reduction as well.

ROM Off-line step

In this case, every geometry within the dataset is parameterised by six parameters which are: mass-flow rate, two parameters describing the radii reduction of the two stenosis (1 parameter each), two parameters for the location of the two stenosis along the axial direction and the last parameter is the length of the tube. The difference between the two stenosis locations along a single coronary domain is defined as distance. The aim is to build a ROM capable of describing the pressure profile along the centreline of the straight tube for every parameterised simulation.

As already presented in section 3.3 the 2D model is coupled with a 0D model describing the microvasculature downstream resistance.

A total of 3663 geometries have been considered to produce Table 3.6 and Figure 3.35.

Table 3.5: Summary of the dataset for ROM construction.

Dataset	# of geometries	$\boldsymbol{R_{mc}}$ value	ROM
1	$[1 : 1221]$	$50mmHg * \frac{s}{ml}$	ROM with (*Severity1, Severity2, Q, Location S1, Location S2, Length*)
2	$[1222 : 2442]$	$70mmHg * \frac{s}{ml}$	
3	$[2443 : 3663]$	$90mmHg * \frac{s}{ml}$	

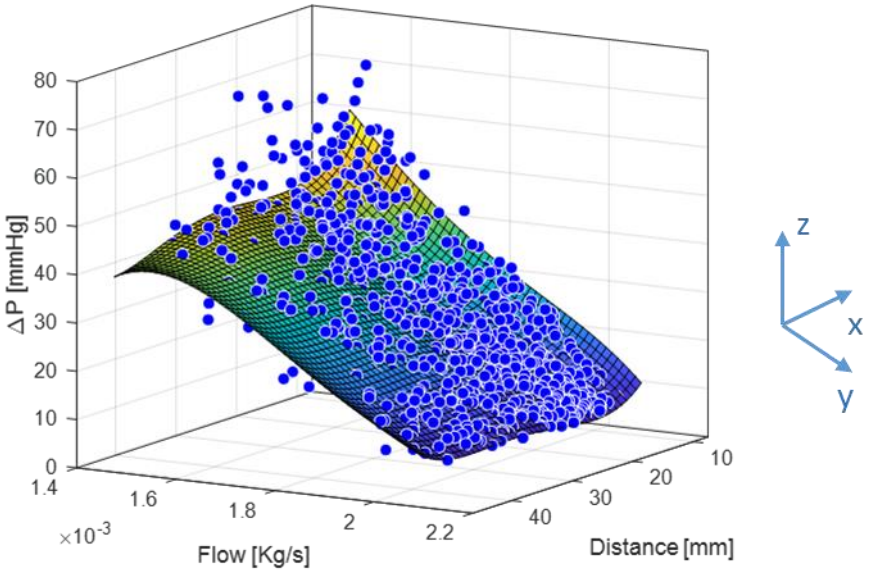

Figure 3.35: Pressure gradient as a variable dependent by Flow (mass-flow inlet) and Distance (distance between the two stenosis along a coronary domain).
Blue dots represent the pressure drop of the 3663 geometries used to train the ROM. Higher flows will produce a lower pressure drop.

In Figure 3.35 the *x*-axis represents the distance in *mm* between the two stenosis in series (interspace distance); the *y*-axis represents the mass-flow inlet used as boundary conditions for the different geometries. The fluid flow has been computed with the Eq. 3.4 starting with a distal resistance and the values of the two radii (inlet and min radius of the two stenosis). However, we would expect high values of pressure drop for high inlet mass flow rates, this is not true in this example since the mass flow rate has been computed to be inversely proportional to the min radius of the stenosis ($Q\ \alpha \frac{1}{r_{min}}$) . Mild stenosis will have a higher flow, but they will not be affected by a high pressure drop (bottom part of the graph). On the contrary, very severe stenosis will be characterised by a low value of mass flow inlet but they will be affected by a higher pressure drop (top part of the 3D scatter plot).

Figure 3.36 is showing the quadratic relationship between the severity of the stenosis and the computed correspondent flow. For very mild stenosis $0.5 \leq \lambda_1, \lambda_2 \leq 0.65$ the computed mass-flows have higher values than severe stenosis; this is still in accordance with Eq. 3.4.

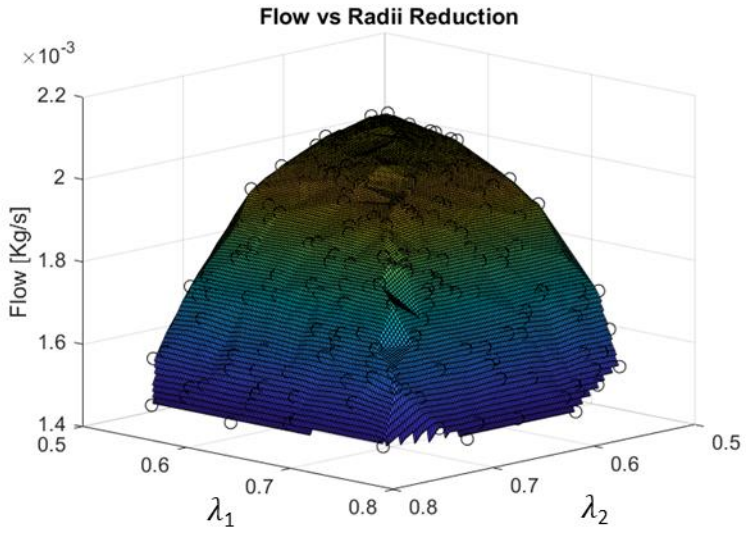

Figure 3.36: Flow dependency (z-axis) by the two stenosis severities (x and y-axis). Mild stenosis produce higher mass-flow inlet (top surface of the cupola red/yellow). Severe stenosis produce low values of mass-flows (blue part of the surface).

The Bernoulli ΔP has been computed in two ways: firstly, considering the average velocity of the fluid flow and secondly considering the maximum velocities (with CFD) which occur along the centreline. It is noted that a diagnostic work flow based on direct Bernoulli computations from clinical velocity measurements are difficult in the coronaries because the measurement of the velocity of the blood within the coronaries is not an easy task. One method uses a Doppler wire introduced into the coronary artery, but the results are often difficult to interpret [13], [61], [108]–[110]. In other vessels the velocities are often measured using an external Doppler probe but this is not generally practicable in the coronaries.

In case the velocity is known through the Doppler probe, the Bernoulli pressure drop using the velocity data can be written as:

$$\Delta P_{Bernoulli\,max} = \frac{1}{2}\rho(v_{sten1}^2 - v_{inlet1}^2 + v_{sten2}^2 - v_{inlet2}^2) \qquad \text{(Eq.3.12)}$$

where $v_{sten1}$and v_{sten2} are the measured maximum velocities at the location of the two stenosis, v_{inlet1} and v_{inlet2} are the velocities measured at the two inlet locations. However, for the numerical values of v_{sten1} and v_{sten2} the two peaks velocities computed with CFD had been used.

ROM On-line step (Validation)

The built ROM with 5 modes had been validated with 51 geometries described by a completely new set of parameters which were not been used for the off-line mode during the training

process. Results of the pressure profiles along the centreline (Figure 3.37) and a comparison between Bernoulli, 2D CFD and ROM ΔP are shown with Bland-Altman graphs.

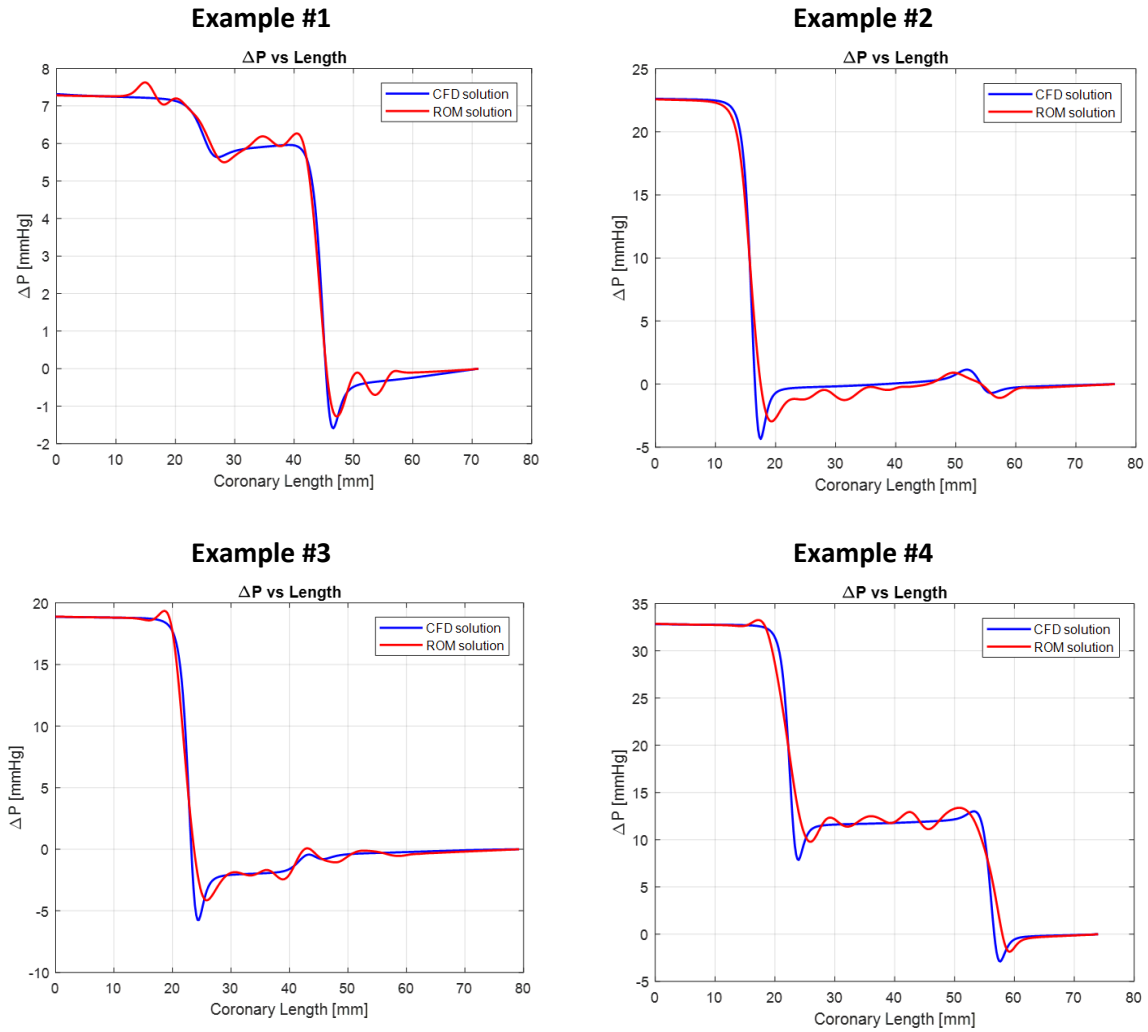

Figure 3.37: Comparison of pressure profiles for different geometries for the validation step (4 examples out of 51 geometries), computed with CFD and ROM with 5 modes.
For all the examples blue lines correspond to the full CFD pressure profile whilst red lines correspond to pressure profiles recomputed using the ROM.

As it can be seen from Figure 3.37 the overall pressure profiles are well captured, the ROM tends to under estimate the pressure drop caused by the major stenosis. Furthermore, the ROM solutions are not very smooth; the number of modes chosen for building the ROM (5 modes) is causing this effect. Increasing the number of modes will cause the ROM solution to converge to the CFD solution (this is proven in chapter 4). However, the pressure drops are perfectly captured with an excellent correlation for the vFFR computed with CFD and the vFFR computed with the ROM (Figure 3.44).

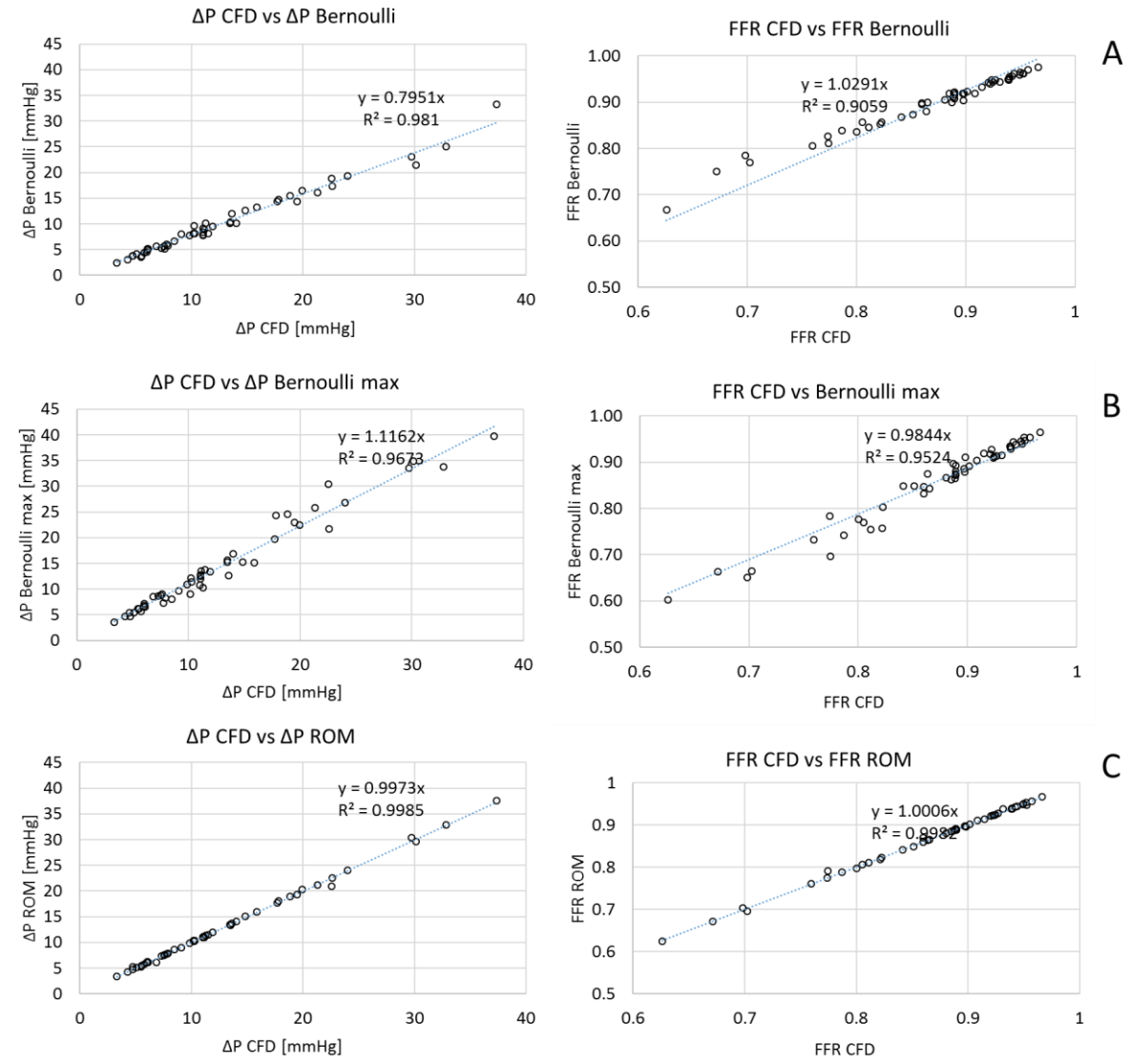

Figure 3.38: Correlation of pressure drops and FFR with the different methods. Full CFD vs Bernoulli (top), full CFD vs Bernoulli max, full CFD vs ROM

As expected, looking at the correlation plots for the overall pressure drops and the computed vFFRs, it is possible to notice the major accuracy of the ROM against the Bernoulli computation using the average velocities and the maximum velocities at the stenosis locations. For the Bernoulli computation a high correlation has been obtained with values of $\Delta PBern \leq 20\ mmHg$ and $\Delta PBern_{max} \leq 10\ mmHg$. Regarding the vFFR values, high correlations are obtained for $vFFR \geq 0.8$ for Bernoulli and $vFFR \geq 0.9$ for Bernoulli$_{max}$. However, for high values of ΔP (or for low values of $vFFR$) the two Bernoulli formulations produce a high error considering the results computed with CFD. The ROM computation of the $vFFR$ is high accurate with a value of $R^2 = 0.9985$.

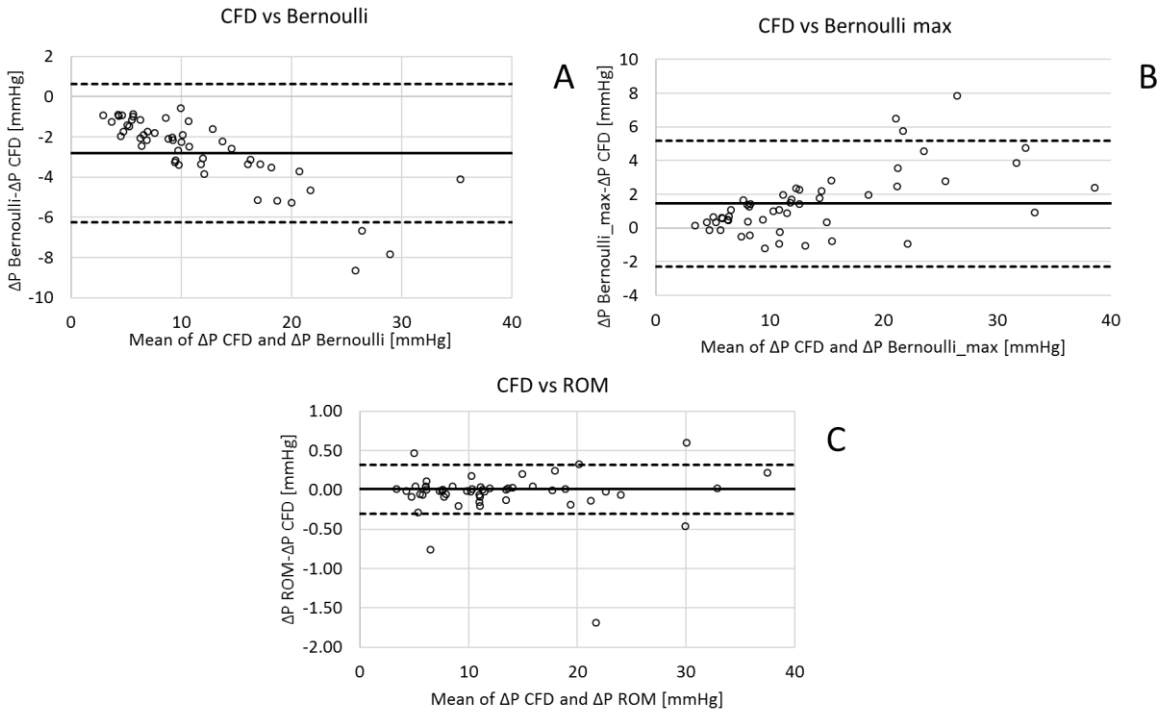

Figure 3.39: Bland-Altman plots for the three different methods on the double stenosis interactions. Top Left) Pressure drop with CFD vs Bernoulli for the 51 validated geometries. Top Right) Pressure drop CFD vs Bernoulli (using maximum velocities). Bottom) Pressure drop CFD vs ROM for the 51 validated geometries.

3.7 Conclusions

In this chapter the ingredients and the process to build a reduced order method have been presented. The mathematical formulations of the projection and the interpolation errors have been described. Multiple ROMs have been built: a ROM described by two input parameters with a single stenosis, and a ROM described by six input parameters with two multiple lesions in series. In order to establish a first estimation of the mass-flow rate for the inlet boundary, the 2D model was coupled with a simple zero-dimensional (lumped parameter) model. The pressure profiles along the centreline for idealised geometries were studied with full 2D CFD axisymmetric simulations, ROM computation and a 1D model. Furthermore, pressure drops and FFR have been computed with the former models and compared with Bernoulli pressure drops. We found that the ROM computation achieved a better accuracy than the Bernoulli computation and the 1D model regarding the pressure drop and the pressure profile for both the single stenosis and the double stenosis geometries. A second study was based on the fluid flow interactions between multiple stenosis in series. It was found that two stenoses are not haemodynamically interfering if there is a large interspace distance between the two.

Furthermore, the total pressure drop computed with CFD considering large interspace distances between the stenoses is compatible with a Bernoulli approximation.

Chapter 4

Shape parameterisation and Reduced Order Method in 2D patient-specific coronary geometries

In the last few decades, invasive and non-invasive clinical imaging techniques have grown constantly. These techniques support the creation of a visual representation of the interior of the human body for clinical analysis and clinical decision making. There is an increasing interest in the use of personalised models of physiology, based on faithful representation of individual anatomy coupled with appropriate description of the boundary conditions, for the diagnosis of disease and for interventional planning [13].

Computational meshes for individual anatomies can be generated from segmented volume representations [111], but for the effective study of the influence of geometrical/anatomical variations it is necessary to find accurate and robust techniques for shape parameterisation. Different studies have been made for shape parameterisation in CFD. These are mainly focused on the parameterisation of the geometry for design optimisation purposes [112], [113], [114]. These techniques are heavily used in CFD studies; an example is the shape optimisation of an airfoil for an aircraft [113], [115], but they are also used in naval engineering and the automotive industry [112], [116]. The goal of the optimiser is to deform the mesh in order to minimise a pre-defined objective (cost) function.

ANSYS Fluent offers such a tool for shape optimisation, based on the usage of control points of a Bernstein polynomial approximation [117]. This method suffers some restrictions for coronary application, partly associated with difficulties of appropriate positioning of the control points and partly because the process supports only relatively small displacements which do not immediately lend themselves to the capture of the anatomical variations of tightly-stenosed coronary arteries.

Several studies of shape parameterisation have been performed for cardiovascular applications, especially for coronary stents or for coronary by-pass [118]–[122]. Furthermore, some shape parameterisation studies include ROM analyses [121], [123]–[130].

In this chapter, shape parameterisation approaches are not used for optimisation purposes but they are deployed in order to extract geometrical parameters which will feed the ROM. There are several possibilities to define the parametric model; however, in this chapter, we present different methods for shape parameterisation of coronary arteries. Furthermore, the methods could be used for any kind of shape analyses or shape optimisation. The analysis will be computed on a clinical dataset of coronary geometries previously segmented using the Philips 3DCA software tool or the 3D reconstruction tool initiated and described in chapter 2 of this thesis, and subsequently further developed by other researchers in the Department.

Parameterising coronary geometries is a necessary step for the computation of the parameterised ROMs [96], [131], [132], [133]. A challenge is that each extra geometrical parameter causes the increase of the dimension of the problem space for the system, and this can rapidly become prohibitive in terms of the characterisation of the solution space. In this chapter the number of parameters required to effectively describe the range of anatomies in the clinical dataset, and subsequently the pressure distribution and computed FFR, is investigated. The number of real anatomies in the clinical dataset is restricted, and it is used primarily to ensure that the anatomies that have been measured are adequately represented. The training set for the ROM is larger, and a synthetic dataset is constructed within the parameter space.

4.1 Shape parametrisation of 2D coronary geometries: features and goals

The features and goals of the shape analysis are presented in this section. Before starting it is important to give a definition of what is meant by coronary shape. Tortuosity, dilatation, curvature, diameter, stenosis, are all parameters that have been used in recent studies to define the shape of coronary geometries [134]. The number of parameters is potentially large, and one of the challenges is to identify a subset that can adequately describe the most important features of the artery in the context of the determination of FFR.

Three different classes of global basis functions for parameterising the coronary shapes have been considered in this thesis: polynomial, Gaussian and Fourier basis functions. These three approaches will be studied in terms of accuracy and flexibility. By accuracy we mean the description of the overall error between original geometry and the approximated geometry, but also the capability of the parameterisation method to maintain unaltered the fields of interest (particularly the variation of pressure along the vessel centreline) when CFD is computed. By flexibility we mean that the parameterisation functions have to be able to describe a wide range of shapes, and they have to be easy to manage and sufficiently concise in order not to make the ROM unfeasible. In summary, the aims of this chapter are:

- Approximation of the shape of the available clinical dataset in order to extract the coronaries geometrical parameters,
- To use a limited number of parameters, the extracted geometrical features have to describe “well” the clinical shapes in order to maintain unaltered the pressure profile along the centreline,
- Use of the extracted geometrical parameters to create a larger phantom dataset for the clinical ROM training dataset;

The number of parameters to describe the approximation of the radius along the length have to be limited in order not to make the building process of the ROM impractical.

4.2 Data Pre-processing

Because the fluid flow is primarily a tube flow, it is likely that the primary determinant of the distribution of pressure along the vessel axis is the variation of radius along it. For this reason, the focus of the first ROM, evaluated in this chapter, is based on a 2D axisymmetric model.
Furthermore some data cleaning has been performed. The available clinical dataset to perform shape analyses consists of 156 3D geometries; however, few of the patient-specific cases were very short or very long, largely deviating from the mean value of coronary length of the dataset. It had been decided to remove these geometries; the purpose is to ensure that the built ROM is most effective for the majority of the dataset. After the cleaning process the dataset is formed by 140 geometries.

Since the aim is to compute a 2D clinical ROM starting from straight tubes, and moreover the available clinical geometries are in 3D, the centreline of every case had been considered and virtually stretched in order to compute a straight line. The total length of every coronary has been computed summing all the distances in the 3D space of the 3D consecutive points. The total vessel length can be computed with the following formula:

$$Vessel\ Length = \sum_{I=1}^{N-1} \sqrt{\sum_{i=1}^{n} \left(\boldsymbol{x}_{i,I+1} - \boldsymbol{x}_{i,I}\right)^2} \qquad \text{(Eq.4.1)}$$

where *N* is the total number of points along the centreline, n is the space dimension and *I* is the considered *Ith* point. From the graph below it is possible to notice that the clinical dataset is forming a cluster between $40\ [mm] < Coronary\ Total\ Length < 120\ [mm]$. This is to justify that the considered ROMs and the synthetic dataset have been computed considering the graph below (Figure 4.1).

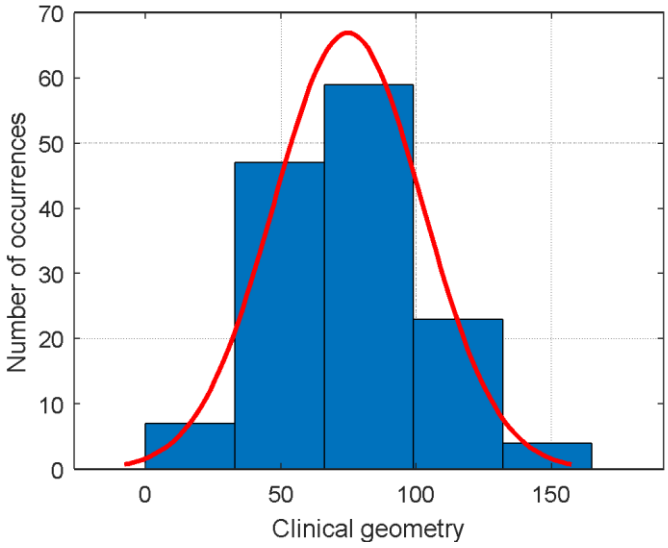

Figure 4.1: Number of occurrences vs Clinical geometry vessel length in [mm].

4.3 Approximation of the radius along the length in 2D patient specific axisymmetric coronary model

In the last decade there has been significant progress on the application of ROM methods to applications in fluid dynamics [59], [131], [137]. However, issues remain when considering ROMs which include turbulent flow or geometrical parameters [116].

The main aim of this section is to study the different examples of shape parameterisation capable of extracting the geometrical parameters for any coronary artery and to maintain unaltered the pressure profile along the centreline when considering clinical geometries and approximated geometries.

4.3.1 Approximation of 2D coronary shape

In a 2D coronary axisymmetric model the variation of the radius along the length can be generally expressed with the following form:

$$r(x) = \sum_{p=1}^{N_P} P_p(x) + \sum_{g=1}^{N_g} G_g(x) + \sum_{i=1}^{N_f} F_i(x) \qquad \text{(Eq.4.2)}$$

Where on the right hand side of the equation the first term represents a combination of polynomial basis functions (P_p), the second term represents Gaussian basis function (G_g) and the last term represents Fourier basis function (F_i). N_P, N_g and N_f are based on the integer

number of polynomial, Gaussian and Fourier basis functions considered to approximate the radius variation.

The goal in this section is to approximate a continuous function *f(x)* defined in an interval [a,b] using a linear combination of a set of global basis functions [138]. Let W be a function space spanned by a set of basis functions $\phi_1, \ldots, \phi_N$, so:

$$W = span\{\phi_1, \ldots, \phi_N\},$$

Every continuous function $f \epsilon W$ can be expressed as a linear combination of global basis functions. By global basis function we mean a function which in general is nonzero on the entire domain. These global basis functions have to be able to approximate the original function along the entire domain.

Each one of the former class of bases functions (Polynomials, Gaussians and Fourier) can be employed to fit any shape; they are competing candidate representations to approximate a function. Furthermore, one might use a combination of different classes, e.g. a finite number of polynomial bases plus a finite number of Gaussian bases.

However, polynomials, Fourier bases and Gaussians have all different properties and in the next section we investigate what are the most suitable candidates to approximate the radius variation along the length for coronary arteries.

Results of the shape parameterisations presented in the next sections have been obtained following an optimisation methods of the parameters which describe the different shapes.

Furthermore, to achieve even better performance in accuracy we have computed a weighted cost function to be optimised.

4.3.2 Introducing a weighted cost function

The most pressure drop considering a coronary artery occurs when the fluid flow encounters a stenosis; very small variations in the description of the minimum radius by the approximated geometries can produce a completely different pressure profile. If the minimum radius of the coronary shape is not captured adequately, the spatial pressure variation error can be big. In order to reduce the error between the clinical CFD pressure profile and the pressure profile computed with the approximated geometry, an optimisation process has been employed. The problem of solving this geometrical optimisation can be thought of as finding the set of parameters and basis functions that best describe the variation of the radius along the length in 2D geometrical models. It is unlikely that any combination of these geometrical parameters will return the clinical original shape, so the problem is to determine the optimum set or combination of shape parameters which minimises the error computed between the original

shape and the parameterised shape. This minimisation problem falls in the optimisation method algorithm. In brief an optimisation method is mainly composed of two parts: the definition of the cost function and the choice of the algorithm employed to minimise it between the two shapes.

When performing an optimisation process it is necessary to specify a cost function. The root mean squared error is commonly used for this purpose and it is also a useful measure of the quality of the prediction:

$$RMS_{er} = \sqrt{\frac{\sum_{t=1}^{n}\left(y_{coronary} - y_{optim}\right)^2}{n}} \qquad \text{(Eq.4.3)}$$

where $y_{coronary}$ is the real value of the function (physiological coronary radius) and y_{optim} is the optimised value from the optimisation. However, if the simple root mean square formula is considered, it can be seen that it does not give special consideration to any pair of differences, all the differences have the same weight. Moreover, the optimal shape fitting using the simple cost function in Eq. 4.2 may lead to very large fitting errors when considering the overall coronary shape and more important very large errors for global minimum values on the minimum radii of the coronary occlusions.

We therefore need to find a compromise in fitting the overall coronary shape, while keeping the minimum radius, the inlet and the outlet radius of the target geometry as close as possible to the real values. In order to resolve this issue, the cost function has to be modified to give extra weight to match the geometrical constraints (inlet, minimum radius, outlet).

The cost function, f_{cost} which has been chosen for the optimisation process represents a linear combination of the root mean square error over the whole geometry, the error at the inlet, the error at the global minimum radius and the error at the outlet.

$$\begin{aligned} f_{cost} = {} & C_{RMS} RMS\left(y_{optim}(t), y_{coronary}(t)\right) \\ & + C_{stenos}\left(\left|\min\left(y_{optim}(t) - \min\left(y_{coronary}\right)\right)\right|\right) \\ & + C_{inlet}\left(\left|\text{inlet}\left(y_{optim}(t) - \text{inlet}\left(y_{coronary}\right)\right)\right|\right. \\ & + C_{outlet}\left(\left|\text{outlet}\left(y_{optim}(t) - outlet\left(y_{coronary}\right)\right)\right|\right. \end{aligned} \qquad \text{(Eq.4.4)}$$

where C_{RMS}, C_{stenos}, C_{inlet} and C_{outlet} are multiplication constants or weights for the cost function, defined as proportion:

$$C_{RMS} + C_{stenos} + C_{inlet} + C_{outlet} = 1 \qquad \text{(Eq.4.5)}$$

There is no optimal way in which to assign the relative weightings: it is a matter of human judgement as to which combination produces the optimal balance of fitting the coronary shapes. Different values of C_{RMS}, C_{Stenos}, C_{inlet} and C_{outlet} have been considered in previous sets of simulation where the aim was to find the best combination of parameters which were best approximating the radius variation for the different clinical geometries. Based on a trial and error process, the values chosen for processing the geometries were: $C_{RMS} = 0.7$, $C_{Stenos} = 0.2$, $C_{inlet} = 0.05$ and finally $C_{outlet} = 0.05$.

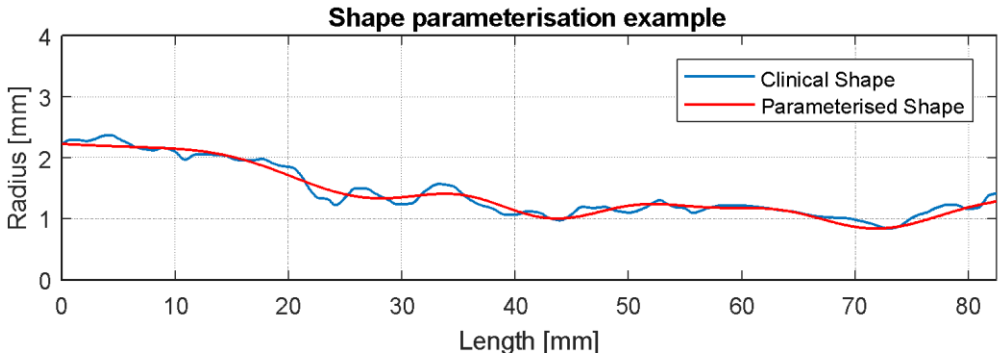

Figure 4.2: An example of parameterised shape using the weighted cost function. Clinical radius variation along the length (blue line), parameterised and optimised shape (red line).

4.3.2.1 Genetic Algorithm and fminsearch

Solving a weighted optimisation problem is strictly necessary because a small error in describing the minimum stenosis along the coronary shape, could lead to large error in the computation of the pressure profile and then to a wrong value of the FFR. An example is shown in Figure 4.4 and Figure 4.5 where it is presented a 2D axisymmetric clinical case; the difference in the description of the stenosis is minimal between the clinical shape and the optimised one (not with weights). However, there is not much correspondence on the two pressure profiles where is possible to notice a large error (Figure 4.6).

In order to find the optimal parameters which minimise the cost function, a Genetic Algorithm and *fminsearch* optimisation techniques had been used. Firstly, a GA had been employed in order to find good candidates for the *fminsearch* process.

Genetic Algorithm is an optimisation technique used to solve non-linear or non-differentiable optimisation problems. They use concepts from evolutionary biology to search for a global minimum. GA work by starting with an initial generation of candidate solutions which are tested against the objective function. Then, subsequent generations evolve from the first generation through selection, crossover and mutation. The process behind the GA is:

$$\min f(\boldsymbol{x})$$

$$\xrightarrow{mutate} guess\ \boldsymbol{x}_j\ \ for\ j = 1,2,3,\dots,m$$

$$keep\ "best"\ \boldsymbol{x}_j\ \ for\ j = 1,2,3,\dots,p$$

$$discard\ \boldsymbol{x}_j\ \ for\ j = p+1, p+2,\dots,m$$

The output of the GA optimisation process is a set of optimal parameters which minimise the *f* function. The parameters computed from the GA optimisation are used as first guess for the *fminsearch* algorithm (Figure 4.3).

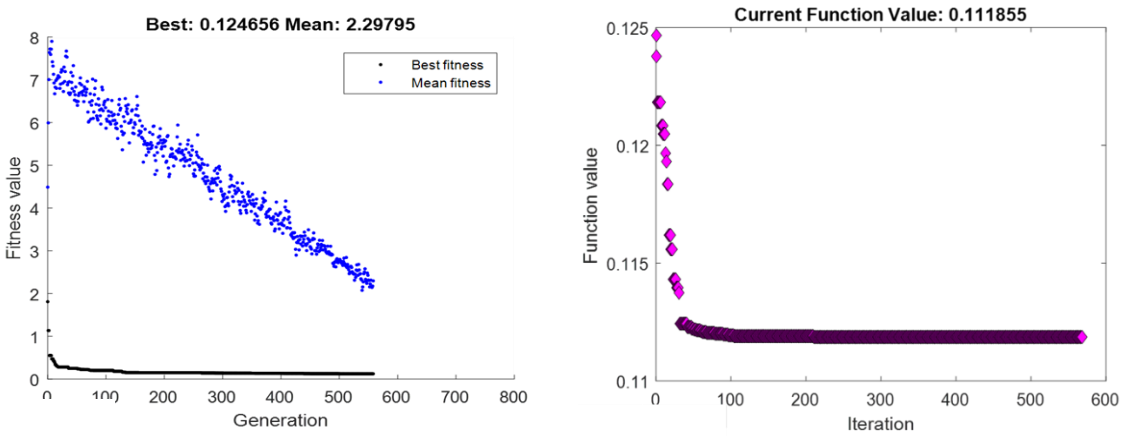

Figure 4.3: Left panel) GA plot for first guess of the parameters. Right panel) fminsearch process to find best parameters in the 'optimal sense'.

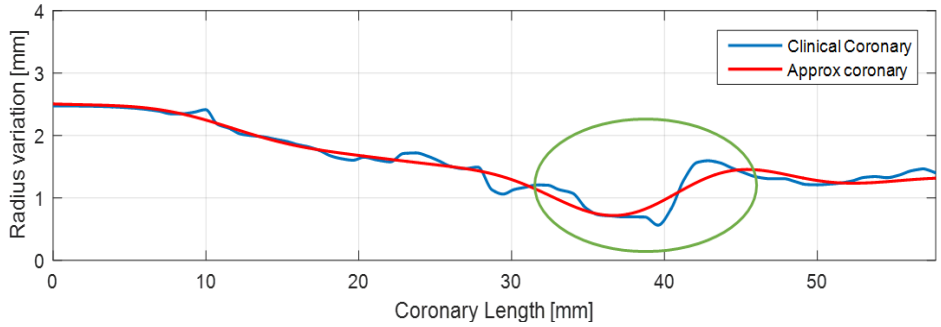

Figure 4.4: Example of coronary shape approximation.
The approximation is computed using standard L2 norm of the RMS error.

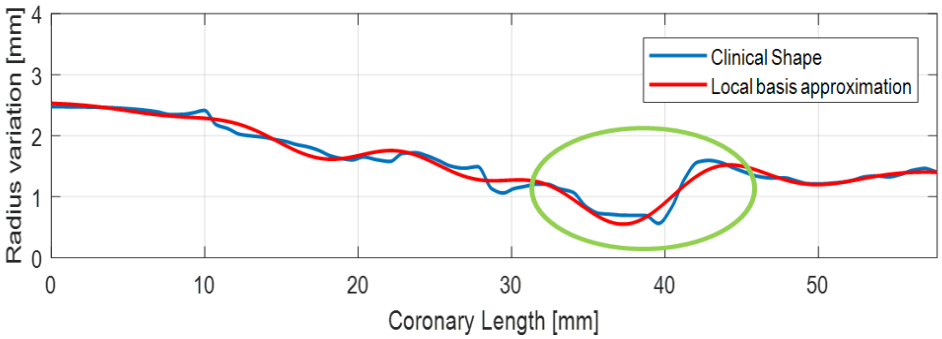

Figure 4.5: Example of coronary shape approximation.
The approximation is computed using L2 norm weighted cost function.

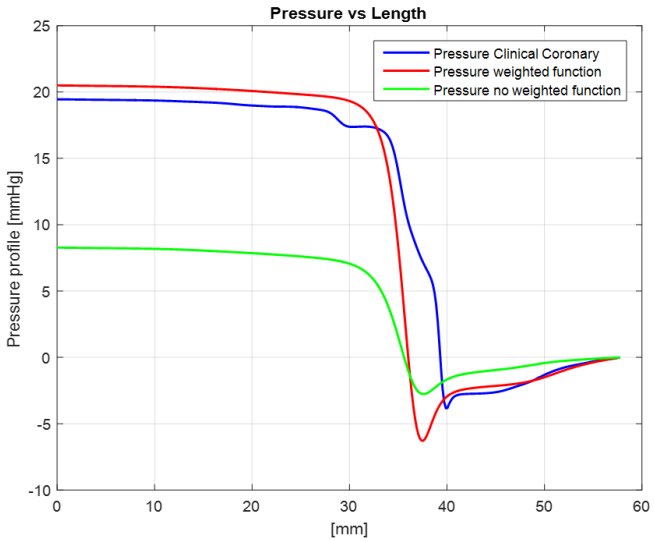

Figure 4.6: Pressure profiles for the three different geometries.
Blue line) Pressure profile for the clinical geometry. Green line) Pressure profile for the approximated geometry using the optimisation function with no weightings. Red line) Pressure profile for the approximated geometry using the weighted cost function.

4.3.3 Radius approximation with polynomial bases

The goal is to approximate a continuous function *f(x)*: [a,b] → R by a linear combination of polynomials [139]:

$$r(x) \approx \sum_{j=0}^{n} c_j \, \phi_j(x) \qquad \text{(Eq.4.6)}$$

where x ∈ [a,b], c_j are the basis coefficients and finally $\phi_j(x)$ are the basis functions which are polynomials of degree ≤ n.

Since radius reduction from inlet to outlet is a general feature of coronary arteries, a linear polynomial is an appropriate and efficient inclusion for capturing the linear taper. The taper is a specific form of first order global basis functions, as it shown in Figure 4.7. However, the polynomial representation is not usually appropriate to get a family of shapes that converge to the original shape as higher order terms are added.

In this thesis will be used for the radius variation a linear approximation plus a series of Gaussian or Fourier basis functions of the form:

$$r(x) \approx c_0 + c_1 x + \sum_{g=1}^{N_g} G_g(x) \qquad \text{(Eq.4.7)}$$

or:

$$r(x) \approx c_0 + c_1 x + \sum_{f=1}^{N_f} F_f(x) \qquad \text{(Eq.4.8)}$$

where $\phi_0(x) = 1$, and $\phi_1(x) = x$.

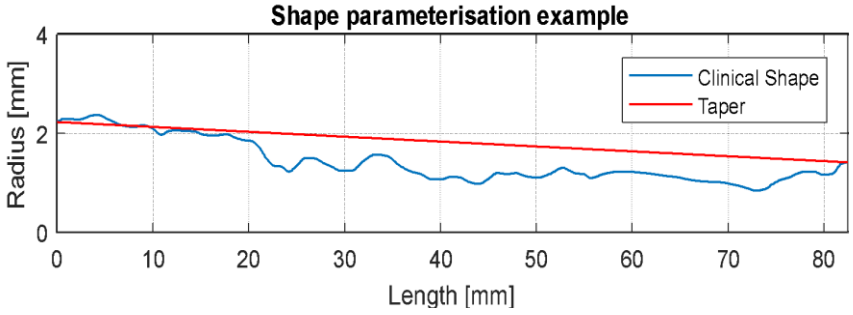

Figure 4.7: Example of taper on a clinical geometry.
Radius variation along the length (blue line), coronary taper (red line).

4.3.4 Approximation of the radius with Gaussian basis

The global basis functions chosen for the approximation are based on 1-D negative Gaussian curves. Gaussians basis are especially suited to the definition of local perturbations of the domain that diminish rapidly away from the locality, whilst global polynomial or Fourier series representations do not have this property.

In fact, for diseased coronaries it is reasonable to ask whether a series of basis functions that best capture local lesions, such as the Gaussians, produce more effective and efficient shape representations than the Fourier series. The function *f(x)* to approximate the radius has the form of linear taper plus a stenosis:

$$f(x) \approx \sum_{i=1}^{N} \phi_i + taper \qquad with\ i = 1,2,3 \ldots N \qquad \text{(Eq.4.9)}$$

where *N* is the number of global basis functions considered for the approximation and ϕ_i is the *ith* Gaussian basis function. Every Gaussian basis function considered in this section depends on three parameters:

$$\phi_i = f(A_i, \sigma_i, x_i) \qquad where\ i = 1 \ldots N \qquad \text{(Eq.4.10)}$$

where A_i describes the amplitude, σ_i represents the width and finally x_i describes the position where the Gaussian is centred for the ith basis considered (**Figure 4.8**).

The general form of the global basis function used is:

$$\phi_i = -A_i * C * exp\left(-\frac{(x - x_i)^2}{2\sigma_i^2}\right) \qquad \text{(Eq.4.11)}$$

The basis functions are all normalised to the length of the vessel, so that every basis is evaluated on the interval $0 \leq x \leq 1$. The C parameter is a constant value which has been used for initialisation of the Gaussian. The whole function $f(x)$ is then approximated using a finite number N of Gaussian global basis functions plus a taper which is collecting the radius reduction between inlet and outlet introduced in the former section.

Different combinations for the C and the σ values have been tried for the GA algorithm; after trial and error the Gaussian basis function is initialised with the following values; $C = 0.75$, $\sigma = 0.05$ (Figure 4.8).

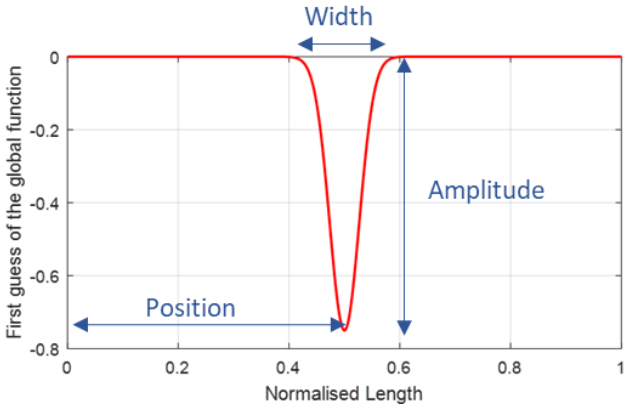

Figure 4.8: Initialisation of the Gaussian basis function with three parameters (Amplitude, width and position).
The three parameters are free to vary accordingly with the optimisation algorithm

Approximation with one global basis function

For N=1 in Eq. 4.9 (only one basis function), the three geometrical parameters are: A_1, x_1 and σ_1. Using the optimisation process introduced in section. 4.3.2 it is possible to compute the best combination of the three parameters which minimises the error between the patient specific coronary shape and the approximated geometry (see Fig 4.9 for examples).

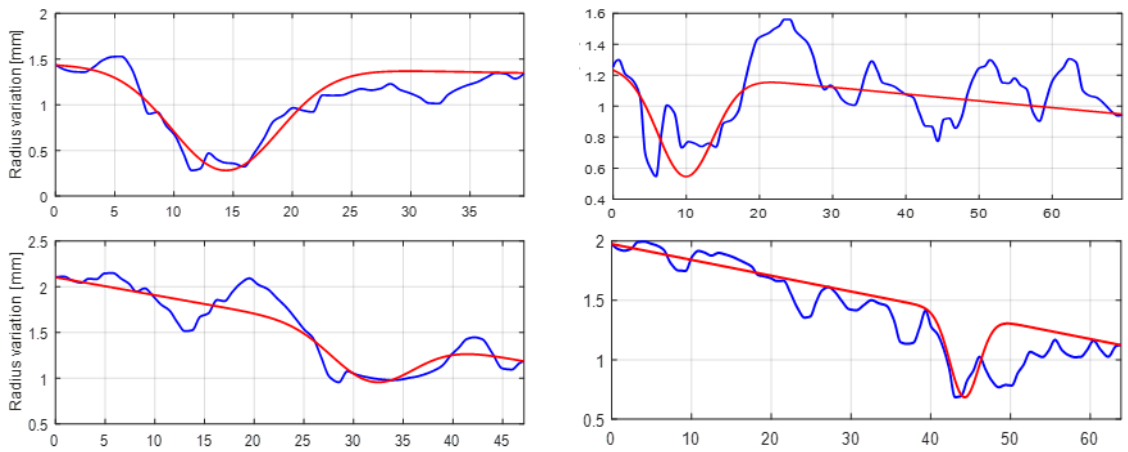

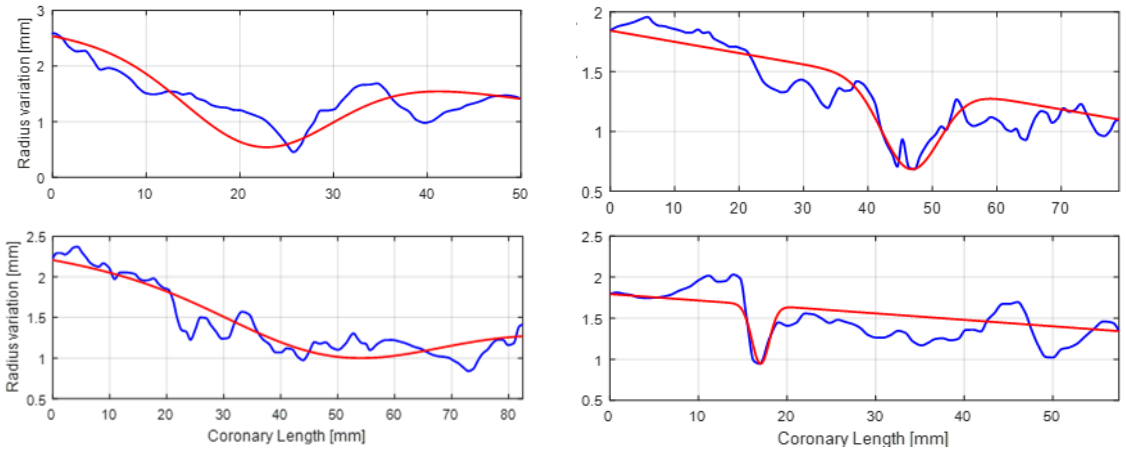

Figure 4.9: Example of clinical shapes approximated with one global basis function. Radius vs Length.

From Fig 4.9 it is possible to notice how the overall coronary shape is maintained. The function of the taper is clear; while the single Gaussian basis function is free to move along the domain and tries to catch the minimum radius and the overall stenosis shape. However, as expected when there are sharp changes for the radius variation along the length one basis function is not enough.

Approximation with two global basis functions

Fig 4.10 shows the approximation of clinical geometries, using two global basis functions, for a total of 6 parameters $(A_{1,2}, \sigma_{1,2}, x_{1,2})$. The global basis functions are described by $\phi_1(x)$ and $\phi_2(x)$ (Figure 4.10, Figure 4.11).

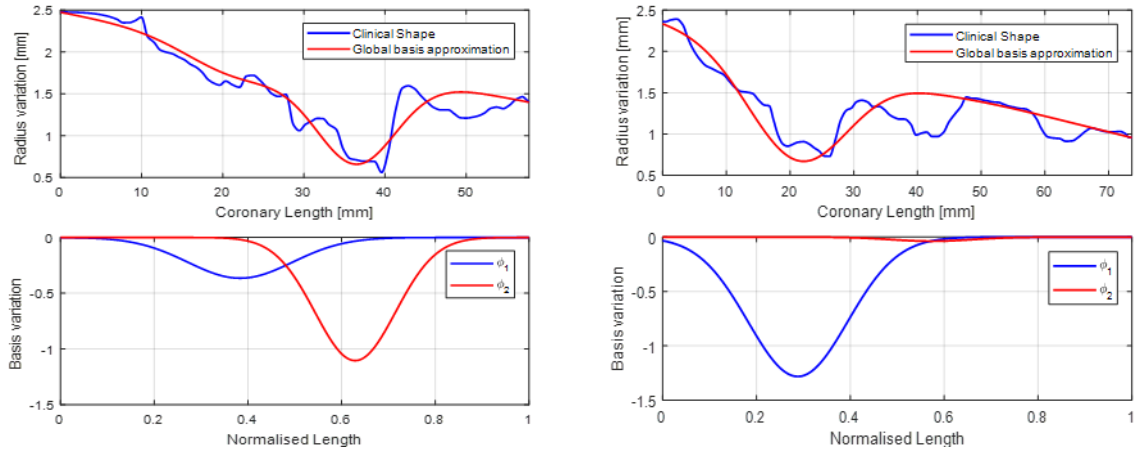

Figure 4.10: Example of clinical shapes approximated with two Gaussian basis functions. The two basis functions are shown on the bottom graph.

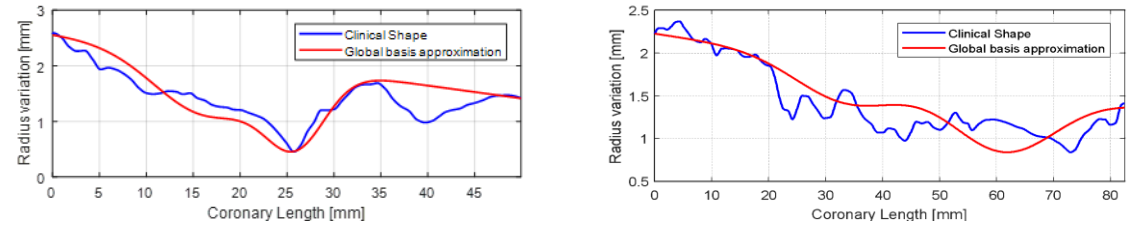

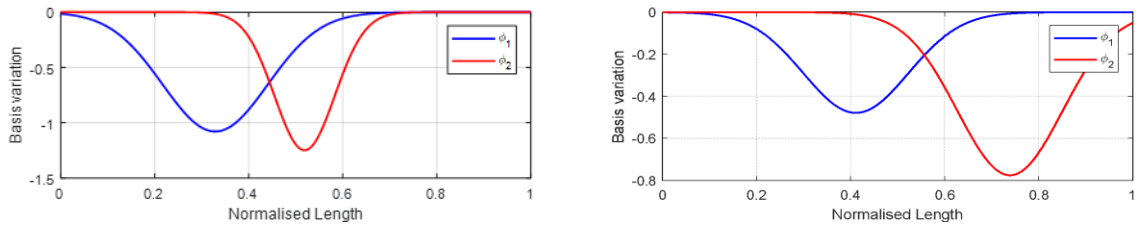

Figure 4.11: Example of clinical shapes approximated with two Gaussian basis functions. The two basis functions are shown on the bottom graph.

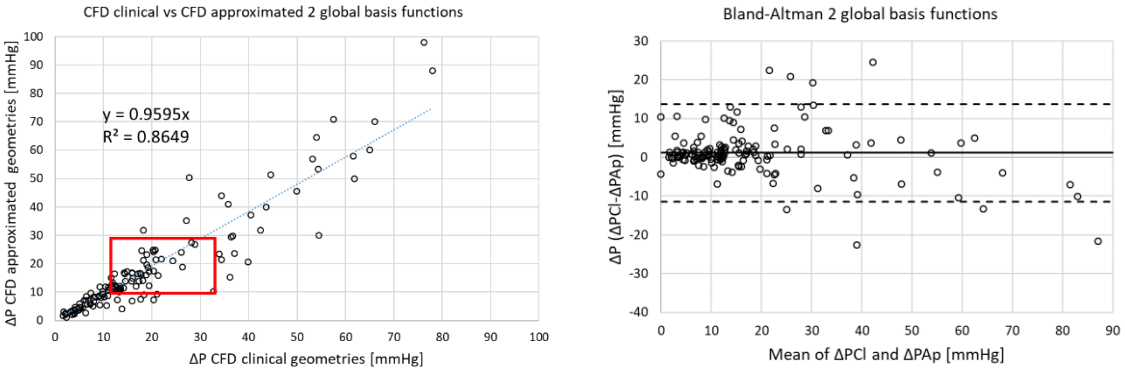

Figure 4.12: Left graphs) Correlation between clinical geometries and approximated geometries on the pressure drop computed with 2 Gaussian basis functions. Right graphs: Bland-Altman plots

From Figure 4.12 it can be noticed an improvement of the overall coronary shape using two global basis functions compared with only one. However, looking at the Bland-Altman graph (Figure 4.12) the CFD pressure drop computed on the clinical geometries and on the approximated geometries, it can be seen that the algorithm doesn't produce accurate results with an $R^2 = 0.86$ and a standard deviation equals to 12.52. Furthermore, data points in the ROI ($10\ mmHg < \Delta P < 30\ mmHg$) are fairly scattered.

Approximation with three global basis functions

Figure 4.13 shows the approximation of the clinical geometries, using three Gaussian basis functions, for a total of 9 parameters ($A_{1,2,3}, \sigma_{1,2,3}, x_{1,2,3}$). The global basis functions are described by $\phi_1(x)$, $\phi_2(x)$ and $\phi_3(x)$ (Figure 4.13).

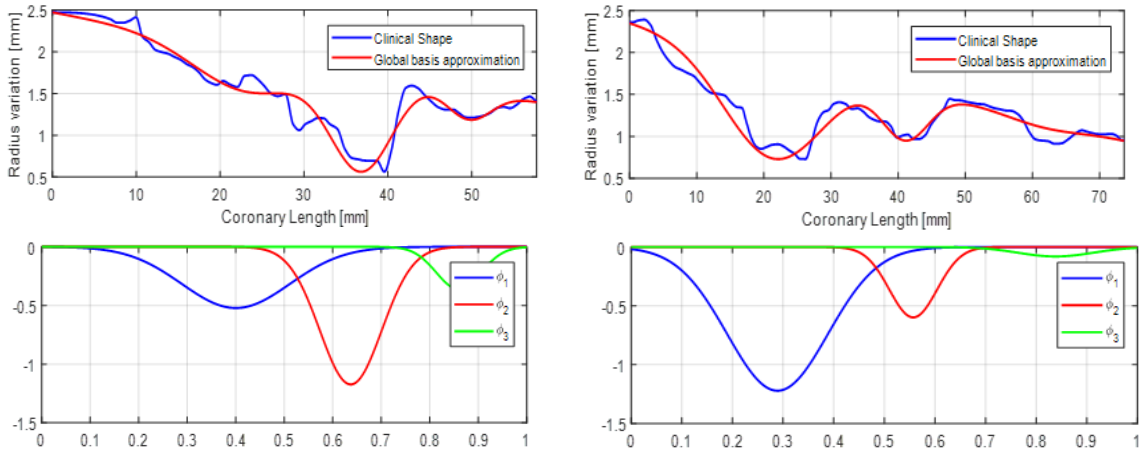

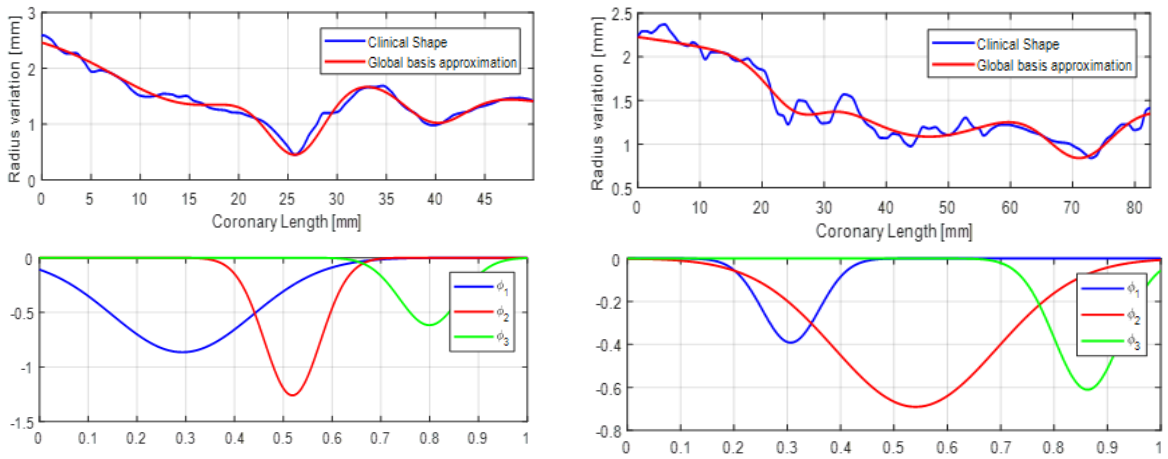

Figure 4.13: Example of clinical shapes approximated with three Gaussian basis functions. 1st and 3rd rows) Blue lines are representing the original clinical shapes whilst the red lines are the approximated clinical shapes with three basis functions. 2nd and 4th rows) Blue, red and green lines represent the three basis functions used to approximate the geometries.

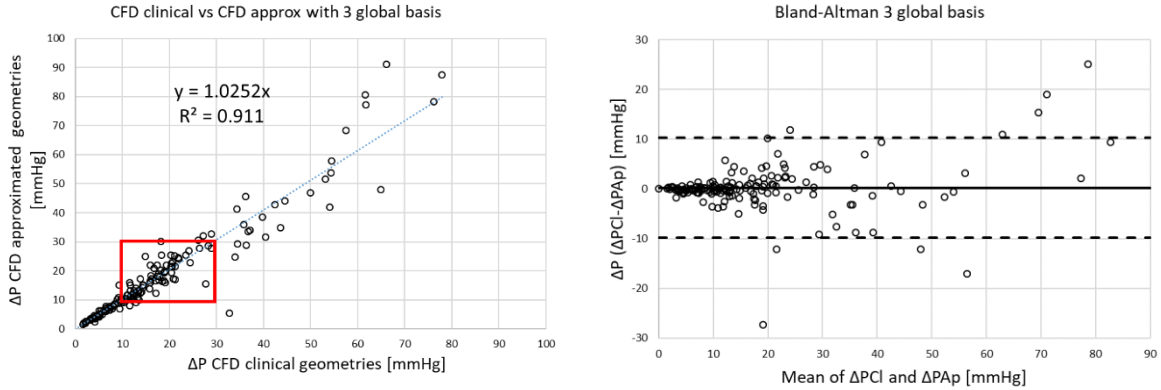

Figure 4.14: Left graphs) Correlation between clinical geometries and approximated geometries on the pressure drop computed with 3 Gaussian basis functions. Right graphs: Bland-Altman plots

As expected, increasing the number of Gaussian basis functions improve the overall correlation between the pressure drop computed on the clinical geometry and the approximated geometry. In fact, comparing the two plots (Figure 4.12 and Figure 4.14) the value of R^2 increased to 0.911 and a standard deviation of 5.10. However, it is possible to notice few outliers even for low values of pressure drop (Figure 4.14).

Furthermore, since the amplitude of the Gaussian basis functions is the most important parameter to collect, it is a reasonable choice to study the behaviour of the approximations considering only one parameter to optimise (amplitude), designing few localised Gaussian basis functions.

4.3.5 One parameter description for the Gaussian basis functions

Since the major pressure drop is caused by the minimum radius of the stenosis, differently from the previous section, it has been decided to approximate the coronary shapes with Gaussian basis functions depending only on the amplitude parameters. The values of the width and the location of the Gaussians had been kept constant:

$$\phi_i = f(A_i) \qquad where\ i = 1 \dots N \tag{Eq.4.12}$$

The normalised domain of the coronary artery has been divided into *N* sub-domains where each Gaussian is trying to approximate one of these sub-domains. Furthermore, the function *f(x)* has the form of:

$$f(x) \approx \sum_{i=1}^{N} \phi_i(x) + taper \tag{Eq.4.13}$$

where ϕ_i is the *ith* basis function described as:

$$\phi_i = -A_i * C * exp\left(-\frac{(x - x_i)^2}{2\sigma^2}\right) \tag{Eq.4.14}$$

An example of a whole initialisation Gaussian global basis family used to approximate the coronary shapes with fixed width and localised in sub-domains is shown in **Figure 4.15.**

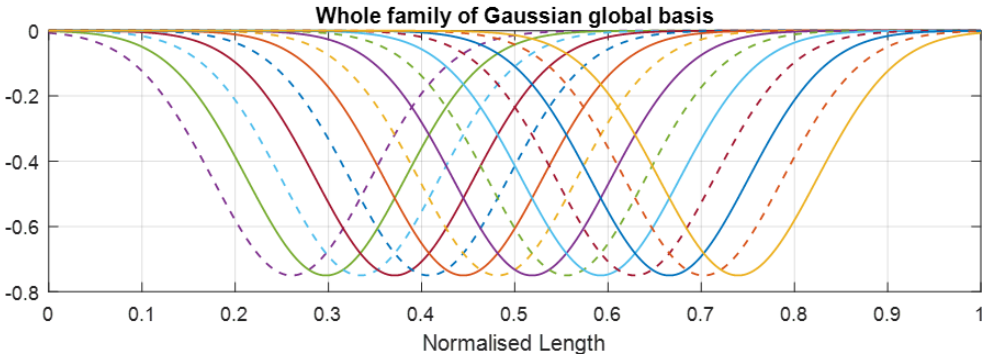

Figure 4.15: Whole family of basis functions. The different basis functions are defined locally along the domain.

Figure 4.16 and Figure 4.17 show the shape approximation using 8 and 19 Gaussian basis functions computed on the same clinical geometries in order to compare the results.

8 Gaussian basis functions approximation (1 parameter each)

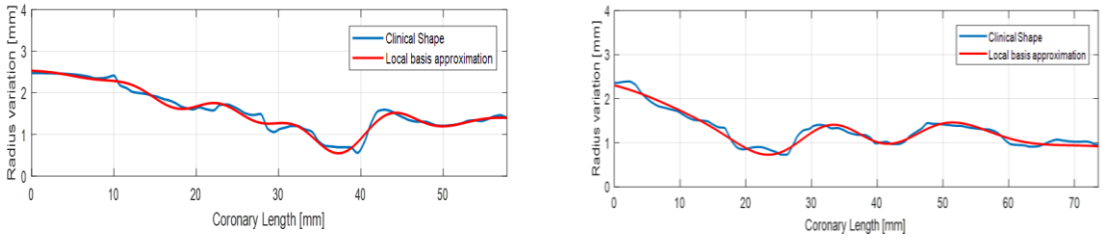

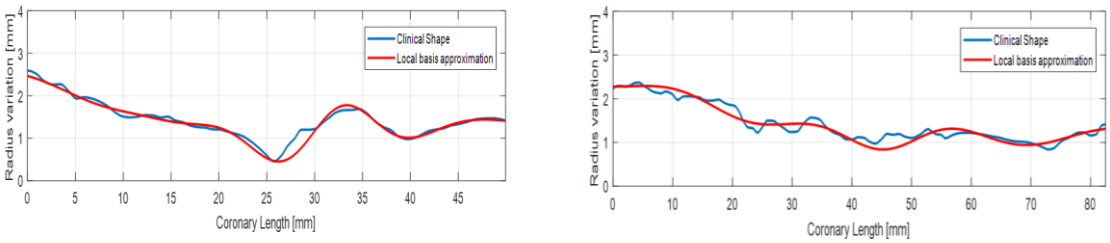

Figure 4.16: Approximation of clinical geometries with 8 global basis functions. Blue line) Clinical geometry. Red line) Approximated geometry.

19 Gaussian basis function approximation (1 parameter each)

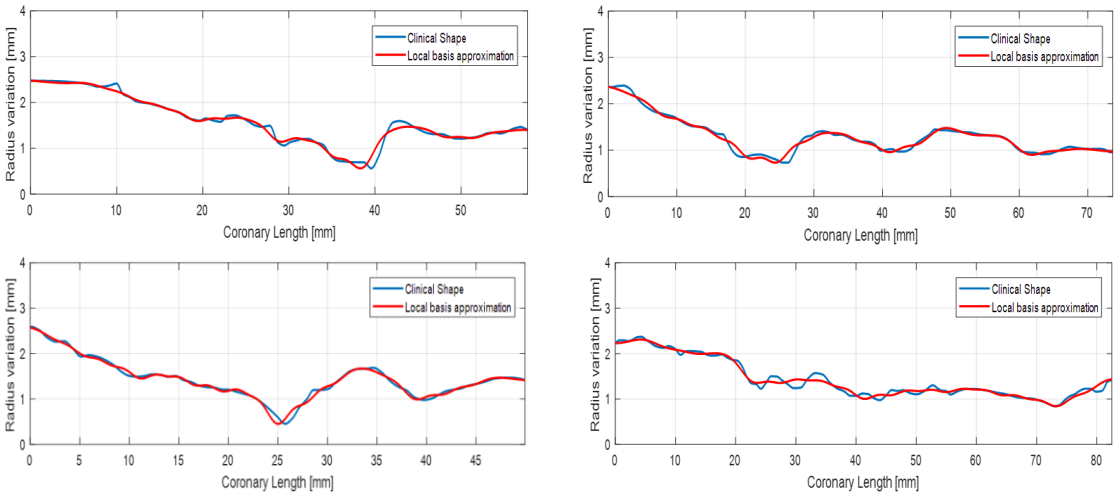

Figure 4.17: Approximation of clinical geometries with 19 global basis functions. Blue line) Clinical geometry. Red line) Approximated geometry.

As expected, using 19 local basis functions to approximate the coronary shapes produces a more accurate representation of the radius distribution along the vessel than that achieved using 8 local basis functions. For the latter the reconstructed geometry is much smoother than the clinical geometry, there is not a high level of detail but the important features (inlet, outlet, min. radius) are still well captured.

It is expected that a more accurate representation of the geometry will naturally produce a more accurate representation of the pressure gradients. The total pressure drop along the whole vessel, computed by CFD for the original and approximated geometries, is illustrated in Figure 4.18. The value of R^2 is 0.96 and the standard deviation is 3.57 for nineteen terms; R^2 is 0.91 and standard deviation is 7.80 for eight terms, but it is noted that there are outliers with high error, up to ≈ 21 mmHg, even for the higher-order representation.

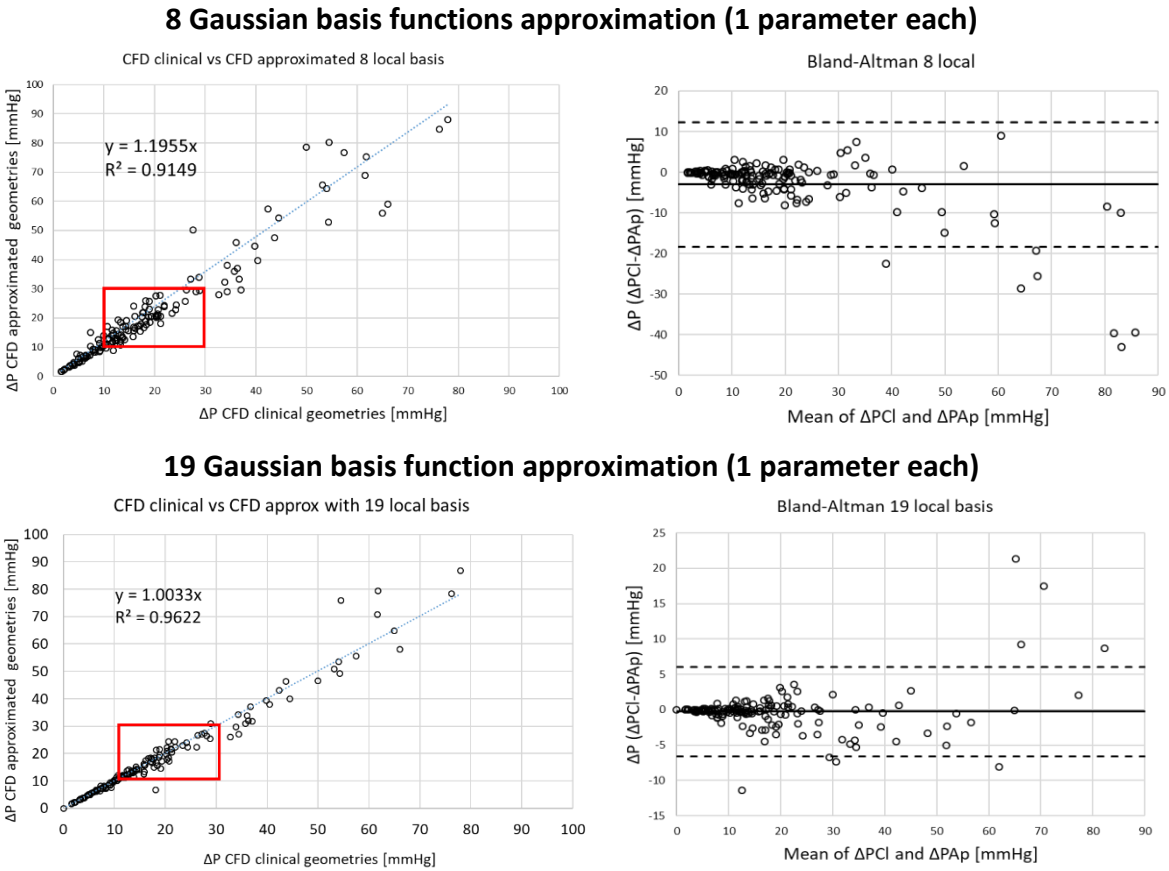

Figure 4.18: Left graphs) Correlation between clinical geometries and approximated geometries on the pressure drop computed with different number of localised Gaussian basis functions.
Right graphs: Bland-Altman plots.

4.3.6 Approximation of the 2D coronary shape by Fourier boundary variations

It is well known that any periodic function described by $f(x) = f(x + T)$ where T is the period of the signal, can be written as a summation of weighted cosine and sine functions waves characterised by increasing their frequencies [140]. Our $f(x)$ function is the variation of the radius along the axial axis for every clinical segmented geometry in our clinical dataset. Using Fourier analyses is possible to decompose the original clinical shape into harmonics components. Our 1-D function *f(x)* with Fourier series will have the form of:

$$f(x) = \frac{A_0}{2} + \sum_{n=1}^{\infty} (A_n \cos\left(\frac{2\pi n}{L} x\right) + B_n \sin(\frac{2\pi n}{L} x)) \quad \text{(Eq.4.15)}$$

Since we are considering a finite number of harmonics to approximate the function $f(x)$, and expanding Eq. 4.14 with cosine and sine we obtain:

$$f_{approx}(x) = \frac{A_0}{2} + \sum_{n=1}^{N} (A_n \cos\left(\frac{2\pi n}{L} x\right) + B_n \sin(\frac{2\pi n}{L} x)) \quad \text{(Eq.4.16)}$$

where A_n and B_n are the cosine and sine harmonic coefficients, A_0 is the fundamental harmonic, *n* is the number of harmonics considered for approximating the function.

The Fourier approximation works well when the function is periodic, however our clinical shapes are non-periodic. In these cases, the quality of approximation with Fourier series near the end points (inlet and outlet) could be poor if the behaviour of the function at both ends does not match. To mitigate this issue, a taper can be added to the description of the function $f(x)$ as in Eq. 4.16 so the values at the inlet and outlet of the function match:

$$f(x) = F_{fourier} + taper \quad \text{(Eq.4.17)}$$

If we compute the difference:

$$f(x) - taper = F_{fourier} \quad \text{(Eq.4.18)}$$

The value of the function at the inlet and outlet is $F_{fourier(inlet)} = 0$ and $F_{fourier(outlet)} = 0$.

Recomposing the signal with:

$$f_{app}(x) = F_{fourier} + taper \quad \text{(Eq.4.19)}$$

where $f_{app}(x)$ is the approximated function with n number of Fourier harmonics.

The approximation of the clinical geometries have been studied four different times using a different number of harmonics: 10, 15, 20 and 25 harmonics. A log file with the root mean

squared error is saved for all the geometries for each of the four datasets. Examples of approximation are shown in Figure 4.19 and Figure 4.20.

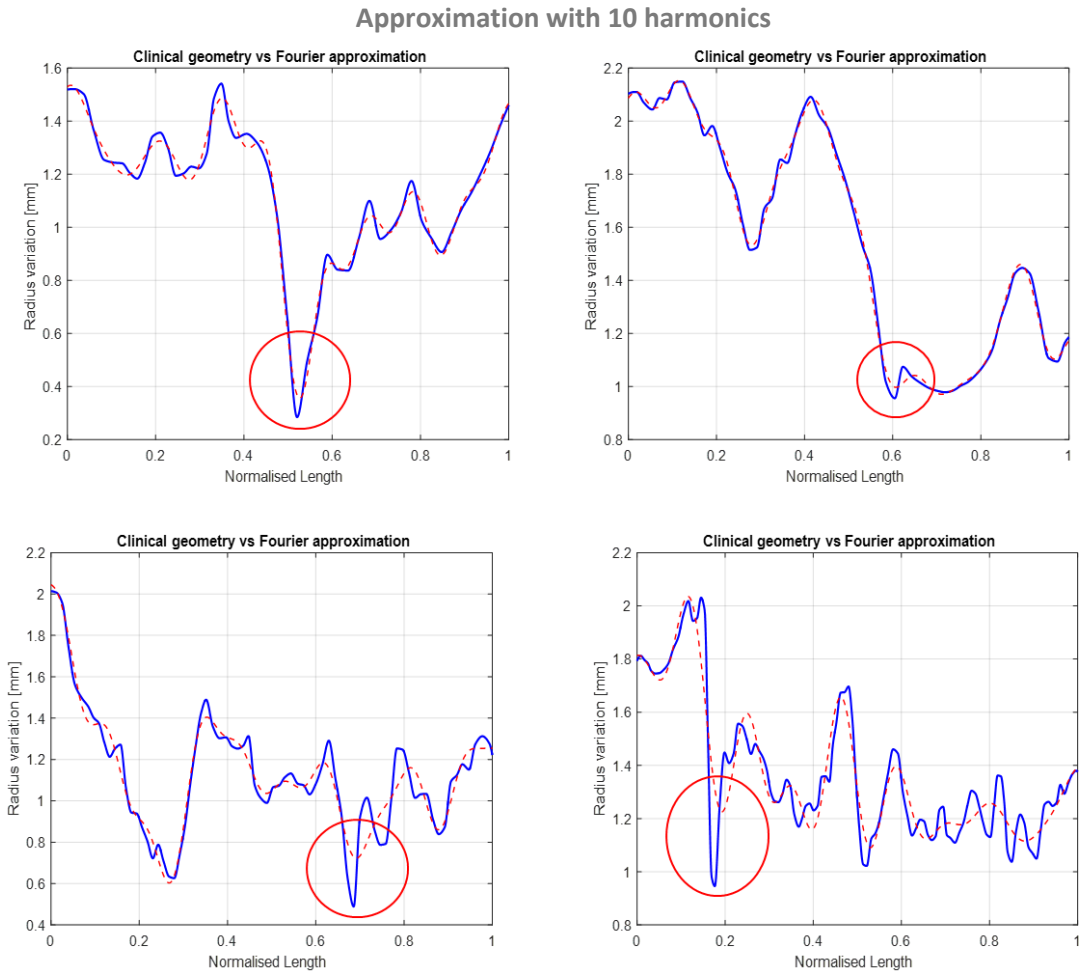

Figure 4.19: Fourier approximation with 10 harmonics. Clinical geometry (blue line). Clinical geometry approximated with Fourier (red dashed line).

On these plots, the coronary shapes have been approximated with 10 harmonics. The overall shape is very well maintained, however looking at the red circles the minimum radii are not caught by the approximations. This means that the pressure profile and the pressure drop for the clinical case and the approximated case will not be maintained very well.

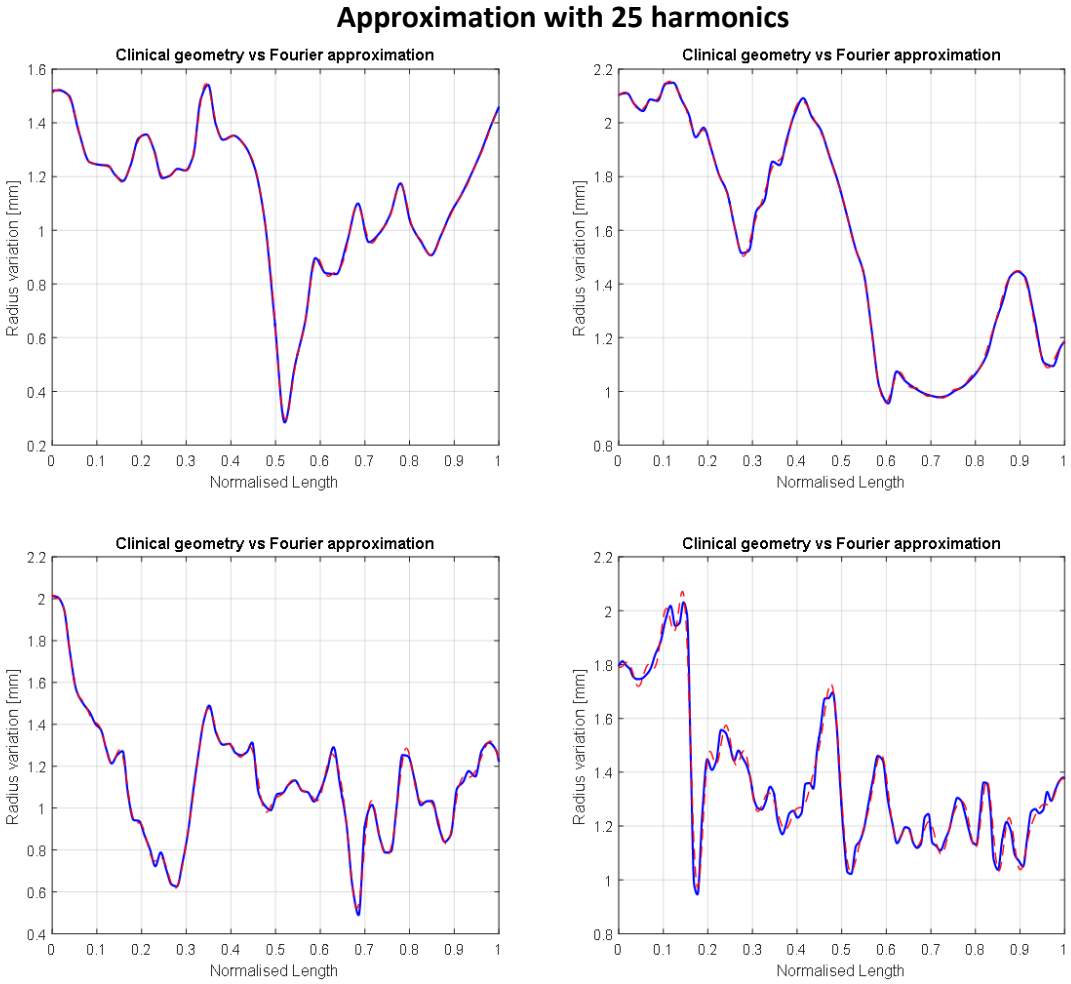

Figure 4.20: Fourier approximation with 25 harmonics.
Blue line clinical geometry. Red dashed line approximation with Fourier.

In Figure 4.20, the coronary shapes have been approximated with 25 harmonics (Figure 4.20). The overall shape is very well maintained even at very sharp variations thanks to the harmonics with high frequencies. The minimum radii are perfectly captured. Computing CFD on both geometries (clinical, approximated) results in a very good correlation regarding the pressure drops. However, the major downside of this approach is that using N harmonics, in the case of a parameterised ROM we have to consider 2 by N number of parameters, because of the cosine and the sine coefficients for the Fourier series. A very high number of parameters would make the ROM impractical.

Having logged all the RMS errors for all the cases approximated by a different number of harmonics is possible to notice how the average error decreases whilst increasing the number of harmonics (Figure 4.21).

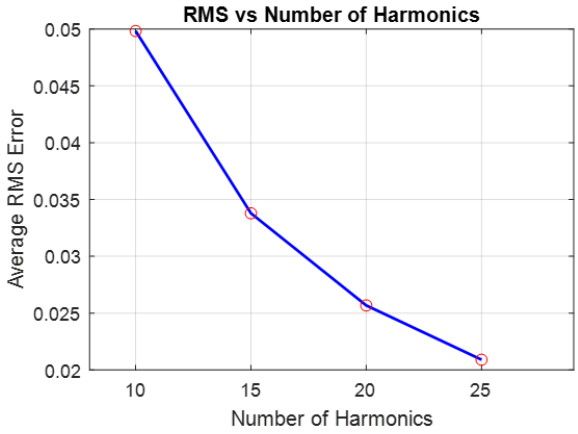

Figure 4.21: RMS error vs Number of Harmonics.
As it can be seen, increasing the number of harmonics the error decreases.

Applying Fourier decomposition to our coronary shapes, we should expect that the power content of the Fourier harmonics should be concentrated in the first few harmonics. In general, at high frequencies the power spectrum of the harmonics should approach the zero value, whilst the first few harmonics contain most of the power.

As can be seen in Figure 4.22, the power spectrum of the Fourier harmonics reaches the zero value for high frequencies. Not surprisingly, a good approximation of coronary shapes is obtained using the first few harmonics.

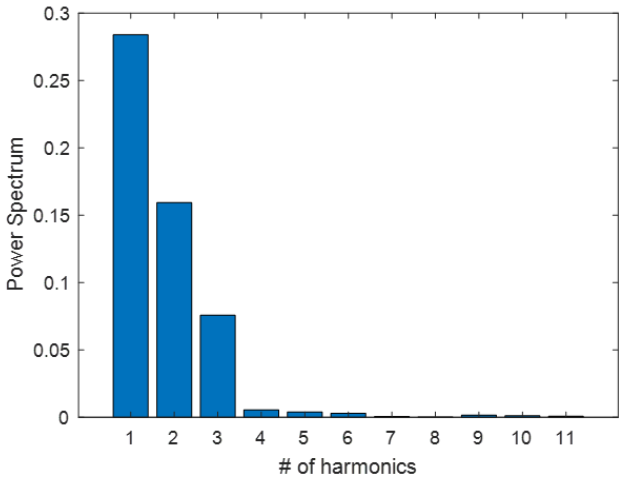

Figure 4.22: Power Spectrum vs number of harmonics.

Using the Fourier approach to parameterise the clinical geometries and their pressure profiles, generates a good representation of the overall shape and well-matched pressure profiles with a good grade of accuracy especially for $10\,mmHg < \Delta P < 30\,mmHg$ (Figure 4.23).

Increasing the number of harmonics on the system allow to capture very sharp variation on the actual shape for local areas. However, the method is not efficient when coupled with ROM applications. The number of the parameters to describe the approximated geometry with high accuracy is very high, e.g. for a Fourier series with 25 harmonics the number of parameters to considered when building a ROM is more than double.

Approximation with 10 harmonics

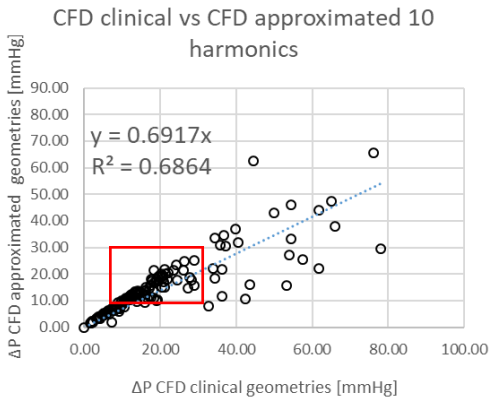

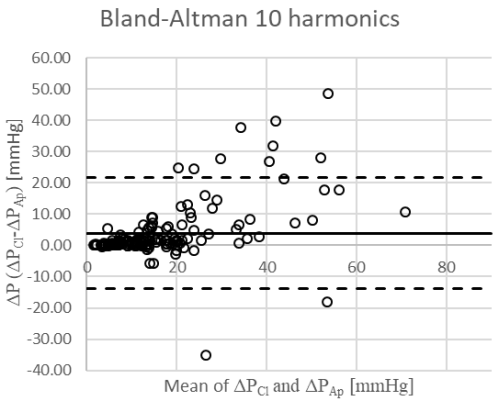

Approximation with 15 harmonics

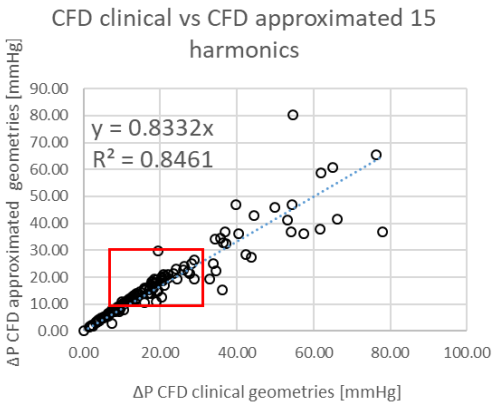

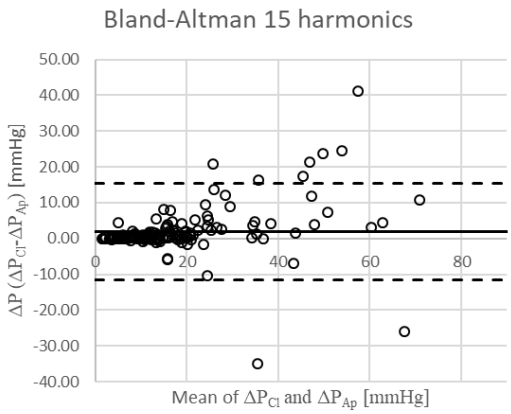

Approximation with 20 harmonics

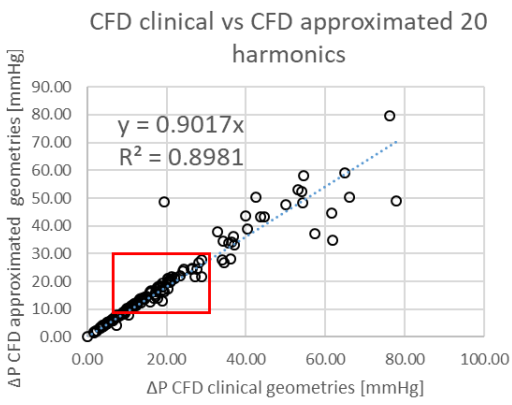

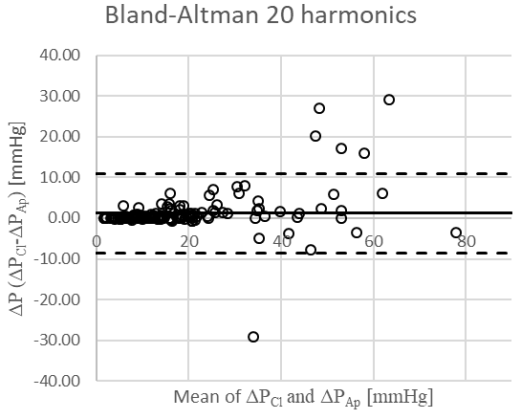

Approximation with 25 harmonics

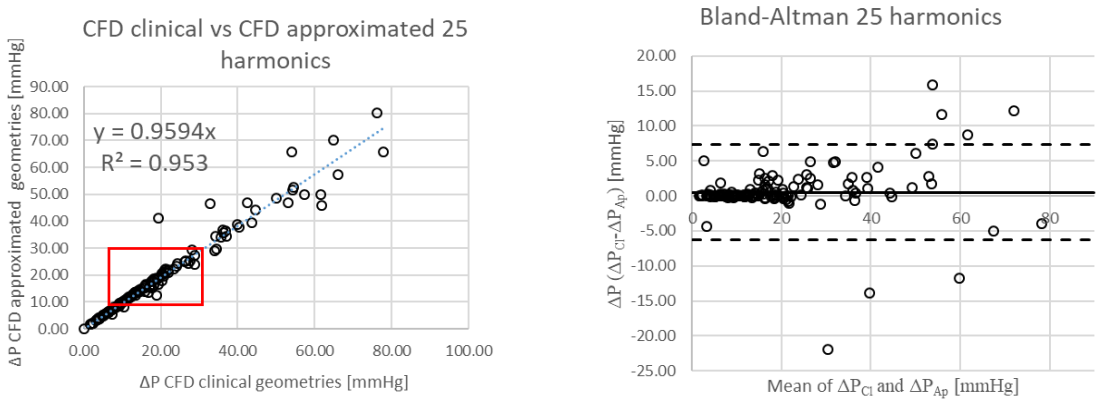

Figure 4.23: Left column) Pressure gradient approximated geometries vs Pressure gradient clinical geometries described with different number of harmonics.
Right column) Bland-Altman for the different descriptions.

4.4 Discussion

In the former section accuracy and flexibility have been taken into consideration for different approaches of geometry parameterisation. Focus has been given to polynomials, Gaussians and Fourier basis functions. Moreover, it has been considered for the shape parameterisation a combination of the basis; a combination of a first order polynomial with a series of Gaussians and a first order polynomial with a Fourier description.

When considering a high number of harmonics, the Fourier approach produces good results in terms of accuracy and it is able to collect very sharp variations of the coronary shape. However, this method is impractical due to the high number of geometrical parameters involved which would result in a very large design space.

The Gaussian basis functions, dependent on three parameters are also affected by the high number of parameters (three parameters for every basis functions). Furthermore, they are not accurate in terms of maintaining an unaltered pressure profile and the error on the pressure gradient diminishes very slowly with increase in number of bases.

The Gaussian basis function with only the amplitude parameter to be optimised produces the best results in terms of flexibility. They are easy to create and easy to manage. Furthermore, a good grade of accuracy for the pressure profile has been obtained using a limited number of basis functions. Limiting the number of parameters is useful for maintaining a low level of computational cost for the ROM construction.

For these reasons, it has to be chosen to create clinical ROMs using the Gaussian basis functions (8 bases) described by only one parameter (the amplitude) while keeping the width and the location of the basis fixed, plus the taper which is useful to collect the common feature of radius reduction on coronary arteries.

4.5 Clinical ROM construction

In this section is presented the process to build a parameterised ROM starting from patient specific coronary geometries [90], [96], [124], [131], [132], [141]. In order to build and populate the training dataset, the geometrical parameters used for creating the synthetic dataset are the 8 basis parameters (amplitudes of the Gaussians), plus 2 parameters for the taper, the vessel length of the coronary and lastly the mass flow inlet for a total of 12 parameters. The set of parameters spanning the parametric space are presented in Table 4.1.

Table 4.1: Maximum and minimum values of each parameter for the ROM.

Parameters	Min	Max
Amplitude 1	-0.78	1.25
Amplitude 2	-0.74	2.08
Amplitude 3	-0.94	1.62
Amplitude 4	-1.02	1.63
Amplitude 5	-0.91	1.65
Amplitude 6	-0.79	1.45
Amplitude 7	-1.14	1.47
Amplitude 8	-0.66	0.59
Taper P1	-1.97	0.19
Taper P2	0.84	2.99
Length (Norm.)	0.33	1
Mass flow rate	0.0010	0.0022

The constructed synthetic dataset consists of 24933 geometries. Different ROMs have been created starting from the same training dataset, in order to study the changes of the projection errors and interpolation errors. The correlation matrix is populated with pressure values along the symmetry axis of every CFD steady state analysis, hence the final matrix dimension of [*Nx699*] where *N* is the number of snapshot considered for the *offline* process.

ROM with 33% of geometries for off-line process

In this example the dataset for constructing the ROMs consists of 8311 geometries (a third of the entire dataset). Two ROMs have been created, the first one with 12 modes, the second one with 15 modes.

Table 4.2: Summary of the two ROMs created with one third of the dataset used for training.

ROM Number	Size of the Training Dataset	# of modes for the ROM
ROM 1	8311	12
ROM 2	8311	15

The projection errors and the interpolation errors are both computed (Figure 4.24).

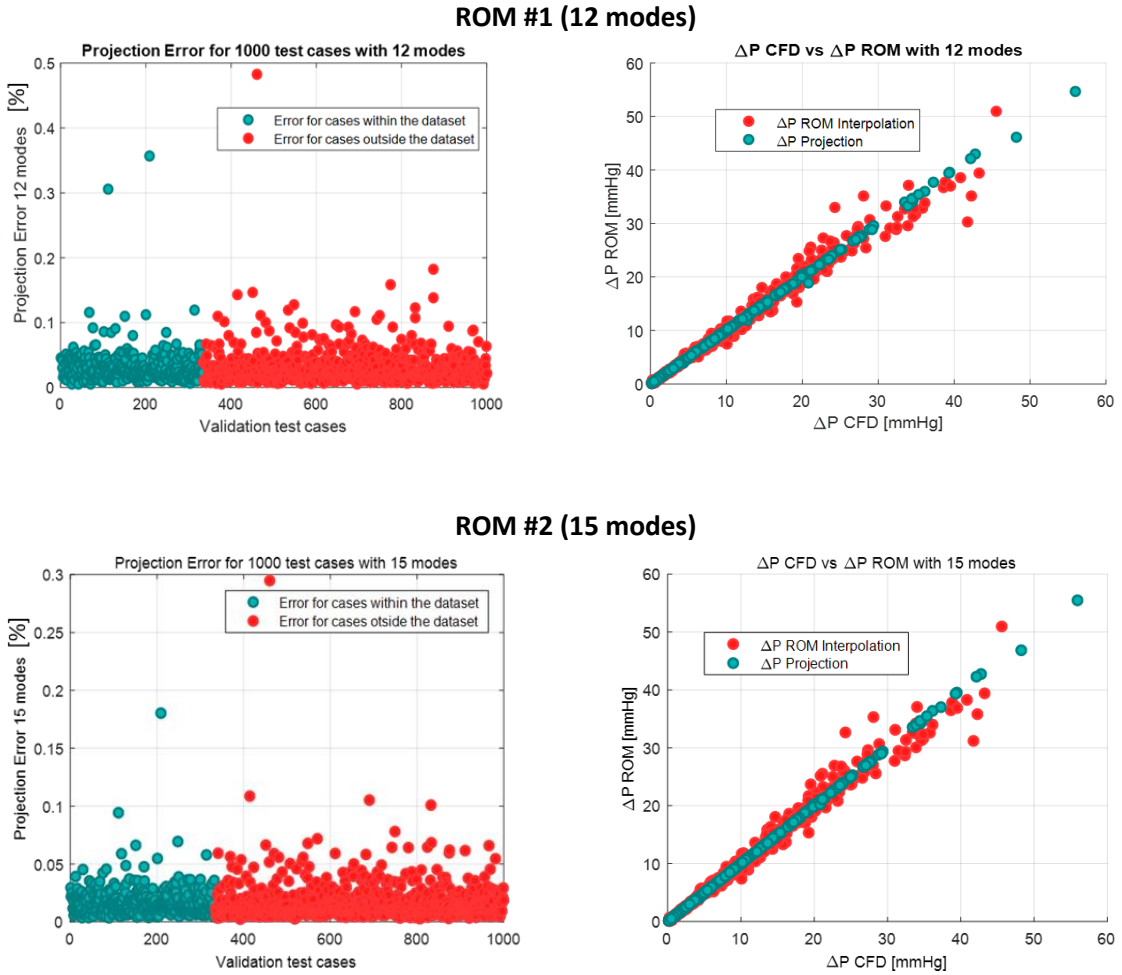

Figure 4.24: Left column) Projection errors in percentage for geometries within the training dataset (blue dots) and outside the training dataset (red dots) for different number of modes.
Right column) Projection errors (blue dots) and interpolation errors for cases outside the training dataset for different number of modes.

It can be seen that the projection errors computed for the geometry within the training dataset are decreasing in magnitude whilst increasing the number of modes. The projection errors for the geometry not used for training follow the same trend. Regarding the interpolation errors on

the right hand side of Figure 4.24, considering a higher number of modes (15 vs 12 modes) does not change the description of the pressure gradient.

ROM with 50% of geometries for off-line process

In this example the constructed ROMs are built considering half the size of the full phantom dataset. The training dataset are composed of 12467 geometries. Four ROMs have been built maintaining same size for the training dataset but changing the number of considered modes (Table 4-3).

Table 4.3: Summary of the ROMs created with half of the dataset used for training.

ROM Number	Size of the Training Dataset	# of modes for the ROM
ROM 1	12467	8
ROM 2	12467	10
ROM 3	12467	12
ROM 4	12467	15

Figure 4.25 shows the comparison between the pressure profiles computed with full 2D axisymmetric simulations and the pressure profiles computed with different number of modes for some cases within the training dataset.

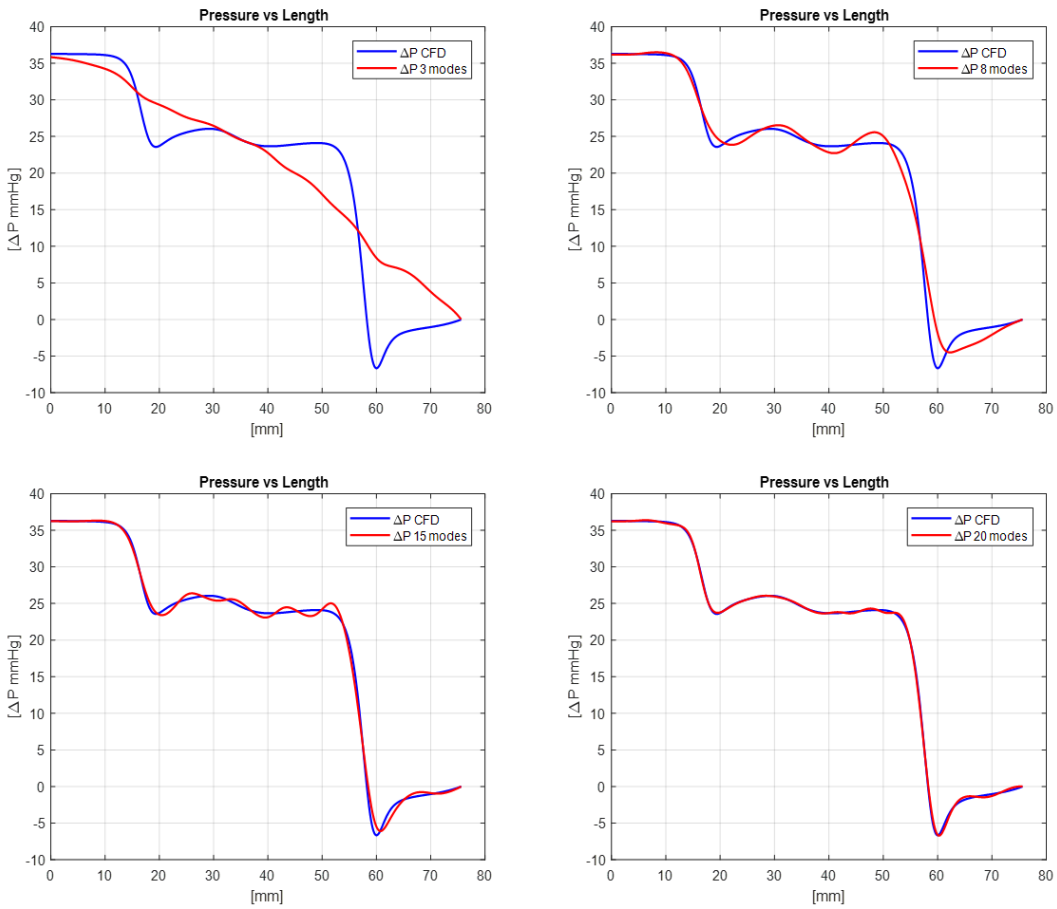

Figure 4.25: Pressure vs Length comparison between full CFD and low order solution varying the number of modes.
Top left) Pressure profile with 3 modes. Top right) Pressure profile with 8 modes. Bottom left) Pressure profile with 15 modes. Bottom right) Pressure profile 20 modes.

The projected solutions converge towards the full CFD solution with increasing number of modes. Furthermore, the computed basis functions are able to capture the overall pressure drop even with a small number of modes (modes = 3). However, the pressure solution with 3 modes is not capable to capture the local variations of the pressure profile and the pressure drops when the fluid flow encounters a stenosis.

In summary, the graphs show that the first few modes are capable of capturing the overall fluid flow pattern. However, increasing the number of modes captures more of the local details. In fact, using 20 modes an excellent accuracy between the full CFD solution and the reduced-order solution.

For the example taken into consideration, the two major pressure drops occurring at 20mm and 60mm are captured very well.

The plot of the average projection error versus number of modes for every computed ROM is shown in Figure 4.26. As expected keeping the same size and same geometries for the training

dataset, but varying the number of modes results in a decreasing of the average projection error. It can be noticed that using 15 modes, the average projection error for the ROM is < *2%*.

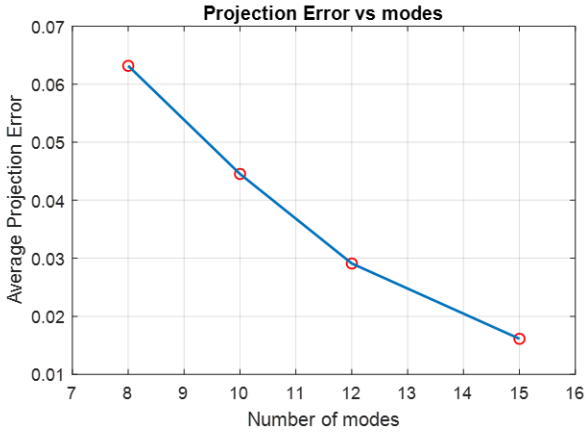

Figure 4.26: Projection error vs number of modes

Once the ROMs have been trained, the evaluation and validation steps for every ROM were performed on a total of 1000 simulations; 500 geometries were within the training dataset, whilst the remaining 500 simulations were outside the training dataset; the latter ones were characterised by completely new parameters (geometrical and inlet flow within the parameters space) [57], [58].

In the graphs shown below, for every different clinical ROM, both the projection error and the interpolation error have been computed. The projection error has been computed for the whole validation dataset (500 + 500 geometries), the interpolation error has been computed only for the geometries which were outside the dataset (500 geometries). As already mentioned in Chapter 3, in order to have an estimation of the projection and interpolation errors, the user has to compute the full CFD solutions in order to compare the ROM to a 'gold standard'.

As expected, the projection error magnitude for the computed ROMs is very similar; this means that the computed modes with the SVD are capturing the most important fluid flow patterns and are also able to describe accurately the geometries outside the dataset.

A detailed comparison between the pressure gradients computed with full CFD and ROM is shown in the plots below using different number of modes (Figure 4.27).

Projection Errors for different # of modes

***ΔP CFD vs ΔP ROM* for different # of modes**

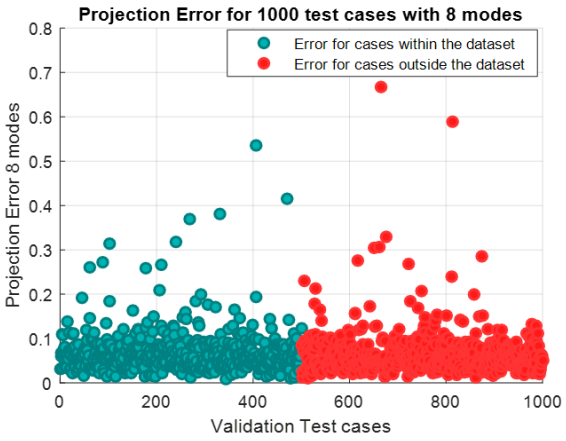
Projection Error for 1000 test cases with 8 modes
Error for cases within the dataset
Error for cases outside the dataset
Projection Error 8 modes
Validation Test cases

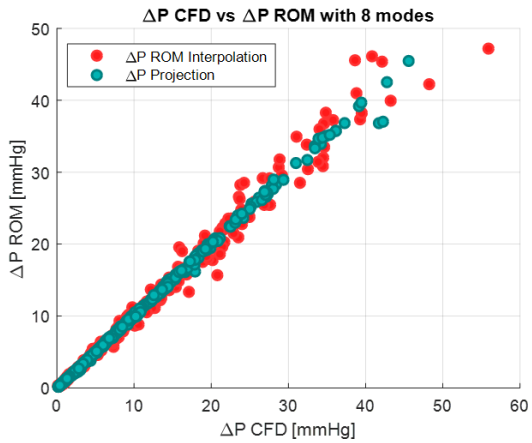
ΔP CFD vs ΔP ROM with 8 modes
ΔP ROM Interpolation
ΔP Projection
ΔP ROM [mmHg]
ΔP CFD [mmHg]

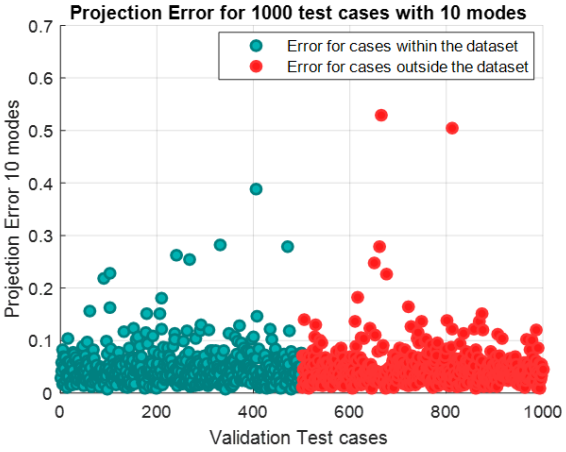
Projection Error for 1000 test cases with 10 modes
Error for cases within the dataset
Error for cases outside the dataset
Projection Error 10 modes
Validation Test cases

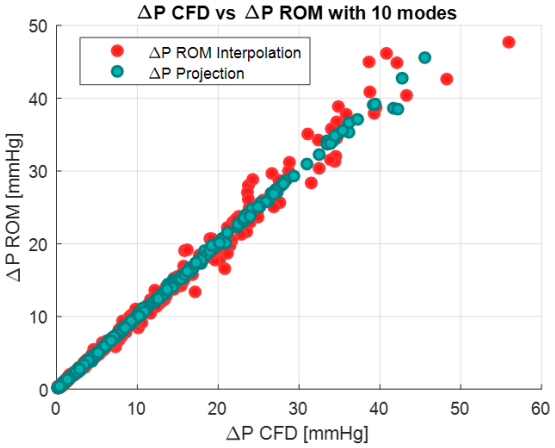
ΔP CFD vs ΔP ROM with 10 modes
ΔP ROM Interpolation
ΔP Projection
ΔP ROM [mmHg]
ΔP CFD [mmHg]

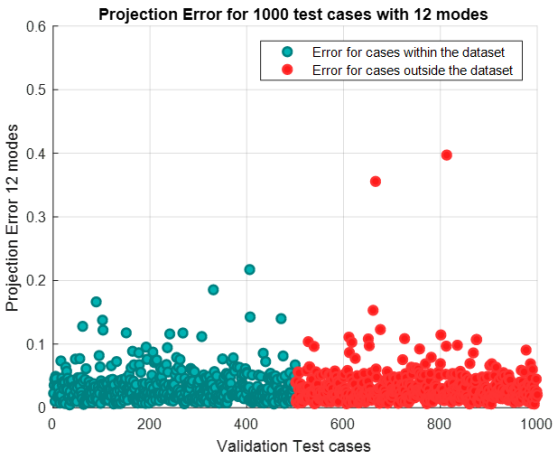
Projection Error for 1000 test cases with 12 modes
Error for cases within the dataset
Error for cases outside the dataset
Projection Error 12 modes
Validation Test cases

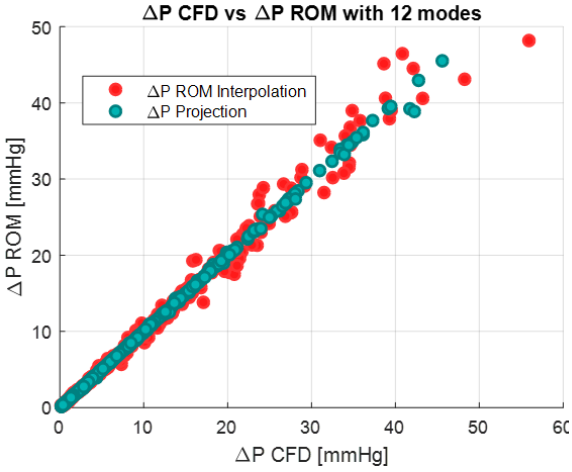
ΔP CFD vs ΔP ROM with 12 modes
ΔP ROM Interpolation
ΔP Projection
ΔP ROM [mmHg]
ΔP CFD [mmHg]

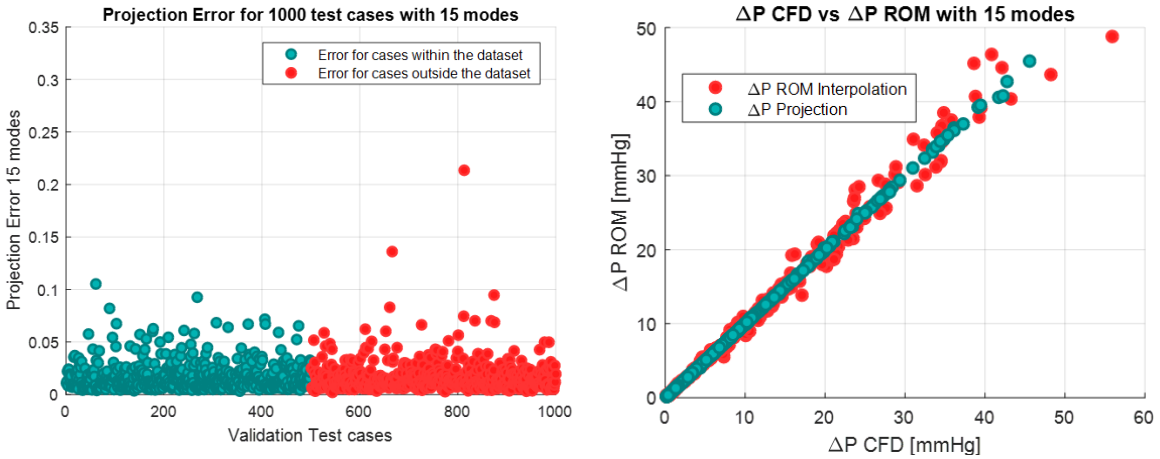

Figure 4.27: Left column) Projection errors in % for geometries within the training dataset (blue dots) and outside the training dataset (red dots) for different number of modes.
Right column) Projection errors (blue dots) and interpolation errors for cases outside the training dataset for different number of modes.

The left column of Figure 4.27 is showing a comparison between the projection errors with different number of modes computed for 500 geometries within the dataset (blue dots) and 500 geometries not used for training (red dots). It is important to notice that the average projection error is very small for all the cases ($Max\ Avg_{err} \leq 0.07$ for 8 modes). Furthermore, the right column of Figure 4.27 is representing both the projection errors and the interpolations errors for 500 geometries, for which the considered geometries were not used for training (new input numerical parameters). The pressure drop computed projecting the full solutions onto the base of modes (blue dots) have an excellent correlation. The pressure drop computed with interpolation (red dots) have still a good correlation for values of $\Delta P \leq 30\ mmHg$, however for high values of the pressure drop the error starts to increase.

Some pressure profiles computed with the four different ROMs are shown in Figure 4.28 in which the pressure profiles are evaluated for new geometries (not used for training) and completely new sets of parameters. The plots are produced with 8, 10, 12 and 15 modes in order to compare the dynamic of the description of the different pressure profiles whilst increasing the number of modes. As it can be seen, with 8 modes the ROM is already capable of describing the full CFD solution with a fairly good degree of accuracy. The overall pressure drop for all the considered geometries is well maintained (Figure 4.28).

Increasing the number of modes, as already shown for the projection errors, it can be seen that the ROMs try to push the low order solutions toward the full order solutions, where sharp variations are better captured. The overall error improves for the pressure profiles description;

however, there are no major improvements for the pressure drop since it was already well captured with 8 modes.

The evaluation step for the on-line mode can be performed on a normal laptop. The ROM pressure profile for each case is computed in ≈ 0.2 s; a full order simulation for a 2D steady state axisymmetric is computed in ≈ 180 s. The improvement in the execution is clear since the ROM computation is ≈ 900 times faster.

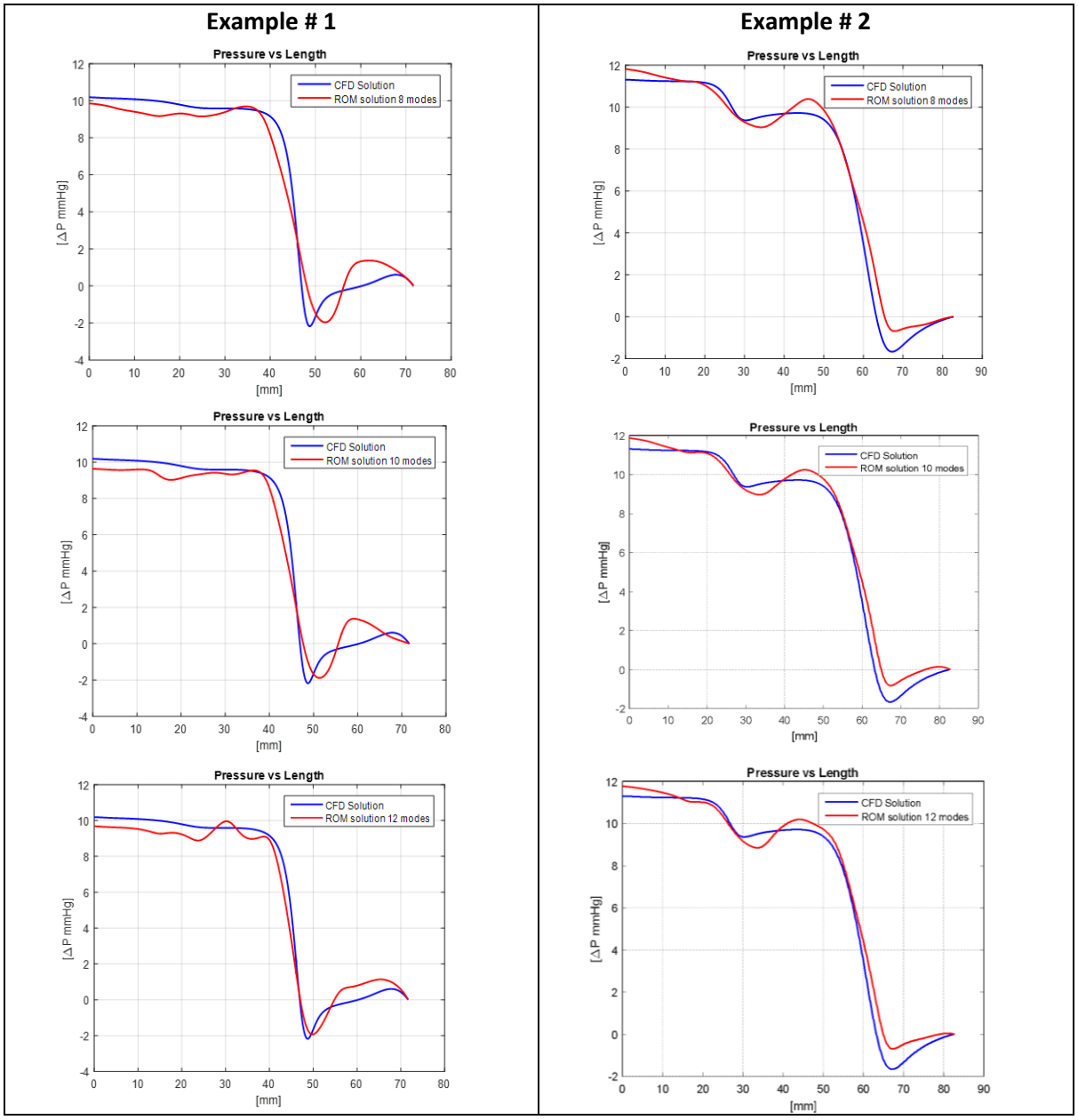

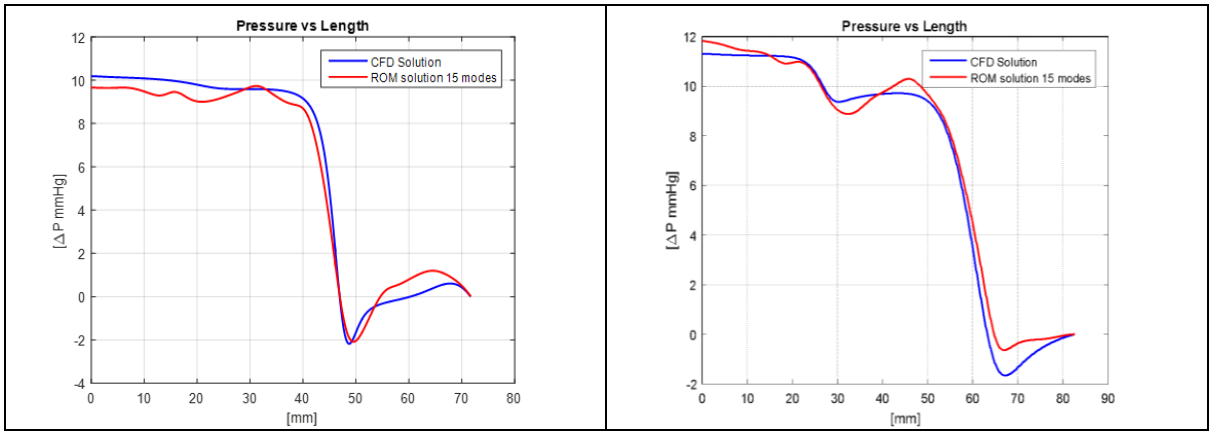

Figure 4.28: Recomputed pressure profiles for cases outside the dataset for different number of modes.

4.6 Validation of the $vFFR_{CFD}$ vs $vFFR_{ROM}$ for patient-specific data

In the previous section, the built ROMs with the parameters extracted from the clinical dataset were validated against synthetic geometries which were not used for the training and are dependent on new set of numerical parameters.

In this section, the ROMs built with the synthetic dataset will be tested against the approximated clinical geometries described by 12 parameters. Only the interpolation error is taken into account in this study. Two ROMs have been considered (described in details in the former section). The two ROMs are characterised by 12 and 15 modes and they had been built considering half the size of the full dataset for training (12467 solutions).

Interpolation Error with 12 modes

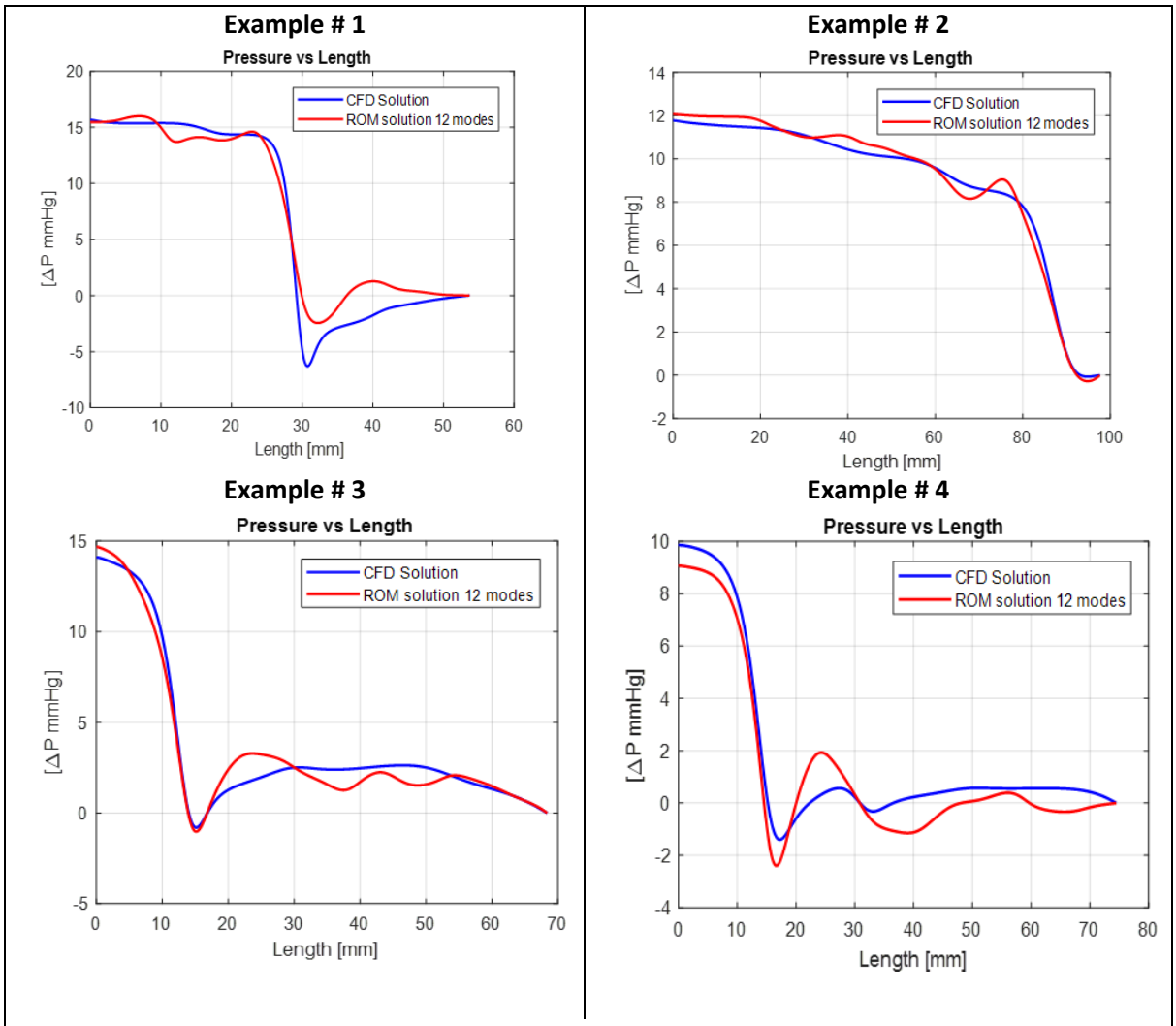

Figure 4.29: Examples of CFD (blue lines) vs computed ROM pressure profiles (red lines) with 12 modes.

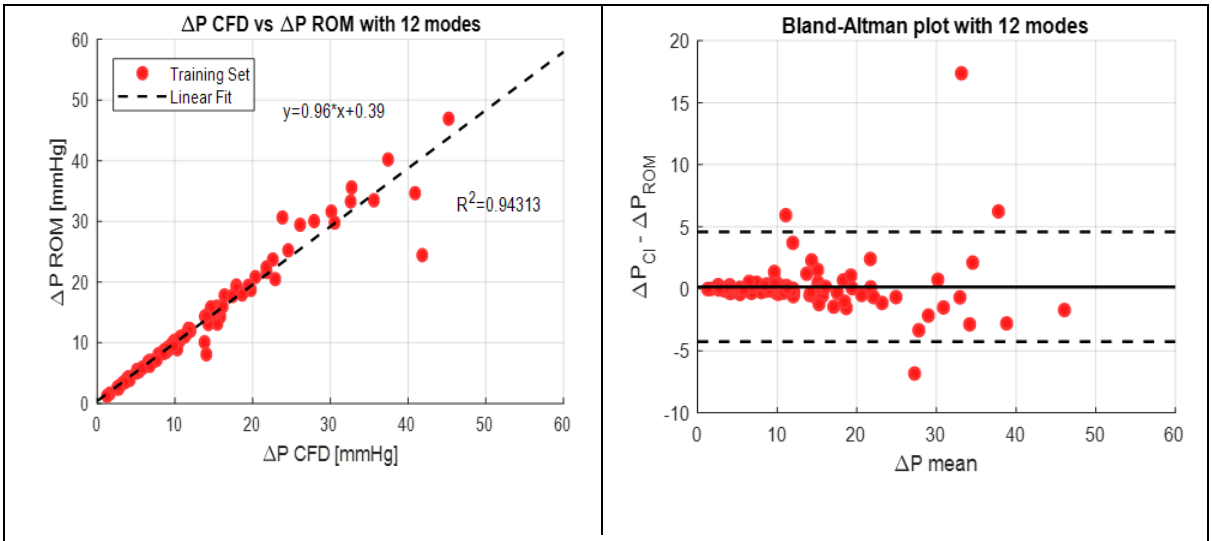

Figure 4.30: Left) Pressure gradient CFD vs Pressure gradient ROM (12 modes). Right) Bland-Altmann plot.

Interpolation Error with 15 modes

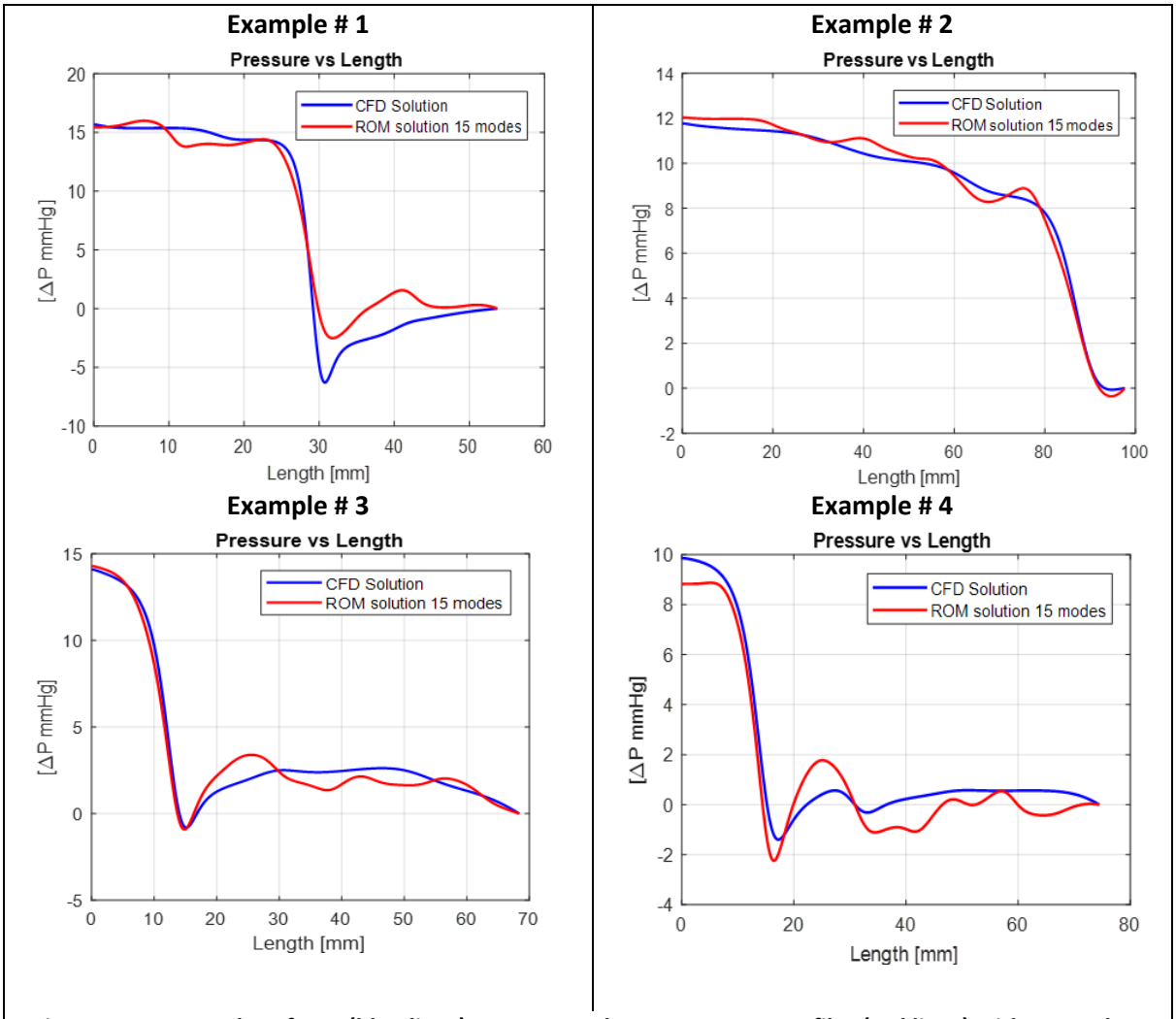

Figure 4.31: Examples of CFD (blue lines) vs computed ROM pressure profiles (red lines) with 15 modes.

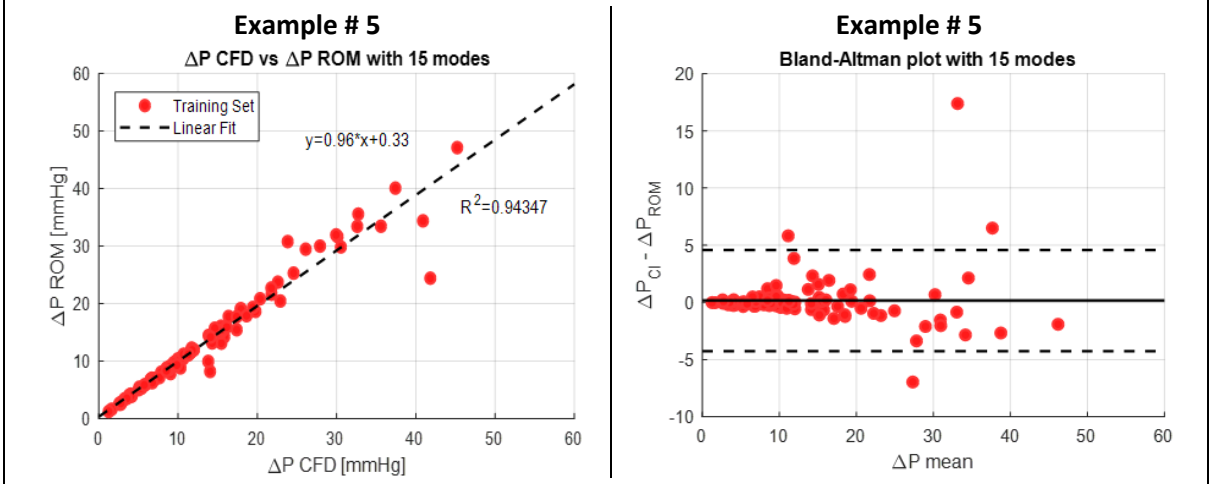

Figure 4.32: Left) Pressure gradient CFD vs Pressure gradient ROM (15 modes). Right) Bland-Altmann plot.

As expected the overall pressure gradients for the evaluated dataset testing the two ROMs is very well maintained, this behaviour also explains the high correlations between the ΔP

computed with full CFD and the ROM ΔP (Figure 4.31). It is also possible to notice how the ROMs try to catch the major pressure gradients due to the presence of lesions, and how increasing the number of modes from 12 to 15 the ROM slowly pushes the solutions to converge towards the high fidelity CFD solutions. Figure 4.32 is showing a very good correlation between the full CFD ΔP and the computed pressure gradient in the region of the ROI, then for high values of pressure drop the accuracy start to decrease. It is also possible to notice this behaviour from the Bland-Altmann plot where there are outliers for values of $\Delta P_{mean} \geq 28\ mmHg$.

4.7 Conclusion and discussion

In the first part of the chapter have been shown different methods and approach of shape parameterisation for the 2D axisymmetric coronary patient specific geometries. Different types of global basis functions have been explored as approximation functions. The best approximation method chosen for creating the clinical ROM is the Gaussian basis described by a single parameter (amplitude); which allowed a good grade of accuracy, maintaining the overall coronary shape of the considered coronary with a well-matching pressure profiles using a small number of parameters. The extracted geometrical parameters have been used to create a large phantom dataset.

In the second part of the chapter, multiple ROMs have been created. The ROMs have been trained using different numbers of fluid flow simulations to populate the correlation matrix. Furthermore, the ROMs have been trained with different number of modes in order to check the level of accuracy and convergence toward the full order solution. Both the projection and the interpolation errors were computed. The accuracy of the ROMs has been studied both on the phantom geometries not used for the training dataset, and on the actual patient specific clinical dataset.

In this chapter it has been shown that the SVD method is a valuable approach to compute the modes necessary to rebuild the full order solutions. In fact, it has been shown that a limited number of modes are capable of capturing the most predominant fluid flow information for 2D steady state axisymmetric CFD simulations. Furthermore, it had been shown that the projected solutions converge towards the full order CFD solutions by incrementing the number of modes.

Coupling the modes with an interpolation method to compute the modes coefficients, the ROMs have shown good grade of predictions when evaluating the pressure profile for

completely new geometries described by a new set of numerical parameters. The prediction of the pressure profiles is possible training the ROM with parameters spanning the parameter space of interest.

Chapter 5

3D CFD coronary arteries simulations: towards a Reduced Order Method for fast haemodynamic prediction

In the previous chapters it has been demonstrated that a ROM can effectively represent the pressure gradients computed by full CFD in a straight axisymmetric tube with radius varying along its length. It has also been shown that the results are comparable with actual clinical measurements, suggesting that the principal governing factor is the variation of radius. There is, however, the obvious question of whether the three-dimensional curvature of the vessel might also be an important factor in the determination of the pressure gradient.

The purpose of this chapter is to extend the analysis to include low-order parameterisation of the 3D shape of the vessel centreline. For clinical applications, reconstruction of 3D geometries from images is the key to develop patient-specific models, which can then be studied to estimate clinical indices avoiding the invasive procedure [68],[69],[70],[71], [72].

Furthermore, 3D CFD simulations are performed in cardiovascular applications in order to capture the dynamic of blood flow patterns (pressure and velocity) and to estimate other parameters of clinical interest such as the wall shear stress, which influences the endothelial proliferation within the vessel wall [142]–[145]. Although there is evidence in the previous chapters that the pressure gradient might be adequately represented by the ROM of the axisymmetric system, and therefore that it might be sufficient for the computation of FFR, it would not be anticipated that the shear stress distribution would be captured using this approximation. This chapter does not address the shear stress distributions themselves, but does examine whether the ROM can be extended by increasing the number of parameters that represent the 3D vessel curvature and remain effective and accurate. Figure 5.1 presents the workflow which has been followed for Chapter 5.

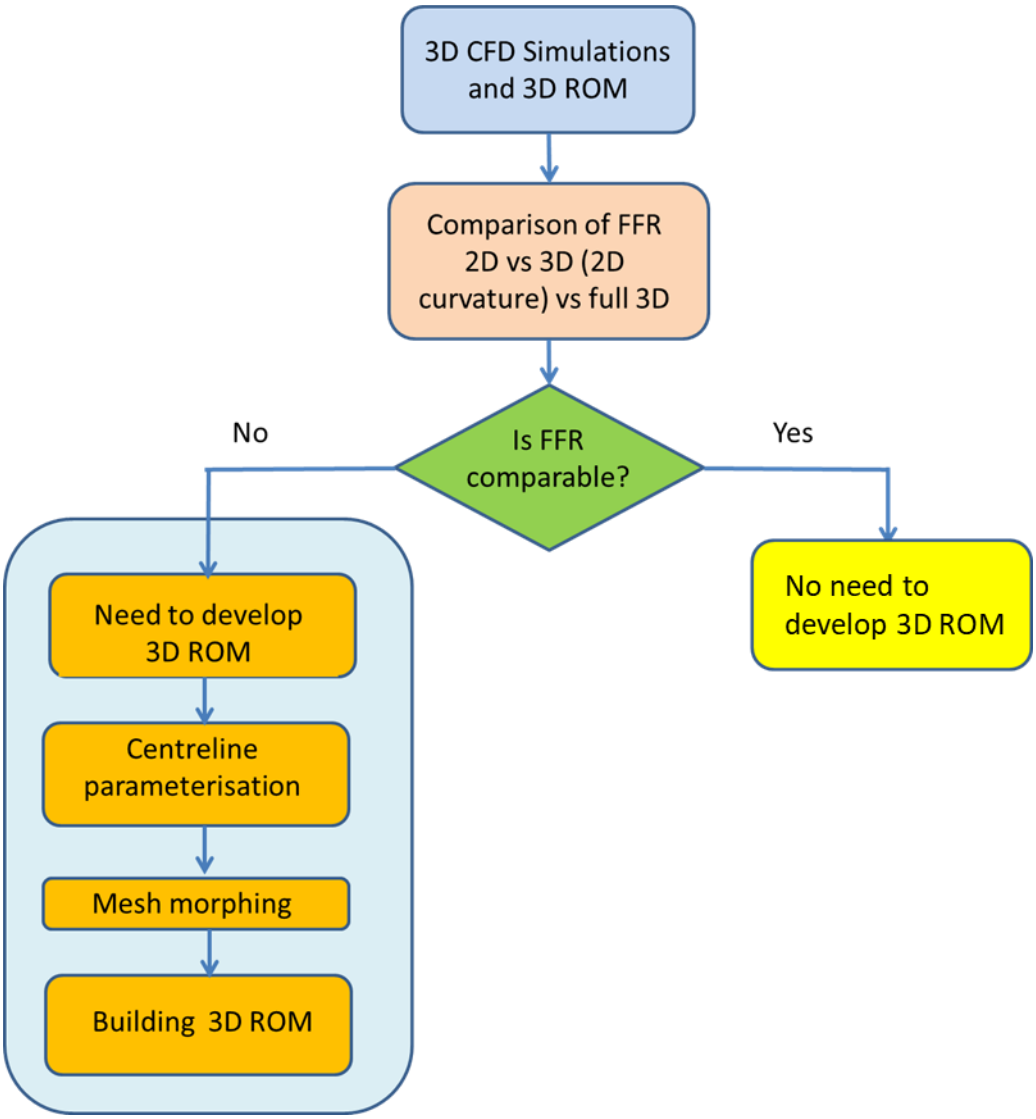

Figure 5.1: Main workflow for Chapter 5.
FFRs computed with 2D vs 3D with 2D curvature and full 3D are compared. When the FFR values are not comparable a 3D ROM needs to be developed following three main steps: centreline parameterisation, mesh morphing and building the 3D ROM.

Section 5.2 focuses on the comparison between three different CFD models: 2D axisymmetric geometries, 3D coronary geometries where the centreline lies on a 2D plane (2D curvature) and full 3D coronary geometries. The main aim is to compare the FFRs which have been computed with the three models. When the computed FFRs are very similar to each other (2D, 3D with 2D curvature and 3D), then there is no need to develop a 3D ROM since the 2D axisymmetric ROM for the clinical cases is already accurate.

If the FFRs are not compatible between each other, then there is the need to build a 3D ROM. In this case, a first step is to find a possible solution for centreline parameterisation; this is covered in section 5.3. Once a satisfactory centreline parameterisation is found, the next step

is to perturb the centreline parameters; this allows the user to morph the geometries in order to obtain isotopological meshes. After introducing and explaining the methods for centreline parameterisation, focus will be given on creating a large synthetic dataset with full 3D geometries and correspondent 3D volumetric meshes (Section 5.3.2).

In Section 5.5 results will be shown in terms of projection errors and interpolation errors as well regarding the built 3D ROM.

In Section 5.6, conclusions for the chapter will be presented.

5.1 Introduction

From the computational point of view, solving numerical 3D fluid flow simulations require a lot of computational power and time. For example, a full transient blood flow simulation on a coronary artery could take more than 24h on a normal desktop PC. The time scale is not compatible with clinical application, where a fast, accurate and reliable patient-specific solution should be available in near real-time.

In this chapter reduced order method for computing pressure profiles along centrelines for coronary arteries in three dimensions is introduced [26]. The numerical complexity of the model is hugely decreased by application of a proper orthogonal decomposition (POD). The creation of a patient-specific dataset is the starting point for the ROM construction [58], [59], [96], [131], [132], [146]. In fact, a similar process for creating a 2D parameterisation, had been followed for the 3D parameterisation of the geometries. There is a combination of human intelligence, testing and experimentation in order to decide the algebraic nature of the parameterisation, which combined with a clinical dataset is useful to determine an appropriate quantitative range of the geometrical parameter to develop the design of experiment. The ROM combines geometrical parameters for shape and centreline approximation and physical parameters. Moreover, coronary geometry variations are handled with the introduction of a centreline parameterisation algorithm.

The main goal of this chapter is to introduce a reduced order method which is capable of a fast pressure profile computation with patient specific clinical data [147]. By construction of a dataset of full CFD solutions, which are used as basis functions, a fast evaluation of pressure profiles is possible.

Many CFD studies have been performed on 3D coronary artery geometries. However, only few of these include parameterised ROMs [121]–[125]. ROMs applied for cardiovascular applications are described in Manzoni *et al*. [59], Ballarin *et al*.[131] and Colciago *et al*. [137].

In Manzoni *et al* ROMs are applied to carotid artery bifurcations to achieve a fast evaluation of the blood flow. Their method is based on the combination of low-dimensional shape parameterisations of the computational domain and the reduced basis method to solve the flow equations. The computational domain is a 2D domain, with a very simplified mesh. In order to use a small number of geometrical parameters to describe the carotid vessel, the mesh was morphed following the displacements of few control points defined along the vessel's wall. The usage of control points can induce a local or a global variation of the computational domain. However, for this study the usage of control points to deform the original shape is restrictive since the control points cannot be chosen freely but their starting position is already pre-determined at the beginning of the study.

Ballarin *et al.* applied ROMs to 3D Coronary Artery Bypass Grafting (CABG) to provide information about haemodynamic conditions for different surgical choices. CABG is a procedure to restore myocardial blood flow when more coronary vessels are occluded, limiting the correct perfusion of myocardium. The use of a CFD solution for each case would require 1 day to produce the results even in modern high-performance computers, while the ROM can provide the solution in few minutes. Their ROM consists of three steps: parameterised formulation, geometrical variation and computation of the solution with a POD method. Ten patients were recruited, each with a different number of grafts. Their model is defined by two geometrical parameters: stenosis severity (between 0% and 90%) and grafting angle (antegrade, T-shaped and retrograde). The stenosis location and extension were kept fixed based on the anatomical data. The centreline-based parametrisation allowed deformation of the patient specific mesh into a parametric one in an automatic way. This is essential to apply the ROM efficiently to different geometrical configurations represented by the same mesh. The group suggested that further improvements were required with regards to the personalisation of the model, using lumped models as inflow-outflow boundary conditions.

Colciago *et al.*applied ROM to a patient specific aortofemoral artery. The aim of the group was to compare the results between a full fluid-solid interaction (FSI) and a reduced fluid-solid interaction study (RFSI). They chose a single parameter for their model, the Young's modulus. Even in this case the group used the POD method to compute the modes. The group stated that the RFSI model can run on a normal laptop in 3.4s achieving good accuracy for pressure, velocities and shear stress. However, their study was limited in that the computed RFSI cannot predict the fluid flow for any patient-specific artery since the trained ROM model was

composed of a single aortofemoral geometry. Changing the patient, would require the recomputation of the *off-line* phase.

5.2 3D CFD vs 3D (2D curvature) vs 2D Axisymmetric simulations on patient specific coronary arteries

The aim of this section is to present a comparison between three levels of representation in models for patient specific geometries: full 3D geometries, 3D geometries described by a 2D curvature and finally 2D axisymmetric models. The same boundary conditions have been applied for every coronary artery included in the study.

The goal is to determine the degree to which the curvature of the coronary artery centreline influences the pressure profile of the coronaries. It is not expected that the pressure profile will remain exactly the same in each of the different models. However, since the radius variation along the length is the same for a single geometry, based on the success of the axisymmetric ROM described in the previous chapter in reproducing clinical measurements of FFR, it is hypothesised that pressure profiles will be similar. If this hypothesis is proven, it might not be necessary to create a 3D ROM since the 2D axisymmetric ROMs are already capable to capture the overall pressure gradient with a sufficient accuracy.

Nine cases (both RCA and LAD vessels) have been considered for this analysis. A number of steps were necessary to develop the models as described in the following sections. In particular, it is necessary to create the volumetric meshes for each case (3D and 3D with 2D curvature) to be imported into the Fluent solver.

5.2.1 Creation of volumetric meshes

Creation of triangular surface meshes

Before starting computing CFD, different .stl files have been created in MATLAB; for CFD simulations in medical application it is common to start with a surface mesh, which is formed by triangles. As a second step, the triangular surface meshes have been imported into Fluent Meshing to create the volumetric meshes.

Create volumetric mesh

Since several 3D full CFD simulations have to be computed, it is impractical to mesh every single geometry one by one, and so journal files were produced to make the process completely automatic. All the necessary journal files were written with MATLAB scripts.

The creation of a good volumetric mesh is a very important step within the workflow. The computed mesh has to be fine enough to capture correctly the complex flow behaviour in detail, and the accuracy of the solution generally depends on the quality of the mesh, although this constraint is less onerous for finite volume methods as opposed to finite element.

Within Fluent Meshing is possible to set the following boundary conditions:

- **Inlet:** Mass-flow rate
- **Outlet:** Pressure Outlet
- **Wall:** No-slip condition

A no slip condition has been set up for the wall boundary and, because this is where the velocity gradients are high, an inflation approach has been used to create a fine and regular mesh in this region. Starting and propagating from the coronary wall, prism layers have been created with an increasing gradient of cell size (Figure 5.1). Furthermore, a refinement of the mesh had been employed using a sizing function depending on the curvature of the geometry.

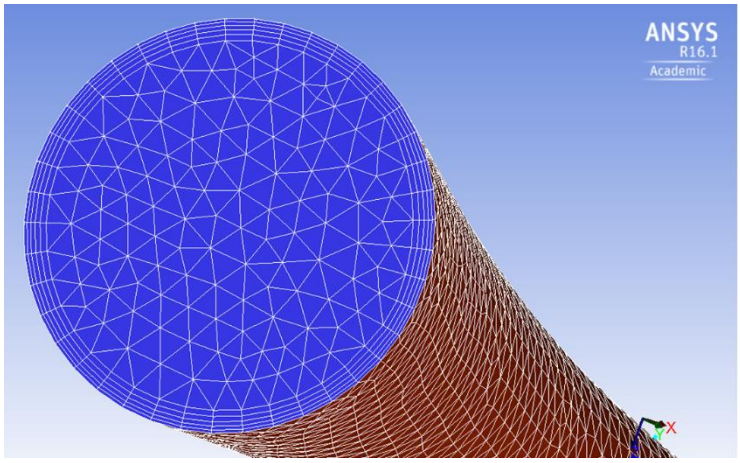

Figure 5.2: Prism layers starting from the wall boundary. Prism layers have been created propagating from the wall with an increasing gradient of cell size.

5.2.2 Convergence Criteria

The root mean squared (RMS) residuals were monitored to ensure convergence of the CFD simulations. The default convergence criteria in ANSYS Fluent is 10^{-3}, however ANSYS states:

- Values larger than 10^{-4} may be sufficient to obtain a qualitative understanding of the flow field;
- 10^{-4} is relatively loose convergence, but may be sufficient for many engineering applications;
- 10^{-5} is good convergence, and usually sufficient for most engineering applications;

- 10^{-6} or lower is very tight convergence, and occasionally required for geometrically sensitive problems. It is often not possible to achieve this level of convergence, particularly when using a single precision solver.

It has been chosen to apply a convergence criteria of 10^{-4} for both the continuity equation and for the momentum equations in all the three dimensions. A study has been carried out in one of the geometries (V048_LCx) to ensure the choice of the convergence criteria has no effect onto the pressure and velocity distribution on the 3D centreline along the length of the domain (Figure 5.2).

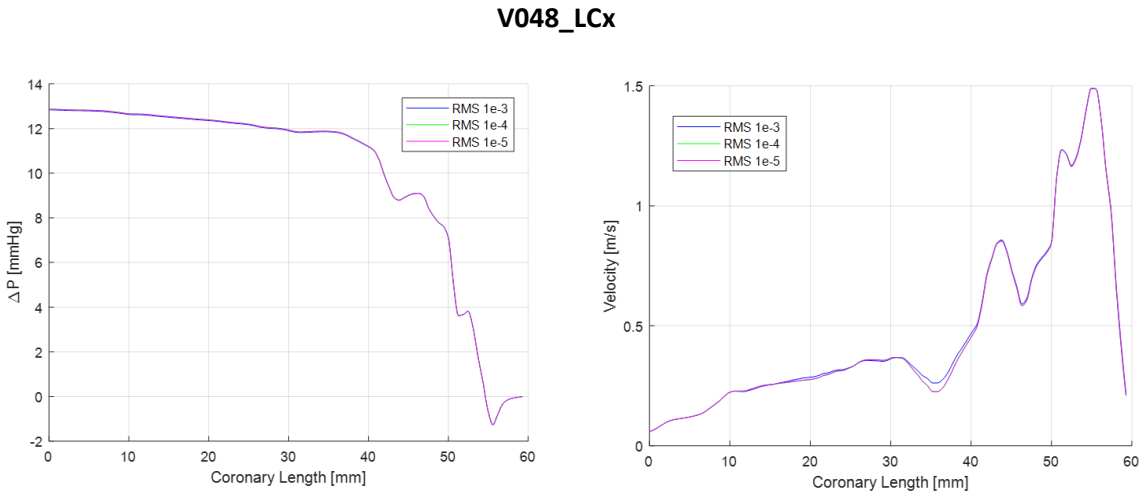

Figure 5.3: Results of different convergence criteria for case V048_LCx.
Left) Pressure drop vs Length along the centreline for different convergence criteria. Right) Blood velocity vs Length along the centreline for different convergence criteria.

As can be seen, the computed pressure and velocity profiles along the centreline are identical for RMS residuals $\leq 10^{-4}$. All the CFD simulations computed in this chapter are set to reach a convergence criteria of 10^{-4} based on these findings.

5.2.3 Full 3D CFD simulations

Starting from the patient specific stl files, nine volumetric meshes have been created for full 3D CFD analyses. The type of boundary conditions were already set up during the creation of the meshes under the Fluent Meshing environment; however, boundary conditions values have to be given during the solver settings. Regarding the rheology, blood had been characterised by a viscosity of $\mu_b = 0.035\ [\frac{g}{cm\ s}]$ and $\rho = 1066\ \left[\frac{Kg}{m^3}\right]$.

The steady state numerical CFD simulations have been performed in parallel using 4 cores of an Intel i7-6700 at 3.4GHz with 32GB of RAM. On average a full 3D simulation took ≈ 15 mins to reach convergence. Figure 5.3 and Figure 5.4 show two examples of results for full 3D

solutions on two patient specific cases. As expected, in the pressure contour plot a sudden decrease in pressure is observed when the blood flow encounters the stenosis, with an associated increase of velocity. The actual pressure profile along the centreline for these two cases (and other 3D geometries) will be presented in the next section.

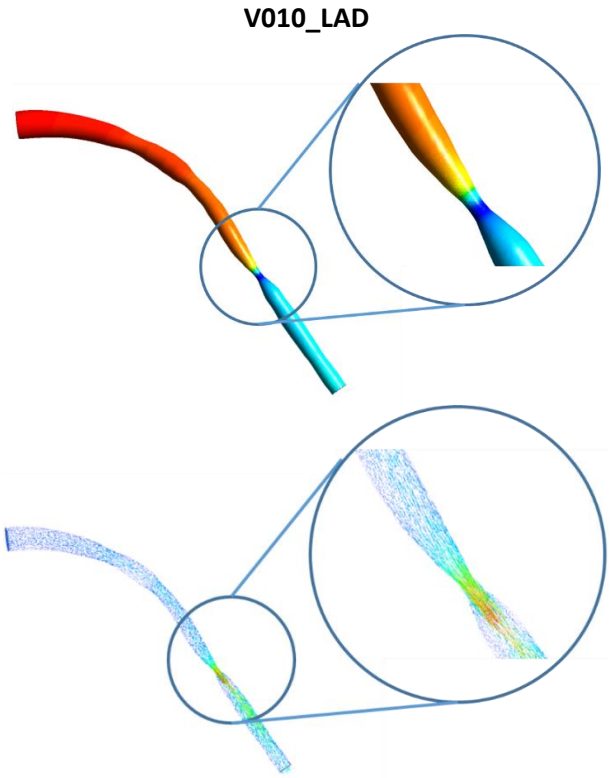

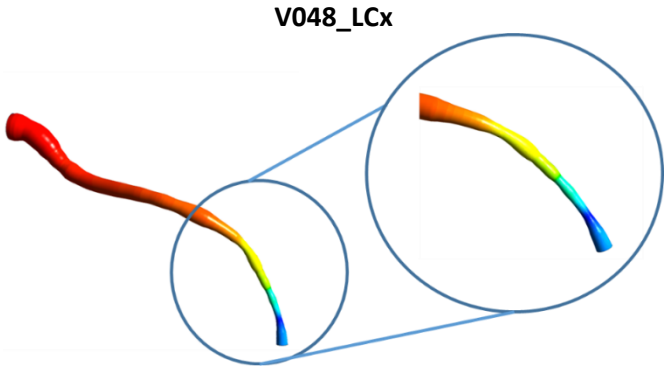

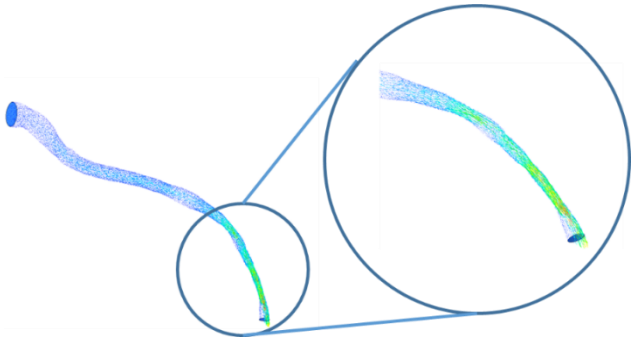

Figure 5.4: CFD results of full 3D pressure profile (top) and velocity field (bottom) for case V010_LAD and V048LCx.
It is possible to notice the pressure drop across and the increase in velocity across the stenosis.

5.2.4 3D CFD simulations with 2D curvature

In this section, 3D CFD simulations have been performed on the same dataset of patient specific geometries considered in the previous paragraph, but with the geometry adjusted so that the vessel centreline lies in a plane. The aim of this section is to study if the fluid flow patterns and the pressure drop remains invariant when considering a coronary centreline with two dimensions rather than three. The motivation for this study is that coronary arteries can have high curvatures, but generally these are in a single plane. The out-of-plane curvatures are usually relatively small, and this might provide the opportunity to reduce the number of parameters needed for a ROM characterisation for clinical application, with benefits in stability, accuracy and computational effort in the construction of the ROM.

Extract 2D coronary centreline from 3D geometries

In order to extract the centreline information starting from the 3D geometry, the first step is to compute the best fitting plane to the *xyz* coordinates of the 3D coronary centreline.

The general equation of a plane is (Eq.5.1):

$$Ax + By + Cz + D = 0 \tag{Eq.5.1}$$

The idea is to compute the best coefficients of the plane (A, B, C and D) employing an optimisation problem. The goal is to minimise a particular cost function starting from an initial guess.

The cost function to be minimised is the sum of the distances between the computed plane and the 3D centreline points. The cost function has the form (Eq.5.2):

$$cost_{func} = \sum_{i=1}^{N} \frac{|Ax_{pi} + By_{pi} + Cz_{pi} + D|}{\sqrt{A^2 + B^2 + C^2}} \tag{Eq.5.2}$$

where x_{pi}, y_{pi} and z_{pi} are the 3D coordinates of the *ith* point P.

All the coefficients have been set equal to 1 for initialisation. This optimisation problem had been solved in MATLAB using the *fminsearch* algorithm. At this stage, the next step is to project the 3D centreline points onto the fitting plane. For any given 3D point $P(x_p, y_p, z_p)$ the problem is to find its projection P' which lies on the plane. Furthermore, P' lies at the same time on the line PP' which is normal to the plane. The coordinates of any point along the line PP' can be written in parametric form as (Eq.5.3):

$$\begin{cases} x = x_P + At \\ y = y_P + Bt \\ z = z_P + Ct \end{cases} \quad \text{(Eq.5.3)}$$

Plugging these equations into the equation of the plane (Eq.5.5) will determine the value of the parameter t such that the point will be at the same time on the plane and along the normal line. The general form of the equation to solve for the parameter t is (Eq.5.4):

$$A(x_P + At) + B(y_P + Bt) + C(z_P + Ct) + D = 0 \quad \text{(Eq.5.4)}$$

An example of the best fitting and the computation of the projection of the 3D points onto the plane is shown in **Figure 5.5.**

The computation of the best fitted plane has been repeated for each of the 9 patient specific cases.

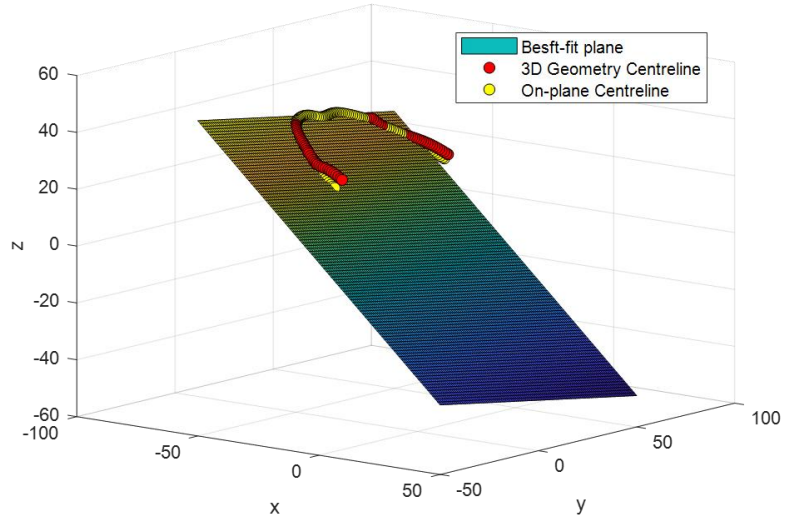

Figure 5.5: Example of best fitting plane for a 3D coronary centreline.
Red line) Original 3D coronary centreline shape. Yellow line) The 3D centreline has been projected on the best fitting plane.

5.2.5 Results of the comparison

A graphical comparison with pressure contours plot for the 3D geometries with 2D curvature and 2D axisymmetric geometries is presented in Figure 5.6. A quantitative comparison with

pressure profiles plots between the three different models is shown in Figure 5.7. For the right hand figures the view is along the plane of the artery to emphasise the planar geometry.

V010_Dx

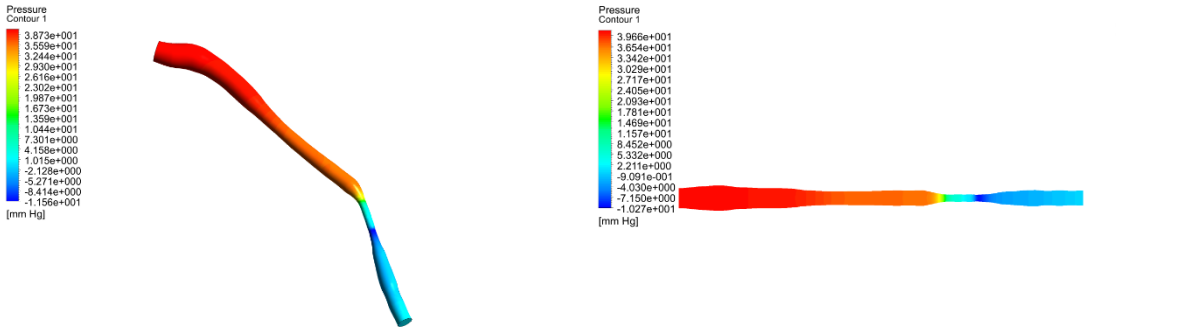

V010_LAD

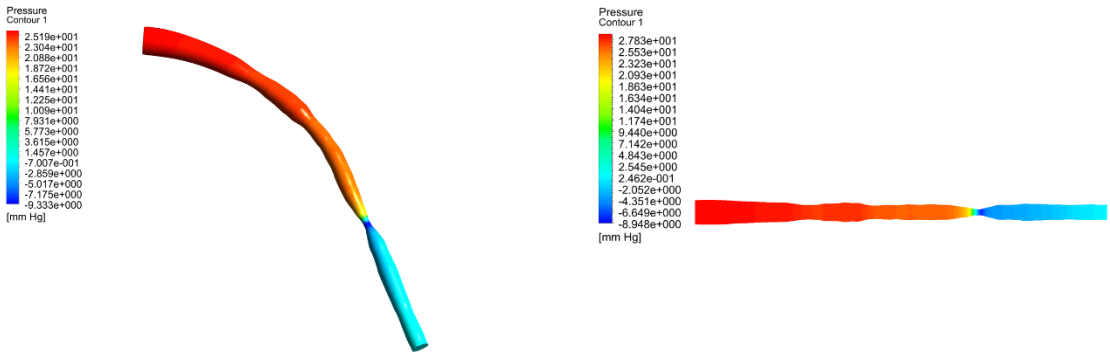

V015_RCA

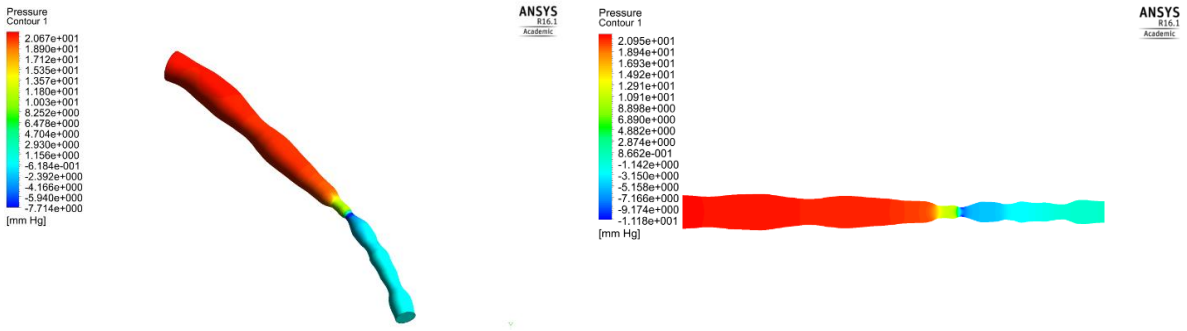

V018_LAD

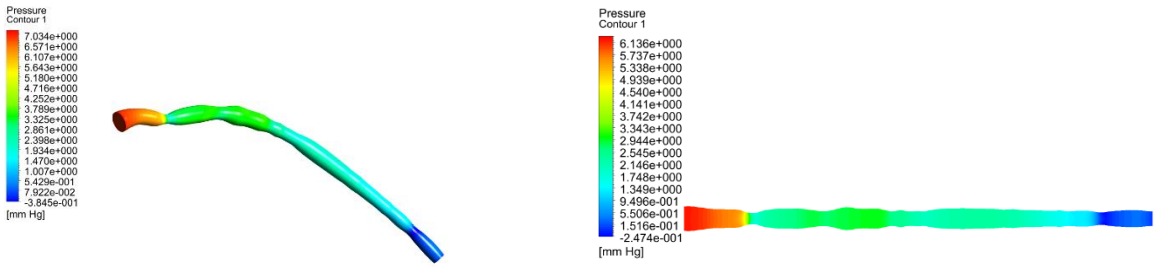

V019_LAD

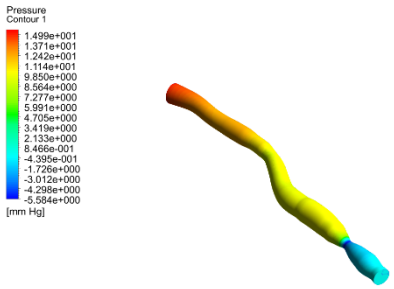

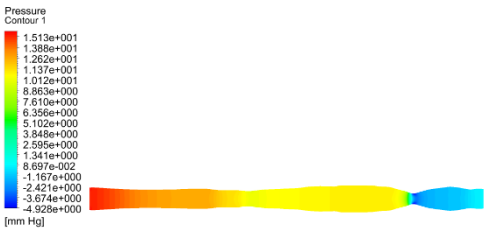

V020_LAD

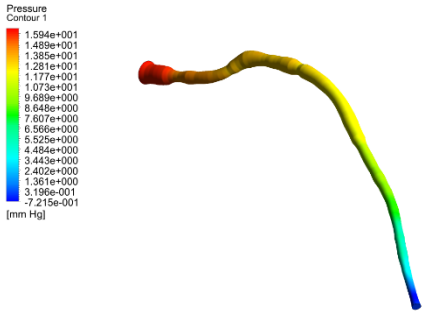

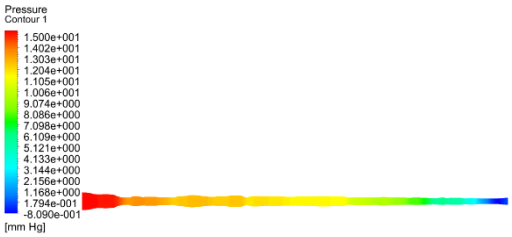

V028_LAD

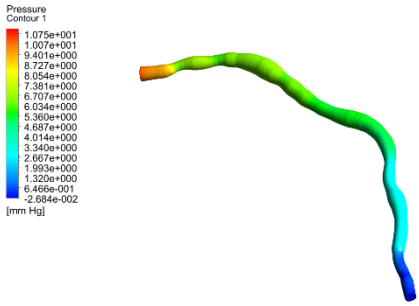

V048_LCx

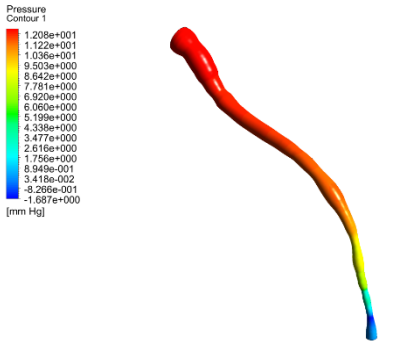

V065_RCA

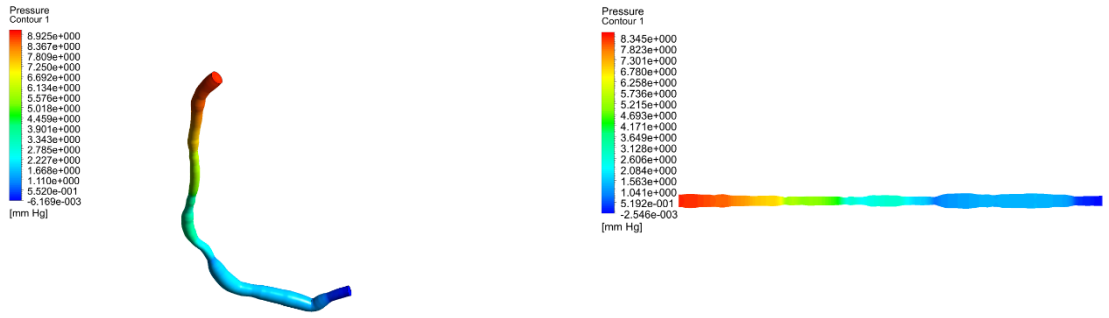

Figure 5.6: Qualitative visual comparison of pressure profiles for the 9 cases. Left column) CFD on the 3D geometries with 2D curvature. Right column) CFD on 2D axisymmetric geometries.

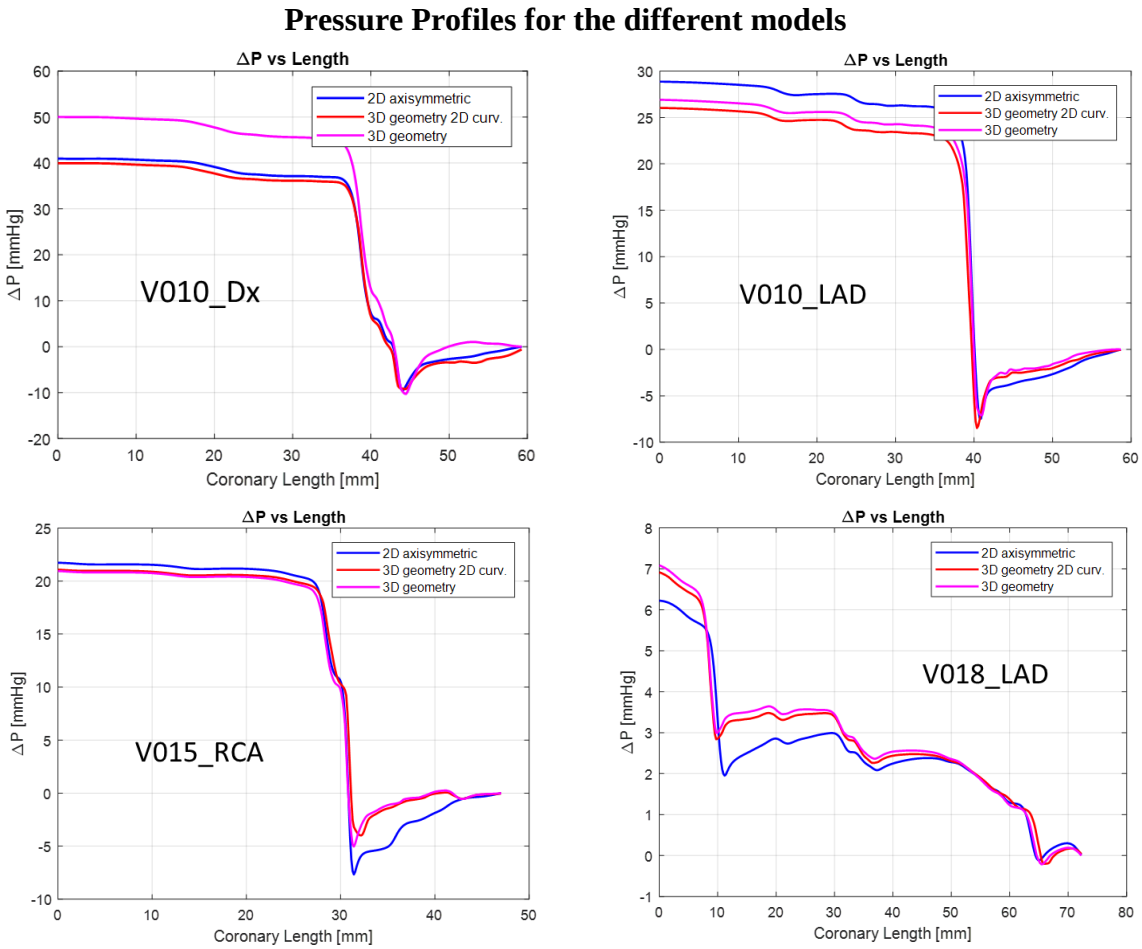

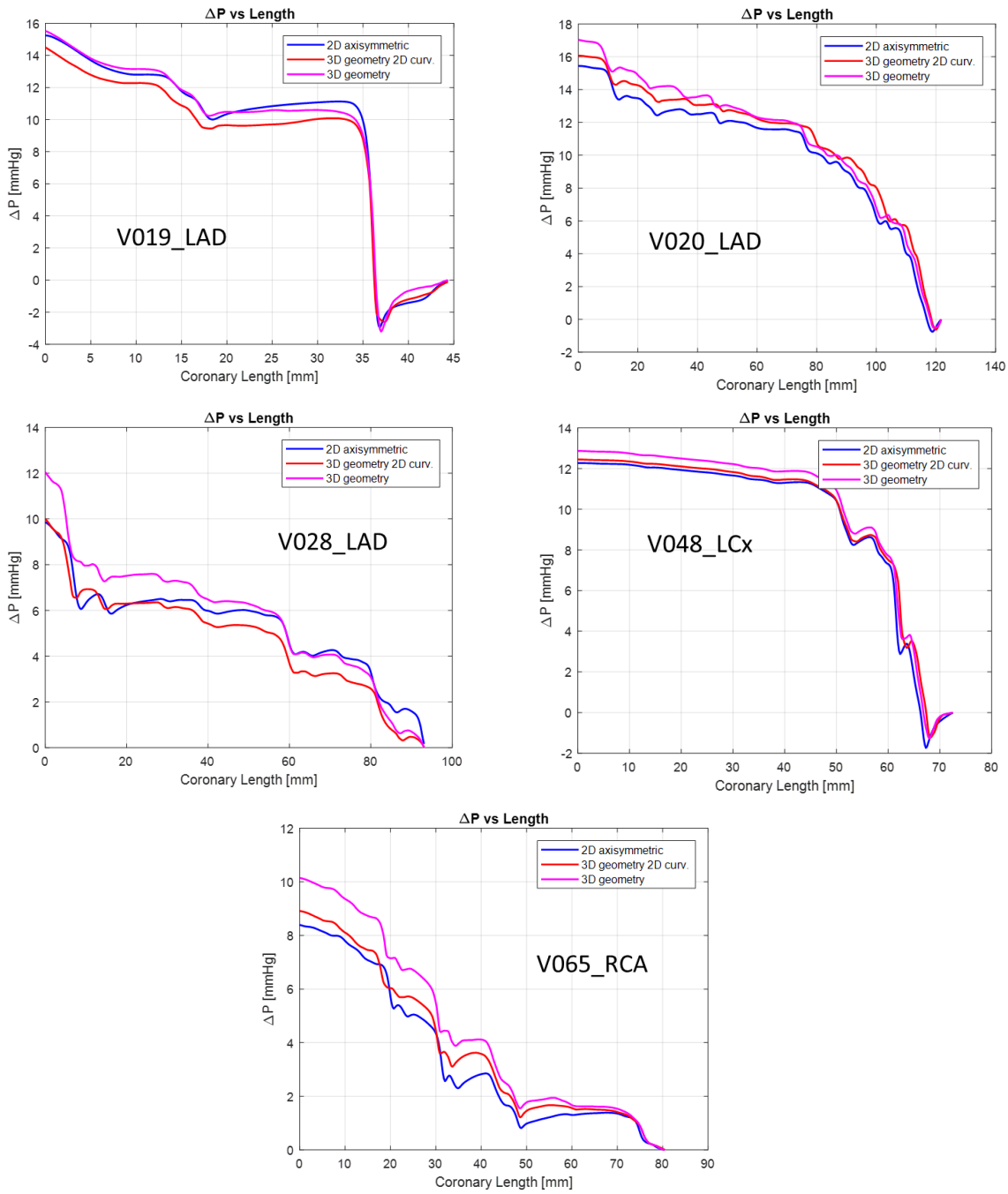

Figure 5.7: Pressure profiles for the 9 patient-specific coronary geometries obtained with different models. Blue lines) Pressure profiles obtained from the 2D axisymmetric models. Purple lines) Pressure profiles obtained from the 3D with 2D curvature models. Red lines) Pressure profiles obtained from the full 3D models

Visual inspection of the individual case results presented in Figure 5.7 indicates that the 2D-curved model and the straight-axisymmetric model both give distributions that are qualitatively similar to the 3D result, and this is quantitatively verified in Table 5-1 and in Figure 5.8 where the different values of FFR for the different models has been compared for each case.

Table 5.1: Comparison of the different FFR values computed with different models and cases.

Case name	2D FFR	3D with 2D curv.	Full 3D
10_Dx	0.5904	0.5948	0.50
10_LCA	0.7112	0.7392	0.73
15_RCA	0.7827	0.7889	0.7906
18_LAD	0.9380	0.9312	0.9202
19_LAD	0.8474	0.8539	0.8447
20_LAD	0.8454	0.8393	0.8297
28_LCx	0.9031	0.9003	0.8796
48_LCx	0.8771	0.8754	0.8713
65_RCA	0.9161	0.9110	0.8986

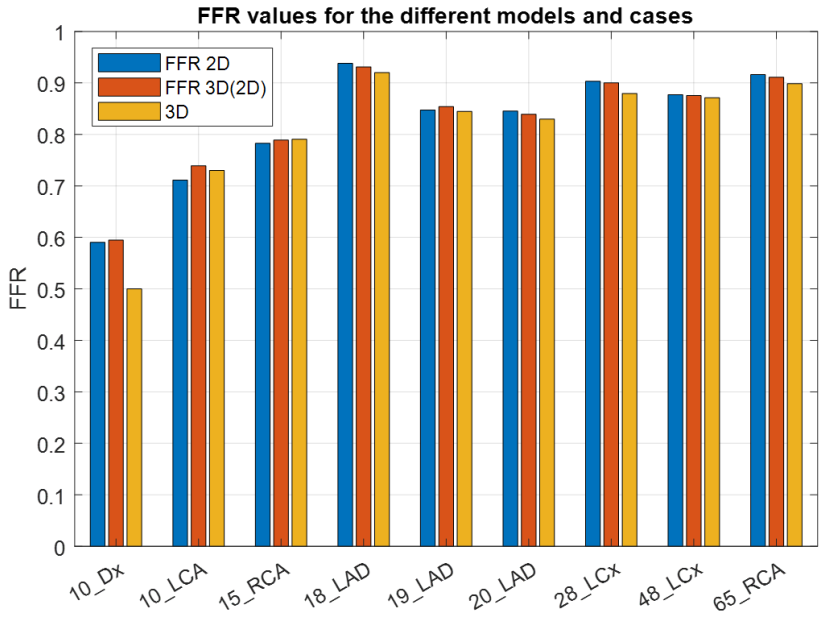

Figure 5.8: Comparison of FFR values for the different nine cases and models.

As would be expected, the 2D-curved results (red curves), as a first level of approximation, are generally closer to the 3D results (pink curve) than are the straight-axisymmetric results (blue curves). For three of the nine cases (cases 10_Dx, 28_LCx and 65_RCA) the 3D curvature appears to be more important: the 2D-curved and 2D-axisymmetric results are similar to each other but less similar to the 3D. In absolute terms the most significant deviation (approximately 10 mmHg) is for case 10_Dx. This case had been studied more carefully in order to understand the reason for the difference on the pressure profiles (Figure 5.9-5.13).

V010_Dx (3D with 2D curvature) **V010_Dx (full 3D)**

Figure 5.9: Geometries for case V010 Dx obtained with the approach 3D with 2D curvature (left) and the full 3D approach (right).

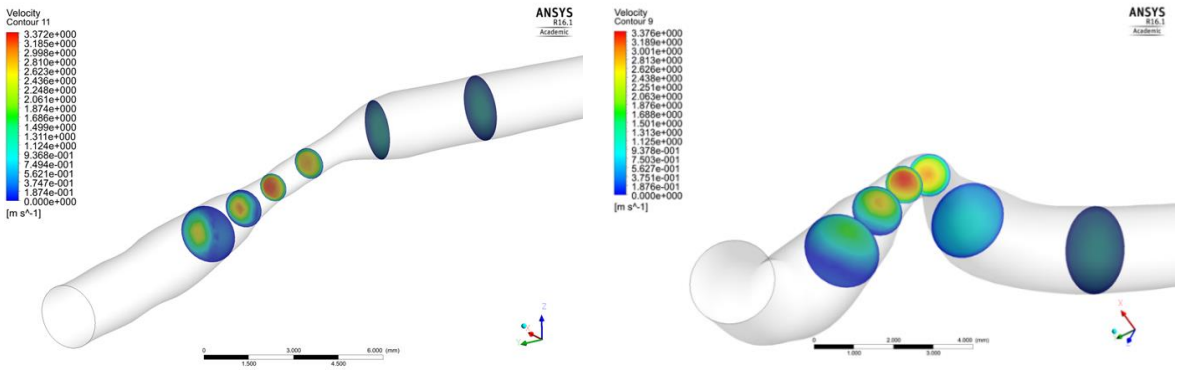

Figure 5.10: Results of velocity contours in selected planes for case V010 Dx obtained with the approach 3D with 2D curvature (left) and the full 3D approach (right).

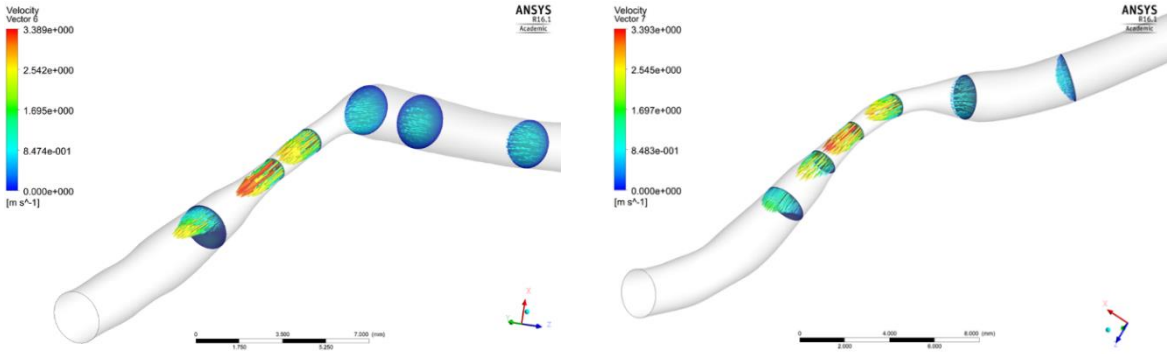

Figure 5.11: Results of velocity vectors in selected planes for case V010 Dx obtained with the approach 3D with 2D curvature approach (left) and the full 3D approach (right).

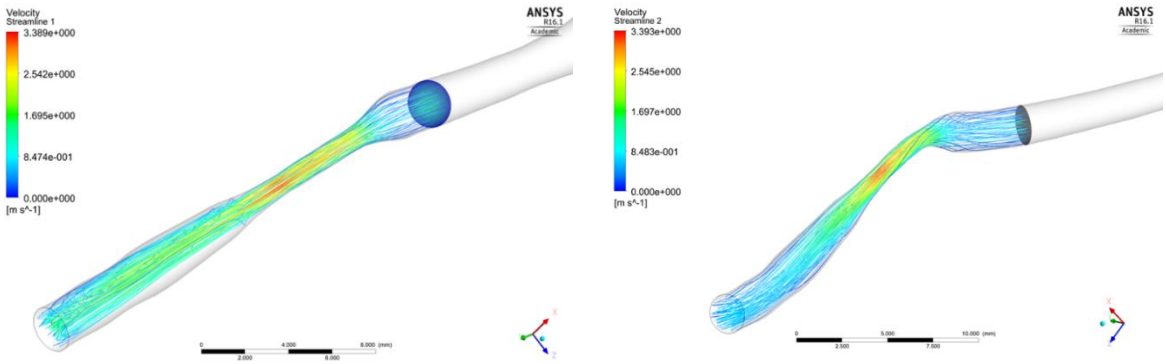

Figure 5.12: Results of velocity streamlines in selected planes for case V010 Dx obtained with the approach 3D with 2D curvature approach (left) and the full 3D approach (right).

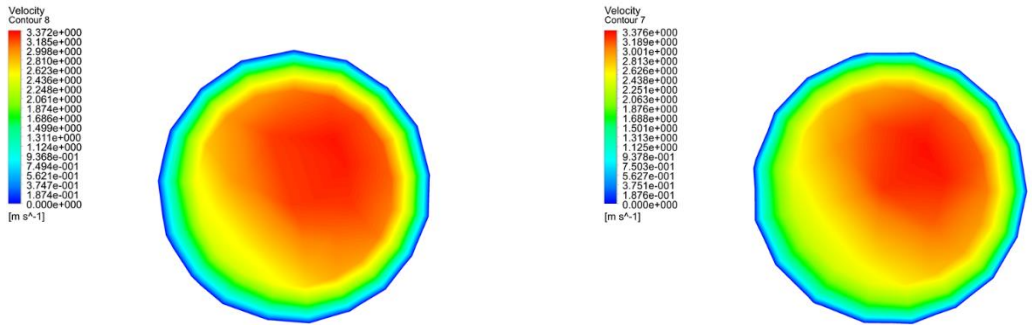

Figure 5.13: Results of velocity contour in a selected for case V010 Dx obtained with the approach 3D with 2D curvature approach (left) and the full 3D approach (right).

It is clear how the sharp curvature of the stenosis is affecting the increasing of pressure gradient. Although the deviation of the centreline out of the plane is small compared with the length of the vessel, and the associated out-of-plane curvatures are low compared with the curvature in-plane, the streamlines indicate a more spiral component of the flow in the full 3D. It might be possible in the future to identify which vessels might require full 3D analysis by a priori examination of the curvature and tortuosity of the vessels, and this is highlighted in the further work chapter.

5.3 Geometrical Parameterisation

In Chapter 4 all the ingredients have been given to create a ROM including geometrical parameters for the shape approximation of the radius along the length. Furthermore, it had been shown that in order to create a ROM a parametric representation of the system is required. In this section will be introduced a centreline parameterisation in order to create ROMs for curved coronary arteries, reflecting the geometries that are typically seen in patients [149]–[152]. As discussed in the previous section, to reduce the number of parameters the coronaries are represented by planar approximations, capturing only the primary curvature. This can readily be extended in the future to a full 3D representation at the cost of an increased number of parameters. The workflow developed for this application is shown below (Figure 5.14):

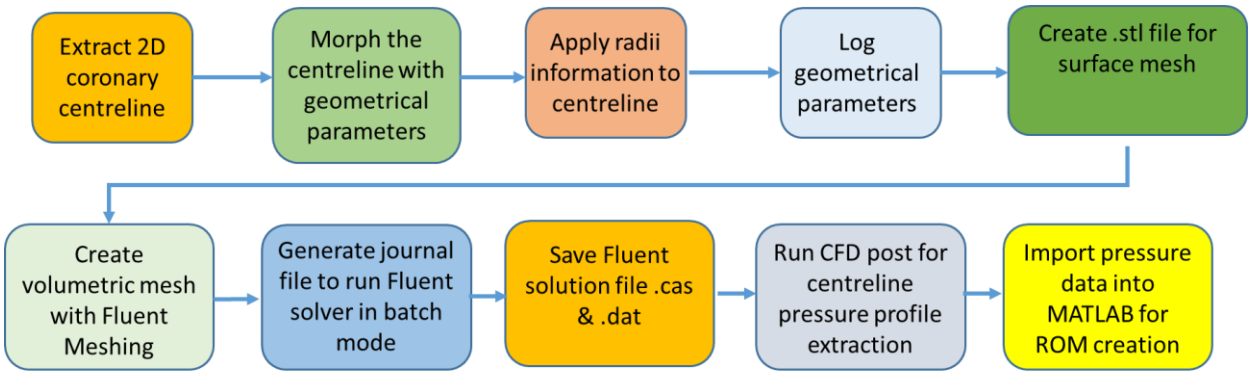

Figure 5.14: Workflow

5.3.1 Patient-specific parameterisation of coronary centreline

In the literature there are multiple methods to parameterise a curve (e.g. polynomials, spline) [131]; in this section a Fourier-based parameterisation method for the 3D curves, combined with a first order polynomial, is chosen for approximating coronary centrelines. A general 3D representation of a centreline using a finite number of harmonics would be of the form:

$$x_n = C_{x_0} + C_{x_1} t_n + \sum_{h=1}^{H} A_{x_h} \cos(2\pi h t_n) + B_{x_h} \sin(2\pi h t_n)$$
$$y_n = C_{y_0} + C_{y_1} t_n + \sum_{h=1}^{H} A_{y_h} \cos(2\pi h t_n) + B_{y_h} \sin(2\pi h t_n) \quad \text{(Eq.5.5)}$$
$$z_n = C_{z_0} + C_{z_1} t_n + \sum_{h=1}^{H} A_{z_h} \cos(2\pi h t_n) + B_{z_h} \sin(2\pi h t_n)$$

However, it has been chosen to represent the different coronary centrelines on a local axis system so that the displacements in the local *z* direction are minimised (Figure 5.15). The Fourier approximation has the desirable property that the lower frequency coefficients remain stable as higher-order terms are added to increase the fidelity of the representation (in contrast as higher order terms are added to improve a polynomial representation all coefficients change). Furthermore, a good approximation is achieved using only few harmonics. For this application the control parameter *t* is chosen to be zero at the inlet and unity at the outlet. The local axis system in which the vessel is defined has its origin at the inlet and the *x*-axis along the line from the inlet to the outlet. Then the linear polynomial coefficients in the *y* and *z* directions are zero and the deviation from the axis is simply a Fourier series. The linear polynomial coefficient in the *x*-direction is a length term. The *xy* plane is defined as that containing the inlet, the outlet and the point on the centreline that is furthest from the x axis. The selection of a local co-ordinate system by this process is appropriate because the 3D parametric representation of the coronary is independent of the pose (i.e. it doesn't matter how the coronary is oriented in space, only the shape matters, so the representation is independent of the image views and image co-ordinate system). The centreline based Fourier approximation plays a key role in the proposed centreline parameterisation algorithm.

Figure 5.16 shows that the coronary centreline using ≈ 150 harmonics overlapps perfectly with the original coronary centreline. It is natural that the error of the approximation is much higher when considering only one Fourier harmonic. However, the overall curvature of the coronary centreline in the 3D space is captured very well (Figure 5.17).

The idea for constructing a parameterised ROM is to consider only 6 parameters for describing the curvature and the other 12 parameters describing the shape parameterisation and mass-flow inlet. The 3D centreline is parameterised with only one harmonic; the chosen parameters shown in Table 5-2Table 5-2: Constant, linear, cosine and sine coefficients for each coordinate. in yellow are the ones considered for parameterisation. The *y*-coordinate constant coefficient represents the average values of the 3D curved centreline along the *y* axis; the *x* coordinate for the linear coefficient is representing the distance between the starting point of the coronary and the end point. Furthermore, the cosine and sine coefficients for the x and y coordinates are considered.

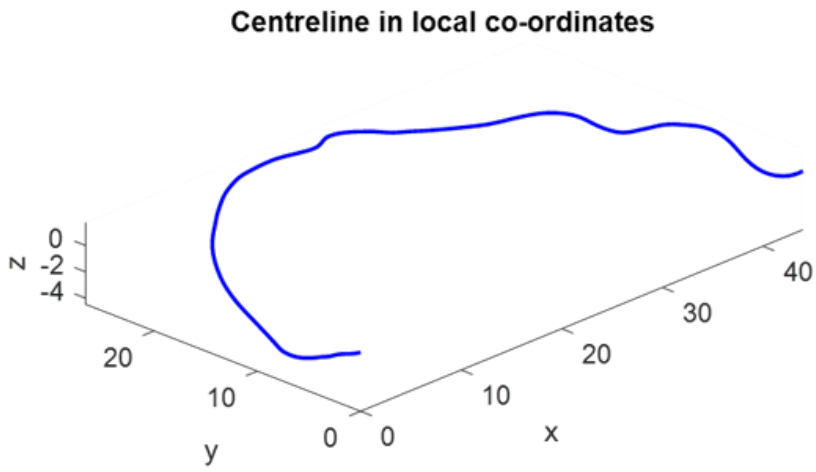

Figure 5.15: Example of 3D coronary centreline in local coordinate system.

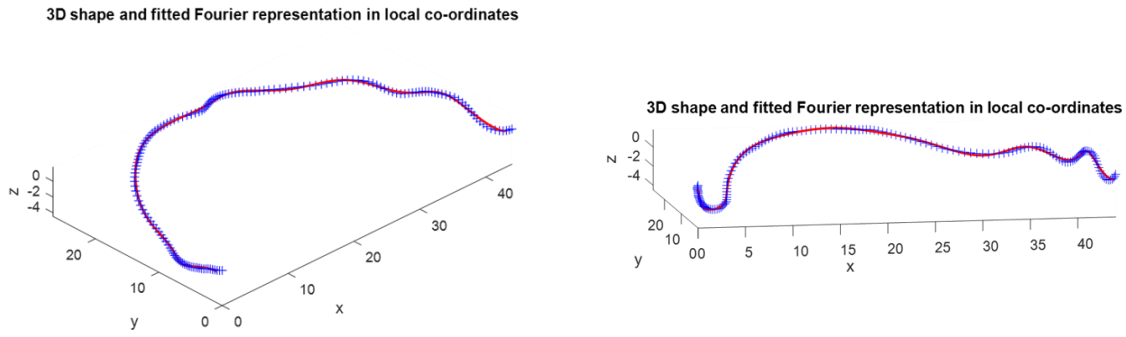

Figure 5.16: Two different views of a coronary centreline parameterised and approximated with ≈ 150 Fourier harmonics.

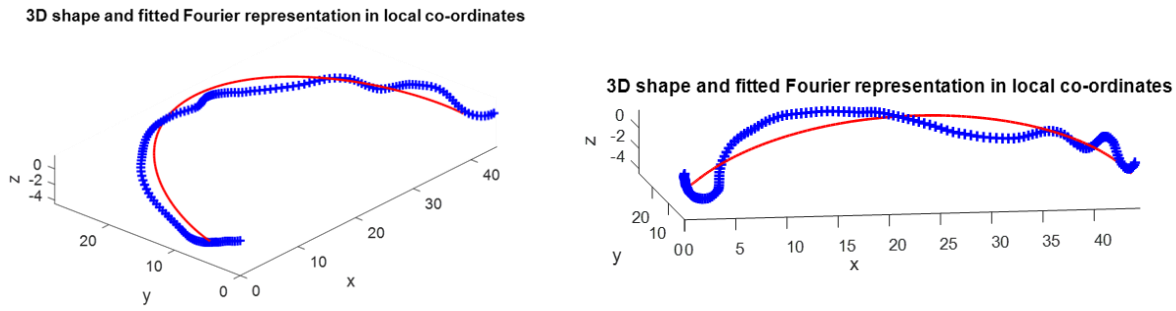

Figure 5.17: Two different views of a coronary centreline parameterised and approximated with only one Fourier harmonic.

As expected the first few harmonics are collecting most of the information achieving a good grade of accuracy (Figure 5.18)

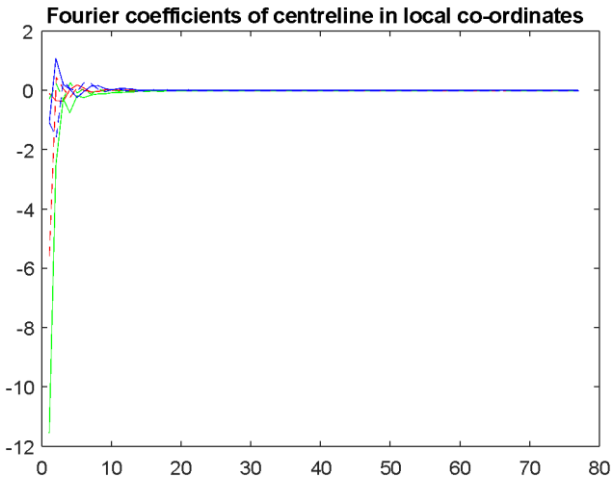

Figure 5.18: Fourier coefficients of centreline in local co-ordinates.

The coefficients matrix with one harmonic is presented in Table 5-2.

Table 5.2: Constant, linear, cosine and sine coefficients for each coordinate.

	Constant Coeff.	Linear Coeff.	First Cosine	First Sine
x-coordinate	**0.601**	**43.980**	**-0.1032**	**-5.5737**
y-coordinate	**16.685**	**0**	**-11.548**	**-0.2789**
z-coordinate	**-0.784**	**0**	**-1.091**	**-1.0804**

The total number of parameters, including geometrical and physical parameters, is 17 (Table 5-3).

Table 5.3: List of geometrical and physical parameters.

Parameters
$\boldsymbol{Amplitude_i\ \ i = 1 \dots 8}$
$\boldsymbol{Taper\ x\ 2}$
$\boldsymbol{Fourier\ x\ 5}$
$\boldsymbol{Mass\ Flow}$
$\boldsymbol{Vessel\ Length}$

Once the centreline for a single geometry had been morphed and parameterised the next step is to apply radius information to the centreline. Geometrical parameters from the previous chapter had been used for the radii information.

5.3.2 Creation of a 3D training dataset

The LCx considered for the parameterisation is shown in Figure 5.19 and Figure 5.21 (V048_LCx). The Fourier parameters for the description of the 3D centreline are presented in Table 5-4.

Table 5.4: Constant, linear, cosine and sine coefficients for each coordinate for V048_LCx

	Constant Coeff.	Linear Coeff.	First Cosine	First Sine
x-coordinate	1.185	62.823	-0.309	-0.4174
y-coordinate	7.178	0	-5.426	-3.825
z-coordinate	-0.285	0	-1.188	1.572

The 6 parameters are perturbed in order to describe different coronary centrelines.

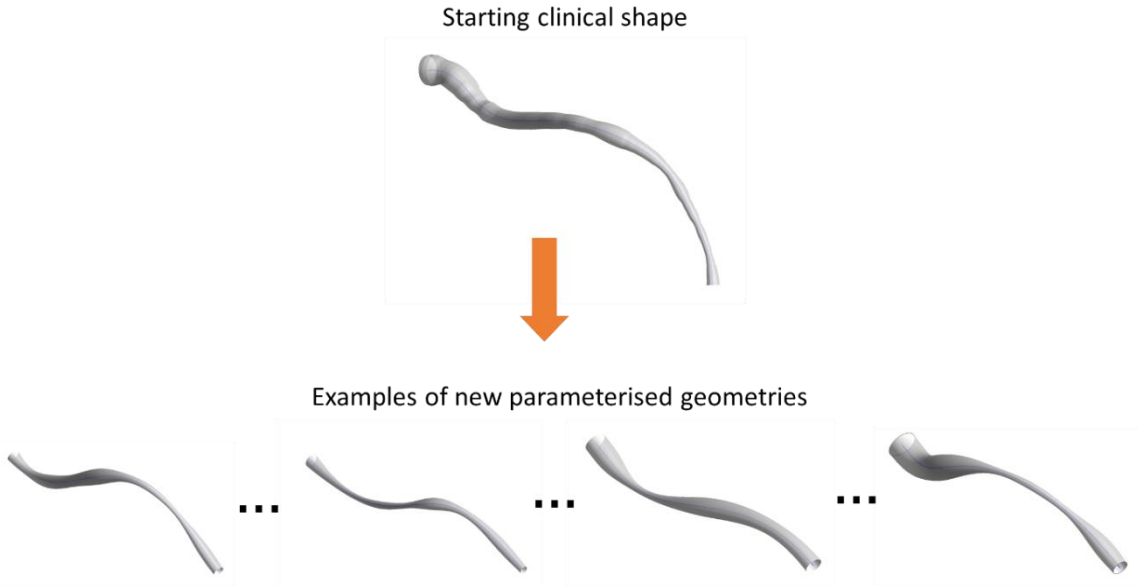

Figure 5.19: 3D morphing of a patient-specific LCA geometry.

In Figure 5.20 it is possible to notice how the four geometries shown in Figure 5.19 vary between them starting from the clinical geometry.

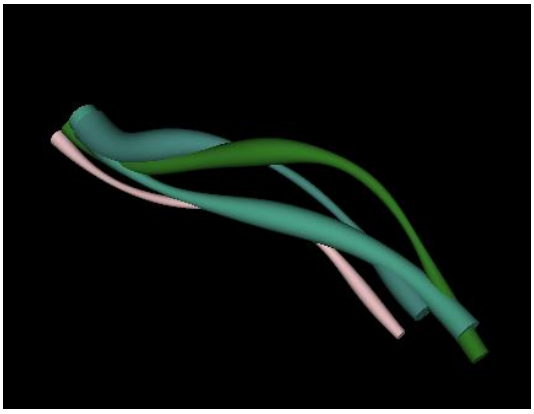

Figure 5.20: The four cases overlapping each other for visualisation.

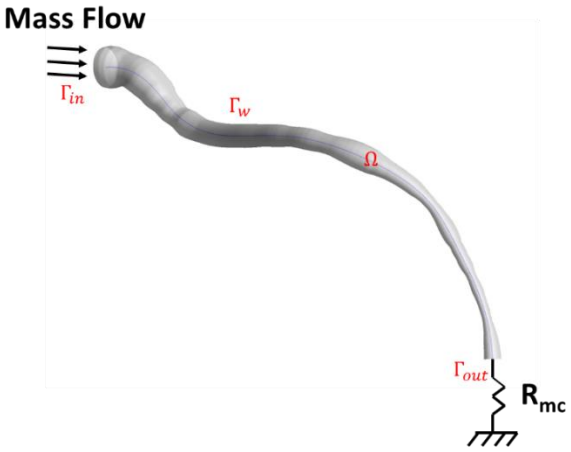

Figure 5.21: Original clinical geometry

Starting from the morphed centrelines, radius variation with shape parameters have been considered for creating cross sectional circles along the centreline to form the coronary skeleton.

5.4 Building the ROM for the 3D single lumen geometries

ROMs have the potential to compute quasi real time analyses which is an extremely useful feature for medical application; moreover they require less RAM and CPU compared to a full CFD simulation. A Proper Orthogonal Decomposition (POD) algorithm is employed to compute the reduced basis (section 1.5.1). However, choosing an appropriate and efficient set of basis functions for a particular application can be challenging.

During the *off-line* phase 3D simulations have to be computed. The correlation matrix S (eq. 1.15) is then formed by the pressure profile along the centreline for every phantom geometry considered. In this application the chosen input parameters are the coefficients of the Fourier harmonics describing the curvature of the centreline, a length term, the shape parameters for

the radius variation and the inlet mass-flow rate (a total of 17 parameters). The main purpose of this section is the computation of the modes and the modes coefficients to reconstruct the pressure profile for 3D coronary geometries.

5.4.1 3D ROMs challenges

A prerequisite for ROM construction is the rectangular form of the solution snapshot matrix *S*. In fact, all the CFD solution vectors have to be of the same dimension. In practice, the construction of the *S* matrix requires computing CFD simulations on isotopological meshes (same connectivity and number of nodes on the meshes) whilst changing the input parameters (geometrical and/or physical parameters). However, if creating isotopological quadrilateral meshes for 2D axisymmetric models in MATLAB had been a fairly easy process to perform, for 3D ROM applications involving input geometrical parameters, creating accurate volumetric isotopological meshes using mesh morphing techniques is still challenging [153].

A practical solution could have been using the mesh morpher tool embedded in ANSYS Fluent, employing the usage of control points. However, this tool is not designed to accommodate severely deformed geometries (both global and local deformations). If any severe deformations occur when using the mesh morpher, a warning message indicates that the morphing is not possible and a re-mesh of the geometry has to be performed. A re-meshing of the morphed geometry would result in a mesh with a completely different number of nodes than the starting non-morphed mesh. Testing with the available clinical data indicated that this re-meshing occurred in a large proportion of the cases.

Therefore, there are some restrictions and limitations in the application of the ROMBuilder tool that was used for the analysis presented in chapter 4 to the 3D curved systems when using the parameterisations developed for the current study. Alternative parameterisations and geometrical representations would have been possible that would have supported the direct application of the ANSYS ROMBuilder tool but for the purposes of this thesis, for consistency of parameterisation, a custom process for development of the ROM has been developed, described below.

1. Extract a series of points on the 3D centreline and the radius as a function of position from segmentation of the image projections;
2. Produce a parametric representation of the centreline in 3D; the case and simulations results (.cas and .dat files) are saved for each geometry onto the dataset;

3. Create a 3D surface with the appropriate radius distribution on the parameterised centreline;
4. Perform CFD analyses;
5. Simulation results are imported into CFD-Post for result visualisation and validation;
6. The .csv file created at step 1 is imported in CFD-Post to create a polyline;
7. Pressure values are saved along the 3D polyline as a .csv file;
8. .csv files are imported into MATLAB to build the snapshot matrix **S** and for building the 3D ROM.

This process supports the population of the *S* matrix with just the pressure profiles along the centreline for different 3D geometries, as required for the construction of a ROM for the purposes of this specific FFR application.

5.5 Results

In this section projection and interpolation errors are presented for the 3D ROM. Several questions arise in the application and validation of the ROM. The first is whether the reconstructed solutions from the modes are equivalent to the original solutions (they should be if the implementation is correct), and how effectively a reduced number of modes retained in the reconstruction can represent the original solution in the training set. The error in this representation is called the projection error. The second is whether the modes computed in a training set can be used effectively to describe a new system, not in the training set, if appropriate coefficients can be found. Finally, can the appropriate coefficients for the new system be found by interpolation in the space of the training set? The following paragraphs address these questions for the ROM constructed for this application.

5.5.1 Projection errors

The decomposition produces a transformation from raw pressure data at each point in the solution space to the representation as a linear combination of the modes. If all modes are included in a reconstruction, with their appropriate coefficients, the original field is recovered. An approximation of the field is recovered by omitting the higher modes. The first validation test is the measurement of the projection errors versus the number of retained modes, exploiting for training the full size of the dataset (N = 329 coronaries). The code, implemented in MATLAB, has been run several times, increasing the number of extracted modes. Table 5-5 presents the mean projection errors and the maximum projection errors (with case number) for specific numbers of modes, whilst Figure 5.22 is showing how the projection errors are decreasing whilst increasing the number of modes.

Table 5.5: Mean and maximum projection errors for specific number of modes.

# of modes	Mean Fractional Projection errors	Max Fractional Projection error
2	0.251	0.721 (168)
8	0.068	0.464 (168)
12	0.032	0.178 (32)
15	0.020	0.140 (32)

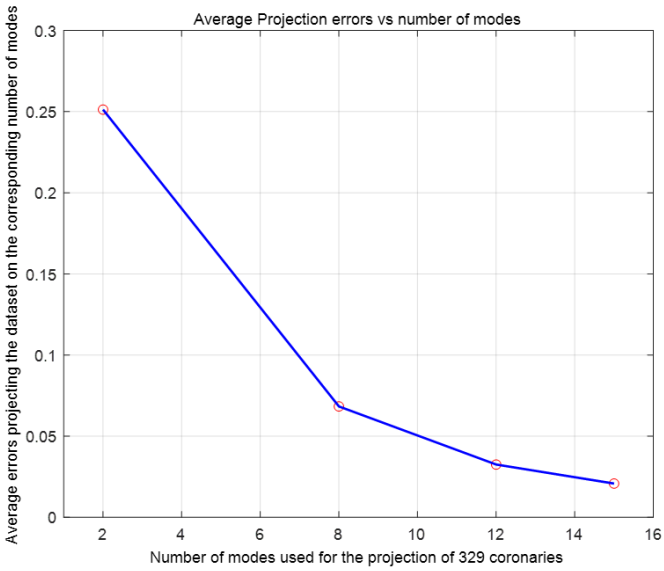

Figure 5.22: Average projection errors vs number of modes. Using the entire dataset for training.

Example #1 (Case #1)

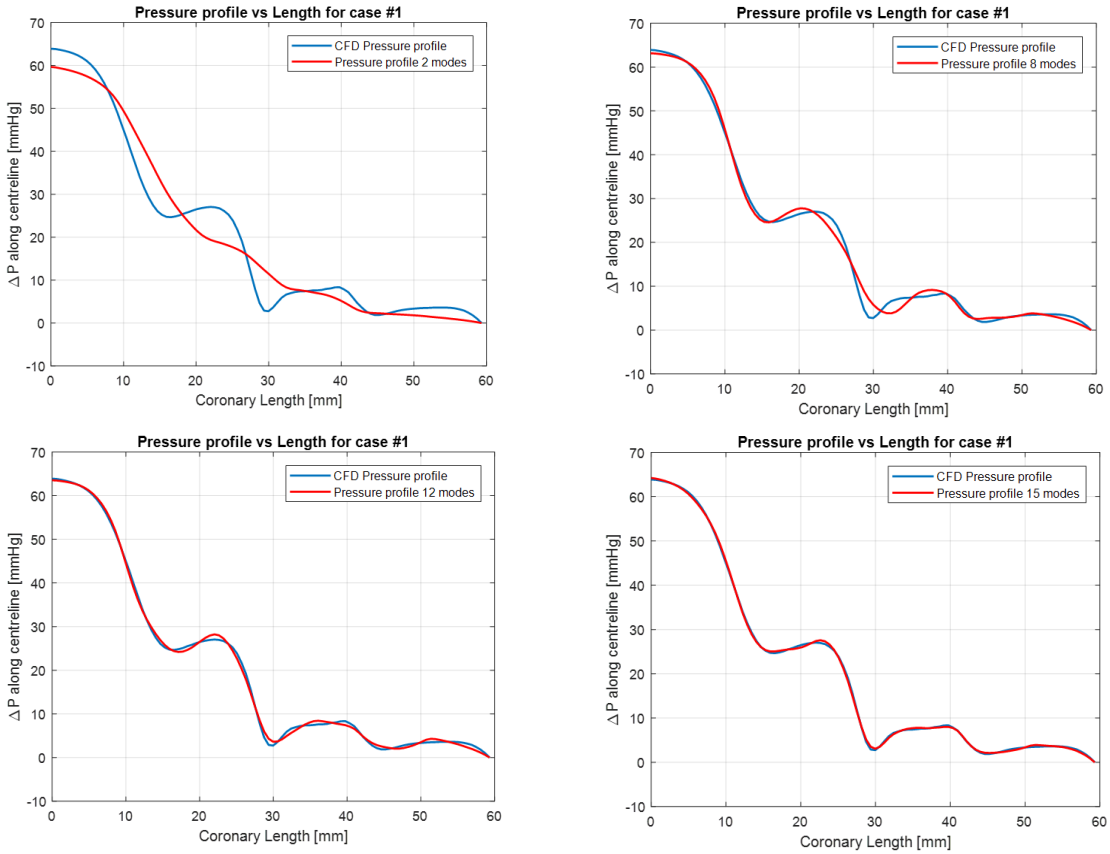

Example #2 (Case #8)

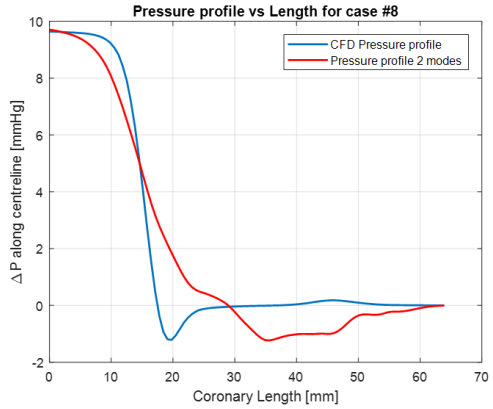

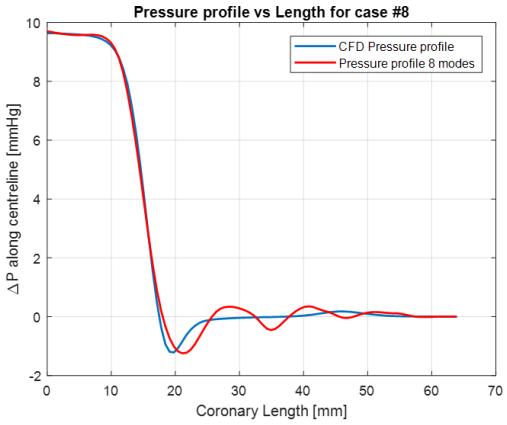

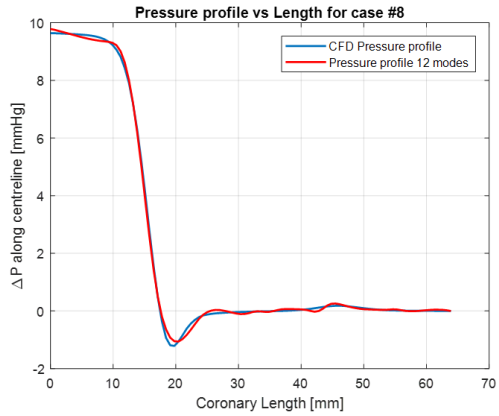

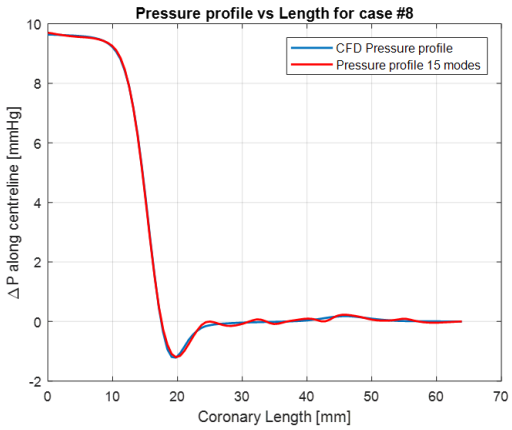

Example #3 (Case #25)

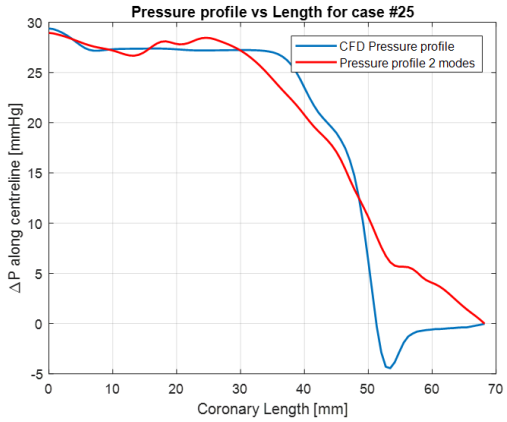
Pressure profile vs Length for case #25
CFD Pressure profile
Pressure profile 2 modes
ΔP along centreline [mmHg]
Coronary Length [mm]

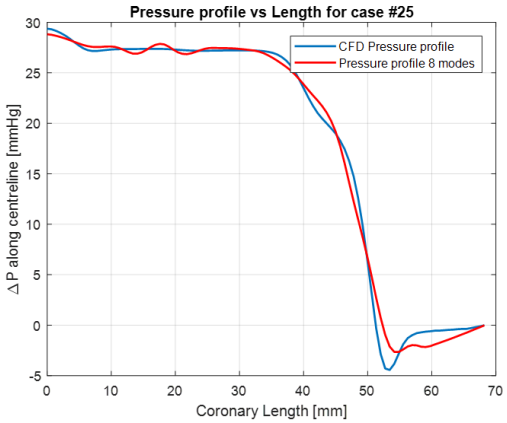
Pressure profile vs Length for case #25
CFD Pressure profile
Pressure profile 8 modes
ΔP along centreline [mmHg]
Coronary Length [mm]

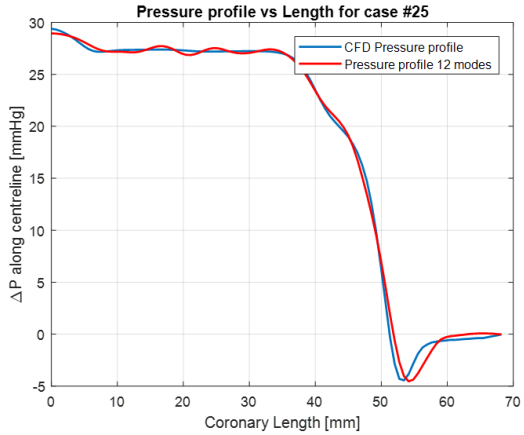
Pressure profile vs Length for case #25
CFD Pressure profile
Pressure profile 12 modes
ΔP along centreline [mmHg]
Coronary Length [mm]

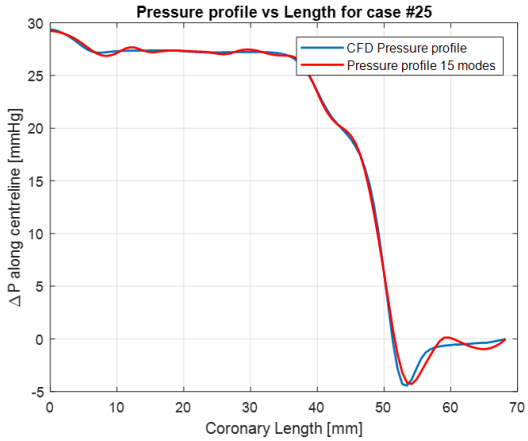
Pressure profile vs Length for case #25
CFD Pressure profile
Pressure profile 15 modes
ΔP along centreline [mmHg]
Coronary Length [mm]

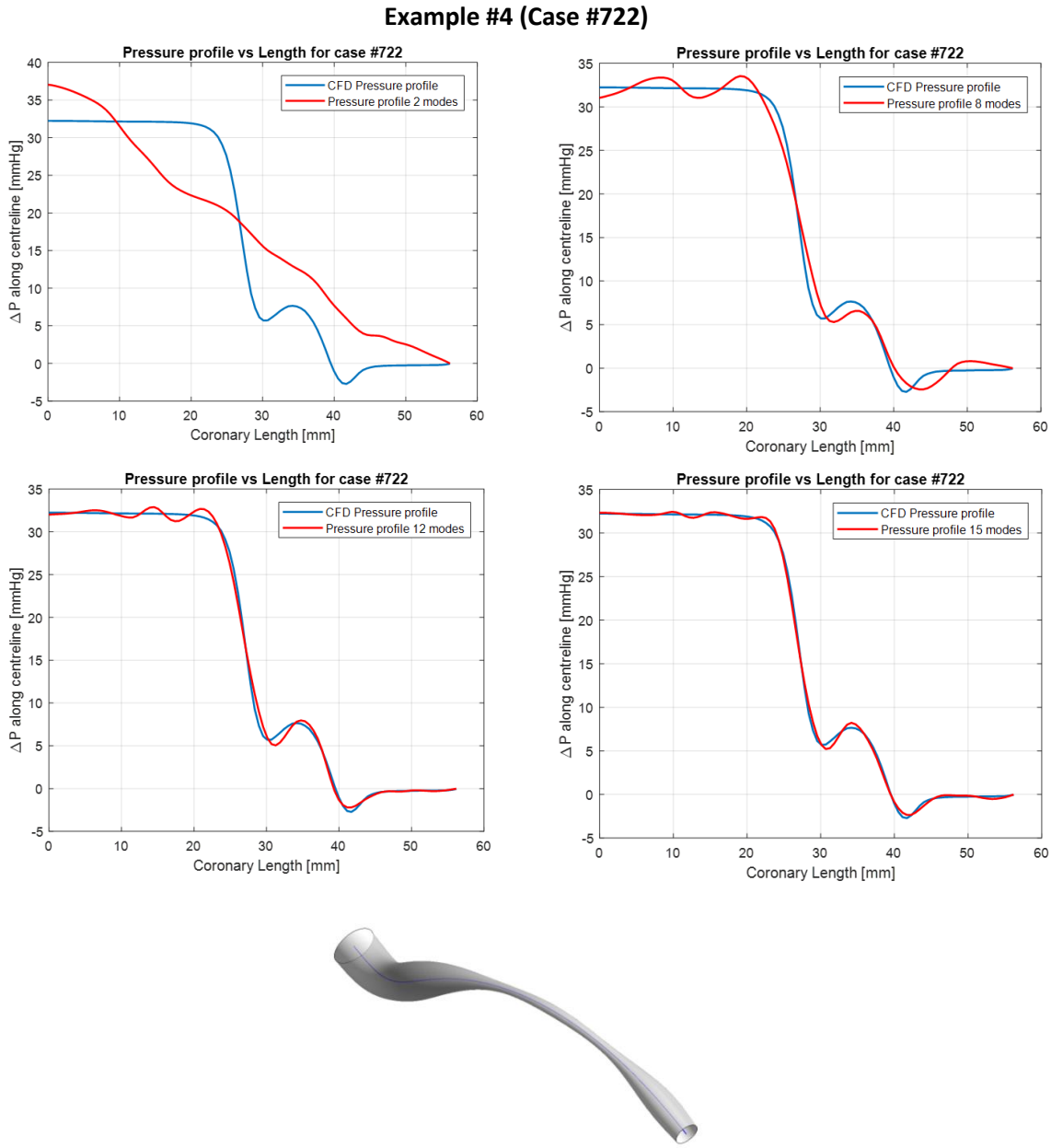

Figure 5.23: Results for a sample of four geometries chosen at random. The pressure profile is recomputed increasing the number of modes.

Figure 5.23 illustrates results for a sample of four of the cases, chosen at random, and indicates that the solutions for any artery in the training dataset can be effectively described by the reconstruction using relatively few modes. As second validation test, it is useful to show and demonstrate how the same set of modes can be employed to represent the pressure profile for a new case, not in the training set. The aim is to determine whether the coronary training dataset is rich enough, in the sense that the training dataset is able to capture all the pressure profiles variability.

To achieve this, the number of computed modes is kept fixed (m= 2 modes) whilst increasing the size of the training dataset (n= 20,100,200,300). The test is repeated multiple times for m= 8, 12, 15. The pressure profiles of the test dataset are projected into the base of modes computed with the training dataset.

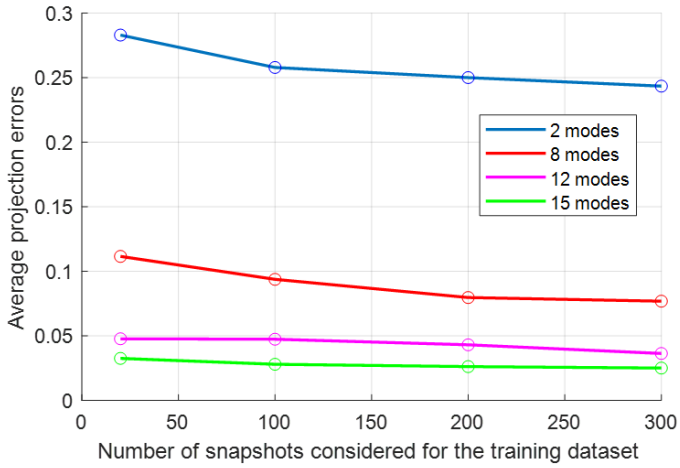

Figure 5.24: Projection errors considering different sizes of the training dataset.

As expected, the average projection errors decrease whilst increasing the number of pressure profiles for the dataset (Figure 5.24). Moreover, the average errors converge using a small number of modes (m= 2, 8, 12, 15) when the training set is composed of 200 arteries. It can be concluded that, assuming the selection of the training set was random, 200 CFD analyses are enough to determine a representative set of modes for this application members of the dataset.

5.5.2 Interpolation Errors

In the previous section it had been shown how the set of modes can represent any other pressure profile not used for the training dataset. However, the full CFD solutions to be recomputed were known and the modes coefficients have been computed projecting the full solutions into the base of modes. In this section it is introduced a method to compute the modes coefficients exploiting the input parameters of the training dataset taken into account when the full CFD solutions (described by new input parameters) are not known. With the input parameters available, the aim is to find a model which is capable of representing the system behaviour (outputs) in between the data points. The appropriate modes coefficients for the new system can be found by interpolation in the high dimensional space of the training set. Using an interpolation method can be advantageous for locating local variations in the behaviour response. This is also beneficial for locating area of the space that may require additional

refinement points. However, employing an interpolation method is not beneficial if the system response is noisy, in fact the fitting of the response surface could create multiple local minimums and/or maximums. Figure 5.25 shows a general example of a response surface with two inputs and one output to help the visualisation [97].

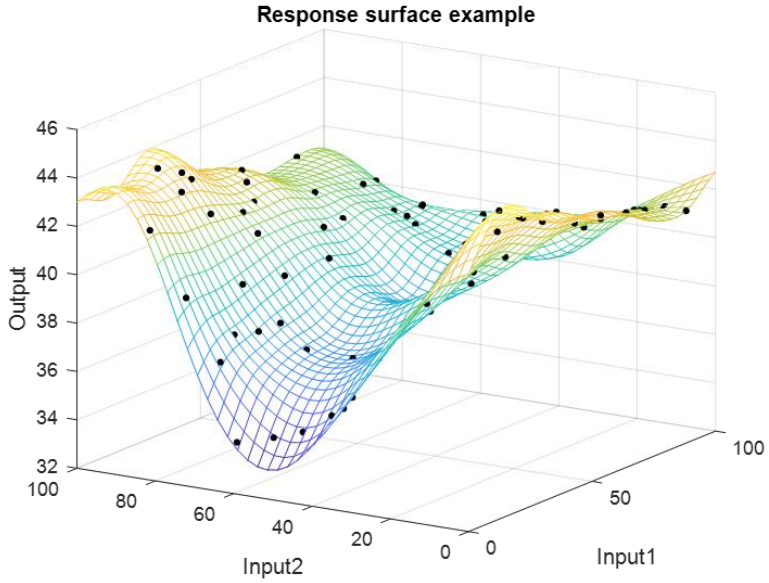

Figure 5.25: Example of a response surface with two inputs and one output.

The 3D phantom dataset consists of 329 different geometries, where every geometry is parameterised by 17 parameters. It had been chosen to consider 200 geometries for training and 129 geometries for evaluation and testing; the number of considered modes for the ROM is 15. Figure 5.26 shows a comparison between full solution, projected solution and ROM solution computed thanks to the interpolation for evaluating the modes coefficients for any new set of input parameters.

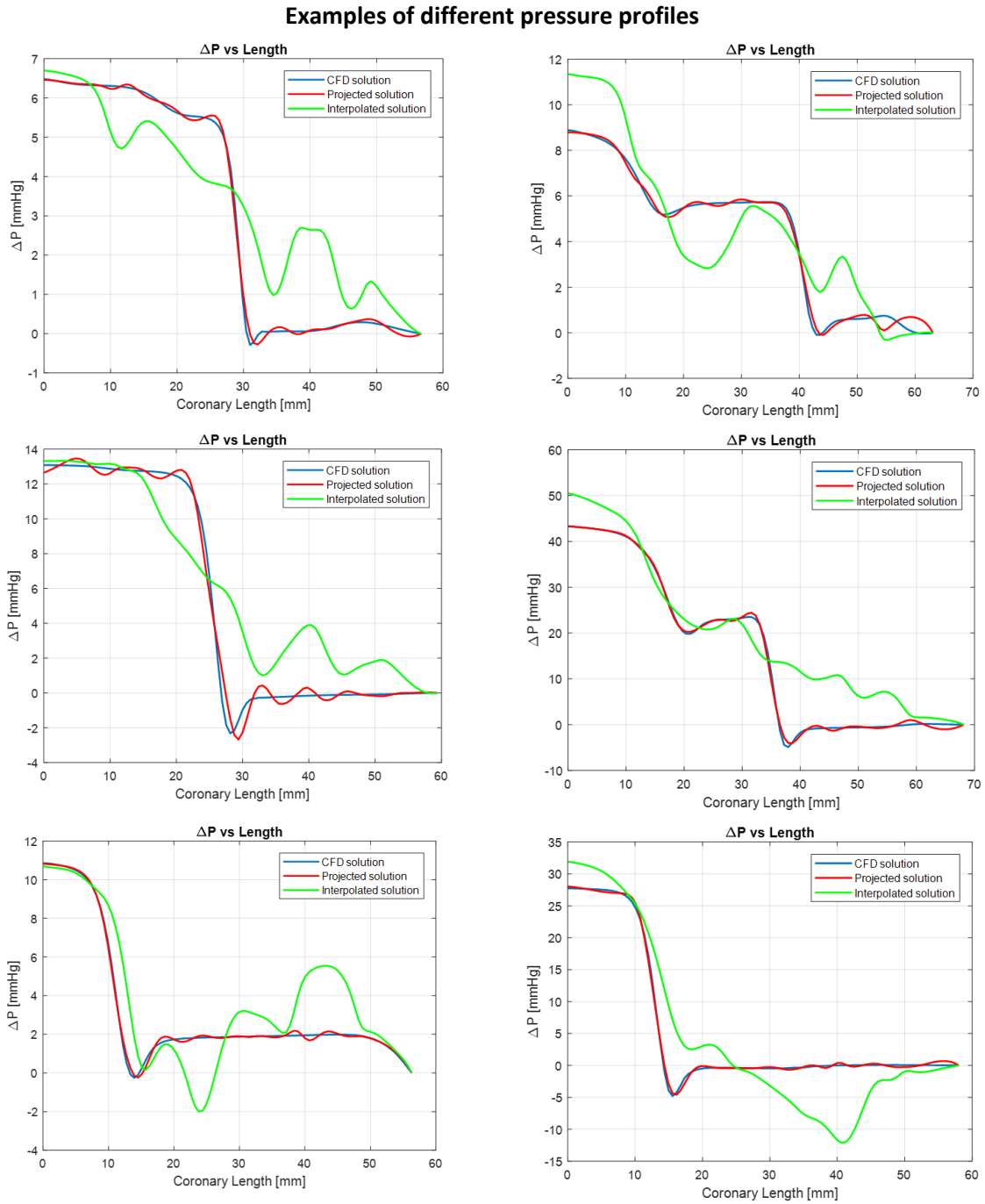

Figure 5.26: Comparison of pressure profiles for geometries outside the dataset between full CFD solution(blue), projected solution (red) and interpolated solution (green).

As it can be seen from Figure 5.26 the 15 modes computed from the training dataset can describe accurately any solution outside of the training dataset. This is also clear looking at the bar plot where the average projection error for the 129 geometries is less than 2.8% (Figure 5.27). The aim of this section was to give a brief introduction on how to compute the modes coefficients (outputs) starting from the parameters of the ROM (inputs). The ROM results

employing the interpolation step implemented in MATLAB are quite poor and it is clear that further improvements are necessary.

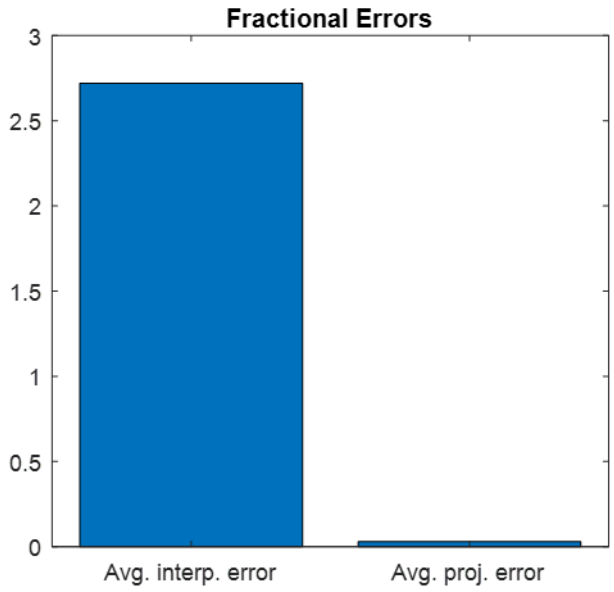

Figure 5.27: Average of the fractional errors (interpolation and projection)

5.6 Conclusions

In the first part of this chapter a comparison between full 3D simulations, 3D simulations with 2D coronary curvature and 2D axisymmetric models was presented. The second part presented a computational reduction algorithm for patient specific coronary artery geometries. A centreline parameterisation method was described, and it has been showed that the parameterisation is capable of capturing the overall curvature of the coronary with a good degree of accuracy. The parameterisation of the variation of the radius along the length introduced in the former chapter is coupled with the centreline parameterisation in order to create full patients-specific parameterised geometries. Following this parameterisation algorithm, a dataset of 329 3D volumetric meshes was created to populate the training dataset. Modes and modes coefficients were computed applying SVD to the correlation matrix. Furthermore, the projection error was computed for every geometry considered within the dataset.

Chapter 6
Conclusions and Future work

In this thesis, patient-specific coronary images and geometries are integrated into computational tools to achieve a computer based representation of the patient's physiology. There is specific focus on the fast computation of pressure profiles for patient-specific coronary geometries characterised by single or multiple lesions in series. The final result of the computational analysis is a quantitative value of the FFR index with sufficient accuracy to help clinicians on their decision making.

At the end of every chapter conclusions have been presented and this final chapter aims to summarise them.

6.1 Conclusions

The aim of this thesis was to characterise the clinical index of coronary Fractional Flow Reserve, using CFD and ROM techniques, for any patient-specific coronary geometry. The study is focused on single arteries, but arterial tree structures could be created by extension of the work flow.

The first step in achieving this goal was the development of a segmentation tool for coronary artery reconstruction. The tool was written in MATLAB and is able to reconstruct coronary arteries in 3D starting from 2D multi-single plane angiographic projection images. The 3D reconstruction supports quantitative assessment of the patient-specific vessel. A novel and simple table movement correction has been developed and successfully implemented in the tool. Coronary centrelines are identified manually, and this requires some user interaction, but it gives to the user more control than an automatic segmentation. A GUI has been designed in order to make the tool easy to use; the developed application can also be exported to any other machine without the need of having MATLAB installed. The output of the reconstruction tool is a 3D surface mesh (.stl) which can be imported to any CFD solver for fluid flow simulations after creating the volumetric mesh. Within this work the tool was validated by reconstructing a 3D printed straight tube with a single stenosis along the domain. Results were satisfactory, but highlighted the necessity to implement a process by which manual corrections could be made. Manual corrections are necessary to help the user to capture correctly the overall radius variation along the domain, but more important the minimum radius occurring at the stenosis location which is the predominant factor for overall pressure drop. Development of the tool has continued within the research group, and further validation was performed by a medical student as part of an intercalated Masters degree, for which a distinction was awarded, using 3D printed representations of patient-specific arteries.

Chapter 3 introduces a 2D ROM approach for idealised coronary arteries characterised by a single stenosis or multiple stenosis in series. The basic capacity of ROMs to reduce the computational demand relative to a full CFD simulation is highlighted. A challenging aspect regarding CFD simulations is the application of appropriate boundary conditions. In this thesis for the 2D and 3D CFD simulations, values of mass-flow rate has been defined at the inlet boundary and static pressure at the outlet boundary. To obtain values of mass-flow rate compatible with the clinical range, a first estimation of the mass-flow rate has been obtained

by coupling the 2D/3D model with a 0D model characterised by a clinical value of the distal resistance of the myocardial coronary vasculature. Multiple ROMs have been created comprising both single lesion and multiple lesions in series for a 2D axisymmetric straight geometry. Excellent results were achieved in terms of accuracy regarding pressure drops and computed FFR compared with high fidelity full 2D CFD simulations. One of the obvious questions is whether the ROM offers significant improvement in accuracy relative to alternative, even simpler, models. Pressure drops for a single stenosis and for multiple stenoses in series have been compared based on Bernoulli, 1D, ROM and CFD computations. The pressure drops and FFR values obtained with ROMs obtained better accuracy than Bernoulli or 1D computations, especially for serial stenoses. As might be expected, two stenosis in series act independently if they are distant from each other, and the total pressure drop is given by the summation of the two independent pressure drops. However, the closer the two stenosis are, the more they interact and the total pressure drop along the geometry is less than the sum of the pressure loss of each stenosis. This is difficult to capture with the simpler models, but the ROM performs well.

Following the study of idealised systems in Chapter 3, Chapter 4 goes on to apply the same 2D axisymmetric approach to the computation of FFR on coronary geometries with patient-specific variations of radius along the length of the artery. It is hypothesised that the radius variation is the most important characteristic of the stenotic artery, more important than any 3D curvatures of the centreline. A shape parameterisation technique is developed, using global basis functions to describe the radius variations. Different types of global basis functions were studied for shape parameterisation. The goal was to maintain unaltered the pressure profile considering a shape approximation. The shape parameterisation is twofold: geometrical parameters have been extracted from a coronary clinical dataset in order to create a large synthetic dataset similar to the clinical one and secondly to study the influence of anatomical variations on flow fields. The ROMs that were developed (which included 12 parameters, 11 geometrical and 1 physical) have been evaluated against both CFD and actual clinical measurements, achieving a good grade of accuracy related to the pressure gradient and FFR. The computation of the pressure drop using the ROMs is ≈ 900 times faster than a full CFD simulation.

The first part of Chapter 5 presents a comparison between different patient-specific representation models in order to establish the influence of coronary curvature on pressure profiles. A centreline based Fourier approximation is introduced, the former parameterisation coupled with the shape parameterisation allows to fully characterise any patient-specific coronary artery. The second part of the chapter assesses the construction of a 3D clinical ROM based on input parameters computed from a clinical dataset. Projection and interpolation errors are computed for a 3D phantom dataset based on 129 geometries. The interpolation errors suggest that further improvements are necessary.

6.2 Future Work

Computer *in silico* modelling in order to predict patient-specific clinical indices has shown great promise for the development of future healthcare. This thesis considered an example of computer-based modelling exploiting patient-specific clinical data in order to improve clinical decision making. However, a number of assumptions and limitations have been required for the development of the project.

Despite limitations in the segmentation tool developed for this thesis, described in detail in Chapter 2, it underpinned the extraction of the radius distributions that were used for development and testing of the ROM. One limiting factor is the construction of the 3D surface mesh with cross-sections formed by circles. Fitting cross sectional ellipses along the centreline would be beneficial in order to have a more natural representation of the coronary vessels. A further development for the tool could be designing an algorithm using more than two projection images to improve the reconstruction accuracy using the extra information given by the multiple views. The first version of the tool did not include the feature of manual corrections for vessel edge detection, but further development has already been made within the research team so that the tool now includes this feature. Since difficulties arise when epipolar lines are parallel to the vessel a hybrid approach for vessel reconstruction has also been implemented (epipolar lines plus other reconstruction method). Although manual centreline extraction gives more control to the user, a robust automatic centreline extraction could be explored in future development.

In chapter 3, ROMs for idealised geometries were introduced. Furthermore, a comparison on pressure drops computed with different methods was shown. A limiting factor in the

comparison for pressure drop between full CFD, ROMs and Bernoulli is the length of the considered idealised coronary. The pressure drop for CFD and ROMs was computed whilst the blood flow was still in recovery mode. This might not be relevant for coronaries, however it could be worth for a future study to consider a much longer tube and compute the pressure drop when pressure starts to diminish again following Poiseuille's law.

Several challenges were encountered in the shape parameterisation process for chapter 4. The first challenge was related to the number of global basis functions with geometrical parameters for describing the variation of the radius along the length. It could be thought that more complex is a model, a better representation of the system might be expected. The number of parameters chosen for the shape parameterisations impacts as well the dimensions of the parameter space for the ROM. Furthermore, as the complexity increases also the number of parameters increases requiring more points for the *off-line* training step of the ROM. However, it is not still clear what is the optimal amount of simulations for training the ROM, quantifying the optimal number of points related to the number of parameters could be beneficial. It might also be expected that the number of points depends on the form of the relationship between input and output parameters, a further development would be to detect the regions of the space characterised by high gradient and then refine the number of points in that region.

A major challenge for the development of the 3D clinical ROM, using the approach described in Chapters 2 and 3, is still the creation of isotopological volumetric meshes. Finding a robust and accurate method which accommodates large variations for the coronary arteries geometry has to be prioritised. Once isotopological meshes are available, a further development would be to consider a full 3D CFD solution for pressure values on the fluid volume instead of considering only the pressure profile along the 3D centreline. Of course, considering only the pressure profile along the 3D centreline is a simplification and does not exploit all the fluid flow information collected by a 3D flow field. In Chapter 5 the creation of the phantom dataset starts from a single LCA geometry which is morphed following a centreline and shape parameterisation; it would be beneficial to consider a larger cohort of clinical geometries for training the ROM. Regarding the 3D CFD simulations, an improvement could be to consider transient 3D simulations instead of a steady state, this change would also impact the way to populate the correlation matrix to compute the modes. In fact, differently from the steady state cases, the rows of the correlation matrix would contain fluid flow solutions at a different time

steps. It could be also interesting to consider a different model for the interpolation process for computing the modes coefficients.

6.3 Thesis in perspective

In this thesis, a new ROM approach for a fast and accurate computation of the FFR in patients with coronary artery diseases has been introduced. This approach provides a non-invasive and objective assessment of FFR from 3D reconstructed coronary geometries obtained from 2D angiography projection images. The proposed method is very fast and it computes FFR and full pressure profile for an unseen geometry in quasi real-time.

To the best of our knowledge, our approach is the first one in the literature which considers a ROM applied to a large cohort of clinical coronary arteries with lots of variability in terms of shapes between them. Furthermore, we considered ROMs in both 2D and 3D geometries with shape and centreline parameterisation.

We have proven that with the 2D ROM approach we obtained better results than the Bernoulli pressure drop computation. Furthermore, the 2D ROM had been tested against a 1D solver and even in this case the ROM performed better. Our ROM method is computationally efficient, in terms of both hardware requirements and computation speed since the on-line stage can run on an average laptop PC in seconds; so potentially it could be suited for clinical applications in the catheterisation laboratories during angiography.

The ROM approach has been shown to be effective on 2D geometries; however, when 3D geometries were considered (Chapter 5) limited success and poor results were achieved. Difficulties arose when the number of geometrical parameters started to increase, furthermore dealing with geometries characterised by very large deformations proved to be challenging. As already discussed, another factor influencing the accuracy of the ROM for the evaluation step is the interpolation method (*kriging*) in order to compute the modes coefficients for a completely new coronary geometry.

Possible paths for new research projects that can advance the work are listed below:

1. The ROM method applied to 2D coronary geometries has effectively proven itself. In Chapters 2, 3 and 4 strong fundamentals of the ROM approaches have been shown and proved. In order to bring the work forward, priority and attention has to be given to: creation of isotopological meshes for geometries with large deformations in 3D and investigation of different interpolation approaches for modes coefficients computation.

When changing the focus to 3D ROMs, it has been found difficult to deal with geometries with large deformations. For this reason, it would be interesting to develop two different 3D ROMs: first a ROM, which takes into account right coronary arteries, whilst the second ROM takes into account only the left coronary arteries. The idea here is that the centreline parameters do not change much when dealing with only one class of coronaries. For example, most of the right coronary arteries have all the same overall shape (C shape), and therefore the parameters describing the curvature should not have a lot of variability. The purpose is to ensure that the built ROM is most effective for the majority of the dataset considered (right or left coronary arteries).

2. A further approach can start from the same idea of computing FFR in an effective and accurate way. The development of machine learning algorithms with the implementation of deep neural networks in order to learn the non-linear relationships between inputs and outputs should be considered. In our case, a neural network could be coupled with POD; predicting the values of the modes coefficients (outputs) giving the set of input parameters.
   A simpler approach would exploit the neural network only to compute a single output (scalar value) such as the FFR values for different geometries. MATLAB (https://uk.mathworks.com/) or open-source deep learning frameworks (TensorFlow https://www.tensorflow.org/, PyTorch https://pytorch.org/) are already providing such powerful tools, with GPU support to speed up the training when large volumes of data are provided. Either way, the key ingredients for the design of a deep learning neural network are the availability of training data and the extraction of features which are most significant to the computation of the FFR.
   In a manner similar to the ROM workflow, the deep learning one would be composed by an off-line and an on-line stage.

   Off-line: In an ideal scenario, the training dataset will be composed by thousands of geometries extracted from different angiography images. However, segmenting thousands of geometries to create such a large dataset would be very time-consuming. To solve this issue, the main idea would be to consider a training dataset, which comprises of synthetic vessel generated from the geometrical parameters extracted from clinical geometries. In this thesis (Chapters 3, 4 and 5) a lot of work has been done in

this direction. The synthetic dataset is parameterised with the basis functions for the radius variation along the length introduced in Chapter 4 and the centreline parameterisation introduced in Chapter 5. CFD will be run for every single parameterised geometry and the corresponding value of the FFR will be logged.

The geometrical parameters will be used as input parameters for the network whilst the corresponding values of FFR (quantity of interest) will be used as output or target parameter. Whilst training, the network will learn the relationship between input and output parameters. Additionally, the set of input parameters could be expanded to include patient's information such as gender, age, weight, smoke etc. etc. which could play a significant role in determine the FFR value.

On-line: The trained neural network is deployed and can return a new value of FFR for a completely new geometry described by the input parameters.

6.4 Conclusion

In conclusion this thesis has demonstrated the value of accelerated computation for prediction of FFR under a range of cases. Feasibility is apparent, but the complexity of the 3D vessel geometry requires further developments and even further hardware. Nonetheless, such advances can be foreseen and consequently this thesis contributes an important element which can be ultimately anticipated to result in personalised computation of FFR in the future.

References

[1] P. D. Morris, F. N. Van De Vosse, P. V. Lawford, D. R. Hose, and J. P. Gunn, "'virtual' (Computed) Fractional Flow Reserve Current Challenges and Limitations," *JACC Cardiovasc. Interv.*, vol. 8, no. 8, pp. 1009–1017, 2015.

[2] G. An and U. Wilensky, "From Artificial Life to In Silico Medicine," in *Artificial Life Models in Software*, M. Komosinski and A. Adamatzky, Eds. London: Springer London, 2009, pp. 183–214.

[3] R. F. Rushmer, *Organ physiology: structure and function of the cardiovascular system*. WB Saunders Company, 1976.

[4] E. O. Feigl, "Coronary physiology.," *Physiol. Rev.*, vol. 63, no. 1, pp. 1–205, Jan. 1983.

[5] G. Baroldi and G. Scomazzoni, *Coronary circulation in the normal and the pathologic heart*. Office of the Surgeon General, Dept. of the Army;[for sale by the Superintendent of Documents, US Govt. Print. Off.], 1967.

[6] I. Kronzon and T. G. Matros, "Intraoperative echocardiography in minimally invasive cardiac surgery and novel cardiovascular surgical techniques," *Am. Heart Hosp. J.*, vol. 2, no. 4, pp. 198–204, 2004.

[7] H. Imamura, Y. Yoshimura, S. Nishimura, A. T. Nakazawa, C. Nishimura, and T. Shirota, "Oxygen uptake, heart rate, and blood lactate responses during and following karate training.," *Med. Sci. Sports Exerc.*, vol. 31, no. 2, pp. 342–347, 1999.

[8] O. Yamanaka and R. E. Hobbs, "Coronary artery anomalies in 126,595 patients undergoing coronary arteriography.," *Cathet. Cardiovasc. Diagn.*, vol. 21, no. 1, pp. 28–40, 1990.

[9] P. D. Morris *et al.*, "Virtual Fractional Flow Reserve From Coronary Angiography: Modeling the Significance of Coronary Lesions: Results From the VIRTU-1 (VIRTUal Fractional Flow Reserve From Coronary Angiography) Study," *JACC Cardiovasc. Interv.*, vol. 6, no. 2, pp. 149–157, Feb. 2013.

[10] P. J. Scanlon *et al.*, *ACC/AHA Guidelines for Coronary Angiography. A report of the American College of Cardiology/American Heart Association Task Force on Practice Guidelines (Committee on Coronary Angiography)*, vol. 33, no. 6. Elsevier Masson SAS, 1999.

[11] M. F. Di Carli and R. Hachamovitch, "New technology for noninvasive evaluation of coronary artery disease," *Circulation*, vol. 115, no. 11, pp. 1464–1480, 2007.

[12] X. Chen *et al.*, "Hemodynamics in coronary arterial tree of serial stenoses," *PLoS One*, vol. 11, no. 9, pp. 1–13, 2016.

[13] P. D. Morris *et al.*, "Computational fluid dynamics modelling in cardiovascular medicine," *Heart*, vol. 102, no. 1, pp. 18–28, 2016.

[14] B. De Bruyne and J. Sarma, "Fractional flow reserve: a review," *Heart*, vol. 94, no. 7, pp. 949–959, 2008.

[15] N. H. Pijls and B. De Bruyne, "Coronary pressure measurement and fractional flow reserve," *Heart*, vol. 80, no. 6, pp. 539–542, 1998.

[16] N. H. Pijls and B. De Bruyne, "Coronary pressure measurement and fractional flow reserve.," *Heart*, vol. 80, no. 6, pp. 539–42, Dec. 1998.

[17] N. P. Johnson *et al.*, "Prognostic value of fractional flow reserve: Linking physiologic severity to clinical outcomes," *J. Am. Coll. Cardiol.*, vol. 64, no. 16, pp. 1641–1654, 2014.

[18] A. Mehra and B. Mohan, "Value of FFR in clinical practice," *Indian Heart J.*, vol. 67,

no. 1, pp. 77–80, 2015.

[19] P. A. L. Tonino *et al.*, “Fractional flow reserve versus angiography for guiding percutaneous coronary intervention.,” *N. Engl. J. Med.*, vol. 360, no. 3, pp. 213–224, Jan. 2009.

[20] NICE - National Institute for Health and Care Excellence, “The Pressure PressureWire Wire fractional flow reserve e measurement system for coronary artery disease,” pp. 1–51, 2014.

[21] B. L. Nørgaard *et al.*, “Diagnostic performance of noninvasive fractional flow reserve derived from coronary computed tomography angiography in suspected coronary artery disease: the NXT trial (Analysis of Coronary Blood Flow Using CT Angiography: Next Steps),” *J. Am. Coll. Cardiol.*, vol. 63, no. 12, pp. 1145–1155, 2014.

[22] M. I. Papafaklis *et al.*, “Fast virtual functional assessment of intermediate coronary lesions using routine angiographic data and blood flow simulation in humans: comparison with pressure wire – fractional flow reserve,” *EuroIntervention*, vol. 10, no. 5, pp. 574–583, Sep. 2014.

[23] B. K. Koo *et al.*, “Diagnosis of ischemia-causing coronary stenoses by noninvasive fractional flow reserve computed from coronary computed tomographic angiograms: Results from the prospective multicenter DISCOVER-FLOW (Diagnosis of Ischemia-Causing Stenoses Obtained Via Noni,” *J. Am. Coll. Cardiol.*, vol. 58, no. 19, pp. 1989–1997, 2011.

[24] K. L. Gould *et al.*, “Anatomic versus physiologic assessment of coronary artery disease: Role of coronary flow reserve, fractional flow reserve, and positron emission tomography imaging in revascularization decision-making,” *J. Am. Coll. Cardiol.*, vol. 62, no. 18, pp. 1639–1653, 2013.

[25] J. K. Min *et al.*, “Diagnostic Accuracy of Fractional Flow Reserve From Anatomic CT Angiography,” *Jama*, vol. 308, no. 12, p. 1237, 2012.

[26] C. A. Taylor, T. A. Fonte, and J. K. Min, “Computational fluid dynamics applied to cardiac computed tomography for noninvasive quantification of fractional flow reserve: Scientific basis,” *J. Am. Coll. Cardiol.*, vol. 61, no. 22, pp. 2233–2241, 2013.

[27] J. A. Garcia *et al.*, “Rotational vs. standard coronary angiography: An image content analysis,” *Catheter. Cardiovasc. Interv.*, vol. 73, no. 6, pp. 753–761, 2009.

[28] B. De Bruyne, J. Bartunek, S. U. Sys, and G. R. Heyndrickx, “Relation between myocardial fractional flow reserve calculated from coronary pressure measurements and exercise-induced myocardial ischemia,” *Circulation*, vol. 92, no. 1, pp. 39–46, 1995.

[29] A. J. Physiol *et al.*, “Influence of hemodynamic conditions on fractional flow reserve : parametric analysis of underlying model Influence of hemodynamic conditions on fractional flow reserve : parametric analysis of underlying model,” no. May 2002, pp. 1462–1470, 2012.

[30] A. Melis, R. H. Clayton, and A. Marzo, “Bayesian sensitivity analysis of a 1D vascular model with Gaussian process emulators,” *Int. j. numer. method. biomed. eng.*, vol. 33, no. 12, pp. 1–11, 2017.

[31] E. Boileau *et al.*, “Estimating the accuracy of a reduced-order model for the calculation of fractional flow reserve (FFR),” *Int. j. numer. method. biomed. eng.*, vol. 34, no. 1, pp. 1–15, 2018.

[32] E. Boileau *et al.*, “A benchmark study of numerical schemes for one-dimensional arterial blood flow modelling,” *Int. j. numer. method. biomed. eng.*, vol. 31, no. 10, p. e02732, 2015.

[33] M. Willemet and J. Alastruey, “Arterial Pressure and Flow Wave Analysis Using Time-

Domain 1-D Hemodynamics," *Ann. Biomed. Eng.*, vol. 43, no. 1, pp. 190–206, 2014.

[34] K. Okrainec, D. K. Banerjee, and M. J. Eisenberg, "Coronary artery disease in the developing world," *Am. Heart J.*, vol. 148, no. 1, pp. 7–15, Jul. 2004.

[35] R. Petraco *et al.*, "Reply," *JACC Cardiovasc. Interv.*, vol. 7, pp. 228–229, 2014.

[36] S. Tu, G. Koning, W. Jukema, and J. H. C. Reiber, "Assessment of obstruction length and optimal viewing angle from biplane X-ray angiograms," *Int. J. Cardiovasc. Imaging*, vol. 26, no. 1, pp. 5–17, 2010.

[37] S.-Y. Chen, C. E. Metz, K. R. Hoffmann, and J. D. Carroll, "Improved Determination of Biplane Imaging Geometry and 3D Coronary Arterial Tree from Two Views," *Comput. Cardiol. 1994*, no. 4, pp. 653–656, 1994.

[38] P. Radeva, R. Toledo, C. Von Land, and J. Villanueva, "3D vessel reconstruction from biplane angiograms using snakes," *Comput. Cardiol. 1998. Vol. 25 (Cat. No.98CH36292)*, vol. 25, pp. 773–776, 1998.

[39] K. R. Hoffmann, A. Sen, L. Lan, K. G. Chua, J. Esthappan, and M. Mazzucco, "A system for determination of 3D vessel tree centerlines from biplane images," *Int. J. Card. Imaging*, vol. 16, no. 5, pp. 315–330, 2000.

[40] A. Wahle and E. Fleck, "Reconstruction from Biplane Angiograms," 1996.

[41] S. Y. J. Chen, J. D. Carroll, and J. C. Messenger, "Quantitative analysis of reconstructed 3-D coronary arterial tree and intracoronary devices," *IEEE Trans. Med. Imaging*, vol. 21, no. 7, pp. 724–740, 2002.

[42] Z. Zhang, "Determining the Epipolar Geometry and its Uncertainty: A Review," *Int. J. Comput. Vis.*, vol. 27, no. 2, pp. 161–195, 1998.

[43] X. Gang, "A Unified Approach to Image Matching and Segmentation in Stereo, Motion, and Object Recognition via Recovery of Epipolar Geometry," *Videre J. Comput. Vis. Res.*, vol. 1, no. 2, pp. 1–27, 1997.

[44] Z. ~Y. Zhang, "Determining The Epipolar Geometry And Its Uncertainty---{A} Review," *Ijcv*, vol. 27, no. 2, pp. 161–195, 1998.

[45] B. Movassaghi, V. Rasche, M. A. Viergever, and W. J. Niessen, "Accurate coronary modeling procedure using 2D calibrated projections based on 2D centerline-points on a single projection," *Proc. SPIE - Int. Soc. Opt. Eng.*, vol. 5370 III, no. May 2004, 2004.

[46] A. C. M. Dumay, J. H. C. Reiber, and J. J. Gerbrands, "Determination of Optimal Angiographic Viewing Angles: Basic Principles and Evaluation Study," *IEEE Trans. Med. Imaging*, vol. 13, no. 1, pp. 13–24, 1994.

[47] Y. Huo, M. Svendsen, J. S. Choy, Z.-D. Zhang, and G. S. Kassab, "A validated predictive model of coronary fractional flow reserve.," *J. R. Soc. Interface*, vol. 9, no. 71, pp. 1325–38, 2012.

[48] A. Andriotis *et al.*, "A new method of three-dimensional coronary artery reconstruction from X-ray angiography: Validation against a virtual phantom and multislice computed tomography," *Catheter. Cardiovasc. Interv.*, vol. 71, no. 1, pp. 28–43, 2008.

[49] J. C. Messenger, S. Y. J. Chen, J. D. Carroll, J. E. B. Burchenal, K. Kioussopoulos, and B. M. Groves, "3D coronary reconstruction from routine single-plane coronary angiograms: Clinical validation and quantitative analysis of the right coronary artery in 100 patients," *Int. J. Card. Imaging*, vol. 16, no. 6, pp. 413–427, 2000.

[50] J. D. Anderson and J. Wendt, *Computational fluid dynamics*, vol. 206. Springer, 1995.

[51] D. A. Steinman, "Image-based computational fluid dynamics modeling in realistic arterial geometries," *Ann. Biomed. Eng.*, vol. 30, no. 4, pp. 483–497, 2002.

[52] Y. Hoi *et al.*, "Effects of arterial geometry on aneurysm growth: three-dimensional

computational fluid dynamics study," *J. Neurosurg.*, vol. 101, no. 4, pp. 676–681, 2004.

[53] R. Krams *et al.*, "Evaluation of endothelial shear stress and 3D geometry as factors determining the development of atherosclerosis and remodeling in human coronary arteries in vivo: combining 3D reconstruction from angiography and IVUS (ANGUS) with computational fluid dyna," *Arterioscler. Thromb. Vasc. Biol.*, vol. 17, no. 10, pp. 2061–2065, 1997.

[54] T. J. Pedley, B. S. Brook, and R. S. Seymour, "Blood pressure and flow rate in the giraffe jugular vein.," *Philos. Trans. R. Soc. Lond. B. Biol. Sci.*, vol. 351, no. 1342, pp. 855–866, 1996.

[55] S. Chaturantabut, "Proper Orthogonal Decomposition (POD)," 2008.

[56] M. Systems, "PROPER ORTHOGONAL DECOMPOSITION FOR MODEL UPDATING OF NON-LINEAR MECHANICAL SYSTEMS," vol. 15, pp. 31–43, 2001.

[57] N. Hraiech, C. Boichon, M. Rochette, T. Marchal, and M. Horner, "Statistical Shape Modeling of Femurs Using Morphing and Principal Component Analysis," *J. Med. Device.*, vol. 4, no. 2, p. 027534, 2010.

[58] V. Luboz *et al.*, "Personalized modeling for real-time pressure ulcer prevention in sitting posture," *J. Tissue Viability*, vol. 27, no. 1, pp. 2–9, 2018.

[59] A. Manzoni, A. Quarteroni, and G. Rozza, "Model reduction techniques for fast blood flow simulation in parametrized geometries," no. October 2011, pp. 604–625, 2012.

[60] H. Chen, D. L. Reuss, and V. Sick, "A practical guide for using proper orthogonal decomposition in engine research," vol. 14, no. 4, pp. 307–319, 2012.

[61] E. K. W. Poon *et al.*, "Advances in three-dimensional coronary imaging and computational fluid dynamics: Is virtual fractional flow reserve more than just a pretty picture?," *Coron. Artery Dis.*, vol. 26, pp. e43–e54, 2015.

[62] B. Movassaghi, V. Rasche, M. Grass, M. A. Viergever, and W. J. Niessen, "A quantitative analysis of 3-D coronary modeling from two or more projection images," *IEEE Trans. Med. Imaging*, vol. 23, no. 12, pp. 1517–1531, 2004.

[63] B. Movassaghi, V. Rasche, R. Florent, M. A. Viergever, and W. Niessen, "3D coronary reconstruction from calibrated motion-compensated 2D projections," *Int. Congr. Ser.*, vol. 1256, no. C, pp. 1079–1084, 2003.

[64] C. H. Lee and H.-J. Yoon, "Medical big data: promise and challenges," *Kidney Res. Clin. Pract.*, vol. 36, no. 1, pp. 3–11, 2017.

[65] F. Miralles, D. Gomez-Cabrero, M. Lluch-Ariet, J. Tegnér, M. Cascante, and J. Roca, "Predictive medicine: outcomes, challenges and opportunities in the Synergy-COPD project," *J. Transl. Med.*, vol. 12, no. 2, p. S12, 2014.

[66] J. S. Rumsfeld, K. E. Joynt, and T. M. Maddox, "Big data analytics to improve cardiovascular care: promise and challenges," *Nat. Rev. Cardiol.*, vol. 13, no. 6, p. 350, 2016.

[67] C. A. Taylor *et al.*, "Predictive medicine: Computational techniques in therapeutic decision-making," *Comput. Aided Surg. Off. J. Int. Soc. Comput. Aided Surg.*, vol. 4, no. 5, pp. 231–247, 1999.

[68] F. Licastro and C. Caruso, "Predictive diagnostics and personalized medicine for the prevention of chronic degenerative diseases," in *Immunity & Ageing*, 2010, vol. 7, no. 1, p. S1.

[69] M. Qattan, C. Demonacos, and M. Krstic-Demonacos, "Roadmap to personalized medicine," *Croat. Med. J.*, vol. 53, no. 4, pp. 294–297, 2012.

[70] F. R. Vogenberg, “Predictive and prognostic models: implications for healthcare decision-making in a modern recession,” *Am. Heal. drug benefits*, vol. 2, no. 6, p. 218, 2009.

[71] R. Bellazzi and B. Zupan, “Predictive data mining in clinical medicine: current issues and guidelines,” *Int. J. Med. Inform.*, vol. 77, no. 2, pp. 81–97, 2008.

[72] B. Regierer, V. Zazzu, R. Sudbrak, A. Kühn, H. Lehrach, and Itf. Consortium, “Future of medicine: models in predictive diagnostics and personalized medicine,” in *Molecular Diagnostics*, Springer, 2013, pp. 15–33.

[73] Y. Lee, H. Bang, and D. J. Kim, “How to establish clinical prediction models,” *Endocrinol. Metab.*, vol. 31, no. 1, pp. 38–44, 2016.

[74] E. Hansis, D. Schäfer, O. Dössel, and M. Grass, “Projection-based motion compensation for gated coronary artery reconstruction from rotational x-ray angiograms,” *Phys. Med. Biol.*, vol. 53, no. 14, pp. 3807–3820, 2008.

[75] U. Jandt, D. Schäfer, M. Grass, and V. Rasche, “Automatic generation of 3D coronary artery centerlines using rotational X-ray angiography,” *Med. Image Anal.*, vol. 13, no. 6, pp. 846–858, 2009.

[76] K. Wiesent *et al.*, “Enhanced 3-D-reconstruction algorithm for C-arm systems suitable for interventional procedures,” *IEEE Trans. Med. Imaging*, vol. 19, no. 5, pp. 391–403, 2000.

[77] N. Navab *et al.*, “3D reconstruction from projection matrices in a C-arm based 3D-angiography system,” in *International Conference on Medical Image Computing and Computer-Assisted Intervention*, 1998, pp. 119–129.

[78] R. Fahrig, A. J. Fox, S. Lownie, and D. W. Holdsworth, “Use of a C-arm system to generate true three-dimensional computed rotational angiograms: preliminary in vitro and in vivo results.,” *Am. J. Neuroradiol.*, vol. 18, no. 8, pp. 1507–1514, 1997.

[79] G. A. Mastin, “Adaptive filters for digital image noise smoothing: An evaluation,” *Comput. Vision, Graph. Image Process.*, vol. 31, no. 1, pp. 103–121, 1985.

[80] F. Cheriet and J. Meunier, “Self-calibration of a biplane X-ray imaging system for an optimal three dimensional reconstruction,” *Comput. Med. Imaging Graph.*, vol. 23, no. 3, pp. 133–141, 1999.

[81] B. Movassaghi, V. Rasche, M. Grass, M. A. Viergever, and W. J. Niessen, “A quantitative analysis of 3-D coronary modeling from two or more projection images,” *IEEE Trans. Med. Imaging*, vol. 23, no. 12, pp. 1517–1531, 2004.

[82] T. V. Nguyen and J. Sklansky, “Reconstructing the 3-D Medial Axes of Coronary Arteries in Single-View Cineangiograms,” *IEEE Trans. Med. Imaging*, vol. 13, no. 1, pp. 61–73, 1994.

[83] B. Movassaghi, V. Rasche, M. A. Viergever, and W. Niessen, “Quantitative analysis of 3D coronary modeling in 3D rotational X-ray imaging,” *2002 IEEE Nucl. Sci. Symp. Conf. Rec.*, vol. 2, pp. 878–880, 2002.

[84] J. C. Shiuh-yung, “On-line 3D reconstruction of coronary arterial tree based on a single-plane imaging system,” *Circulation*, vol. 96, no. 8S, p. 308–I, 1997.

[85] Wai-Shun Tong, Chi-Keung Tang, and Gerard G. Medioni, “Epipolar Geometry Estimation for Non-Static Scenes by 4D Tensor Voting,” *Cvpr*, pp. 926–933, 2001.

[86] A. M. Vukicevic, S. Çimen, N. Jagic, G. Jovicic, A. F. Frangi, and N. Filipovic, “Three-dimensional reconstruction and NURBS-based structured meshing of coronary arteries from the conventional X-ray angiography projection images,” *Sci. Rep.*, vol. 8, no. 1, pp. 1–20, 2018.

[87] J. Yang, Y. Wang, Y. Liu, S. Tang, and W. Chen, "Novel approach for 3-D reconstruction of coronary arteries from two uncalibrated angiographic images," *IEEE Trans. Image Process.*, vol. 18, no. 7, pp. 1563–1572, 2009.

[88] P. a Zisserman, "C4 Computer Vision 4," 2004.

[89] Z. Zhang, R. Deriche, O. Faugeras, and Q. T. Luong, "A robust technique for matching two uncalibrated images through the recovery of the unknown epipolar geometry," *Artif. Intell.*, vol. 78, no. 1–2, pp. 87–119, 1995.

[90] A. Quarteroni and G. Rozza, *Reduced Order Methods for Modeling and Computational Reduction*. 2014.

[91] R. Milani, A. Quarteroni, and G. Rozza, "Reduced basis method for linear elasticity problems with many parameters ∗," 2008.

[92] Y. Lang *et al.*, "Reduced Order Model Based on Principal Component Analysis for Process Simulation and Optimization †," no. 3, pp. 1695–1706, 2009.

[93] C. W. Rowley, "MODEL REDUCTION FOR FLUIDS , USING BALANCED PROPER ORTHOGONAL DECOMPOSITION," pp. 1–24, 2005.

[94] J. H. Citriniti and W. K. George, "Reconstruction of the global velocity field in the axisymmetric mixing layer utilizing the proper orthogonal decomposition," vol. 418, pp. 137–166, 2000.

[95] D. Amsallem, M. J. Zahr, and C. Farhat, "Nonlinear Model Order Reduction Based on Local Reduced-Order Bases."

[96] F. Ballarin *et al.*, "CORONARY ARTERY BYPASS GRAFTS BASED ON A POD – GALERKIN."

[97] S. N. Lophaven, J. Søndergaard, and H. B. Nielsen, "DACE A Matlab Kriging Toolbox," *IMM Informatiocs Math. Model.*, pp. 1–28, 2002.

[98] A. Hoare, D. G. Regan, and D. P. Wilson, "Sampling and sensitivity analyses tools (SaSAT) for computational modelling," *Theor. Biol. Med. Model.*, vol. 5, pp. 1–18, 2008.

[99] S. Blower and H. Dowlatabadi, "Sensitivity and uncertainty analysis of complex models of disease transmission: an HIV model, as an example," *Int. Stat. Rev.*, vol. 62, no. 2, pp. 229–243, 1994.

[100] F. Donati *et al.*, "Beyond Bernoulli: Improving the Accuracy and Precision of Noninvasive Estimation of Peak Pressure Drops," *Circ. Cardiovasc. Imaging*, vol. 10, no. 1, pp. 1–9, 2017.

[101] J. J. Heys, N. Holyoak, A. M. Calleja, M. Belohlavek, and H. P. Chaliki, "Revisiting the Simplified Bernoulli Equation," *Open Biomed. Eng. J.*, vol. 4, pp. 123–128, 2010.

[102] M. F. Rubby, M. S. Rana, and A. B. M. T. Hasan, "Hemodynamics of physiological blood flow through a double stenosed artery," *Procedia Eng.*, vol. 105, no. Icte 2014, pp. 893–901, 2015.

[103] V. Damodaran, G. W. Rankin, and C. Zhang, "Numerical study of steady laminar flow through tubes with multiple constrictions using curvilinear co-ordinates," *Int. J. Numer. Methods Fluids*, vol. 23, no. 10, pp. 1021–1041, 1996.

[104] M. K. Banerjee, D. Nag, R. Ganguly, and A. Datta, "Stenotic interaction on haemodynamic parameters in double stenoses," *Int. J. Comut. Fluid Dyn.*, vol. 22, no. 9, pp. 609–622, 2008.

[105] P. R. Johnston and D. Kilpatrick, "Mathematical modelling of paired arterial stenoses," *[1990] Proc. Comput. Cardiol.*, pp. 229–232, 1990.

[106] M. A. K. Azad and L. S. Andallah, "An Analytical Solution of 1D Navier-Stokes

Equation," vol. 5, no. 2, 2014.

[107] A. Brault, L. Dumas, and D. Lucor, "Uncertainty quantification of inflow boundary condition and proximal arterial stiffness coupled effect on pulse wave propagation in a vascular network," no. July, pp. 1–33, 2016.

[108] C. M. Otto, "Valvular Aortic Stenosis. Disease Severity and Timing of Intervention," *J. Am. Coll. Cardiol.*, vol. 47, no. 11, pp. 2141–2151, 2006.

[109] F. Galassi *et al.*, "3D reconstruction of coronary arteries from 2D angiographic projections using nonuniform rational basis splines (NURBS) for accurate modelling of coronary stenoses," *PLoS One*, vol. 13, no. 1, pp. 1–23, 2018.

[110] H. Ha *et al.*, "Estimating the irreversible pressure drop across a stenosis by quantifying turbulence production using 4D Flow MRI," *Sci. Rep.*, vol. 7, no. April, pp. 1–14, 2017.

[111] G. Rozza, F. Ballarin, and Y. Maday, "Reduced order methods for parametric Fluid-Structure Interaction problems: applications to haemodynamics," 2017.

[112] I. Marinić-Kragić, D. Vučina, and M. Ćurković, "Efficient shape parameterization method for multidisciplinary global optimization and application to integrated ship hull shape optimization workflow," *CAD Comput. Aided Des.*, vol. 80, pp. 61–75, 2016.

[113] M. J. Aftosmis and G. R. Anderson, "Adaptive Shape Parameterization for Aerodynamic Design," no. NAS Technical Report: NAS-2015-02 Adaptive, p. 58, 2013.

[114] J. A. Samareh, "A survey parameterization," pp. 333–344, 2001.

[115] W. Song and A. Keane, "A Study of Shape Parameterisation Methods for Airfoil Optimisation," *10th AIAA/ISSMO Multidiscip. Anal. Optim. Conf.*, pp. 1–8, 2004.

[116] G. Rozza *et al.*, "ADVANCES IN REDUCED ORDER METHODS FOR PARAMETRIC INDUSTRIAL PROBLEMS IN COMPUTATIONAL FLUID DYNAMICS," no. June, pp. 11–15, 2018.

[117] J. Nava, O. Kosheleva, and V. Kreinovich, "Why bernstein polynomials are better: Fuzzy-inspired justification," *IEEE Int. Conf. Fuzzy Syst.*, 2012.

[118] N. Li, H. Zhang, and H. Ouyang, "Shape optimization of coronary artery stent based on a parametric model," *Finite Elem. Anal. Des.*, vol. 45, no. 6–7, pp. 468–475, 2009.

[119] W. Wu *et al.*, "Finite element shape optimization for biodegradable magnesium alloy stents," *Ann. Biomed. Eng.*, vol. 38, no. 9, pp. 2829–2840, 2010.

[120] O. Dur, S. T. Coskun, K. O. Coskun, D. Frakes, L. B. Kara, and K. Pekkan, "Computer-aided patient-specific coronary artery graft design improvements using CFD coupled shape optimizer," *Cardiovasc. Eng. Technol.*, vol. 2, no. 1, pp. 35–47, 2011.

[121] S. Pant, N. W. Bressloff, and G. Limbert, "Geometry parameterization and multidisciplinary constrained optimization of coronary stents," *Biomech. Model. Mechanobiol.*, vol. 11, no. 1–2, pp. 61–82, 2012.

[122] P. Morin, R. H. Nochetto, M. S. Pauletti, and M. Verani, "Adaptive finite element method for shape optimization∗," *ESAIM Control. Optim. Calc. Var.*, vol. 18, no. 4, pp. 1122–1149, 2012.

[123] A. Quarteroni and G. Rozza, "Optimal control and shape optimization of aorto-coronaric bypass anastomoses," *Math. Model. Methods Appl. Sci.*, vol. 13, no. 12, pp. 1801–1823, 2003.

[124] G. Rozza, A. Quarteroni, "Shape design by optimal flow control and reduced basis techniques: applications to bypass configurations" 2005, PhD Thesis, EPFL Lousanne.

[125] G. Rozza, "On optimization, control and shape design of an arterial bypass" no. April 2004, pp. 1411–1419, 2005.

[126] V. Agoshkov, A. Quarteroni, and G. Rozza, "A mathematical approach in the design of

arterial bypass using unsteady Stokes equations," *J. Sci. Comput.*, vol. 28, no. 2, pp. 139–165, 2006.

[127] V. Agoshkov, A. Quarteroni, and G. Rozza, "Shape design in aorto-coronaric bypass anastomoses using perturbation theory," *SIAM J. Numer. Anal.*, vol. 44, no. 1, pp. 367–384, 2006.

[128] A. Manzoni, A. Quarteroni, and G. Rozza, "Shape optimization for viscous flows by reduced basis methods and free-form deformation," *Int. J. Numer. Methods Fluids*, vol. 70, no. 5, pp. 646–670, 2012.

[129] L. Toni, M. Andrea, Q. Alfio, and R. Gianluigi, "Boundary control and shape optimization for the robust design of bypass anastomoses under uncertainty" vol. 47, pp. 1107–1131, 2013.

[130] T. Lassila and G. Rozza, "Parametric free-form shape design with PDE models and reduced basis method," *Comput. Methods Appl. Mech. Eng.*, vol. 199, no. 23–24, pp. 1583–1592, 2010.

[131] F. Ballarin *et al.*, "Fast simulations of patient-specific haemodynamics of coronary artery bypass grafts based on a POD-Galerkin method and a vascular shape parametrization," *J. Comput. Phys.*, vol. 315, no. 25, pp. 609–628, 2016.

[132] F. Ballarin *et al.*, "A fast virtual surgery platform for many scenarios haemodynamics of patient-specific coronary artery bypass grafts."

[133] N. Demo, M. Tezzele, and G. Gustin, "Shape Optimization by means of Proper Orthogonal Decomposition and Dynamic Mode Decomposition arXiv : 1803 . 07368v2 [math . NA] 12 Apr 2018," pp. 1–12, 2018.

[134] S. Lorthois, F. Lauwers, and F. Cassot, "Tortuosity and other vessel attributes for arterioles and venules of the human cerebral cortex," *Microvasc. Res.*, vol. 91, pp. 99–109, 2014.

[135] M. Willemet and J. Alastruey, "Arterial pressure and flow wave analysis using time-domain 1-D hemodynamics," *Ann. Biomed. Eng.*, vol. 43, no. 1, pp. 190–206, 2015.

[136] Y. Shi, P. Lawford, and R. Hose, "Review of zero-D and 1-D models of blood flow in the cardiovascular system," *Biomed. Eng. Online*, vol. 10, no. 1, p. 33, 2011.

[137] C. M. Colciago, S. Deparis, and D. Forti, "7. Fluid-structure interaction for vascular flows: From supercomputers to laptops," *Fluid-Structure Interact.*, no. 140184, pp. 1–51, 2017.

[138] K. A. Kopecky, "Function Approximation," no. x, pp. 1–12, 2007.

[139] G. Pruessner, "Numerical methods and data analysis," pp. 210–240, 2012.

[140] S. Amherst, G. Konidaris, and S. Osentoski, "Value Function Approximation in Reinforcement Learning using the Fourier Basis," 2008.

[141] F. Salmoiraghi, F. Ballarin, G. Corsi, A. Mola, M. Tezzele, and G. Rozza, "Advances in geometrical parametrization and reduced order models and methods for computational fluid dynamics problems in applied sciences and engineering: overview and perspectives," 2016.

[142] J. F. LaDisa Jr *et al.*, "Stent design properties and deployment ratio influence indexes of wall shear stress: a three-dimensional computational fluid dynamics investigation within a normal artery," *J. Appl. Physiol.*, vol. 97, no. 1, pp. 424–430, 2004.

[143] J. F. LaDisa *et al.*, "Three-dimensional computational fluid dynamics modeling of alterations in coronary wall shear stress produced by stent implantation," *Ann. Biomed. Eng.*, vol. 31, no. 8, pp. 972–980, 2003.

[144] D. R. Wells, J. P. Archie Jr, and C. Kleinstreuer, "Effect of carotid artery geometry on

the magnitude and distribution of wall shear stress gradients," *J. Vasc. Surg.*, vol. 23, no. 4, pp. 667–678, 1996.

[145] L. Boussel *et al.*, "Aneurysm growth occurs at region of low wall shear stress: patient-specific correlation of hemodynamics and growth in a longitudinal study," *Stroke*, vol. 39, no. 11, pp. 2997–3002, 2008.

[146] A. Coenen *et al.*, "Fractional Flow Reserve Computed from Noninvasive CT Angiography Data: Diagnostic Performance of an On-Site Clinician-operated Computational Fluid Dynamics Algorithm," *Radiology*, vol. 274, no. 3, pp. 674–683, 2015.

[147] L. Antiga, M. Piccinelli, L. Botti, B. Ene-Iordache, A. Remuzzi, and D. A. Steinman, "An image-based modeling framework for patient-specific computational hemodynamics," *Med. Biol. Eng. Comput.*, vol. 46, no. 11, p. 1097, 2008.

[148] T. Lassila, A. Manzoni, A. Quarteroni, and G. Rozza, "Boundary control and shape optimization for the robust design of bypass anastomoses under uncertainty," *ESAIM Math. Model. Numer. Anal.*, vol. 47, no. 4, pp. 1107–1131, 2013.

[149] D. N. Ghista and F. Kabinejadian, "Coronary artery bypass grafting hemodynamics and anastomosis design: a biomedical engineering review," *Biomed. Eng. Online*, vol. 12, no. 1, p. 129, 2013.

[150] F. Migliavacca and G. Dubini, "Computational modeling of vascular anastomoses," *Biomech. Model. Mechanobiol.*, vol. 3, no. 4, pp. 235–250, 2005.

[151] A. L. Marsden, "Optimization in Cardiovascular Modeling," 2014.

[152] A. A. Owida, H. Do, and Y. S. Morsi, "Numerical analysis of coronary artery bypass grafts: An over view," *Comput. Methods Programs Biomed.*, vol. 108, no. 2, pp. 689–705, 2012.

[153] Al Akhras H., "Automatic Isogeometric Analysis Suitable Trivariate Models Generation – Application to Reduced Order Modeling,", T. De Doctorat, 2016.